Sources and detection of high-energy cosmic events

Valentin Decoene

▶ To cite this version:

Valentin Decoene. Sources and detection of high-energy cosmic events. High Energy Astrophysical Phenomena [astro-ph.HE]. Sorbonne Université, 2020. English. NNT : 2020SORUS028 . tel-03153273v4

HAL Id: tel-03153273
https://theses.hal.science/tel-03153273v4
Submitted on 26 Feb 2021

HAL is a multi-disciplinary open access archive for the deposit and dissemination of scientific research documents, whether they are published or not. The documents may come from teaching and research institutions in France or abroad, or from public or private research centers.

L'archive ouverte pluridisciplinaire **HAL**, est destinée au dépôt et à la diffusion de documents scientifiques de niveau recherche, publiés ou non, émanant des établissements d'enseignement et de recherche français ou étrangers, des laboratoires publics ou privés.

Sorbonne Université
École Doctorale Astronomie et Astrophysique d'Ile-de-France

Thèse de doctorat

réalisée
à l'Institut d'Astrophysique de Paris
sous la direction de
Kumiko Kotera et Olivier Martineau

présentée par

Valentin Decoene

Sources and detection of high-energy cosmic events

Sera soutenue publiquement le **22 Septembre 2020**, devant un jury compos de :

Marie-Christine Angonin, Professeur - Sorbonne Université, Présidente du Jury

Mathieu de Naurois, Directeur de recherche CNRS - LLR, Rapporteur

Abigail Vieregg, Associate Professor, Chicago University, Rapportrice

Ralph Engel, Professor, IKP-KIT, Examinateur

Philippe Zarka, Directeur de recherche CNRS, LESIA, Examinateur

Kumiko Kotera, Chargée de recherche CNRS, IAP, Directrice de thèse

Olivier Martineau, Maitre de conférence - Sorbonne Université, Co-directeur de thèse

Contents

List of Acronyms

ADF	Angular Distribution Function: angular model for the signal amplitude distribution of inclined EAS on ground.
AIRES	AIRshower Extended Simulations: Monte-Carlo simulation code for the development and evolution of particles shower. Similar to CORSIKA.
BH	Black Hole: most compact object of the Universe and described as a space time singularity from which even light cannot escape.
CMI	Cyclotron Maser Instability (or Electron Cyclotron Maser): plasma instability which under specific conditions leads to a coherent emission from non thermal electrons population.
CoREAS	Corsika Radio Emission from Air Showers: Monte-Carlo simulation code, combining the CORSIKA simulation code and the End-Point formalism to compute the radio emission from particles shower. Similar to ZHAireS.
CORSIKA	COsmic Ray SImulations for KAscade: Monte-Carlo simulation code for the development and evolution of particles shower. Similar to AIRES.
DANTON	DecAyiNg Taus frOm Neutrinos: Monte-Carlo simulation of tau neutrino interactions inside the Earth.
DM	(radio-astronomy) Dispersion Measure: quantity describing the time delay between high and low frequencies in a measured dynamical spectrum and related to the electron column density crossed by the measured emission.
EAS	Extensive Air Shower: atmospheric particle shower.
EM	Electro-Magnetic
EPOS	Energy conserving quantum mechanical multiple scattering approach based on Partons (parton ladders) Off-shell remnants, and Splitting of parton ladders: hadronic

interaction model used in Monte-Carlo simulation code of particle shower.

FM (band) Frequency Modulation: radio-diffusion process commonly used for radio broadcasts. By extension it is also the name given to the $87-107\,\mathrm{MHz}$ bandwidth of the civilian radio.

FRB Fast Radio Burst: newly discovered class of radio transient sources. The exact emission mechanism and population source of these phenomenon remain unknown yet.

GRB Gamma Ray Burst: well-known source of transient gamma ray emissions. Two populations have been observed with two distinct emission length: long GRB and short GRB. The first one is believed to result from the collapse of massive stars (collapsar) and the second one is believed to be produced by the merger of two neutron stars.

HBA (LOFAR) high-band antennas: high frequency sub-array of the LOFAR telescope.

HE High Energy: energy regime typically above $10^{15}\,\mathrm{eV}$.

HorizonAntenna Antenna designed for the GP300 experiment.

IC Inverse Compton: interaction process between photons and massive particles and leading to an energy transfert from the particles to the photons.

LBA (LOFAR) low-band antennas: low frequency sub-array of the LOFAR telescope.

LF Low Frequency.

LSS (NenuFAR) LOFAR Super Station: observation mode involving both the NenuFAR telescope and the LOFAR telescope.

MA Mini Array: name of the sub-arrays composing the NenuFAR telescope.

MGMR Macroscopic Geo-Magnetic Radiation: formalism to describe analytically the radio emission from EAS from a macroscopic point of view, using only the geo-magnetic contribution to the emission.

MHD Magneto-Hydro-Dynamics: formalism to describe the physical coupling of hydrodynamics and electro-magnetic forces. Used in particular in the description of plasma.

NEC4 Numerical Electromagnetic Code 4: computation software for the antennas response.

NKG (lateral distribution function) Nishimura-Kamata-Greisen: model of particle density lateral profile, used for the description of EAS.

NS	Neutron Star: one of the three possible end-state of commons stars, created during core collapse super novae and resulting the most compact object of the Universe after the black holes.
PREM	Preliminary Earth Model: model for the underground rocks compositions of the Earth.
Radio Morphing	semi analytic procedure to simulate radio emissions from EAS.
RASPASS	Radio Aires Special Primary for Atmospheric Skimming Showers: extension to the ZHAireS simulation code for up-going trajectory and multi particles shower development.
RFI	Radio Frequency Interferences: radio emissions characterised with narrow frequencies and from human origin. Generally considered as noise in radio-astronomy.
RM (radio-astronomy)	Rotation Measure: quantity describing the evolution of the polarisation vectors in a measured dynamical spectrum and related to the magnetic field intensity, parallel to the measured emission path.
SFR	Star Formation Rate: describes the rate of stars birth (or formation) evolving with the Universe history.
SNR (astrophysics)	Super Nova Remnant.
SNR (experimental)	Signal to Noise Ratio.
Sybill	Hadronic interaction model Monte-Carlo simulation code of particles shower.
UHE	Ultra High Energy: energy regime typically above 10^{18} eV.
UHECR	Ultra High Energy Cosmic Rays: Cosmic rays with energies typically above 10^{18} eV.
ZHAireS	ZHS Aires simulation software: Monte-Carlo simulation code, combining the AIRES simulation code and the ZHS formalism to compute the radio emission from particles shower. Similar to CoREAS.
ZHS	Zas Halzen Stanev: formalism for particles shower radio emission computation. See ZHAireS.

Experiments

AERA Auger Engineering Radio Array `https://www.auger.org/index.php/observatory/aera`

ANITA ANtartic Impulsive Transient Antenna `https://www.phys.hawaii.edu/~anita/new/html/collaboration.html`

ARIANNA Antarctic Ross Ice-shelf AnteNna Neutrino Array `http://arianna.ps.uci.edu`

ASKAP Australian SKA Pathfinder `https://www.atnf.csiro.au/projects/askap/index.html`

CHIME Canadian Hydrogen Intensity Mapping Experiment `https://chime-experiment.ca/en`

CODALEMA COsmic ray Detection Array with Logarithmic ElectroMagnetic Antennas `http://codalema.in2p3.fr`

Fermi-LAT Fermi Large Area Telescope: imaging high energy gamma-ray space telescope `https://fermi.gsfc.nasa.gov`

GMRT Giant Metrowave Radio Telescope `http://www.gmrt.ncra.tifr.res.in`

GP300 GRANDProto 300 `https://grand.cnrs.fr/grand/grandproto300/`

GRAND Giant Radio Array for Neutrino Detection `https://grand.cnrs.fr`

IceCube Neutrino observatory located in Antartica `https://icecube.wisc.edu`

IceCube Gen2 Second generation upgrade of IceCube `https://icecube.wisc.edu/science/beyond`

INTEGRAL INTErnational Gamma-Ray Astrophysics Laboratory: imaging gamma-ray space telescope `http://www.esa.int/Science_Exploration/Space_Science/Integral`

KASCADE KArlsruhe Shower Core and Array DEtector `https://web.ikp.kit.edu/KASCADE/`

KASCADE-Grande Extension of the KASCADE detector

KM3NET Cubic Kilometer Neutrino Telescope, located in the Mediterranean sea `https://www.km3net.org`

LIGO Laser Interferometer Gravitational-wave Observatory `https://www.ligo.org`

LOFAR LOw Frequency ARray `http://www.lofar.org`

LOPES LOfar ProtoypE Station `https://www.etp.kit.edu/english/lopes.php`

LWA Long Wavelength Array `http://www.phys.unm.edu/~lwa/index.html`

NenuFAR	New Extension in Nançay Upgrading LOFAR `https://nenufar.obs-nancay.fr/en/homepage-en/`
NRO	Nançay Radio Observatory `https://www.obs-nancay.fr`
NRT	Nançay Radio Telescope `https://www.obs-nancay.fr/radiotelescope-decimetrique/`
PAO	Pierre Auger Observatory `https://www.auger.org`
POEMMA	Probe Of Extreme Multi-Messenger Astrophysics `https://poemma.uchicago.edu`
Pushchino	Russian radio observatory located in Pushchino-on-Oka `http://www.prao.ru/English/`
RNO	Radio Neutrino Observatory `https://arxiv.org/abs/1907.12526`
SKA	Square Kilometer Array `https://www.skatelescope.org`
TREND	Tianshan Radio Experiment for Neutrino Detection `https://grand.cnrs.fr/grand/prototypes/`
uGMRT	Upgrade of GMRT
Virgo	Laser interferometer for gravitational waves detection `https://www.virgo-gw.eu`

Units and Constants

α_e	Fine structure constant: $7.2973525664(17) \times 10^{-3}$ (SI)
ϵ_0	Vacuum electric permittivity: $8.8541878128(13) \times 10^{-12}\,\mathrm{F.m^{-1}}$ (SI)
$\mu 0$	Vacuum electric permeability: $\sim 12.57 \times 10^{-7}\,\mathrm{H.m^{-1}}$ (SI)
Ω	Ohm: $1\,\mathrm{m^2.kg.s^{-3}.A^{-2}}$ (SI)
Ω_Λ	Cosmological dark energy density parameter ($\Lambda - CDM$ model): 0.685 (SI)
Ω_M	Cosmological density parameter ($\Lambda - CDM$ model): 0.315 (SI)
σ_T	Thompson cross section: $6.652 \times 10^{-29}\,\mathrm{m^{-2}}$ (SI)
c	Vacuum speed of light: $2.99792458 \times 10^{8}\mathrm{m.s^{-1}}$ (SI)
H_0	Hubble constant: $\sim 67.4\,\mathrm{km.s^{-1}.Mpc^{-1}}$ (SI)
k_B	Boltzmann constant: $1.380649 \times 10^{-23}\,\mathrm{J.K^{-1}}$ (SI) $= 1.380649 \times 10^{-16}\mathrm{erg.K^{-1}}$ (CGS)
$M_\odot$	Solar Mass: $(1,9884 \pm 0.0002) \times 10^{30}\,\mathrm{kg}$ (SI)
m_e	Electron mass: $9.10938356 \times 10^{-31}\,\mathrm{kg}$ (SI)
m_p	Proton mass: $1.6726219 \times 10^{-27}\,\mathrm{kg}$ (SI)
a	Stefan-Boltzmann constant: $\sim 5.6703\times10^{-8}\,\mathrm{W.m^{-2}.K^{-4}}$ (SI) $= 5.6703\times10^{-5}\,\mathrm{erg.cm^{-2}.K^{-4}.s^{-1}}$ (CGS)
A.U.	Astronomical Unit: $1.49597870700 \times 10^{11}\,\mathrm{m}$ (SI)
CGS	Centimetres Grams Seconds: alternative units system commonly used in astrophysics and astronomy
erg	erg (CGS): $= 10^{-7}\,\mathrm{J}$ (SI)
eV	electron Volt: $\sim 1,602176634 \times 10^{-19}\mathrm{J}$ (SI) $\sim 1,602176634 \times 10^{-12}\,\mathrm{erg}$ (CGS)
G	Gauss (CGS): $= 10^{-4}\,\mathrm{T}$ (SI)
G	Gravitational constant: $6.67408 \times 10^{-11}\,\mathrm{m^3.kg^{-1}.s^{-2}}$ (SI)
g	grams
h	Planck constant: $6.6260755(40)\times10^{-34}\,\mathrm{J.s}$ (SI) $= 6.6260755(40)\times10^{-27}\,\mathrm{erg.s}$ (CGS)
Hz	Hertz: $1\,\mathrm{s^{-1}}$ (SI)
J	Joule: $1\,\mathrm{kg.m^2.s^{-2}}$ (SI) $= 10^{7}\mathrm{erg}$ (CGS)
Jy	Jansky: $10^{-26}\,\mathrm{W.m^{-2}Hz^{-1}}$ (SI) $= 10^{-23}\,\mathrm{erg.s^{-1}.cm^{-1}Hz^{-1}}$ (CGS).
K	Kelvin (SI and CGS)

m	Metre (SI)
pc	Parsec: $\sim 3,085677581 \times 10^{16}\,\mathrm{m}$ (SI)
R	Perfect gas constant: $\sim 8.32\,\mathrm{J.K^{-1}.mol^{-1}}$ (SI)
s	Second (SI)
SI	International System
T	Tesla (SI)
V	Volt (SI)
yr	sideral year: $315581498 \times 10^{7}\,\mathrm{s}$ (SI)

Introduction

In the last decade, new classes of powerful sources (binary neutron star mergers, fast radio bursts, tidal disruption events, superluminous supernovae, ...) have been discovered thanks to progress in photon astronomy at all wavelengths. With the advent of multi-messenger astronomy, we were able to scrutinize these sources with cosmic rays (mostly atomic nuclei constantly bombarding the Earth), neutrinos, photons and gravitational waves [1].

In October 2017, one month after I started my Ph.D., the detection of the first gravitational waves from a neutron star merger was announced [2]. Spectacularly, this merger, GW170817, was observed not only in gravitational waves, but also in photons, from radio to gamma-ray wavelengths [3, 4]. This joint observation provided many answers to secular puzzles (e.g., the origin of short gamma-ray bursts, the nucleosynthesis of elements heavier than iron, tests of the equivalence principle, etc.), but obviously also opened many questions. For the high-energy astroparticle physics community, one obvious question that arose was: why was no neutrino detected in coincidence to this event [5, 6], and could there have been any?

During the three years of my Ph.D., two other important multi-messenger detections were reported. In 2018, a gamma-ray flare from blazar TXS0506+056 (an active galactic nucleus with a relativistic jet directed towards the observer) was detected by the Fermi-LAT satellite [7] and was observed in coincidence with a high-energy neutrino at the IceCube Observatory [8]. This remarkable observation could be explained by the production of high energy neutrino via the acceleration and interaction of cosmic rays inside the black hole jet of the blazar, although complex models have to be invoked to explain the whole spectral observations (e.g., [9, 10, 11, 12, 13, 14]).

More recently, in 2020 an a-posteriori search of high energy neutrinos in the IceCube archival data led to the discovery of an event coinciding with a radio emission (measured by various radio astronomical facilities) from tidal disruption event AT2019dsg (a flaring event that occurs when a star approaches a supermassive black hole) [15]. It is believed that during the tidal disruption phase the accreted material from the disrupted star, around the black hole, powers a relativistic jet which would be at the origin of neutrinos emissions in a similar way as the blazar model evoked above (e.g., [16, 17]).

These observations, and the well of information and questionings that they have brought, show that high-energy neutrinos have definitely started to play a crucial role in our understanding of the workings of the most powerful sources. Indeed, neutrinos are valuable messengers for multi-messenger *astronomy*. Unlike cosmic rays, they are not deflected by the ubiquitous magnetic fields of the Universe, and can directly point back to their sources. Neutrinos are hardly absorbed, contrarily to gamma-rays, enabling the observation of sources at much larger distances. Finally, they are a clear signature of hadronic processes taking place inside cosmic accelerators [18].

But neutrinos are also elusive: their low interaction probability with matter makes them challenging to detect, and very large volumes or areas have to be instrumented in order to collect them. This is particularly the case at the highest energies, where the neutrino fluxes are expected to be extremely low – this can be roughly understood by scaling from their parent cosmic-ray flux. Since 2013, IceCube has been detecting high-energy neutrinos up to a few PeV ($= 10^{15}\,$eV) [19]. Beyond this energy lies a completely uncharted territory for neutrino astrophysics and astronomy. These ultra-high energy neutrinos are guaranteed to exist, as by-products of the interactions of ultra-high energy cosmic rays with the photons of the cosmic microwave background, while propagating through the Universe. The flux level of these so-called *cosmogenic* neutrinos strongly varies according to the source models, but robust predictions have been made for the most pessimistic scenarii [20, 21]. Note however that this guaranteed flux may be much dimmer than the high and ultra-high energy neutrino flux directly produced inside astrophysical sources.

One possible technique to cover very large areas at affordable cost could be radio detection. Ultra-high energy neutrinos can be observed through the following processes: first a tau neutrino produces the associated tau lepton through a charge current interaction under the Earth surface, then the tau lepton decays after emerging in the atmosphere, finally, the electromagnetic radiation of the induced particle shower can be detected by its radio emission [22]. This is the detection mechanism envisioned by the Giant Radio Array for Neutrino Detection (GRAND) project [23], in the framework of which this Ph.D. work was carried out. GRAND is a high energy observatory dedicated to ultra-high energy astroparticles (cosmic rays, neutrinos and gamma-rays). It will also be able to scan the sky in search of radio-transient events (FRBs, Giant Radio Pulses, etc.). It is designed to reach a sensitivity which should ensure the detection of the cosmogenic neutrino fluxes even under the pessimistic scenario.

A major achievement for the radio community was reported in 2016 by two experiments: LOFAR and AERA both demonstrated that the primary particle parameters could be reconstructed with radio data as precisely as with other standard detection techniques such as scintillators, fluorescence, water tanks, etc. [24, 25, 26, 27, 28]. However, several great challenges remain to be overcome in order to make of radio-detection a fully efficient technique, and to build a gigantic array such as GRAND. In particular, the autonomous radio detection of inclined air showers and their reconstruction are critical questions. Promising efforts for autonomous radio detection have recently been carried out by AREA and TREND [28, 29], but with limited efficiency. Regarding the reconstruction of inclined air showers, the angular resolution achievable on the arrival direction of the primary is of paramount importance for neutrino astronomy. The 300 antenna array GRANDProto300 will investigate these questions by providing a large scale test-bench.

While multi-messenger astronomy was taking off, another –somehow related– field was flourishing: millisecond transient radio astronomy and Fast Radio Burst (FRB) astrophysics. The origin of FRBs, these brief, coherent and numerous radio pulses, has not been identified yet. At the beginning of my Ph.D., a dozen FRBs had been detected. Today, the ASKAP and CHIME surveys reports > 700 of them, among which 21 identified repeaters, while only 2 were known three years ago. Very recently, some light has been shed on the mystery with the detection of X-ray flares from source SGR1935+2154, in coincidence with two millisecond radio bursts [30, 31]. The source appears to be a Galactic magnetar –a highly magnetised class of neutron star. The detected radio bursts were however 40 times dimmer than the dimmest FRB known.

Until the recent discovery of SGR1935+2154, in almost twenty years of FRBs search, no multi-wavelength (nor multi-messenger) observations had been achieved. The situation appears quite similar to that of the gamma ray bursts (GRB) community in the 1950s: the lack of experimental constraints does not allow for a discrimination of the multiple theoretical models. Even though the ASKAP and CHIME surveys have achieved a large number of observations, providing preliminary information, many questions remains.

From a theoretical perspective, no consensual emission mechanism has been found, neither an explanation for the two observed populations of repeaters and non repeaters. From the observational perspective, the existence of FRBs at frequencies below Pushchino observations (111 MHz), as well as the polarisation signatures (if any) have not been evidenced yet. During my Ph.D., the low frequency observatory NenuFAR (located in the Nançay Radioastronomy Station) started its commissioning phase, with a call for early science observation programs. This gave me the unique opportunity to launch an observation program on the search for FRBs in this novel frequency band. The results of this program could have important implications for the design of GRAND and GRANDProto300.

Fast radio bursts and high-energy astroparticles could have the same origin, with similar physics at play. Many models of FRBs source, such as the compact binary or the magnetar origin for example, could also lead to the emission of other messengers [32, 33, 34, 35]. The questions explored in the context of millisecond transient radio astronomy are thus interlinked with all the problems and challenges invoked above about multi-messenger astronomy and high-energy neutrino astronomy. Working at the interface between these two communities allows us to build bridges between them, and lead to a mutual enrichment of the methods, techniques and theoretical approaches. As the advent of the multi-wavelength astronomy resulted in unprecedented breakthroughs in the understanding of GRBs at the end of the previous century, the advent of the multi-messenger astronomy will drive the future discoveries of this century.

The first part of this thesis is dedicated to the study of cosmic neutrinos. In Chapter 1, I introduce some basics of particle acceleration and interactions inside the radiative background of powerful sources, and present a model for the production of high-energy neutrinos from the merger of binary neutron stars systems. A published version of this work can be found in Ref. [36]. Chapter 2 and Chapter 3 of this thesis focus on the questions of the observation of UHE neutrinos. I first introduce some principles of air-shower emission physics and present a study on the optimisation for the GRAND project (Chapter 2 and Ref. [23, 37]). I then propose in Chapter 3 a full reconstruction method for the arrival direction and the maximum longitudinal development of the air-shower, in the framework of the GRAND and GRANDProto300 projects, a work to be submitted for publication soon.

The second part of this thesis is dedicated to the study of fast radio bursts. In Chapter 4, I present a model of fast radio bursts which successfully models the population of repeaters and non-repeaters, using the population of neutron-star-black hole binary systems with an asteroid belt surrounding the neutron star (work to be submitted soon). Finally, in Chapter 5, I present an observational program which aims at detecting fast radio bursts at low frequencies with the NenuFAR radio array, located at the Nançay Radioastronomy Station. More information on this program can be found here [38]. I also present some preliminary studies for the use of GRAND and GRANDProto300 as radio transient observatories.

Part I

Cosmic neutrinos

Chapter 1

Cosmic neutrino source: a Neutron Star Merger based model

1.1 Introduction

A large number and variety of explosive transient sources (magnetar flares, blazar flares, tidal disruption events, neutron star mergers, etc.) are being routinely discovered thanks to progress on instrumental sensitivity and time resolution. Many of these sources were found to be promising producers of high energy neutrinos, and a great volume of literature has been written on this subject (see [39] and references therein). The possibility to observe these transient populations is also being examined by future experiments [23, 40]. In a generic study, Ref. [39] assessed the capability of various sources to produce high energy cosmic rays and neutrinos, as a function of the two main parameters describing transient sources, namely their time variability and their bolometric luminosity. From these parameters and simple phenomenological modelings as described in the next section, the maximum energy achieved for particles is calculated. The results are represented in the diagrams of Figures 1.1, where the location of various types of sources is over-layed. It appears that from this criterion, binary neutron star mergers are a priori a promising source of high-energy and ultra-high energy neutrinos [1].

The recent coincident detection of the binary neutron star (NS) merger GW170817 in gravitational waves and across the electromagnetic spectrum[2, 3, 6], has launched a new era in multi-messenger astronomy. Combined information provides new insights into the workings of particle acceleration and of the emissions taking place in compact objects and

---

[1] We consider here only the case of non-relativistic acceleration regions (Lorentz boost $\Gamma \sim 1$). Relativistic scenarios are also promising, and have been explored by other authors [41, 42, 43, 44, 45].

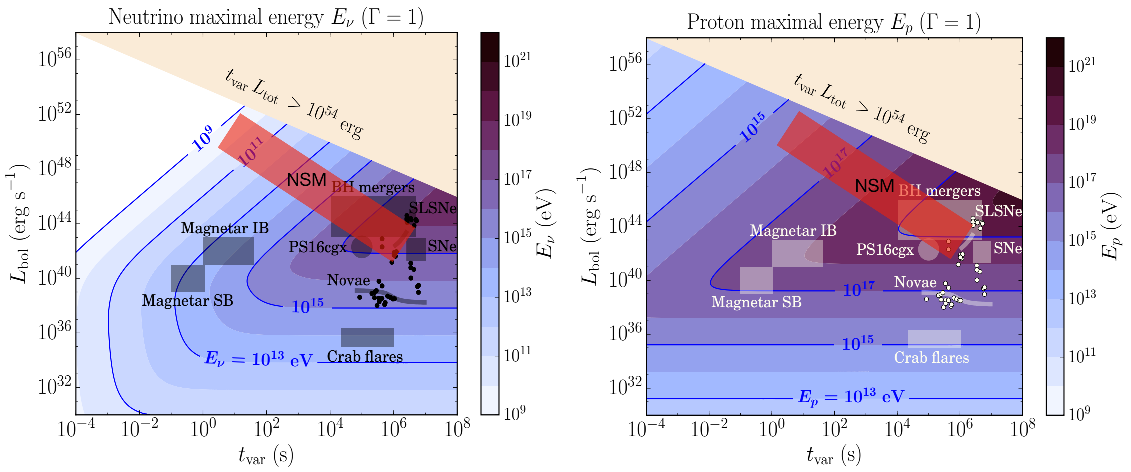

Figure 1.1: Maximal neutrino energy (*left*) and maximal proton energy (*right*) as function of the time variability and bolometric luminosity of the source. Examples of sources, with their parameter ranges, are overlayed (Magnetar IB and SB indicate respectively intermediate bursts and short bursts, and SNe and SLSNe, supernovae and superluminous supernovae). Neutron star mergers (NSM) are shown with a red band, with a luminosity-time variability dependency following Equation 1.12), which we will explain in this Chapter. Neutron star mergers appear to be a good candidate for the production of high and ultra-high energy neutrinos and cosmic rays. Adapted from [39].

their environments. Among the discoveries from GW170817 was thermal optical/infrared emission (”kilonova”) powered by the radioactive decay of heavy nuclei synthesised in the merger ejecta (e.g. [46]). Therefore a study of the neutrino emissions from these events would greatly benefit from these observations and would enrich our picture for future observations.

Indeed, observations from GW170817 already taught us that environments of NS mergers are *a priori* ideal sites to produce copious neutrino fluxes, due to their large energy reservoirs, abundant source material to accelerate, and sizeable radiative background fields for the accelerated particles to interact with. Recent studies have shown that cosmic rays production up to energies near the so-called “ankle” feature in the Galactic cosmic ray spectrum ($\lesssim 3 \times 10^{18}$ eV) may be plausible in such merger events [42, 47]. Searches for GeV-EeV neutrinos directionally coincident with GW170817 within various time windows, were conducted with ANTARES, IceCube and the Pierre Auger Observatory, but no detections were reported [5]. The non-detection of GW170817 was found to be consistent with the models of neutrino production in binary NS mergers that had been postulated then [41, 48].

The end state of a binary neutron star merger is likely to be a black hole (BH) surrounded by a gaseous accretion disk, which powers a collimated relativistic jet producing a short gamma-ray burst (GRB) (e.g., [49, 50, 51, 52, 53]). Hence many of the existing models that estimate neutrino fluxes from NS mergers are related to GRBs observed at different viewing angles. The most promising neutrino-production mechanism from GRBs is related to the temporally extended X-ray/gamma-ray emission seen from a fraction of short GRBs (e.g. [54]), for which the mild Lorentz factor of the outflows responsible for powering this emission enables a high meson production efficiency [41, 42, 43, 44, 45] (see Section 1.2). Other studies [55, 48] assume that the merger forms a magnetar capable of accelerating UHE particles, and calculate the abundant neutrino emission produced via interaction with the surrounding merger ejecta shell.

In this work, we examine a different scenario for neutrino production from NS mergers. At late times after the merger, a small fraction of the ejecta (e.g. from the tidal tail, or the promptly-formed accretion disk) remains marginally bound to the black hole, falling back to it over a range of timescale from seconds to days or longer. Being too cold to cool effectively through (thermal) neutrino emission, yet too dense to cool through photon emission, the resulting accretion flow is radiatively-efficient (e.g. [56]) and susceptible to produces powerful disk winds (e.g. [57]) or a wide angle jet from the inner regions close to the black hole as depicted in Figure 1.2. These outflows will emerge into the cavity behind the higher mass ejecta shell released earlier during the merger and its immediate aftermath (that responsible for powering the observed kilonova emission) and will collide with its backside, generating shocks or forcing magnetic reconnection. We assume that such an interaction will result in efficient cosmic-ray acceleration in a nebula behind the ejecta shell (see Section 1.3) and focus on the interaction of high-energy particles with the surrounding ejecta shell. We model for this purpose the evolution of the radiative and baryonic density of the dynamical ejecta over time, including heating via nuclear and fallback processes (Section 1.4). We calculate self-consistently via a Monte-Carlo code the energy losses and interactions experienced by cosmic rays, as well as their secondary neutrino fluxes as a function of time (Section 1.5). We present our neutrino fluxes from single sources and integrated over whole populations for standard sets of source parameters, as narrowed down by the observation of GW170817, and for an optimistic scenario which can lead to an enhanced neutrino flux. We also estimate the rate of neutrino events expected from a merger population jointly detected in gravitational waves.

Quantities will be labelled $Q_x \equiv Q/10^x$ in CGS units unless specified otherwise, and except for particle energies which are in $E_x \equiv E/10^x\,\mathrm{eV}$.

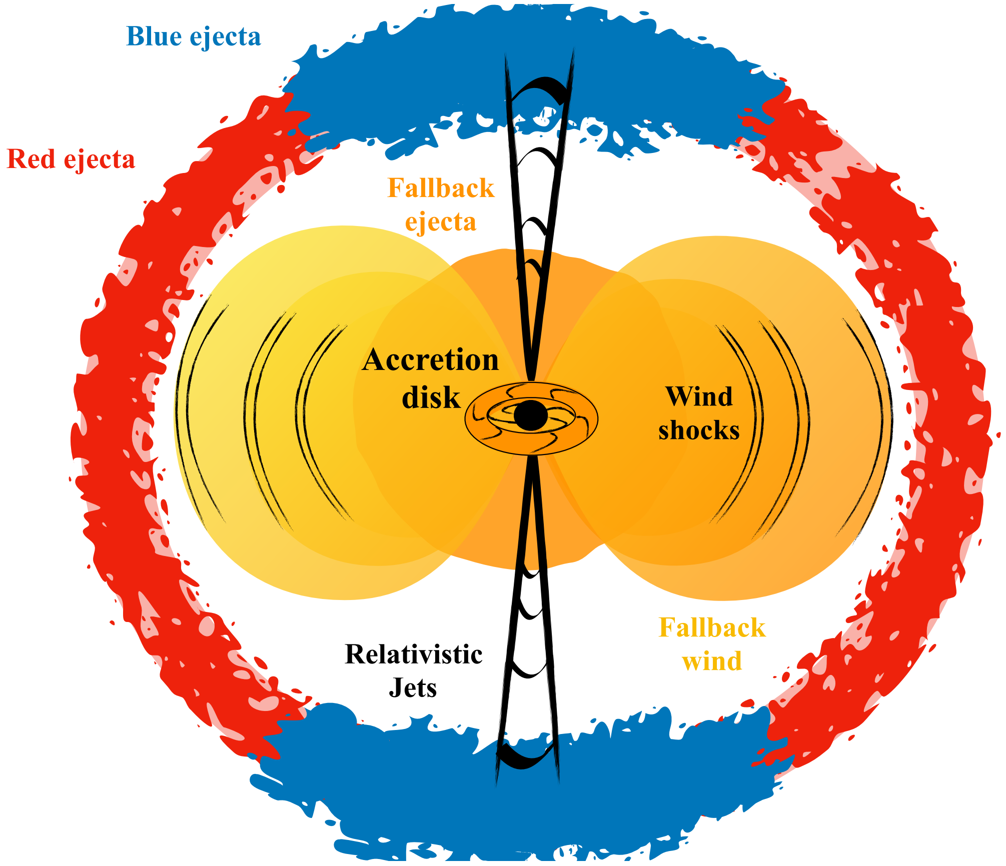

Figure 1.2: Sketch of the regions of the neutron-star merger remnant at play for the acceleration and interaction of cosmic rays in our scenario. The red and blue envelopes indicate the location of the so-called blue and red kilonovae ejecta, that emit thermal UV/optical/IR radiation over timescales of hours to days (blue) and a week (red). Models related to the GRB jet have been explored in scenarios involving GRBs. In this work, we focus on the interaction of a fast wide-angle outflow from the accretion disk powered by late-time fall-back of merger debris, with the slowly-expanding red kilonova ejecta. This interaction results in the dissipation of the accretion power as shocks or magnetic reconnection, accelerating relativistic particles, in a nebula behind the ejecta shell.

1.2 Principles of phenomenological modelling

Modelling astroparticles emissions from high energy sources require to take into account various complex processes. The key element in that respect, is the interplay between the particles and the background environment provided by the source. The particles undergoes interactions that can be distinguished in two categories: interactions leading to particle acceleration, and interactions leading to particle energy losses, and even in some cases to the modification of the nature of the particle.

The interplay between these processes can be modelled using a one-zone approach, in which one assumes that acceleration and energy losses happen in a same source region, with identical characteristics. The maximal particle energies achieved in this region, as well as the particle fluxes, can then be calculated by comparing the timescales for the different processes involved. Indeed particles will be accelerated until another process becomes dominant and lead to energy losses rather than energy gain (acceleration). The following criterion is fulfilled at maximal energy $E_{\rm max}$: $t_{\rm acc}/t_{\rm loss}|_{\rm E=E_{max}} = 1$, where $t_{\rm loss}$ represents the timescale of the dominant energy loss process and $t_{\rm acc}$ is the acceleration timescale.

Particle acceleration frequently takes place in an inner region of the source, and further energy losses happen in outer regions or in the surroundings of the source. This is the case for example for pulsars surrounded by supernova ejecta, where acceleration can happen in the wind close to the star, and particles experience massive energy loss while crossing the supernova envelope [58]. The binary neutron star merger model presented in this chapter also follows this two-zone picture. In this framework, an initially accelerated cosmic-ray spectrum is injected in the outer region. A suppression factor to be applied to the injected spectrum, typically expressed as $e^{-\tau}$, can be calculated by deriving the opacity τ of the energy loss process. The opacity can be expressed as $\tau = t_{\rm cross}/t_{\rm loss}$, where $t_{\rm cross}$ is the timescale for a particle to cross the energy loss region.

In the following, we introduce some of the processes that generally come into play in dense radiative environments, as in most powerful transient sources. The processes listed here are also specifically relevant to the source study presented in this chapter and further details are given in the next sections. Note that we focus on the restrictive case of non relativistic outflows, with bulk Lorentz boost $\Gamma \sim 1$. The comoving frame can thus be identified to the observer frame. A more exhaustive description of the intervening processes can also be found in Refs. [59, 60].

Acceleration Since astrophysical plasmas are almost always good conductors, it implies that $\left\|\vec{E}\right\| < \left\|\vec{B}\right\|$, where $\vec{E}$ and $\vec{B}$ are respectively the electric field and magnetic field of the plasma. Therefore the acceleration of particles results from electromagnetic interactions, leading to the gyration of particles along the magnetic field lines, over a time proportional to the Larmor time $t_{\rm L} = E/(qBc)$, with E the particle energy, q its electric charge and c the vacuum speed of light. The acceleration timescale in the comoving frame can be expressed as $t_{\rm acc} = g^{-1}\, t_{\rm L}$, where $g^{-1} < 1$ [61] is an efficiency coefficient, describing how efficient various acceleration processes (shock acceleration, jet acceleration, stochastic acceleration etc.) are, compared to the ideal Larmor acceleration.

Dynamical expansion governs the size of the acceleration and/or energy loss region. A non-relativistic plasma outflow expanding dynamically with velocity $\beta_{\rm dyn}$ will see its size evolve as $R_{\rm dyn} = \beta_{\rm dyn}\, ct$ over time t. The corresponding timescale $t_{\rm dyn} = R_{\rm dyn}/c$ can be compared to the acceleration timescale to derive a maximal achievable energy. It can be also compared to the timescales of other energy loss processes to derive the interaction opacities and the suppression factors to be applied to the injected spectra.

Magnetic diffusion results from the propagation of charged particles in a turbulent magnetic field. The escape of particles from the acceleration region, depending on their Larmor radii $r_{\rm L}$ and diffusion length l_D. This diffusion length, depends on the coherence length l_c of the magnetic field and the particle energy E via $l_D \sim (E/E_c)^\alpha$, where E_c corresponds to the critical energy for which $r_L(E_c) = l_c$ and α is the spectral index of the magnetic field turbulences [62]. Numerical simulations show that various spectral indices can be obtained in the complex magnetic configurations encountered in astrophysical plasmas. Three benchmark turbulence spectra are however used in the literature: the Bohm regime ($\alpha = 1$), the Kolmogorov regime ($\alpha = 1/3$) and the Kraichnan regime ($\alpha = 1/2$). Consequently the smaller the diffusion length is and the more the particles remain confined in the acceleration region, leading to a longer acceleration. In these conditions, the Bohm regime represents the least favorable diffusion regime in terms of particle acceleration.

Synchrotron radiation is predicted by classical-electrodynamics [63, 64]. The motion of a charged particles in an electromagnetic field, describes a helicoidal trajectory around the magnetic field lines, and with a pitch angle formed by the direction of the particle and the magnetic field. The change of direction of the particle at each gyration around the magnetic field line, induces an acceleration, leading to electromagnetic emission. For an observer, the total power radiated can be written as

$$P_{\rm rad} = \frac{2q^2\gamma_{\rm part}}{3m_{\rm part}^2 c^3}\left[(\vec{E} + \vec{\beta}_{\rm part} \times \vec{B})^2 - (\vec{\beta}_{\rm part} \cdot \vec{E})\right] , \tag{1.1}$$

where $m_{\rm part}$ is the mass of the particle and $\gamma_{\rm part}$ its Lorentz factor. In the particle rest frame, the timescale of this energy loss process is given by

$$t_{\rm sync} = \frac{6\pi m_{\rm part} c}{\sigma_{\rm T} B^2} \frac{A^3}{Z^4} \gamma_{\rm part}^{-1} \, , \tag{1.2}$$

with $\sigma_{\rm T}$ the Thomson cross section. For strong magnetic fields, the energy loss is so important that the pitch angle of the particles changes rapidly leading to a dominant emission from the changes in direction in the motion of the particle along the magnetic field line, and not anymore from the gyration motion. This regime is called curvature radiation [65]. Synchrotron cooling can strongly affect the maximum energy of cosmic rays and of their secondary particles in strongly magnetised environments.

Inverse Compton scattering results from the interaction of a photon with a charged particle (lepton or baryon), and leads to an energy transfer from the charged particle to the photon, through the channel $X + \gamma \to X + \gamma$, where X is any charged particles. Formally, in the case of an isotropic photon background, the energy loss timescale of this process can be written as [59]

$$t_{\rm IC}^{-1} = \frac{1}{2\gamma_{\rm part}^3 m_{\rm part} c} \int_0^\infty \frac{{\rm d}\epsilon}{\epsilon^2} \frac{{\rm d}n_\gamma(\epsilon)}{{\rm d}\epsilon} \int_{\bar\epsilon=0}^{\bar\epsilon=2\gamma\epsilon} {\rm d}\bar\epsilon \, \bar\epsilon \left[\left\langle \epsilon_s^0 \sigma \right\rangle - \bar\epsilon \left\langle \epsilon_s^1 \sigma \right\rangle \right] \, , \tag{1.3}$$

where ${\rm d}n_\gamma(\epsilon) \, / \, {\rm d}\epsilon$ is the photon energy density as a function of the photon energy ϵ, in the scattering frame, and $\left\langle \epsilon_s^0 \sigma \right\rangle$ and $\left\langle \epsilon_s^1 \sigma \right\rangle$ are respectively the zeroth order and first order momenta of the differential cross section of the interaction. The cross section depends on the energy of the two incident particles, and two regime can be distinguished: the Thomson regime at low energy and the Klein-Nishina regime at high energy, where the photon interaction cross section is modified due to quantum field corrections [66]. In the Thomson regime, Equation 1.3, reduces to

$$t_{\rm IC} = \frac{3 m_{\rm part} c}{4 \sigma_{\rm T} U_{\rm rad}} \frac{A^3}{Z^4} \gamma_{\rm part}^{-1} \, , \tag{1.4}$$

with $U_{\rm rad} = \int_0^{m_{\rm part} c^2 / \gamma_{\rm part}} {\rm d}\epsilon \, \epsilon \, {\rm d}n_\gamma(\epsilon) \, / \, {\rm d}\epsilon$.

Beithe-Heitler scattering (pair-production) is produced when a photon scatters on a virtual photon from the Coulomb barrier surrounding a nucleus, via the channel $N + \gamma \to N + e^+ + e^-$, with N a given nucleus. In the first Born approximation, where the electrons and positron do not interact with the nucleus after creation, the timescale of the process can be described as [67]

$$t_{\rm BH}^{-1} = \frac{3}{8\pi} \frac{\alpha_e \sigma_{\rm T} c \left(m_e c^2 \right)^3}{\gamma_{\rm part} m_{\rm part} c^2} \int_{2 m_e c^2}^\infty \frac{{\rm d}\epsilon}{\epsilon^2} \frac{{\rm d}n_\gamma}{{\rm d}\epsilon} \left(\frac{\epsilon}{2\gamma} \right) \phi\left(\epsilon / m_e c^2 \right) \, , \tag{1.5}$$

where ϕ is a parametrisation given by

$$\phi(x) = \begin{cases} \frac{\pi}{12} \frac{(x-2)^4}{1+\sum_{i=1} c_i (x-2)^i} \text{ for } 2 \leqslant x < 25 \ , \\ \frac{x \sum_{i=0}^{3} d_i (\ln(x))}{1-\sum_{i=1}^{3} f_i x^{-i}} \text{ for } x \geqslant 25 \ , \end{cases} \tag{1.6}$$

with the parameters c_i, d_i and f_i given in [67].

Photomeson production and photodisintegration result from the interactions of baryons (proton, neutron, nuclei) with the photon background, and produce a significant amount of secondary particles: hadrons, neutrinos and photons. They are therefore extensively studied in astrophysical contexts (see Section 1.5). Since the ultra-high energy regime of these interactions do not allows for direct measurements of their cross-sections, current models are based on phenomenological approaches combined with parametrisations [68]. In these models, protons (and neutrons) undergo energy losses from the interaction with photons, while nuclei experience mass changes through nucleus fragmentation. The cross section are composed of different resonant regimes, resulting into different productions of secondary particles and mesons (see Figure 1.3). Finally, the resulting energy loss timescale can be estimated as [69]

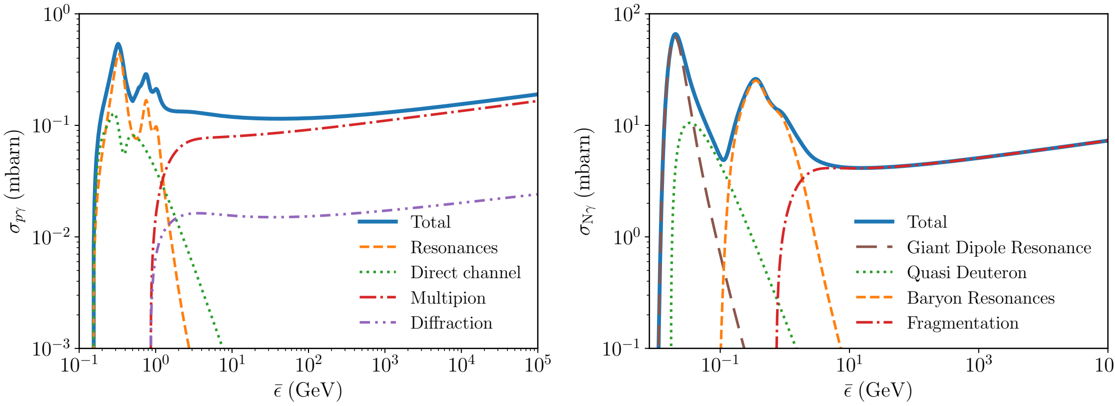

Figure 1.3: Photoadronic cross sections (photomeson and photodisintegration regimes) for Proton (*left*) and Iron (*right*) as function of the photon energy $\bar{\epsilon}$ in the particle rest frame. The total cross section (in blue) results from the combination of the various resonant regimes (as displayed). Taken from [60].

$$t^{-1}_{\mathrm{part}\,\gamma} = \frac{c}{2\gamma_{\mathrm{part}}} \int_0^\infty \frac{\mathrm{d}\epsilon}{\epsilon^2} \frac{\mathrm{d}n_\gamma(\epsilon)}{\mathrm{d}\epsilon} \int_{\bar{\epsilon}=0}^{\bar{\epsilon}=2\gamma_{\mathrm{part}}\epsilon} \mathrm{d}\bar{\epsilon}\, \bar{\epsilon} \sigma_{\mathrm{part},\gamma}(\bar{\epsilon}) \ , \tag{1.7}$$

for an isotropic photon spectra and where $\sigma_{\rm part,\gamma}$ is the photodisintegration cross section. We recall that $\gamma_{\rm part}$ is the Lorentz factor of the particle and $\bar{\epsilon}$ is the photon energy in the particle rest frame. Note that in the specific case of fragmentation this timescale can not be strictly labeled as an energy loss timescale since the primary nucleus is destroyed, resulting in the creation of lighter nuclei.

Hadronic interactions represents the interactions between two hadrons. A large variety of these interactions exists, however we focus only on the case of proton-proton (or neutron-proton) interaction, since it is a common configuration of baryons interaction in astrophysical contexts. Proton-proton (or neutron-proton) interactions, also results in a large production of secondary hadrons, gamma rays and neutrinos via similar channels as the photomeson production, e.g., $p+p \rightarrow p+p+\pi^0$, $p+p \rightarrow p+n+\pi^+$ (or $n+p \rightarrow n+p+\pi^0$, $n+p \rightarrow p+p+\pi^-$ and $n+p \rightarrow n+n+\pi^+$). The typical interaction timescale can be estimated as

$$t_{\rm pp} = [n_{\rm baryon}\sigma_{\rm pp}c]^{-1} \ , \tag{1.8}$$

where $n_{\rm baryon}$ is the baryon density and $\sigma_{\rm pp}$ is the proton-proton cross section (similar to $\sigma_{\rm np}$).

The complex interplay between particle acceleration and particle energy losses inside high energy sources can be either simulated thanks to Monte Carlo simulations or modelled through a phenomenological approach of these processes. This approach relies on the understanding of the timescales and the conditions in which these interactions may happen. In the following sections, we apply these principles to the case of NS mergers.

1.3 Particle acceleration in binary neutron star mergers

The merger of a NS-NS or NS-BH binary can lead to a spinning BH surrounded by an accretion disk of mass $0.01 - 0.1\,M_\odot$ (e.g., [70, 71, 72]). The accretion torus powers a collimated relativistic jet and creates a short gamma-ray burst (e.g., [49, 50, 51, 52]). At early times ($\lesssim 0.1 - 1\,$s) this disk can be effectively cooled by thermal neutrino emission [73, 74, 75]. At later times, it becomes radiatively inefficient as the accretion rate drops [76, 77]. Some fraction ($\sim 10^{-3} - 0.1\,M_\odot$) of the debris injected into the surrounding medium remains bound and gradually returns to the central BH as fallback matter. It accretes at a super-Eddington rate and can drive a powerful, radiation-driven wind [77]. We call this outflow the *late-time disk wind* (not to be confused with the early short-lived disk directly resulting from the coalescence).

1.3.1 Fallback mass and luminosity

The ejecta which are marginally gravitationally bound to the black hole will return at late times $t \gg t_0$ at the following observed approximate rate (e.g., [78, 79, 80]):

$$\dot{M}_{\rm fb} = \dot{M}_{{\rm fb},t=t_0} \left(\frac{t}{t_0}\right)^{-5/3} , \tag{1.9}$$

where [2]

$$\begin{aligned} \dot{M}_{{\rm fb},t=t_0} &= M_{\rm fb} \left[\int_{t_0}^{t_{\rm end}} \left(\frac{t}{t_0}\right)^{-5/3} {\rm d}t\right]^{-1} & (1.10) \\ &\sim 3.3 \times 10^{-1} M_\odot\, {\rm s}^{-1}\; t_{0,-1}^{-1} \left[\left(\frac{t_{0,-1}}{t_{{\rm end},7}}\right)^{2/3} + 1\right]^{-1} \left(\frac{M_{\rm fb}}{0.05 M_\odot}\right) , & (1.11) \end{aligned}$$

Here $M_{\rm fb}$ is the total fall-back mass (normalized to a value similar to the total unbound ejecta mass inferred from the kilonova emission in GW170817), while t_0 and $t_{\rm end}$ correspond respectively to ad-hoc onset and fading times of the fallback process. The kinetic luminosity of the plasma outflow powered by fall-back accretion can then be parameterized as[3]

$$\begin{aligned} L_{\rm fb} &= \epsilon_{\rm fb}\, \dot{M}_{\rm fb}\, c^2 & (1.12) \\ &\sim 1.3 \times 10^{46}\, {\rm erg\, s^{-1}}\, \epsilon_{{\rm fb},-1} t_3^{-5/3} \left(\frac{M_{\rm fb}}{0.05\, M_\odot}\right) , \end{aligned}$$

where $\epsilon_{\rm fb} \sim 0.01 - 0.1$ is an efficiency factor (e.g., [79]). The numerical values above, extrapolated to the first epoch at $t = 11$ hr of the observed kilonova from GW170817, leads to a fallback luminosity of $\sim 3 \times 10^{43}\, {\rm erg\, s^{-1}}$ for $\epsilon_{\rm fb} = 0.1$. In Section 1.4 we show how this luminosity heats the ejecta, leading to a thermal kilonova luminosity several orders of magnitude below the fallback luminosity. The parameters chosen above are thus compatible with the electromagnetic observations of GW170817 [81], and in line with the recent numerical studies [82].

If the fall-back accretion-powered outflow expands faster than the slowest inner tail of kilonova ejecta (~ 0.1 c in GW170817) [79], then the disk outflows will catch up and shock with the inner edge of the ejecta shell, generating a nebula of gas behind it. Alternatively, if the flow is magnetically dominated, forced reconnection in the flow could lead to a similar dissipation of a portion of its Poynting flux. In this way, a portion of the fall-back power $L_{\rm fb}$ could be channelled into cosmic-ray acceleration and subsequent neutrino production. Here and in the following, we provide numerical quantities at $t = 10^3$ s, when neutrino

---

[2] we recall the notation $Q_x \equiv Q/10^x$ which in this case, gives $t_{0,-1} = t_0/0.1$ and $t_{{\rm end},7} = t_{\rm end}/10^7$

[3] Again, $t_3 = t/10^3$

production is most important in the case of pure proton injection for some of the ejecta parameter sets examined in this work.

The amount of fallback mass is generally believed to be at most comparable to that of the unbound dynamical ejecta, in which case numerical simulations suggest an upper limit $M_{\rm fb} \lesssim 0.05\,M_\odot$ [79]. However, several factors could increase the amount of ejected mass (and therefore the fallback mass). For instance, the dynamical ejecta is larger if the neutron stars are spinning rapidly at the time of merger (e.g. [83]) or for a particularly low binary mass ratio $q \ll 0.7$. Although such properties are not compatible with the Galactic population of double neutron stars systems, such constraints may apply to the extra-galactic population. Indeed, the second binary neutron star merger discovered by Advanced LIGO, GW190425, possessed a total binary mass far in excess of known Galactic double neutron star systems, thus hinting at selection biases in the Galactic sample or wider diversity in the properties of the extragalactic binary population [84]. Numerical simulations of the merger itself also do not generally account for fallback of matter ejected from the post-merger accretion disk winds. The disk wind ejecta can be very large; hence $M_{\rm fb} \sim 0.05 - 0.1\,M_\odot$ is not unreasonable, e.g. [82], and this likely produced most of the ejecta in GW170817. In light of these arguments, we will also examine in this study a case with a higher level of total fallback mass $M_{\rm fb} = 0.1\,M_\odot$.

1.3.2 Particle acceleration in the late-time accretion disk

The late-time disk wind arises from an radiatively-inefficient accretion flow [85], in which one may expect stochastic acceleration to take place (e.g., [86]). On the other hand, accelerated particles can experience important energy losses on the dense baryonic background. The disk can be parametrized as a function of the black hole mass $M_{\rm BH}$, disk radius $R_{\rm disk}$, and Keplerian velocity $v_{\rm r} = \alpha_{\rm r}(GM_{\rm BH}/R_{\rm disk})^{1/2}$, where G is the gravitation constant, $\alpha_{\rm r}$ is the alpha parameter [87] and the accretion or fallback mass $M_{\rm fb} \sim 5\times10^{-2} M_\odot$ [78]. Assuming that the disk radius scales as the gravitational radius $R_{\rm disk} = rR_{\rm g}$ with $R_{\rm g} = GM_{\rm BH}/c^2$, and considering a thin disk of negligible thickness (see [88] for a review) one can estimate the baryonic density in the disk

$$\begin{aligned} n_{\rm p,disk} &= \frac{\dot{M}_{\rm fb}}{2\pi R_{\rm disk}^2 v_{\rm r} m_{\rm p}} \qquad (1.13)\\ &= 1.2\times10^{27}{\rm cm}^{-3}\ r_1^{-3/2}\alpha_{\rm r,-1}^{-1}\ t_3^{-5/3}\left(\frac{M_{\rm bh}}{6M_\odot}\right)^{-3/2}\left(\frac{M_{\rm fb}}{0.05M_\odot}\right)\,. \end{aligned}$$

Such high densities lead to drastically short hadronic interaction timescales for ultra-high energy cosmic rays: $t_{\rm pp} = (n_{\rm p,disk}\sigma_{\rm pp}c\kappa_{\rm pp})^{-1} \sim 4.2\times10^{-12}\,{\rm s}\ n_{\rm p,disk,27}^{-1}[\sigma_{\rm pp}(1\,{\rm EeV})/\sigma_{\rm pp}]$, with the proton-proton interaction cross section $\sigma_{\rm pp} = 6.6 \times 10^{-26}\,{\rm cm}^2$ and inelasticity $\kappa_{\rm pp} \sim 0.5$ at $1\,{\rm EeV}$ [89]. These inevitable energy losses prevents any kind of acceleration process to succeed in the disk environment, even by invoking very efficient magnetic reconnection mechanisms in the magnetic rotational instability turbulence as was studied in [90, 91, 92, 93].

1.3.3 Particle acceleration in the outer fallback wind region

A mildly-relativistic wind powered by fallback can be launched from the accretion disk and propagate out to large distances $r = R_{\rm g}/R_{\rm disk} > 10^2 - 10^3$ (see sketch of Figure 1.2). This region could be an alternative promising region for efficient acceleration. Indeed, the encounter of this outflow with the slower but higher mass outer ejecta would produce a shocked shell [94]. Particles could in principle be shock-accelerated in this region. One may caution however that these internal shocks may be radiation-mediated due to the high optical depths at the early times considered here (see Section 1.4). Radiation-mediated shocks are not efficient to accelerate relativistic particles, unless a neutron-proton conversion mechanism is invoked to ease the particles escape from the shock, once accelerated [95, 96, 97]. On the other hand, the optical depth across the shocked region is likely to be much smaller than through the entire kilonova ejecta shell and thus the reverse shock which acts to decelerate the wind may still be collisionless, even at relatively early times.

Particle Acceleration could also take place via other processes in this region, e.g., via magnetic reconnection (see e.g., [98] in the case of binary white dwarf mergers). It is not trivial to infer the level of large-scale magnetization in the post-merger phase of a binary neutron-star. Most numerical relativity simulations focus indeed on the disk formed after merger [99, 100, 101], following its evolution up to typically $\sim 100\,{\rm ms}$. The magnetic field should be amplified by several orders of magnitude because of turbulence developing in the fluid during and after the merger (mainly via Kelvin-Helmholtz instability). Although this is difficult to resolve numerically because of the small length-scales involved, the effects of such large magnetic fields have been studied for example in Refs. [100, 101]. These works indicate that the equatorial outflow can be Poynting-flux dominated and hence enable reconnection processes [102, 103, 104].

For radii less than the diffusion radius, $R < R_D$, it is likely that any magnetic reconnection process is suppressed, due to the high photon drag. In this regime, radiation pressure works against the development of turbulence and against regions of approaching opposite magnetic polarity. Beyond R_D, however, radiation pressure starts to drop, and reconnection may start to occur, although the transition threshold from one regime to the other is not well-known ([105], and references therein). The Thomson optical depth at the diffusion radius $\tau_{\rm T}(R_{\rm D}) \sim 1/\beta_{\rm wind}$ remains above unity for at least two orders of magnitude in radii beyond R_{D}, and the dependence of the magnetic reconnection rate on the flow parameters in this still optically thick regime is speculative.

In the following, we will estimate the maximum achievable acceleration energy assuming that acceleration can operate. We will discuss how the numerical results would change depending on the considered acceleration mechanism.

The magnetic energy in the shell of the shock front forming the acceleration zone is assumed to follow an equipartition, and to be a fraction ϵ_B of the bulk kinetic energy of the wind dissipated into this region

$$\frac{B_{\mathrm{acc}}^2}{8\pi} 4\pi\, R_{\mathrm{acc}}^2\, c = \frac{1}{2} \epsilon_B\, \epsilon_{\mathrm{fb}} \dot{M}_{\mathrm{fb}} (\beta_{\mathrm{wind}} c)^2 \ , \tag{1.14}$$

where the size of the region $R_{\mathrm{acc}} = rR_g$, with $r = 10^3$. The magnetic field strength in the region can then be expressed as

$$\begin{aligned} B_{\mathrm{acc}} &= \sqrt{\epsilon_B \epsilon_{\mathrm{fb}} \frac{\dot{M}_{\mathrm{fb}}\, \beta_{\mathrm{wind}}^2 c}{R_{\mathrm{acc}}^2}} \\ &= 1.5 \times 10^7\ \mathrm{G}\ \epsilon_{B,-2}^{1/2} \epsilon_{\mathrm{fb},-1}^{1/2} r_3^{-1} \beta_{\mathrm{wind},-1} t_3^{-5/6} \left(\frac{M_{\mathrm{bh}}}{6M_\odot}\right)^{-1} \left(\frac{M_{\mathrm{fb}}}{0.05M_\odot}\right)^{1/2} \ . \end{aligned} \tag{1.15}$$

As argued in Section 1.2, the acceleration timescale can be written as $t_{\mathrm{acc}} = gt_{\mathrm{L}}$, where t_{L} is the Larmor timescale and $g \geq 1$ the acceleration inefficiency factor. $g = 1$ corresponds to a maximally efficient acceleration process. As function of the particle energy E, the acceleration timescale then reads

$$\begin{aligned} t_{\mathrm{acc}} &= \frac{g\, E}{\beta_{\mathrm{wind}} c Z e B_{\mathrm{acc}}(t)} \\ &\sim 4.1 \times 10^{-1}\ \mathrm{s}\ E_{18}\, \beta_{\mathrm{wind},-1}^{-2}\ Z^{-1}\ t_3^{5/6} \epsilon_{B,-2}^{-1/2} \epsilon_{\mathrm{fb},-1}^{-1/2} r_3 \left(\frac{M_{\mathrm{bh}}}{6M_\odot}\right) \left(\frac{M_{\mathrm{fb}}}{0.05M_\odot}\right)^{-1/2} \ , \end{aligned} \tag{1.16}$$

where Z is the charge particle and e the elementary charge. The above numerical estimate assumes that efficient acceleration operates with an inefficiency factor $g = 1$. For shock acceleration for instance, this would correspond to a Bohm diffusion regime. Less efficient processes and other types of acceleration mechanisms could be considered by setting $g > 1$ [61]. For instance, for subrelativistic reconnection flows $g \gtrsim 10$ [106].

One may estimate the baryonic density of the outflow as the baryonic mass over the outflow volume

$$\begin{aligned} n_{\mathrm{p,wind}} &= \frac{3\, \dot{M}_{\mathrm{fb}}}{4\pi (\beta_{\mathrm{wind}}\, c)^3\, t^2\, m_{\mathrm{p}}} \\ &= 7.5 \times 10^{14}\, \mathrm{cm}^{-3}\ \beta_{\mathrm{wind},-1}^{-3}\ t_3^{-14/3} \left(\frac{M_{\mathrm{bh}}}{6M_\odot}\right)^{-2} \left(\frac{M_{\mathrm{fb}}}{0.05M_\odot}\right) \ . \end{aligned} \tag{1.17}$$

In the wind, at these times, the baryonic density is no longer an issue for particle acceleration since the interaction timescale for UHECR will be $t_{\rm pp} = 3.4\,{\rm s}\ n_{\rm p,14.6}^{-1}[\sigma_{\rm pp}(1\,{\rm EeV})/\sigma_{\rm pp}] > t_{\rm acc}$. On the other hand, the strong magnetic fields will also induce synchrotron cooling with timescale

$$\begin{aligned} t_{\rm sync} &= 6\pi\left(\frac{m_{\rm p}}{m_{\rm e}}\right)^3\frac{A^3}{Z^4}\frac{\left(m_{\rm p}c^2\right)^2}{\sigma_{\rm T}c\beta B_{\rm sh}(t)^2\ E} \\ &\sim 2.9\times10^{-3}\,{\rm s}\ E_{18}^{-1}\ A^3Z^4\ t_3^{5/3}\ , \end{aligned} \tag{1.18}$$

with A the mass particle number, $\sigma_{\rm T}$ the Thomson cross section and β the particle velocity ($\beta \to 1$ as ultra relativistic particle). Equation 1.18 demonstrates that synchrotron cooling will be the main limiting factor to cosmic rays acceleration in this region. The maximal acceleration energy, computed for $t_{\rm acc} = t_{\rm syn}$, reads

$$\begin{aligned} E_{\rm max} &= \sqrt{\frac{6\pi\chi}{g(\chi^2-1)}\left(\frac{m_{\rm p}}{m_{\rm e}}\right)^3\left(\frac{A}{Z}\right)^3}\,e\frac{m_{\rm p}c^2}{\sqrt{\sigma_{\rm T}B_{\rm sh}}} \\ &\sim 1.2\times10^{17}\,{\rm eV}A^{3/2}Z^{-3/2}t_3^{5/12}\ . \end{aligned} \tag{1.19}$$

One notices that the rapid decrease of the magnetic field with time implies that particles can be accelerated up to increasingly higher energies at later times. It appears from this equation that the efficiency of the acceleration process will only influence the maximum energy by a factor of $1/\sqrt{g}$, with $g \gtrsim 10$ for reconnection/shear acceleration/non-Bohm diffusion. We assume in the following that $g = 1$, although one should bear in mind that $E_{\rm max}$ might be overestimated.

As discussed in Ref. [42], the diffusion timescale in the shock region can be estimated as $t_{\rm diff} \propto t_{\rm acc}$ in the Bohm regime. It is thus possible that diffusion prevents cosmic rays from escaping from the shock, except at the highest energies, naturally leading to hard or monoenergetic spectra peaking at $E_{\rm max}$. In the following, we will adopt a power-law spectrum $\propto E^{-\alpha}$ for the accelerated particles, with an index of either $\alpha = 2.1$ (as commonly assumed for shock-acceleration) and 1.5 (to depict a harder spectrum due to diffusion), with maximum energy $E_{\rm max}$. The hard spectral index also has the advantage of mimicking spectra obtained with other types of acceleration mechanisms that could be taking place, such as magnetic reconnection [107].

1.3.4 Particle acceleration in the corona

In addition to fallback outflows, acceleration may happen in the corona of the accretion disk. The corona region is defined as the immediate surrounding of the accretion disk, on

Figure 1.2 it can be located as the region trapped between the red and blue ejecta and the accretion disk/fallback region. The corona is filled with a plasma coming from the accretion disk, this plasma is subject to turbulent phenomena leading to resonant Alfvén waves modes, that can accelerate particles stochastically. On the other hand, it is possible that the corona is immersed in an intense radiation field [108], leading to photo-hadronic losses that hinder efficient acceleration process.

1.4 Radiative and baryonic backgrounds of the dynamical ejecta

The neutron-star merger ejects unbound matter, that can be observed as a kilonova [79]. On the polar axis, the lanthanide-free material induces light r-process nuclear reactions, that power a blue day-long emission.

The merger ejecta received sustained heating due to the radioactive decay of r-process nuclei, as well as due to outflows from the fallback accretion disk. Cosmic rays accelerated in the inner regions of the ejecta will experience synchrotron cooling and interactions on the radiation field and the baryonic material of this red ejecta (as depicted on the sketch of Figure 1.4). In order to evaluate the energy loss and interaction rates, we model the evolution of the thermal radiation background, magnetic field strength and baryon density of the merger ejecta.

In the following, we compute our numerical values based on two fiducial parameter sets. One stems from the observation of GW170817, referred to as "GW170817-like", with total ejecta mass $M_{\rm ej} = 10^{-2}$ and $\beta_{\rm ej} = 0.3$. The other, referred to as "optimistic", is chosen to enhance the neutrino flux, with a lighter ejecta mass $M_{\rm ej} = 10^{-4}$ and $\beta_{\rm ej} = 0.3$ [109, 110, 4]. The more dilute radiative and baryonic environments induce less secondary meson cascades, which inhibit efficient neutrino production. References [79, 110] review the mass and velocity ranges allowed for the various binary-neutron-star systems studied analytically and numerically. Following the discussion in Section 1.3.1, the fallback mass is set to $M_{\rm fb} = 0.05\,M_\odot$, and to $M_{\rm fb} = 0.1\,M_\odot$, for the GW170817-like and optimistic scenarios respectively. Table 1.1 summarizes the key parameters chosen for these two scenarios.

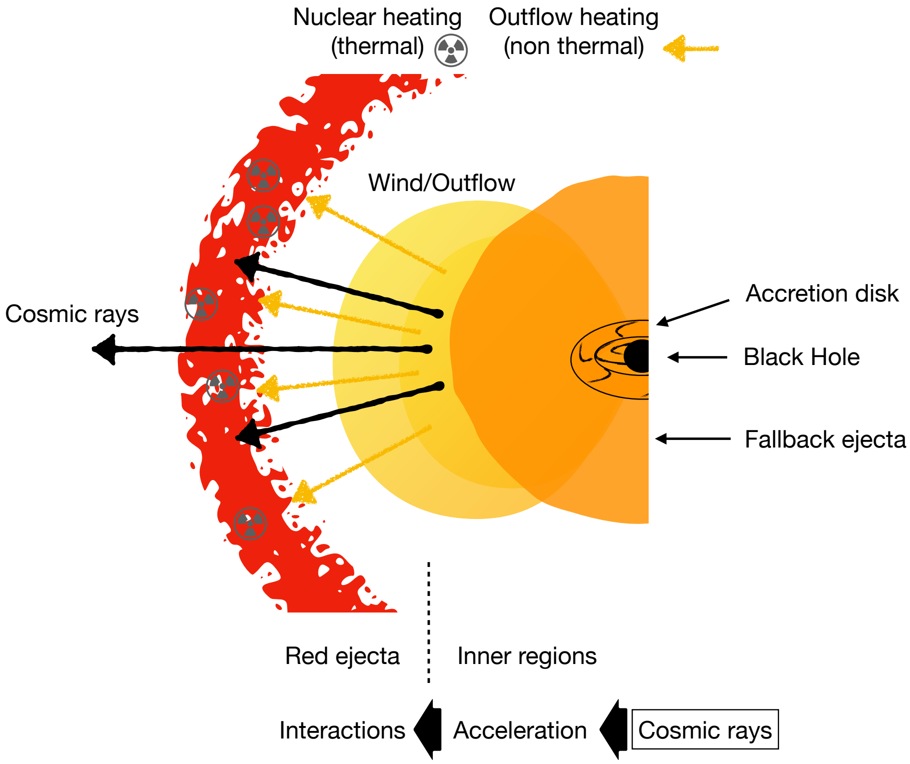

Figure 1.4: Sketch of the regions of the neutron-star merger remnant at play for the acceleration and interaction of cosmic rays in our scenario. Cosmic rays are accelerated in the inner regions of the neutron-star merger before interacting inside the red ejecta where the nuclear heating and outflow heating result in a strong interaction environment, especially for photopion production.

Scenario	$M_{\rm ej}$ $[M_\odot]$	$\beta_{\rm ej}$	$M_{\rm fb}$ $[M_\odot]$	$\beta_{\rm wind}$	$\epsilon_{\rm fb}$	$\dot{n}_0$ $[\rm Gpc^{-3}yr^{-1}]$	$\mathcal{R}(z)$
GW170817-like	10^{-2}	0.3	5×10^{-2}	0.1	0.1	600	1
Optimistic	10^{-4}	0.3	1×10^{-1}	0.1	0.1	3000	$\mathcal{R}_{\rm SFR}(z)$

Table 1.1: Key parameters of binary neutron star merger remnants chosen for the two fiducial scenarios examined in this work: dynamical ejecta mass $M_{\rm ej}$ and velocity $\beta_{\rm ej}$, wind fallback mass $M_{\rm fb}$ and velocity $\beta_{\rm wind}$, population rate $\dot{n}_0$ and emissivity evolution with redshift $\mathcal{R}(z)$. GW170817-like model based on parameters obtained from the observation of GW170817. Optimistic case chosen so as to enhance the neutrino flux, while staying consistent with the allowed ranges for extragalactic populations of mergers. See Sections 1.3.1 and 1.4.

1.4.1 Thermal photon background

The ejecta material being in free expansion, its radius $R_{\rm ej}$ evolves linearly in time: $R_{\rm ej} = \beta_{\rm ej} c\, t$. The thermal energy E of the ejecta evolves according to

$$\frac{{\rm d}E}{{\rm d}t} = -3\frac{E}{R_{\rm ej}}\frac{{\rm d}R_{\rm ej}}{{\rm d}t} - \frac{E}{t_{\rm d}} + \dot{Q}_{\rm r} + L_{\rm fb} \ . \tag{1.20}$$

The first term on the right hand side of Equation 1.20 describes the $P{\rm d}V \sim (E/V){\rm d}V$ work done by pushing the ejecta. The second term corresponds to the escape of thermal radiation from the mass layer, which can be written as

$$t_{\rm d} \approx (\tau+1)\frac{R_{\rm ej}}{c} = \left(\frac{3M_{\rm ej}\kappa}{4\pi R_{\rm ej}^2}+1\right)\frac{R_{\rm ej}}{c} = \left[\left(\frac{t_{\rm d,0}}{t}\right)^2+1\right]\beta_{\rm ej}\, t \ , \tag{1.21}$$

where τ is the opacity, where $\tau = 0$ corresponds to a perfectly transparent ejecta. We define the transparency time

$$\begin{aligned} t_{\rm d,0} &\equiv \left(\frac{3M_{\rm ej}\kappa}{4\pi(\beta_{\rm ej}c)^2}\right)^{1/2} \\ &\sim 0.89 \text{ days} \left(\frac{M_{\rm ej}}{10^{-4}M_\odot}\right)^{1/2}\left(\frac{\kappa}{10\,{\rm cm}^2\ {\rm g}^{-1}}\right)^{1/2} \ . \end{aligned} \tag{1.22}$$

Here we adopt $\kappa = 10\ {\rm g}^{-1}\ {\rm cm}^2$ as the opacity of the lanthanide-rich ejecta [4].

The third and fourth terms in Equation 1.20 are the source terms of heating due to radioactivity $\dot{Q}_{\rm r}$ and fallback accretion $L_{\rm fb}$ respectively. We already described and expressed the fallback luminosity $L_{\rm fb}$ in Section 1.3 (Equation 1.12).

The heating from radioactive decay of heavy nuclei synthesised in the ejecta by r-process can be parametrised as [111]:

$$\dot{Q}_{\rm r} = M_{\rm ej} X_{\rm r} \dot{e}_{\rm r}(t) \ , \tag{1.23}$$

where $X_{\rm r}$ is the mass fraction of lanthanides in the ejecta and $\dot{e}_{\rm r}$ is the nuclear mass energy, which can be expressed, fitting simulation data, as [112]

$$\dot{e}_{\rm r}(t) = 4\times 10^{18}\epsilon_{\rm th}\left[0.5 - \frac{1}{\pi}\arctan\left(\frac{t-t_0}{\sigma}\right)\right]^{1.3} {\rm erg\,s^{-1}\,g^{-1}} \ , \tag{1.24}$$

with $t_0 = 1.3$ s and $\sigma = 0.11\,$s, the starting time and the characteristic time of the decay, it can be noticed that the decay start only after $\sim 1\,$s due to the absorption of the free neutrons in the ejecta, and $\epsilon_{\rm th}$ the thermal efficiency of the nuclear processes, accounting for the energy deposit in the ejecta of the radioactive decay products of non-thermal beta-particles, alpha-particles, fission fragments, and gamma-rays by [111] and parametrised as follow

$$\epsilon_{\rm th} = 0.36 \left[\exp\left(-a\, t_{\rm day}\right) + \frac{\ln\left(1 + 2b\, t_{\rm day}^{d}\right)}{2b\, t_{\rm day}^{d}} \right] , \tag{1.25}$$

with $a = 2.19$, $b = 0.31$, $d = 1.52$. The numbers are valid for $M_{\rm ej} = 0.01 M_{\odot}$ and initial velocity $v = 0.3c$ (from [111]).

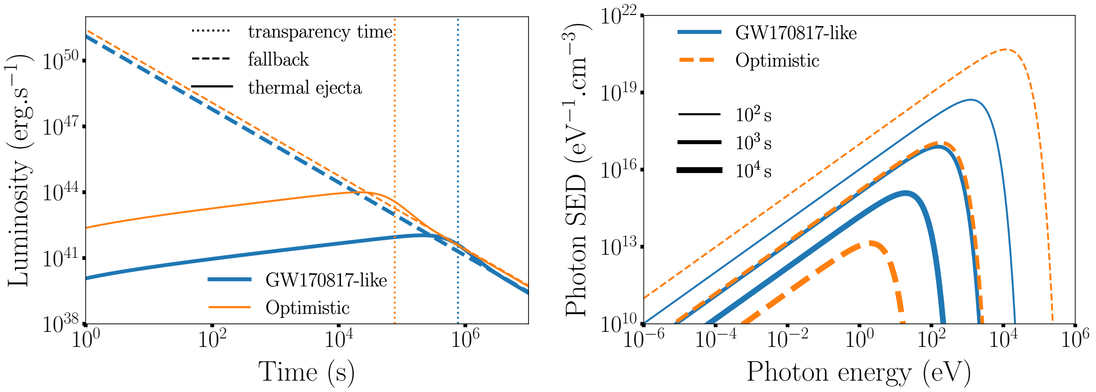

Figure 1.5: Ejecta luminosity and spectral evolution in time for our two fiducial scenarios (Table 1.1). *Left:* Time evolution of the ejecta luminosity (solid), fallback luminosity (dashed). The vertical lines correspond to the transparency times $t_{\rm d,0}$, when the dynamical ejecta turns optically transparent. *Right:* Corresponding black body photon spectral energy density of the dynamical ejecta at various times.

The thermal luminosity is then given by

$$L_{\rm th} = \frac{E}{t_{\rm d}} \tag{1.26}$$

and is shown in the left panel of Figure 1.5. The luminosity first increases rapidly in time and reaches a regime where $L_{\rm th} \propto t^{1/3}$ for $t \ll t_{\rm d,0}$. Considering a homogeneous repartition of nuclear reactions, one can assume that the ejecta emission follows a black-body distribution, with a flux density at photon frequency ν

$$F_\nu(t) = \frac{2\pi h\nu^3}{c^2}\frac{R_{\rm ej}}{D^2}\left(e^{h\nu/kT_{\rm eff}} - 1\right) \ , \tag{1.27}$$

where D is the distance to the source and the effective temperature is computed following the Stefan-Boltzman law:

$$T_{\rm eff} = \left(\frac{3E}{4\pi a R_{\rm ej}^3}\right)^{1/4} \ . \tag{1.28}$$

In principle, the radius of the shell $R_{\rm ej}$ in the equations above (Equations 1.27 and 1.28) corresponds to the photosphere radius. We consider here that the photosphere radius can be approximated as the ejecta radius $R_{\rm ej} = \beta_{\rm ej} ct$. The thermal radiation spectra of the dynamical ejecta is presented at various times in the right panel of Figure 1.5.

1.4.2 Magnetic field strength

The magnetic field strength can be computed following the same reasoning as in Equation 1.14, assuming that the magnetic energy density in the ejecta is sourced by the non-thermal inflow of the fallback in a shell of radius $R_{\rm ej}$ and expanding at speed c:

$$\frac{B_{\rm ej}^2}{8\pi}\left(4\pi\, R_{\rm ej}^2\, c\right) = \epsilon_{\rm B} L_{\rm fb} \ , \tag{1.29}$$

leading to

$$\begin{aligned} B_{\rm ej} &= \sqrt{2\epsilon_{\rm B}\epsilon_{\rm fb}\frac{\dot{M}_{\rm fb}\, c}{R_{\rm ej}^2}} \qquad (1.30) \\ &\sim 3.3\times 10^3 \ {\rm G}\ \epsilon_{\rm B,-3}^{1/2}\epsilon_{\rm fb,-1}^{1/2}\left(\frac{\beta_{\rm ej}}{0.3}\right) t_3^{-5/6}\left(\frac{M_{\rm bh}}{6M_\odot}\right)^{-1}\left(\frac{M_{\rm fb}}{0.05M_\odot}\right)^{1/2} \ . \end{aligned}$$

This magnetic field will determine the level of cooling processes inside the kilonova.

1.4.3 Baryonic density

The baryonic density determines the hadronic processes happening inside the kilonova ejecta. We compute the total mass of the ejecta in the volume of the ejecta, assuming that the mean mass number of nuclei in the ejecta is $\langle A\rangle \sim 100$. Indeed, r-process simulations driven by the observation of GW170817 indicate that nucleosynthesis is efficient, and most nuclei lie in the mass range $80 \lesssim A \lesssim 200$ in the inner parts of the ejecta. The lanthanide mass fraction is smaller, within the range $X_{\rm r} \approx 10^{-3} - 10^{-2}$ [113, 114]. The baryonic density then reads

$$\begin{aligned} n_{\rm ej} &= \frac{3M_{\rm ej}}{4\pi R_{\rm ej}^3}\frac{1}{\langle A\rangle m_{\rm p}} \\ &\sim 6.5\times10^{13}\ {\rm cm}^{-3}\left(\frac{\beta_{\rm ej}}{0.3}\right)^{-3} t_3^{-3}\left(\frac{M_{\rm ej}}{10^{-4}\,M_\odot}\right) . \end{aligned} \tag{1.31}$$

Studies also show that the decay of remnant free neutrons in the outer ejecta, where the velocities are important, produces a high abundance of Hydrogen, which dominates the composition in the outer layers of ejecta [111]. This can have a mild effect on the hadronic interaction timescale, as the relevant quantity for its calculation is the column density, and the outer layers are important, given their large radii.

1.5 Cosmic-ray interactions in the dynamical ejecta

Particles accelerated in the inner regions propagate in the equatorial ejecta (the so-called red kilonova), and experience various interaction and cooling processes, that are described in this section. In particular, they interact with the radiative and hadronic backgrounds presented in Section 1.4. We calculate the secondary neutrino flux produced by the relevant interactions: i) analytically for protons as a basis for comparison, and ii) numerically using a Monte-Carlo propagation and interaction code.

1.5.1 Numerical setup

We use the numerical propagation and interaction code developed in [16], with modules from CRPropa3 [115] and the code described in [116], which accounts for all relevant interaction and energy-loss processes for nucleons and heavier nuclei. Nucleons experience pion production through photohadronic and hadronic interactions, as well as neutron and unstable nuclei decay. All charged particles, including charged pions and muons, undergo synchrotron, inverse Compton and Bethe-Heitler processes. The interaction cross sections and products are obtained from analytic formulae [68, 59] or tabulated from SOPHIA [117] for photopion production, TALYS [118] for photonuclear interactions, and EPOS [119] for hadronic interactions. We assume that the photofragmentation products are similar to the products of hadronic interactions, which is reasonable to a first approximation, as argued in [16]. In the following, we outline the main interactions, and provide analytical estimates of the proton mean free paths.

1.5.2 Primary cosmic-ray interactions

In the equatorial ejecta, the interaction with the radiative background leads to photomeson production, photodisintegration, inverse Compton (IC) and Bethe-Heitler processes. Charged particles undergo synchrotron energy losses, due to the magnetic field produced by the non-thermal heating from the inner regions. As shown in Equation 1.30, the intensity of this interactions is linked to the fallback luminosity L_{fb} and the ejecta expansion R_{ej}. Moreover, the interaction with the baryonic background leads to purely hadronic interactions.

As shown in Section 1.4, the equatorial ejecta is characterised by two main parameters: M_{ej} and β_{ej}. The radiative and hadronic backgrounds depend on these two parameters, and so do the photonuclear and hadronic interactions. Therefore, M_{ej} and β_{ej} eventually influence the high-energy neutrino production, as photonuclear and hadronic interactions produce neutrinos, for instance through the channels $\mathrm{p}+\gamma \to \pi^{+}+\mathrm{n}$, $(\mathrm{n}+\gamma \to \pi^{-}+\mathrm{p})$ and $\mathrm{p}+\mathrm{N} \to n_{\pi}\pi^{\pm}+n_{\mathrm{p}}\mathrm{p}+n_{\mathrm{n}}\mathrm{n}+\mathrm{N}'$, and the decays $\pi^{\pm} \to \mu^{\pm}+\nu_{\mu}$ and $\mu^{\pm} \to e^{\pm}+\nu_{e}+\nu_{\mu}$.

In the following, we describe the energy-loss timescales $t_{\star}$, the mean free paths $l_{\star} = ct_{\star}$ and the interaction depths $\tau_{\star} = t_{\mathrm{dyn}}/t_{\star}$, where the subscript $\star$ corresponds to any interaction and $t_{\mathrm{dyn}} = R_{\mathrm{ej}}(t)/c$ characterises the expansion of the ejecta (so-called dynamical time). These quantities allow us to identify dominant interaction processes and evaluate their efficiencies. In particular, an interaction depth larger than 1 indicates an efficient interaction process. The photopion production energy-loss timescale $t_{\mathrm{p}\gamma}$ is

$$t_{\mathrm{p}\gamma}^{-1}(\gamma_{\mathrm{p}}) = \frac{c}{2\gamma_{\mathrm{p}}^{2}} \int_{0}^{\infty} \mathrm{d}\epsilon\, \sigma_{\mathrm{p}\gamma}(\epsilon)\kappa_{\mathrm{p}\gamma}(\epsilon)\epsilon \int_{\epsilon/2\gamma_{\mathrm{p}}}^{\infty} \mathrm{d}\bar{\epsilon}\, \bar{\epsilon}^{-2} n_{\mathrm{BB}}(\bar{\epsilon})\,, \tag{1.32}$$

where γ_{p} is the Lorentz factor of the accelerated proton, $\sigma_{\mathrm{p}\gamma}(\epsilon)$ the photopion production cross section as function of the photon energy ϵ, $\kappa_{\mathrm{p}\gamma}(\epsilon)$ the proton inelasticity and $n_{\mathrm{BB}}(\epsilon)$ the black body spectral energy density of the ejecta derived from Equation 1.27.

Using Equation 1.32 and assuming a Heaviside function for the cross section with pion production threshold $\epsilon_{\mathrm{thres}} = 145\,\mathrm{MeV}$ (see [120] Equation 3), we derive an analytical estimate of the interaction depth of photopion production

$$\begin{aligned} \tau_{\mathrm{p}\gamma}(\gamma_{\mathrm{p}}) &= \frac{8\pi}{(hc)^{3}} \sigma_{\mathrm{p}\gamma}(\gamma_{\mathrm{p}})\kappa_{\mathrm{p}\gamma} R_{\mathrm{ej}} (k_{\mathrm{B}} T_{\mathrm{ej}})^{3} \times \mathcal{I}(\gamma_{\mathrm{p}}; T_{\mathrm{ej}})\,, \\ &\sim 1.1 \times 10^{4} \left(\frac{\beta_{\mathrm{ej}}}{0.3}\right) t_{3}\, T_{\mathrm{ej},6}^{3}(M_{\mathrm{ej}}, \beta_{\mathrm{ej}}) \left[\frac{\sigma_{\mathrm{p}\gamma}(\gamma_{\mathrm{p}})\kappa_{\mathrm{p}\gamma}}{70\,\mu\mathrm{barn}}\right]\,, \end{aligned} \tag{1.33}$$

where h is the Planck constant, T_{ej} is given by Equation 1.28 and $\mathcal{I}(\gamma_{\mathrm{p}}; T_{\mathrm{ej}})$ is an integral given by

$$\mathcal{I}(\gamma_{\rm p};T_{\rm ej}) = \int_r^\infty {\rm d}x\, \frac{x^2-r^2}{e^x-1}\,, \tag{1.34}$$

$$\simeq \begin{cases} \Gamma(3)\zeta(3) + r^2\left[\ln\left(1-e^{-r}\right) - \frac{1}{2}\right]\,, & r \ll 1 \\ 2(1+r)e^{-r}\,, & r \gg 1 \end{cases} \tag{1.35}$$

where $r = \epsilon_\Delta/2\gamma_{\rm p}k_{\rm B}T_{\rm ej}$.

The hadronic interaction time with target nuclei N, $t_{\rm pN}$, is described by

$$t_{\rm pN}(\gamma_{\rm p}) = \left[n_{\rm ej}\,\sigma_{\rm pN}(\gamma_{\rm p})\kappa_{\rm pN}c\right]^{-1}, \tag{1.36}$$

where $n_{\rm ej}$ is the proton density of the ejecta, given by Equation 1.31, $\sigma_{\rm pN}(\gamma_{\rm p})$ the proton-nucleus interaction cross section as function of the proton cosmic rays Lorentz factor. The interaction mean free paths are illustrated in Figure 1.6.

Using Equation 1.36, we derive an analytical estimate of the hadronic interaction depth

$$\begin{aligned} \tau_{\rm pN}(\gamma_{\rm p}) &= R_{\rm ej}\,n_{\rm ej}\,\sigma_{\rm pN}(\gamma_{\rm p})\,\kappa_{\rm pN}\,, \qquad (1.37)\\ &\sim 16\left(\frac{\beta_{\rm ej}}{0.3}\right)^{-2} t_3^{-2}\left(\frac{M_{\rm ej}}{10^{-4}M_\odot}\right)\left(\frac{\langle A\rangle}{100}\right)^{1/3}\left[\frac{\sigma_{\rm pp}(1\,{\rm EeV})}{6.6\times10^{-26}\,{\rm cm}^2}\right]\,, \end{aligned}$$

with the inelasticity $\kappa_{\rm pp} = 0.5$. Here, we have used the superposition theory, assuming a dependency (which we also directly checked with EPOS) $\sigma_{\rm pN} \propto \langle A\rangle^{2/3}$, for a mean mass number for nuclei in the ejecta $\langle A\rangle$. We have also used Equation 1.31, with $n_{\rm ej} \propto 1/\langle A\rangle$.

Hence the hadronic interaction timescale only depends mildly on $\langle A\rangle$: $t_{\rm pN} \propto \langle A\rangle^{1/3} \sim 2$ for $\langle A\rangle = 100$. One should caution that the outer layers of the ejecta could be dominantly composed of Hydrogen. As the relevant quantity here is the column density through the entire ejecta, the overall cross-section experienced by the particles would be lower. This effect could absorb the factor of $\langle A\rangle^{1/3} \sim 2$ quoted above.

All interaction mean free paths are presented at time $t = 10^3\,$s in the top panels of Figure 1.6. The bottom panels of Figure 1.6, illustrate the time evolution of the numerical mean free paths computed for proton and iron primaries with Lorentz factor $\gamma = 10^8$. One can see that at these energies, photopion production will operate efficiently from early times to several days and up to weeks. This is also valid at lower energies, until the photo-hadronic cross-section vanishes. The figure also shows that photopion production remains the dominant process over time for both proton and iron primaries. As a consequence the neutrino production is more likely to happen through photopion production (see Section 1.6) than hadronic processes.

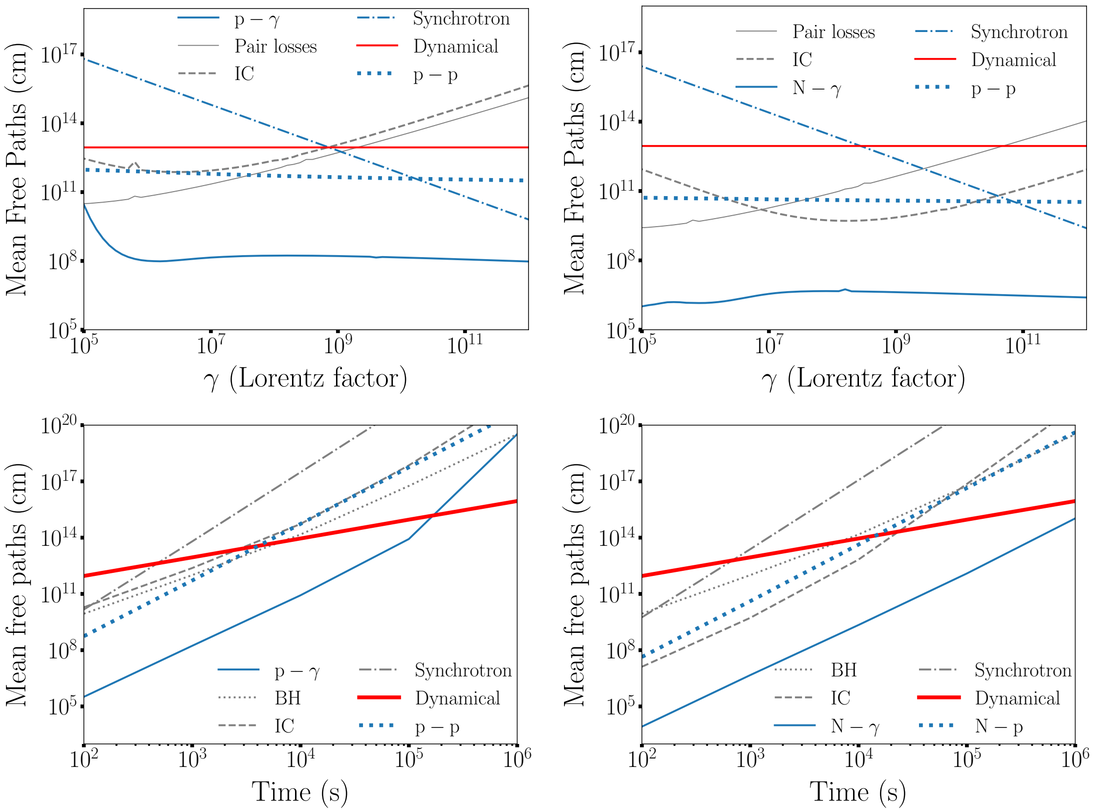

Figure 1.6: Mean free paths for protons (*left*) and iron nuclei (*right*), for photohadronic and purely hadronic interactions, compared to the typical cooling lengths for inverse Compton, synchrotron, pair-production and dynamical expansion (optimistic scenario). *Upper panels:* Mean free paths as a function of particle Lorentz factor for $t = 10^3$ s. *Lower panel:* Mean free paths as a function of time for $\gamma = 10^8$.

Note also that, as the proton-proton interaction mean free path is many orders of magnitude above the photo-hadronic interaction mean free path, adding or not a factor of $\langle A \rangle^{1/3} \sim 2$ would have no noticeable consequence. For simplicity, in the following sections, we will implement interaction cross-sections for Hydrogen backgrounds. For the interaction products, the superposition theory describes the interaction products between a projectile nucleus of mass and energy $(A_{\rm proj}, E_{\rm proj})$ and a target nucleus of mass $A_{\rm targ}$, as the same as for an interaction between a projectile $(A_{\rm proj}, E_{\rm proj}/A_{\rm targ})$ and a target proton. This can result in a pile-up of lower-energy nucleons. The neutrinos produced by this process are however subdominant compared those produced by photo-hadronic interactions.

1.5.3 Secondary pion and muon cascades

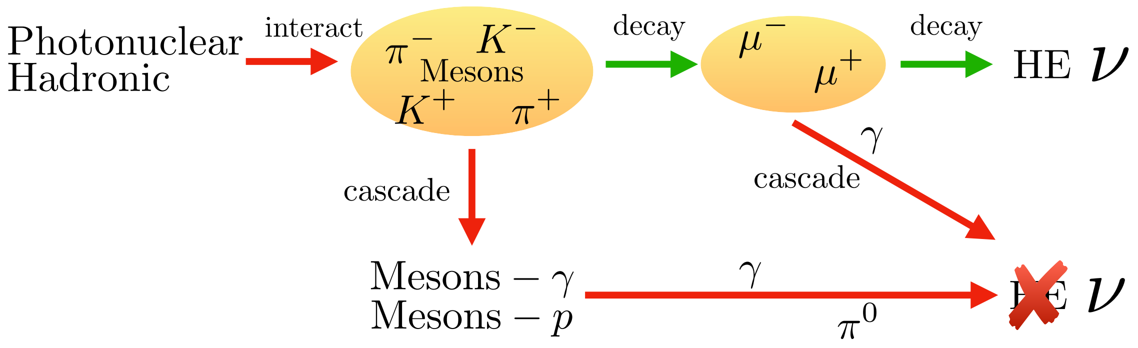

Figure 1.7: Sketch of the mesons and muons interactions on the baryon and photon backgrounds, leading to a suppression of the high energy neutrino flux. The mesons produced via photonuclear and hadronic interactions either decay into muons or interact with photons and/or baryons, leading to a decrease of their energies before decaying into muons. The muons undergo the same process, leading to a decrease of their energies or directly to the production of neutrinos. The resulting neutrino are therefore produced via three channels: i) the meson and muon progenitor do not suffer any energy loss, hence from energy conservation principles, the neutrino energy is of order 5% of the cosmic-ray progenitor. ii) either the meson or the muon suffers energy losses, thus the resulting neutrino energy is decreased. iii) both meson and muon suffer energy losses, leading to a drastically reduced neutrino energy.

Primary cosmic-ray interactions produce mesons through photo-nuclear and hadronic interaction channels (see Section 1.5.2). These mesons can in turn interact with radiative and hadronic backgrounds or undergo synchrotron radiation, before they decay and produce neutrinos. Meson cascades can therefore play an important role in the limitation of the neutrino flux (see sketch on Figure 1.7). In the following, we focus on the charged pions cascades, as the pion channel is the most favoured for neutrino production in $p-\gamma$ and $p-p$ interactions. In addition we include the description of muon cascades since their decay is responsible for 2/3 of the neutrino production in the charged-pion decay chain.

Following the computations of Section 1.5.2, we calculate analytical estimates of energy-loss timescales of charged pions. The photon-mesons interaction time can be written as

$$
\begin{aligned}
t^{-1}_{\pi\gamma}(\gamma_\pi) &= \frac{c}{2\gamma_\pi^2}\int_0^\infty \mathrm{d}\epsilon_r\, \epsilon_r \sigma_{\pi\gamma}(\epsilon_r) K_{\pi\gamma}(\epsilon_r) \int_0^{\epsilon_r/2\gamma_\pi} \mathrm{d}\epsilon\, \frac{n_{\rm photon}(\epsilon)}{\epsilon^2}\,, \\
&= 8\pi\, c \left(\frac{k_{\rm B}T}{h\, c}\right)^3 \left(e^{-x_1}(x_1+1)\,\langle \sigma_1\, K_1\rangle + e^{-x_2}(x_2+1)\,\langle \sigma_2\, K_2\rangle\right), \qquad (1.38)
\end{aligned}
$$

where $x_1 = (\epsilon_a - \epsilon_b)/(2\gamma\, k_\mathrm{B}T)$ and $x_2 = (\epsilon_b - \epsilon_c)/(2\gamma\, k_\mathrm{B}T)$, with the following resonance parametrisation $\epsilon_a = 0$, $\epsilon_b = 2\, m_\pi c^2$ and $\epsilon_c = 3 m_\pi c^2$, $\sigma_1 = 10\,\mu\mathrm{b}$, $\sigma_2 = 25\,\mu\mathrm{b}$ [121] and assuming $K_1 = K_2 = 0.5$.

The pion-hadron and muon-hadron interaction times can be analytically estimated by

$$t_{\pi\mathrm{p}}^{-1} = n_{\mathrm{p,ej}}\, \sigma_{\pi p}\, K_{\pi\mathrm{p}}\, c \ , \tag{1.39}$$

$$t_{\mu\mathrm{p}}^{-1} = n_{\mathrm{p,ej}}\, \sigma_{\mu p}\, K_{\mu\mathrm{p}}\, c \ , \tag{1.40}$$

where $\sigma_{\pi p} = 5 \times 10^{-26}$ cm^2, $\sigma_{\mu p} = 1 \times 10^{-30}$ cm^2 and $K_{\pi\mathrm{p}} = K_{\mu\mathrm{p}} = 0.8$ [44]. For comparison, the typical decay times for pions and muons are $t_{\mathrm{decay},\pi} \sim 2.6 \times 10^{-1}\, \gamma_{\pi,7}\, \mathrm{s}$ and $t_{\mathrm{decay},\mu} \sim 2.2\, \gamma_{\mu,6}\, \mathrm{s}$[4].

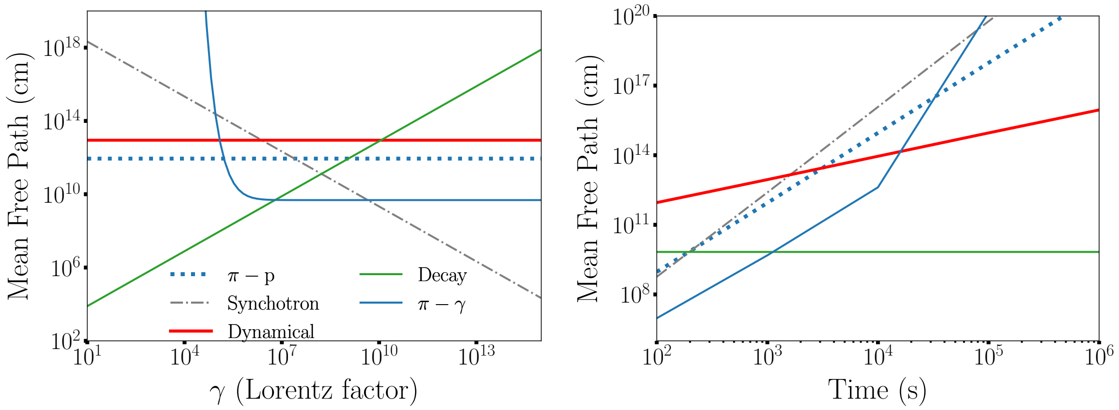

Figure 1.8: Comparison between typical cooling/decay lengths for secondary mesons. *Left:* Typical cooling lengths for π as a function of the particle Lorentz factor, at 10^3 s. *Right:* Mean free paths for π as function of time for a fixed Lorentz factor $\gamma = 10^7$.

Figure 1.8 shows the evolution of the typical lengths related to interactions, cooling processes and decay of charged pions in the optimistic scenario. The plot for muons is similar, with larger decay length and no photomeson interactions. On the left panel, we show the mean free paths as a function of Lorentz factor, for a given time $t = 10^3$ s after the merger. The lower intersection of the decay length with the typical length of any cooling/interaction process indicates the maximum energy at which charged pions or muons can decay and produce neutrinos.

In the left panel of Figure 1.8, charged pions with Lorentz factor above $\gamma \sim 10^6$ do not directly decay but first undergo a cascade of photo-mesons processes (solid blue lines), losing energy and ending up in the left-hand side of this plot, where the decay length is the shortest.

---

[4] For recall, $\gamma_{\pi,7} = \gamma_\pi/10^7$ and $\gamma_{\mu,6} = \gamma_\mu/10^6$

The backgrounds evolve with time, leading to changes in the hierarchy of the interactions lengths. For a given Lorentz factor, charged pions and muons can produce neutrinos, only if they decay before losing energy or escaping the interaction region, i.e., only if their decay length is shorter than the typical lengths of the other processes. Hence, as illustrated in Figure 1.8, no direct decay is possible before $t = 10^3\,\mathrm{s}$ for pions with $\gamma = 10^7$, for the optimistic scenario.

For each Lorentz factor, there is a specific *decoupling* time at which the decay processes become dominant. For each kilonova configuration parameter set (see Table 1.1) this decoupling time is different. The convolution of the decoupling time, corresponding to the highest secondary meson Lorentz factor, with the cosmic rays luminosity, $L_{\rm cr} = \eta_{\rm p} L_{\rm fb}$, where $\eta_{\rm p}$ is the baryon loading, the fraction of fallback luminosity dissipated to cosmic-ray luminosity, gives the maximum neutrino flux at the highest neutrino energy. In our case, since the cosmic-ray luminosity decreases as the fallback luminosity (with a time dependence of $t^{-5/3}$), kilonova configurations associated with the earliest decoupling times will lead to the highest neutrino flux scenarios.

1.6 Neutrino fluxes from NS-NS mergers

In this section we derive the neutrino emissions from neutron stars merger events, taking into account all processes described in the previous section, as well as the remnant evolution in time. We first compute neutrino spectra for single sources and then integrate over the whole population of neutron star mergers to estimate the diffuse flux.

1.6.1 Neutrino spectra from single sources

The neutrino emission from a single source can be analytically estimated using the interactions depths presented in Section 1.5.2 as

$$E_\nu^2 \frac{{\rm d}N_\nu}{{\rm d}E_\nu} = E_{\rm p}^2 \frac{{\rm d}N_{\rm p}}{{\rm d}E_{\rm p}} \, f_\pi \, f_{{\rm supp},\pi} \left[\frac{1}{4} + \frac{1}{2} f_{{\rm supp},\mu} \right] \,, \tag{1.41}$$

with ${\rm d}N_{\rm p}/{\rm d}E_{\rm p} = \mathcal{A} E_{\rm p}^{-\alpha} \exp\left(-E_{\rm p}/E_{\rm p,max}\right)$, the injected cosmic-ray spectrum. $\mathcal{A}$ is a normalisation factor which scales with the cosmic-ray luminosity $L_{\rm cr} = \eta_{\rm p} L_{\rm fb}$, the duration of the emission Δt and $E_{\rm min}$ and $E_{\rm max}$ the minimal and maximal injection energies: $\mathcal{A} = (2-\alpha) \times L_{\rm cr}\, \Delta t \,/ \big(E_{\rm max}^{2-\alpha} - E_{\rm min}^{2-\alpha}\big)$. For numerical applications and for our results, we choose a value of $E_{\rm min} = 10^6\,\mathrm{GeV}$. $f_\pi = \min[1, \max(\tau_{p\gamma}, \tau_{pp})] \times 1/2$ or $2/3$ denotes the chance of the production of charged pions in pγ or pp interactions, respectively. $f_{{\rm supp},*}$ describes the suppression of pions and muons due to cooling processes. Specifically, $f_{{\rm supp},*} = 1 - \exp(-t_{{\rm eff},*}/t_{{\rm decay},*})$, $t_{{\rm eff},*} = \left(t_{*\gamma}^{-1} + t_{*{\rm p}}^{-1} + t_{*,{\rm sync}}^{-1}\right)^{-1}$ and $t_{{\rm decay},*} = \gamma_* \tau_*$, where

τ_* is the mean life time of the particle $*$ and the subscript $*$ represents a charged pion or muon. The numerical terms in front of the suppression factors denote the chances that an energy loss interaction happens.

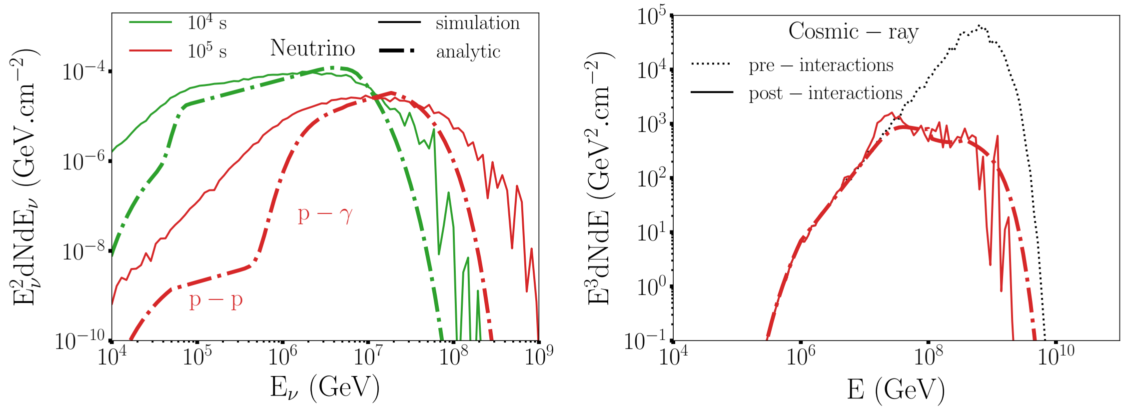

Figure 1.9: Comparison between numerical simulations (solid) and analytical estimates (dot-dashed) for two different times 10^4 (green) and 10^5 s (red) after the merger. *Left:* Neutrino spectra, *Right:* Cosmic-ray spectra. At 10^4 s, no cosmic ray survive the interactions. The fluctuations at high energy are caused by the lack of statistics. See text for details.

Figure 1.9 compares the numerical simulations and analytical estimates for two specific times after the merger: $t = 10^4$ s and $t = 10^5$ s. The right-hand panel represents the cosmic-ray spectra. The agreement between the numerical simulation and the analytical estimates is overall good, with errors below 1%, when we do not account for the statistical noise. The left-hand panel represents the neutrino spectra. The mismatch between the numerical and analytical lines is larger and can be explained as follows.

First, the difference between the analytical estimates and the numerical simulations seen in the cosmic ray spectra at energies $\sim 10^7$ GeV (for $t = 10^5$ s) is responsible for part of the mismatch around $E = 10^6$ GeV in the neutrino spectra (since about 5% percent of the energy of the proton goes into neutrinos). In this energy range, the conversion of proton energy into neutrino energy is not well reproduced by the analytical estimate. The discrepancies at lower energies and in the high energy tail of the neutrino spectra is due to the photopion production model. Our analytical estimates only considers a constant interaction cross section for photopion production, while the accurate implementation of other channels smooth out the secondary particle energies over a wider range. Note however that the peak of each spectra is accurately reproduced, and the good agreement in the cosmic-ray spectra implies that the fraction of proton energy converted into meson (pion) energy is correctly estimated.

Regarding the cosmic rays spectra it can be seen that already at $t = 10^5$ s the primary cosmic rays undergo severe interactions leading to a large depletion of ~ 2 orders of magnitude between the pre and post interaction spectra. At time 10^4 s, most cosmic rays lose energy via drastic photo-pion interactions, hence the absence of cosmic-ray flux at this time in the right-hand side plot. In the final picture, at early times (> 1 s) no cosmic rays can escape the kilonova as the number of interaction is too large, at longer times ($> 10^4$ s) a mixed composition appear and in between a transition from pure proton to mixed composition can be seen. However the diminution of the baryon loading with time result in a negligible cosmic-ray flux.

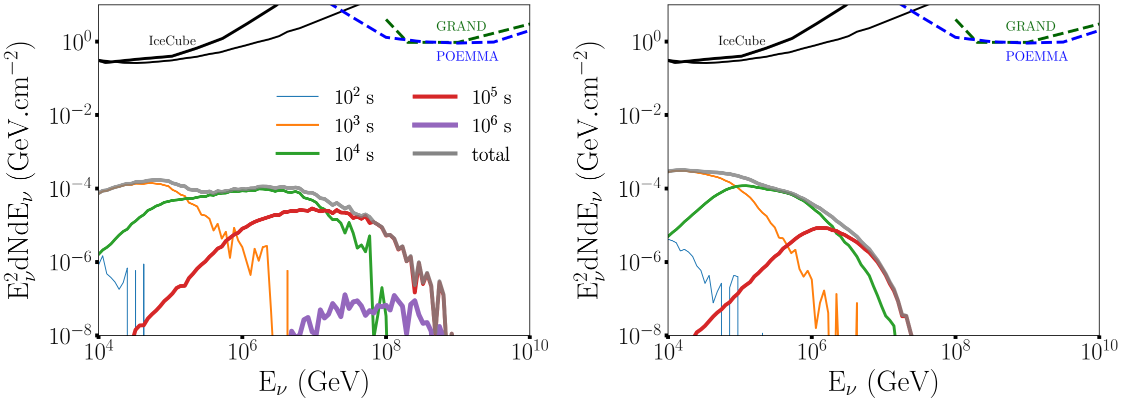

Figure 1.10: Neutrino spectra for one source at distance 40 Mpc (optimistic scenario), for an injection spectral index $\alpha = 1.5$ and baryon loading $\eta_{\rm p} = 0.1$. Lines with increasing thickness represent neutrino fluences integrated up to the indicated (increasing) times after the merger. *Left:* pure proton injection and *Right:* pure iron injection. Black solid lines represent the IceCube point-source sensitivity for two declination configurations of the source in the sky: $0° < \delta < 30°$ (best sensitivity) and $30° < \delta < 60°$ [19]. Dashed lines are projected point-source sensitivities for future experiments: POEMMA [40] (blue) and GRAND (green) [23].

The numerical spectra for one source are shown in Figure 1.10 for different times after the merger, for pure proton (left) and pure iron (right) injections at the kilonova input, for the optimistic scenario. We can clearly identify an optimum neutrino production time around $t = 10^3 - 10^4$ s. The optimum time is the result of a combination between i) a high cosmic-ray luminosity, ii) a high efficiency of cosmic-ray interactions leading to mesons production, and iii) a sufficiently low rate of meson (and muon) cascades leading to neutrino production. Consequently at earlier times, the neutrino flux is low (and with limited neutrino energy) because of the strong meson cascade rates and at later times it is low due to the decrease of primary interactions and also the decrease in the cosmic rays luminosity (scaling as the fallback luminosity $\sim t^{-5/3}$ see Equation 1.12). Finally by comparing the left panel corresponding to proton primaries with the right panel corresponding to iron primaries, one can notice that in this model, the iron primaries leads to a higher neutrino flux at early times, with a softer spectral index overall. This can be explained by the accumulation at low energies of neutrinos produced by secondary nucleons created during the photonuclear interactions with the iron. Another noticeable effect is the lower maximal energies achieved by the neutrinos generated by iron primaries. This is due to fact that in our model, the maximal acceleration energy scales as $(A/Z)^{3/2}$ (Equation 1.19), yielding roughly $E_{\rm Fe}^{\rm max} \approx 3 \times E_{\rm p}^{\rm max}$. However, the energy transferred to each pion through the photonuclear interactions scales as $E_{\rm Fe}^{\rm max}/A$. Consequently, the average pion energy will be lower by a factor ~ 20 for iron primaries compared to proton primaries, hence the lower maximal energies. Additionally, this difference implies that, at earlier times, iron-induced pions directly decay, while proton-induced pions cool down via photo-hadronic interactions (see Figure 1.8). This effect also accounts for the slightly higher neutrino fluxes at low energies and early times. Note that this effect no longer operates at times $t > 10^4\,$s, because pions produced at the cosmic-ray maximal acceleration energy always directly decay (in other words, the photon background decreases sufficiently fast to compensate the increase of the maximal acceleration energy).

We overlay in these plots the IceCube fluence sensitivity, calculated from the effective area presented in [19] for the optimal declination range $0^\circ < \delta < 30^\circ$ (thin lines), and for the declination range $30^\circ < \delta < 60^\circ$(thick lines). The IceCube-Gen2 effective area is projected to be $\sim 10^{2/3}$ times larger [122]. At ultra-high energies, we also indicate the projected sensitivities of the GRAND [23] and POEMMA [40] experiments. The neutrino spectrum from single sources presents a plateau in the IceCube energy range ($10^{4-6}\,$GeV), at times $t \sim 10^{3-4}\,$s after merger. Even for optimistic scenarios, the low-flux levels would only allow detection with IceCube-Gen2 if the sources are located at distances $\lesssim 4\,$Mpc, which correspond to rare events.

Finally, Figure 1.11 shows the ratio of electronic neutrinos and muonic neutrinos as function of their energy for a pure proton injection (left) and a pure iron injection (right) at the source (i.e at production). From [123], the production of neutrinos through the decay of high-energy pions, which leads to a composition ratio of $1:2:0$ at the source, is favored by IceCube data. The scenario involving strong muon energy losses, which produces a ratio of $0:1:0$ at the source, is also slightly favored. As shown in Figure 1.11, none of these two scenarios correspond to our models. Only the model with pure iron injection above $10^7\,$GeV approximately gives a ratio of $1:2:0$. However, we note that no neutrino detection has been performed at these energies and that this part of the spectrum presents a high statistical noise. The deviation from expected scenarios of [123] roots in the high pion and muon energy losses (see Section 1.5.3) or in the mixed pion production channels involving both $p-\gamma$ and $p-p$ interactions (see Section 1.5.2).

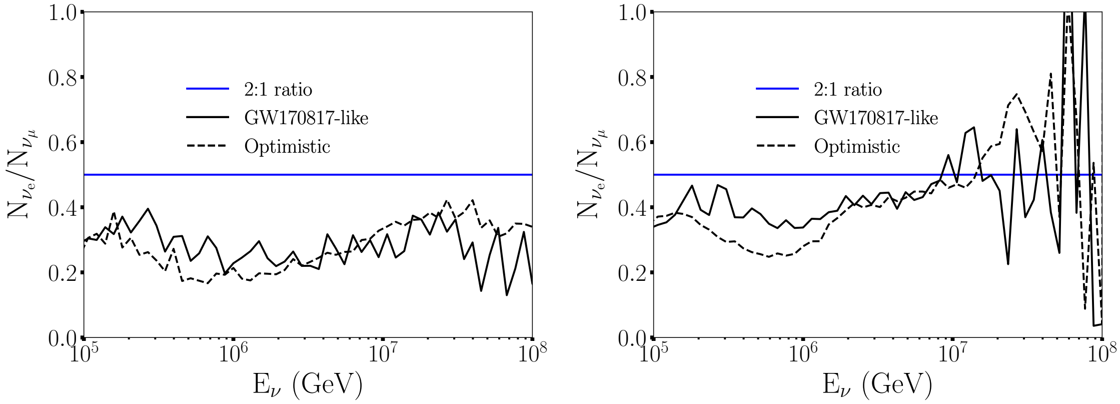

Figure 1.11: Ratio of electronic neutrinos and muonic neutrinos as function of their energy for a pure proton injection (*left*) and a pure iron injection (*right*) at the source.

1.6.2 Diffuse neutrino flux

Assuming that similar particle acceleration and interaction processes happen in binary-neutron-star merger remnants, the integrated high-energy neutrino flux due to relativistic ions interacting with kilonovae photons is calculated by

$$\Phi(E_\nu) = \frac{c}{4\pi H_0} \int_0^\infty \mathrm{d}z \, \frac{\dot{n}(z)}{\sqrt{\Omega_\mathrm{M}(1+z)^3 + \Omega_\Lambda}} \frac{\mathrm{d}N_\nu}{\mathrm{d}E'_\nu} \left[E'_\nu = (1+z)E_\nu\right] , \tag{1.42}$$

where $\mathrm{d}N_\nu/\mathrm{d}E'_\nu$ is the neutrino emission by one merger event at redshift z at the energy $E'_\nu = (1+z)\,E_\nu$. In the above expression, we have assumed a flat universe. We adopt the cosmological parameter values $\Omega_\mathrm{M} = 0.315$, $\Omega_\Lambda = 0.685$, and the Hubble constant $H_0 = 67.4\,\mathrm{km\,s^{-1}\,Mpc^{-1}}$ [124]. $\dot{n}(z)$ describes the rate of binary neutron-star mergers, $\dot{n}(z) = \dot{n}_0\mathcal{R}(z)$, with $\mathcal{R}(z)$ being the source emissivity evolution.

We calculate the time-integrated neutrino flux from one source, $\mathrm{d}N_\nu/\mathrm{d}E_\nu$, by integrating over the neutrino fluences at time t_i obtained numerically (as in Figure 1.10): $\mathrm{d}N_\nu/\mathrm{d}E_\nu \approx \sum_i(\mathrm{d}N_\nu/\mathrm{d}E_\nu\,\mathrm{d}t_i)\,\Delta t_i$, with a resolution of 6 logarithmic bins in time.

The local rate of NS-NS merger events was estimated to by LIGO/Virgo to lie in the range $\dot{n}_0 \sim 110 - 3840\,\mathrm{Gpc^{-3}\,yr^{-1}}$ (90% confidence level), based on the single GW170817 event [2]. More refined estimates seem to converge towards rates of $\sim 600\,\mathrm{Gpc^{-3}\,yr^{-1}}$ [2, 125, 126].

The cosmic evolution of NS-NS merger events is poorly known from observation. Recent theoretical studies based on neutron-star progenitors and binary-system evolution indicate a flat behaviour of the population with redshift (e.g., [127, 128]). On the other hand, the connection of these systems with short GRBs, and the observation of the latter can indicate a source emissivity following the star formation rate (SFR) [129, 130].

In order to be conservative, we adopt a flat evolution model with $\dot{n}_0 = 600\,\mathrm{Gpc}^{-3}\mathrm{yr}^{-1}$ for the GW170817-like scenario. Such a hypothesis represents the simplest model and does not presume of any enhancement of the population at earlier times in the Universe history. For the optimistic scenario, we assume a SFR evolution rate following Ref. [131] and a local merger rate $\dot{n}_0 = 3000\,\mathrm{Gpc}^{-3}\mathrm{yr}^{-1}$. The SFR evolution can enhance the diffuse neutrino flux level by a factor of $\xi_z \sim 2-4$ [132].

One can estimate the maximal diffuse neutrino flux expected in different energy ranges via

$$
\begin{aligned}
E_\nu^2 \Phi_{\max}(E_\nu, \Delta t) &\sim \frac{c}{4\pi H_0}\frac{3}{8}\xi_z \dot{n}_0 \eta_{\mathrm{p}} L_{\mathrm{fb}} \Delta t && (1.43)\\
&\sim 1.9\times 10^{-9}\ \mathrm{GeV\,cm^{-2}\,s^{-1}\,sr^{-1}}\,\eta_{\mathrm{p},-1}\frac{\xi_z}{4} && (1.44)\\
&\quad\times\left(\frac{\dot{n}_0}{3000\ \mathrm{Gpc^{-3}yr^{-1}}}\right)\left(\frac{L_{\mathrm{cr}}}{5.6\times 10^{44}\ \mathrm{erg\,s^{-1}}}\right)\left(\frac{\Delta t}{10^4\,\mathrm{s}}\right),
\end{aligned}
$$

assuming a SFR evolution. At each time step, the neutrino flux peaks at one specific energy range and corresponds to a given cosmic-ray luminosity. The IceCube energy range $\sim E_\nu \gtrsim 10^4\,\mathrm{GeV}$ is reached from times $t = 10^3\,\mathrm{s}$, as can be seen in the time-dependent fluxes presented in Figure 1.10. In the optimistic scenario, assuming a fiducial $\eta_{\mathrm{p}} = 10\%$ baryon loading, a SFR evolution with $\xi_z = 4$, the diffuse flux at $t = 10^4\,\mathrm{s}$ estimated above corresponds to $\sim 6\,\%$ percent of the observed IceCube flux of order $E_\nu^2\Phi_{\mathrm{IC}}\big(E_\nu = 10^6\,\mathrm{GeV}\big) \sim 3\times 10^{-8}\ \mathrm{GeV\,cm^{-2}\,s^{-1}\,sr^{-1}}$.

Figure 1.12 displays the diffuse neutrino fluxes computed by Equation 1.42 for two representative cosmic-ray injection indices, $\alpha = 1.5$ and $\alpha = 2.1$ and two primary cosmic-ray compositions, proton and iron. In all panels, the dashed lines and solid lines correspond respectively to the optimistic scenario and the more conservative model based on the observation of GW170817.

Consistent with the calculation above, we find that high-energy neutrinos from proton primaries can contribute to about $\sim 6\%$ of the diffuse flux measured by the IceCube Observatory [133] in the optimistic scenario, for spectral index $\alpha = 1.5$ and slightly lower for $\alpha = 2.1$. Although the assumed event rate is 5 times higher than the standard value being recently advocated from the recent LIGO/Virgo data, the reasonable values of η_{p} leaves room for lower event rates, at the cost of higher baryon loading. In particular, in this optimistic model, a baryon loading of 20% would enable to reach a larger fraction 12% of the observed IceCube flux. With an order-of-magnitude better sensitivity, IceCube-Gen2

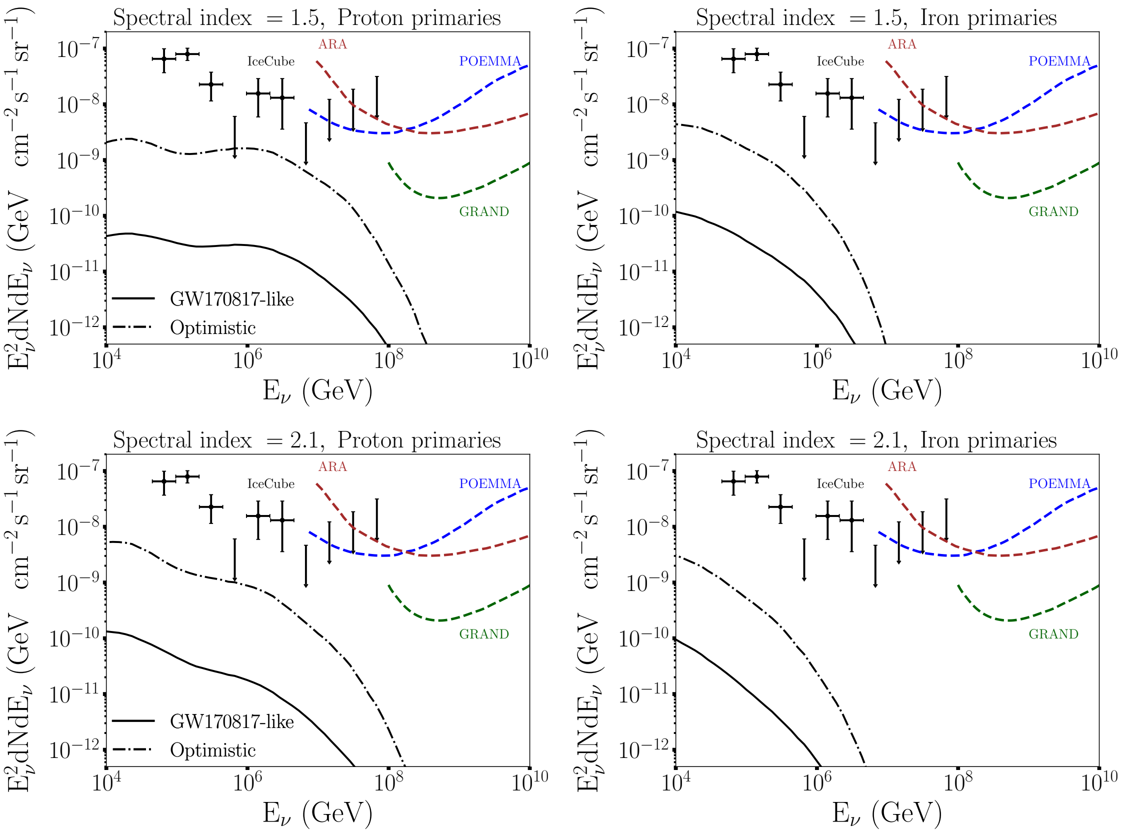

Figure 1.12: Diffuse neutrinos spectra for injection spectral index $\alpha = 1.5$ *(top)* and $\alpha = 2.1$ *(bottom)* of proton primaries *(left)* and iron primaries *(right)*, with baryon loading $\eta_{\rm p} = 0.1$. The GW170817-like scenario follows a flat source evolution with rate $\dot{n}_0 = 600\,{\rm Gpc}^{-3}\,{\rm yr}^{-1}$, while the optimistic scenario follows a SFR source evolution with rate $\dot{n}_0 = 3000\,{\rm Gpc}^{-3}\,{\rm yr}^{-1}$.

could be able to detect such underlying signals, in particular if cross-correlation analysis are done with other gravitational-wave and gamma-ray signals.

The iron primaries produce a slightly higher diffuse flux at low energies thanks to the accumulation of secondary nucleons, but the steeper spectra due to cut-offs at lower energies than for protons lead to overall lower diffusive fluxes. The neutrinos produced in the conservative GW170817-like scenario account for a negligible < 1% fraction of the observed IceCube flux.

Muon neutrinos induce tracks in the detector and can accurately point to the sources, enabling stacked point-source searches. In that framework, one can calculate the muon-neutrino event rate of a population of sources jointly observed in gravitational waves, as done in Ref. [42]. Following these authors, we estimate the expected number of muon neutrino events expected in IceCube-Gen2 by $\mathcal{N}_\mu = \int (\mathrm{d}N/\mathrm{d}E_\nu) A_{\mathrm{eff}}(\delta, E_\nu)\mathrm{d}E_\nu$, with $A_{\mathrm{eff}}(\delta, E_\nu)$ the instrument effective area. We consider only the upgoing and horizontal events that have declination $\delta > 5^\circ$, as the detectability of downgoing events is uncertain for IceCube-Gen2. We assume that sources are standard candles with equal luminosity, and are distributed uniformly in the local Universe within 300 Mpc. Up to that distance, LIGO/Virgo should be sensitive enough to ensure the gravitational-wave detection of any occurring BNS merger as powerful as in our optimistic scenario (but also as in the GW170817-like model). In the optimistic scenario, the BNS event rate of $n_0 = 3000\,\mathrm{Gpc}^{-3}\mathrm{yr}^{-1}$ implies a local rate within 300 Mpc of ~ 340 mergers per year. The neutrino flux in our model being isotropic, this yields a rate of ~ 184 observable events per year within the $\delta > -5^\circ$ sky. The expected rates in this optimistic configuration are of order $\sim 0.1\,\mathrm{yr}^{-1}$ with IceCube-Gen2, for baryon loading $\eta_{\mathrm{p}} = 0.1$. One can thus expect a detection with several years of operation.

The rates could be linearly scaled up with higher baryon loading. Also, taking into account downgoing events could double the rate, depending on the final experimental performances. Finally, as noted in Ref. [42], it is likely that LIGO/Virgo significantly improves their sensitivity, increasing thereby the coincident detection rate.

1.7 Conclusion, Discussion

We have calculated the high-energy neutrino fluxes from binary neutron star merger remnants, focusing on their production by relativistic particles accelerated in unbound outflows from the central black hole accretion disk fed by the fall-back of marginally bound debris. The relativistic particles generate neutrinos through their interaction with the kilonova radiation field and inner (red) kilonova baryon ejecta shell. We examined two scenarios. The first scenario, motivated by observations and modeling of LIGO's first neutron star merger GW170817, adopts an ejecta mass of $M_{\mathrm{ej}} = 10^{-2}\,M_\odot$, a velocity of $\beta_{\mathrm{ej}} = 0.3$ and a mass accretion disk $M_{\mathrm{fb}} = 5 \times 10^{-2}\,M_\odot$. The second scenario assumes a much lower ejecta mass, along with a larger fall-back mass $M_{\mathrm{ej}} = 10^{-4}\,M_\odot$, $\beta_{\mathrm{ej}} = 0.3$ and $M_{\mathrm{fb}} = 10^{-1}\,M_\odot$. The second scenario, called "optimistic", was designed to maximize the produced neutrino fluxes, within the parameter space of physically-allowed ejecta properties. We use a Monte-Carlo code to model the propagation and interactions of accelerated particles inside the kilonova ejecta, thereby computing the time-dependant neutrino fluxes resulting from the configurations described above.

The neutrino flux is found to peak in the IceCube energy range ($10^{4-6}\,\mathrm{GeV}$), at times $t \sim 10^{3-4}\,\mathrm{s}$ after merger. Single sources have low fluxes that can only be detected with IceCube-Gen2 for optimistic scenarios, if located at distances $\sim 4\,\mathrm{Mpc}$. The diffuse flux is below detectability for the GW170817-like scenario. For the optimistic scenario, we find that, for baryon loading $\eta_{\rm p} \sim 20\%$, the diffuse flux could contribute to $\sim 12\%$ of the observed IceCube flux. This leaves room for a future experiment with increased effective area such as IceCube-Gen2, to detect an underlying flux. In particular, cross-correlation searches with gravitational wave signals could lead to an enhanced signal-detection power below detection thresholds, using spatial and temporal information [134]. The detection of muon neutrinos from stacked local sources detected in gravitational waves is possible for several decades of operation, for the optimistic scenario with baryon loading $\eta_{\rm p} = 0.1$, with event rates of 0.1 neutrinos per year with IceCube-Gen2 for population rates of $\dot{n}_0 = 3000\,{\rm Gpc^{-3}yr^{-1}}$. As discussed in the previous section, these rates could become higher with higher $\eta_{\rm p}$, but also with experimental improvements: e.g., if downgoing events can be efficiently detected with IceCube-Gen2 and if LIGO/Virgo improves its detection sensitivity.

We note that the actual uncertainties on the structure of the the inner region of the binary neutron star merger remnants still leave room for higher fallback luminosities than examined here, due to larger fallback ejecta masses or super-Eddington regime. In this case, the flux could be boosted up to one order of magnitude and comfortably fit the observed IceCube diffuse flux. We caution that such fluxes would assume also the optimistic population rate and evolution scenario discussed in the previous section. Although such an exercise is speculative, it motivates the search for cross-correlation searches between neutrino, gravitational-wave and gamma-ray diffuse signals. It is also likely that more observations of single sources and of the overall population will soon put strong constraints on such scenarios.

In our computation, no element heavier than iron was included. The matter falling back to the disk and thus ejected in the disk wind could ultimately be of heavier composition. Although the fraction of lanthanides is low (of the order of $X_{\rm r} = 10^{-3} - 10^{-2}$) most of the mass becomes trapped in atomic numbers of $A \sim 100 - 200$. If acceleration happens in a region where the temperature is still $> 10^9\,{\rm K}$, and/or the entropy is particularly high, nuclei may have not time to assemble yet. In addition, the cross section for hadronic interactions of nuclei scales roughly as $A^{2/3}$. This implies that for such particles, the hadronic interaction timescales in the acceleration region would be shorter of more than an order of magnitude, i.e., $t_{A{\rm p}} \lesssim 0.1\,{\rm s} < t_{\rm acc}$ at $t = 10^3\,{\rm s}$ (see numbers in Section 1.3.3). These nuclei would hence be mostly disintegrated into nucleons and lower mass nuclei, which can then be accelerated to the energies calculated in Section 1.3.3. Note that a surviving nucleus with large mass is not likely to have an important contribution to the neutrino flux calculated here. Indeed, the neutrino maximum energy is limited by a combination of the synchrotron cooling of the primary, scaling as $(A/Z)^{3/2}$ and the photonuclear interactions, scaling as $1/A$. So for heavy primaries, neutrinos could pile up due to numerous secondary nucleons, but at an overall energy roughly 2 orders of magnitude lower than for protons, where they would be dominated by atmospheric neutrinos.

In many existing models in the literature [41, 42, 43, 44, 45], the production of high-energy neutrinos in neutron star mergers takes place in relativistic jets during the prompt or extended phases (times $t < 10^3\,\mathrm{s}$). In these models, the energetics of the emission are up to a couple of orders of magnitudes higher than in our model, as arises due to the earlier emission time (higher available luminosity) and the Lorentz boost. The escape of secondary mesons without catastrophic cascades is possible because of the more diluted radiation field at the larger distances where processes occur. However, the directional emission from the collimated relativistic jet could reduce the detection probability. In contrast, the emission in our model, where the deflection of the cosmic rays accelerated in the equatorial plane and crossing the kilonova, result in an isotropic emission and could be in principle connected to objects for which the prompt photon emission is not observed. This is the reason why the detection rates found in our optimistic case are of the same order as the ones computed in the works of Refs. [42, 45].

Another interesting side product of this model could be gamma-ray photons, that could be produced through synchrotron and curvature radiations in the kilonova ejecta [65, 9]. At 10^3 s when secondary neutrinos and gamma rays are produced, the fallback radiation rate is $L_{\mathrm{fb}} \sim 10^{46}\,\mathrm{erg\,s^{-1}}$. For a source located at 40 Mpc, this corresponds to a secondary flux of $F_{\nu,\gamma} \sim 5.2 \times 10^{-8}\,\mathrm{erg\,cm^{-2}\,s^{-1}}$. This is below the point-source sensitivity of IceCube but close to that of *Fermi*-LAT. The observation of such gamma-ray emissions could probe the existence of non-thermal interactions inside the kilonova ejecta.

Chapter 2

Cosmic neutrino detection: optimisation of a kilometric-sized radio array

2.1 Introduction

As seen in Chapter 1 for the case of NS mergers, ultra high energy neutrinos (UHE ν) are one of the few messengers of violent phenomena and of their hadronic processes in the Universe ([23, 135] and references therein). Their low interaction probability with matter, and their non deflection by the ubiquitous magnetic fields in our Universe, allow them to carry unaltered information from sources located at cosmological distances, but on the other hand makes their detection challenging: non-negligible detection probability can be achieved only with large volumes of dense targets. In the high energy regime, neutrino observatories such as IceCube and KM3NET already scrutinise the sky thanks to Cerenkov light detection from neutrinos crossing the Earth or directly coming from the sky.

Since the neutrino cross section increases with the energy, at neutrino energies targeted here ($E > 10^{16}\,\mathrm{eV}$), the Earth is opaque to neutrinos [136]. Therefore only Earth-skimming trajectories yield significant probability of neutrino interaction with matter, leading to a subsequent tau decay[1] in the atmosphere, eventually inducing an extensive air-shower

---

[1] Rigorously, all neutrino flavours interact inside the Earth, however, only the tau neutrino interactions result in a particle (a tau) heavy enough to escape the Earth and decay inside the atmosphere. Electron neutrino interactions lead to electrons which are absorbed within a few tens of meters inside the Earth and muon neutrino interactions produce muons which emerge in the atmosphere but propagate too far before inducing an EAS.

(EAS). The detection of these EAS has been proposed as a possible technique to search for these cosmic particles [137].

Angular convention In the the following chapters, the angles are displayed in the emitter convention. This description is identical to the natural spherical base convention, with the x-axis pointing towards North and the y-axis pointing towards West. Therefore, a shower flying towards North is represented with an azimuth $\phi = 0°$, and a shower flying towards East with an azimuth $\phi = 270°$. Similarly, an up-going shower is represented with a zenith $0° \leqslant \theta \leqslant 90°$ (from vertical to horizontal trajectories) and a down-going shower with a zenith $90° \leqslant \theta \leqslant 180°$ (see sketch of Figure 2.1).

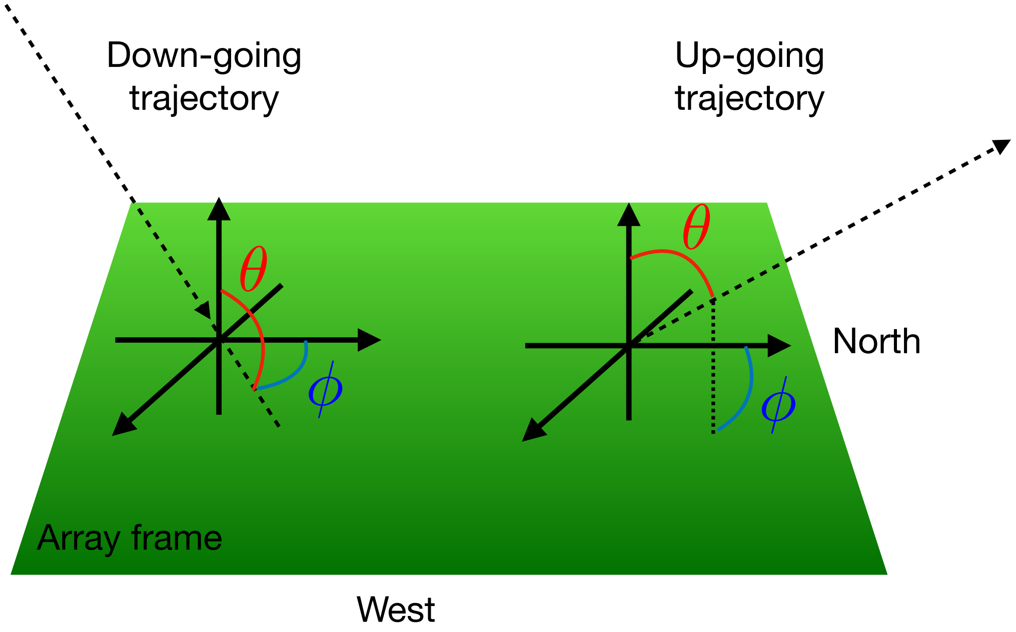

Figure 2.1: Sketch of the GRAND angular conventions. The reference frame is colocated with the array frame, resulting in up-going trajectories with zenith angles defined as $0° \leqslant \theta \leqslant 90°$, and thus down-going trajectories have zenith angles such that $90° \leqslant \theta \leqslant 180°$. Finally, the origin of the azimuth is oriented toward the North and counting clockwise toward the West.

2.1.1 Description of EAS

High-energy cosmic particles (cosmic rays, gamma rays, neutrinos or even neutrino induced leptons in the case of Earth-skimming neutrinos) generate EAS when they interact with molecules of the Earth's atmosphere.

2.1.1.1 Particle cascades and EAS structure

The collision with molecules of the atmosphere produces secondary particles, which then collide again with atmospheric particles, creating a cascade of decay products as depicted on Figure 2.2. This plasma of particles moves at relativistic speed, boosted in the direction of the primary particle resulting in the so-called shower. The particles inside this plasma continue to interact with each other and with the atmosphere, until they either reach the ground in the case of down-going EAS or die out due to energy losses during the cascade process. These processes are well known and extensively studied [138]. We summarise them below.

Depending on the nature of the primary particle, the initial collisions either result in a purely electromagnetic cascade (gamma ray and electron-positron primaries) or a hadronic cascade (comic rays and neutrinos).

In the case of a hadronic cascade, the primary particle is fragmented into subsequent hadronic particles. These subsequent particles collide with the molecules of the atmosphere again until, there is not enough energy left for further interactions. The secondary hadronic particles are mostly composed of pions, kaons but also baryons and nuclear fragments.

The neutral pions π^0 have an extremely short lifetime (about $\sim 10^{-8}\,\mathrm{ns}$) and decay through the channel $\pi^0 \to \gamma\,\gamma$. The photons initiate purely electromagnetic sub-cascades of electrons e^-, positrons e^+ and γ via pair production, Compton scattering, ionisation and Bremsstrahlung. The electromagnetic component increases until the electrons and positrons reach an energy threshold below which the dominant energy loss processes are ionisation and excitation, resulting in a very quick loss of their remaining energy.

The charged pions $\pi^\pm$ have a longer lifetime of about $\sim 25\,\mathrm{ns}$, and they interact until their energy reaches a value of $E_{\pi^\pm} \lesssim 30\,\mathrm{GeV}$, below which they decay through the channel $\pi^\pm \to \mu^\pm + \nu_\mu/\bar{\nu}_\mu$. The resulting muons $\mu^\pm$ have a lifetime of about $\sim 2.2\,\mu\mathrm{s}$ and a small cross section, implying that they propagate with the shower for a longer time, creating a muonic component of the EAS. The muonic component suffer very small energy losses in the atmosphere and therefore have a high probability to reach the ground.

The charged kaons have a shorter lifetime than the charged pions (about $\sim 10\,\mathrm{ns}$), and

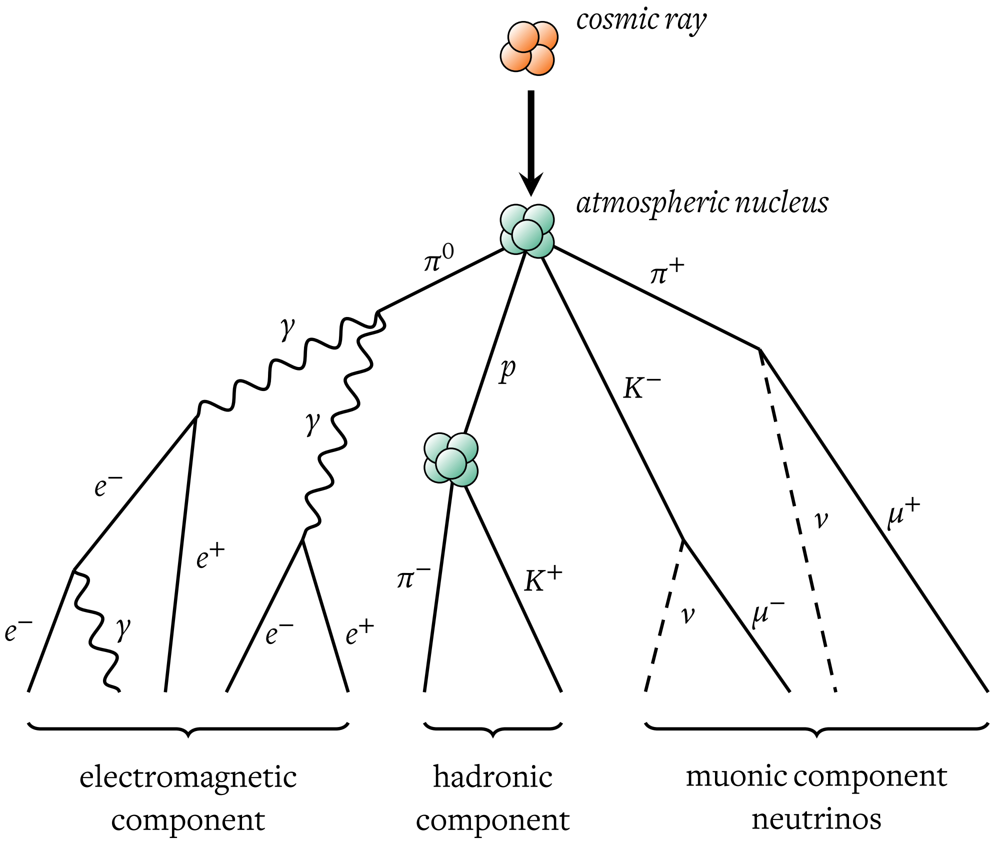

Figure 2.2: Schematic description of the shower cascades process. The primary particle here is a cosmic-ray (but it is similar for any other primary: gamma-ray or neutrino induced tau). Taken from [139].

therefore decay at a higher energy through the channels $k^{\pm} \rightarrow \pi^{\pm} + \pi^{0}$ or directly $k^{\pm} \rightarrow \mu^{\pm} + \nu_{\mu}/\bar{\nu}_{\mu}$.

The EAS structure is therefore composed of a hadronic core, where the heaviest particles are the closest to the shower propagation axis as imposed by momentum conservation. This hadronic core feeds the muonic component which extends to larger distances from the core and which itself contributes to source the electromagnetic component (in addition to the hadronic component) located farther away from the shower axis. Depending on the energy content of the shower, the injection altitude and the crossed atmospheric depth, the EAS components cannot all reach the ground. In general, only the muonic component is guaranteed to reach the ground as it suffer minimal energy losses in the atmosphere. In second position comes the electromagnetic component and finally the hadronic component with the highest interaction rates (and so the highest energy losses rates).

2.1.1.2 EAS profiles

The EAS can be described as one object travelling at relativistic speed through the atmosphere, with lateral and longitudinal profiles, the characteristics of which can give information on the primary particle.

Lateral profile Due to their high velocities, the particles in the EAS concentrate in a thin layer called "pancake". Its thickness is a few meters close the the shower axis [140]. The multiple Coulomb scattering of electrons from the air molecules result in a lateral spread of the shower front. It is characterised by the Molière radius [141] $r_{\mathrm{M}} \sim \left(\frac{21\,\mathrm{MeV}}{\epsilon_c}\right) X_0$, where $\epsilon_c = 86\,\mathrm{MeV}$ in the air is the critical energy below which energy losses due to ionisation is equal to the bremsstrahlung losses, and $X_0 \sim 37\,\mathrm{g.cm}^{-2}$ is the air radiation length. At sea level, this typical radius is about 80 m [142] and increases with altitude. The particle front is on average a quasi-parabolic profile centred on the shower axis [143]. The whole structure moves towards the direction of the EAS.

The lateral particle density is commonly described by the Nishimura-Kamata-Greisen (NKG) parametrisation [144, 145] for a pure electromagnetic EAS

$$\rho_{\mathrm{NKG}}(r) = \frac{N_{\mathrm{e}}}{r_{\mathrm{M}}^2} \frac{\Gamma(4.5 - s_{\mathrm{nkg}})}{2\pi\Gamma(s_{\mathrm{nkg}})\,\Gamma(4.5 - 2s_{\mathrm{nkg}})} \left(\frac{r}{r_{\mathrm{M}}}\right)^{s_{\mathrm{nkg}}-2} \left(1 + \frac{r}{r_{\mathrm{M}}}\right)^{s_{\mathrm{nkg}}-4.5}, \tag{2.1}$$

where N_e is the total number of electrons, $s_{\mathrm{nkg}} = 3/\left[1 + \frac{2\ln(E_0/\epsilon_c)}{t}\right]$ is the EAS "age" parameter, with $t = \int_z^\infty \frac{\rho_{\mathrm{atm}}}{X_0}(z')\,\mathrm{d}z'$ the slant depth (normalised to one radiation length) [146], E_0 is the primary particle energy, and r the lateral distance to the shower axis.

The shower lateral profile depends on the shower stage (age s_{nkg}) and therefore, on the primary particle energy E_0.

Longitudinal profile The longitudinal profile of the EAS refers to the time varying longitudinal development. During the cascade processes, the number of particles grows to reach its maximal value, which depends on the primary particle energy, and then decreases as particle energies are gradually absorbed by the atmosphere, until the EAS reaches the ground or dies out. The maximum of development is noted X_{max}: it corresponds both to a physical location along the longitudinal axis of the EAS and to a time. Because the amount of crossed atmosphere determines the interactions length, the natural unit for X_{max}

is the atmospheric depth in $g.\text{cm}^{-2}$, representing the integrated column density, and can be expressed as

$$X_{\max}(h_{X_{\max}}) = \int_{h_{X_{\max}}}^{h_{\text{Atmosphere}}} \rho(h)\,\mathrm{d}h\ , \tag{2.2}$$

where $h_{X_{\max}}$ corresponds to the $X_{\max}$ altitude, $h_{\text{Atmosphere}}$ is the maximum altitude of the atmosphere and $\rho(h)$ is the atmosphere density at height h. The $X_{\max}$ parameter is sensitive to the nature of the primary, as gamma rays and neutrinos are expected to interact deeper in the atmosphere than cosmic rays, while protons are expected to interact deeper than iron nuclei (see Figure 2.3). Indeed, the binding energy of $\sim 5\,\text{MeV}$ per nucleon is much lower than the interaction energies at play. Therefore, cosmic rays are expected to be depleted nucleon by nucleon, and at a same nucleus energy the heavier nuclei will interact earlier on average. In addition a $X_{\max}$ value can be associated to each component of the EAS and formally we have $X_{\max}^{\text{Hadron}}$, $X_{\max}^{\mu}$, $X_{\max}^{\text{EM}}$.

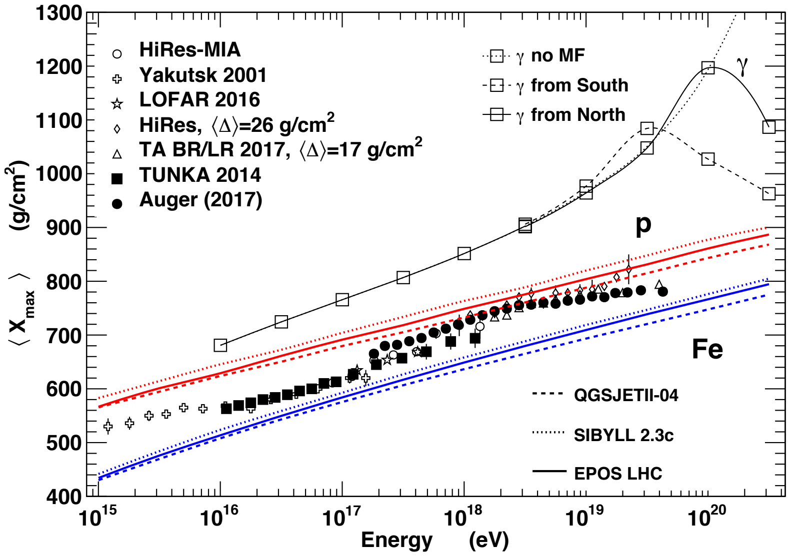

Figure 2.3: Measurements of $\langle X_{\max}\rangle$ from UHECR EAS. Compared to simulations performed using hadronic interaction models, assuming a pure-proton or pure-iron composition. Taken from [23].

The Heitler model [147] (originally introduced by Carlson and Oppenheimer [148]) is a simple scaling model, for pure electromagnetic showers, that allows us to understand the processes leading to quantities such as $X_{\max}$. In this model a particle of energy E interacts and produces two particles of energy $E/2$ after propagating over an interaction depth λ. After n interactions, we end up with a propagation depth $X = n\,\lambda$, a particle number

$N(X) = 2^n = 2^{X/\lambda}$ and an energy $E(X) = E_0/2^{X/\lambda}$, where E_0 is the primary particle energy. Since the interaction processes stop when the particles have reached the critical energy ϵ_c, it leads to

$$N_{\max} = \frac{E_0}{\epsilon_c} \ , \tag{2.3}$$

$$X_{\max} = \lambda \ln \left(\frac{E_0}{\epsilon_c} \right) \ . \tag{2.4}$$

From these results we should expect an energy dependency on the $X_{\max}$ position, called elongation rate

$$\Lambda = \frac{\mathrm{d}X_{\max}}{\mathrm{d}\log\left(E_0\right)} = \lambda \ln\left(10\right) \ , \tag{2.5}$$

this elongation rate is an upper limit of the *Linsley elongation rate theorem* [149]. In addition, in this model, the nucleus can be seen as independent nucleons of energy $E_n = E_0/A$, where A is the atomic number of the nucleus, and yields to

$$X^A_{\max} = X_{\max}\left(\frac{E_0}{A} \right) \ . \tag{2.6}$$

Hence, heavier elements are expected to have a smaller $X_{\max}$ value. Similar models [150] can be applied to the hadronic and muonic components of the EAS. However the complexity of the interactions makes the results less accurate. Furthermore at the energies considered here, the hadronic processes are not well understood, which makes the analysis of the mass composition of EAS more difficult.

Finally, it is worth mentioning that the physical location of $X_{\max}$ along the shower direction depends on the shower inclination. Indeed, the shower longitudinal development and therefore $X_{\max}$ depends on the amount of crossed atmospheric depth. Since the distance between the injection point and the shower core is much larger for very inclined showers than for vertical ones, scaling roughly as $1/\cos\left(\theta\right)$ with θ the zenith angle of the shower, the same amount of atmospheric depth from the shower core for an inclined event is reached at a much larger distance from the shower core. Therefore the physical location of $X_{\max}$ is much farther for an inclined shower than for a vertical one. This effect has great consequences for the reconstruction as shown in Section 3.2.

The longitudinal profile of the EAS depends on the energy of the primary particle but also on its composition. It is important to mention that all the EAS characteristics are obviously subject to fluctuations from one shower to another due to the probabilistic nature of the fundamental interactions at play (stochastic processes), inducing fluctuations on the measured shower parameters. Therefore quantities such as $X_{\max}$ are only statistically measured on a large sample of events.

2.1.2 Radio emission from EAS

Classical electrodynamics predicts the electromagnetic emissions from charged particle acceleration [63, 64]. In the EAS, the electromagnetic component (electrons and positrons) produces a highly beamed coherent emission in the MHz regime. The beaming is a direct consequence of the relativistic speed of the emitting particles, while the coherence results from the small size of the emission region compared to the observed wavelength. Since most of the emission is produced where the electron-positron density is the highest, only the few meters around the shower axis of the particle pancake [151] significantly contribute to the emission (as the density quickly decreases with the lateral extension see Section 2.1.1.2). This results in a coherent emission below $\sim 100\,\mathrm{MHz}$. Consequently, the amplitude of the radio signal scales linearly with the number of electrons and positrons and its power scales quadratically [152]. The relativistic motion of the EAS and its electromagnetic content in the atmosphere result in additional features. The relevant part of the shower contributing to the coherent emission depends on the observer angle because the emission propagates at speed c/n, where n is the atmosphere refractive index, while the source travels at a speed of the order of the speed of light in vacuum c. In order to produce a coherent emission, the source needs to emit on phase radiations. In this configuration, this is achieved only for

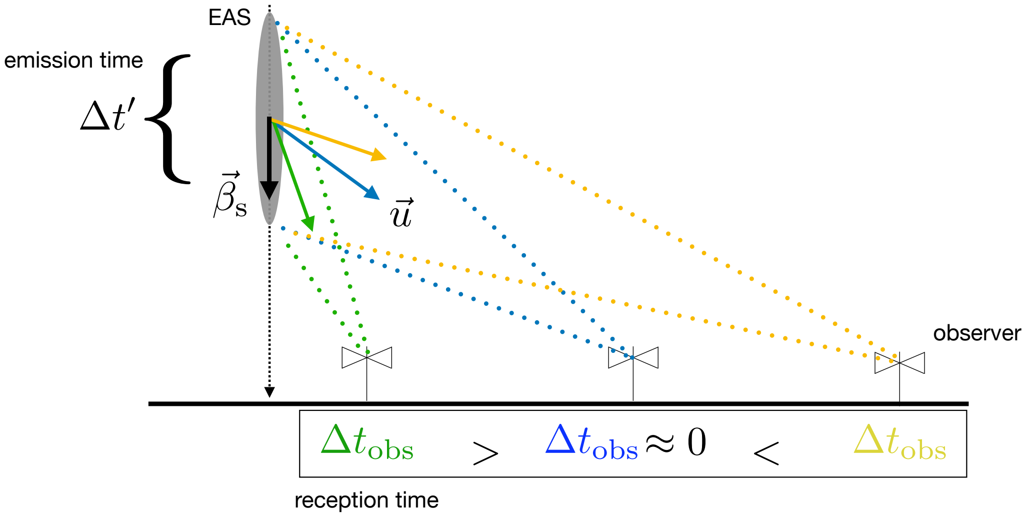

Figure 2.4: Sketch of the Cerenkov angle effect. At specific observer positions with respect to the shower axis, the relative time between two emissions from two distinct parts of the shower is almost zero as the two emissions arrive almost at the same time. The exact position depends on the shower velocity and the refractive index of the medium which delays the propagation of the emissions. Under realistic conditions, the situation is much more complex than this two emission zones illustrated here.

small observer angles. At larger observer angles, the coherence is ensured only for lower frequencies [153]. At a specific angle called Cerenkov angle, the projected speed of the electrons along the observer line of sight is equal to the speed of the emission (see sketch on Figure 2.4). This leads to simultaneous arrival times for all radiations at the observer position. The observed signal is therefore composed of very brief and intense pulse in the time domain, and an emission extending to GHz in the frequency domain [154, 155]. This effect is called Cerenkov compression.

Two mechanisms dominate the radio emission from EAS: the geomagnetic emission and the Askaryan (also called charge-excess) mechanisms (see Figure 2.5). In atmospheric showers, the geomagnetic emission is dominant but the Askaryan emission induces specific asymmetries effects in the signal distribution. On the other hand, in dense media such as ice or rocks, the geomagnetic effect is negligible due to the small deflection radius induced by the smaller shower development, resulting in a pure Askaryan-like emission.

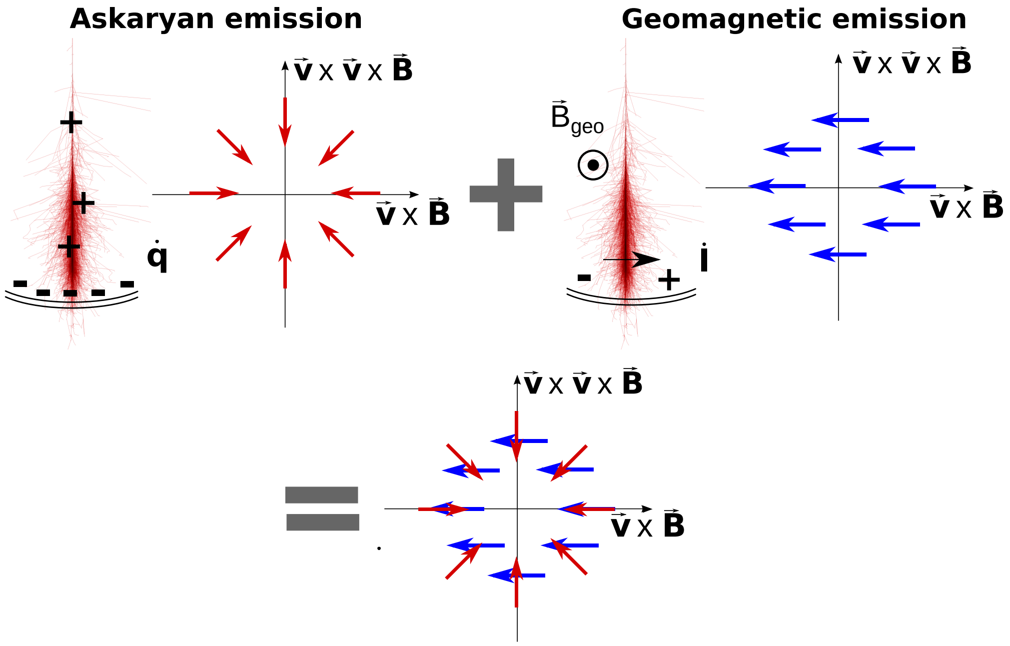

Figure 2.5: Sketch of the main radio emission mechanisms inside an EAS and their polarisation signatures, in the shower frame: $\{\vec{v} \times \vec{B}, \vec{v} \times \vec{v} \times \ \vec{B}, \vec{v}\}$. Taken from [156].

2.1.2.1 Geomagnetic emission

The geomagnetic emission mechanism consists in the deflection of the electrons and positron in opposite directions, because the Lorentz force acts in opposite directions for opposite charges, resulting in a transverse drift current in the air (see Figure 2.5). In addition, this drift currents varies in times due to the longitudinal development of the EAS (see Section 2.1.1.2). The time (and spatial) variations of this current leads to a radio emission [157]. Since the emission is related to the Lorentz force which drives this process

$$\vec{F}_{\text{Lorentz}} = q\vec{v} \times \vec{B} \ , \tag{2.7}$$

where q is the charge of the particles, $\vec{v}$ is the velocity vector of the EAS and $\vec{B}$ is the geomagnetic field, the polarisation of the geomagnetic emission is along the $\vec{v} \times \vec{B}$ direction and the amplitude proportional to the strength of the Lorentz force. Also, in principle, higher emission intensities are expected for very inclined EAS as the longitudinal development takes place at a higher altitude, leading to a larger amount of charged particles and for a longer time [153].

2.1.2.2 Askaryan (charge-excess) emission

The particles of the EAS ionise the molecules of the atmosphere along their path and positrons from the EAS annihilate with electrons of the air molecules, resulting in an accumulation of electrons in the front of the shower. The negative charge excess can be up to $20 - 30\%$ [158] and induces a dipole between the positively charged plasma behind the shower front and the electrons in front. The time variation of the net charge excess leads to the so-called Askaryan (charge-excess) emission [159]. The projected polarisation on the observer plane is oriented radially towards the shower axis [160] as the field lines of a dipole projected along its symmetry axis (see Figure 2.5).

The combination of the two emission mechanisms induces specific asymmetries in the footprint (see Section 3.3) with a ratio of Askaryan strength over geomagnetic between $1 - 20\%$, depending on the magnetic field orientation with respect to the shower direction.

2.1.2.3 Microscopic description

From a microscopic point-of-view the whole EAS radiation results from the superposition of the radiation of all individual particles, where the radiation from each particle can be described with the Liénart-Wiechert equations

$$\Phi(\vec{x},t) = \frac{1}{4\pi\epsilon_0}\left[\frac{e}{\left(1-\vec{\beta}\cdot\vec{u}\right)R}\right]_{\text{ret}} , \tag{2.8}$$

$$\vec{A}(\vec{x},t) = \frac{\mu_0 c}{4\pi}\left[\frac{e\,\vec{\beta}}{\left(1-\vec{\beta}\cdot\vec{u}\right)R}\right]_{\text{ret}} , \tag{2.9}$$

where ϵ_0 is the vacuum permittivity, μ_0 is the vacuum permeability, c is the vacuum speed of light, e is the electron charge, $\vec{\beta}$ is the particle velocity vector inside the medium, in unit of c, $\vec{u}$ is the unit vector along the line of sight of the observer, R is the distance between the observer and the particle and the "ret" index implies that the quantity under brackets are evaluated at the retarded time (defined from standard electrodynamics as the time corrected of the propagation to the observer location). From these potentials, the electric-field is simply derived as

$$\vec{E}(\vec{x},t) = -\vec{\boldsymbol{\nabla}}\Phi(\vec{x},t) - \frac{\partial\vec{A}(\vec{x},t)}{\partial t} . \tag{2.10}$$

From these first principle equations, the Cerenkov condition already appears in the denominator of the potential where the radiation amplitude tends to infinity if

$$1-\vec{\beta}\cdot\vec{u} = 0 , \tag{2.11}$$

which is satisfied for a specific angle between $\vec{u}$ and $\vec{\beta} = \vec{v}/c$. With $n = v/c$ the air refractive index, this gives

$$\omega_{\text{C}} = \text{acos}\left(1/n\right) , \tag{2.12}$$

the standard Cerenkov angle formula.

The microscopic description already allows us to describe the basic features of the EAS radio emission, but in order to capture the collective effects of the billions of charged particles inside a particle shower, either a numerical approach or a macroscopic description is needed.

2.1.2.4 Macroscopic description

Rather than describing the potentials generated by one charged particle, the macroscopic description intends to directly derive the potentials from the charge current density. The Liénart-Wiechert equations can be generalised to a charge current density $j^\mu(\vec{x},t)$ through

$$A^\mu(\vec{x},t) = \frac{1}{4\pi\epsilon_0}\int_{\text{EAS}} \left.\frac{j^\mu(\vec{x},t)}{R\left(1-\vec{\beta}\cdot\vec{u}\right)}\right|_{\text{ret}} , \tag{2.13}$$

evaluated over the shower distributions and where the zeroth component of the four-dimensional potential corresponds to the scalar potential presented in Equation 2.8 $A^{\mu=0}(\vec{x},t) = \Phi(\vec{x},t)$, and the three other components corresponds to the vectorial potential presented in Equation 2.9 $A^{\mu=1,2,3}(\vec{x},t) = \vec{A}(\vec{x},t)$.

From this we derive the electric field

$$E^{\nu}(\vec{x},t) = \partial_{\nu} A^{\mu}(\vec{x},t) \ . \tag{2.14}$$

Again in this description, all the Cerenkov effects are present through the term $1 - \vec{\beta} \cdot \vec{u}$ but all the collective effect of the EAS charged particles is captured in the integral over the EAS of the charge current density.

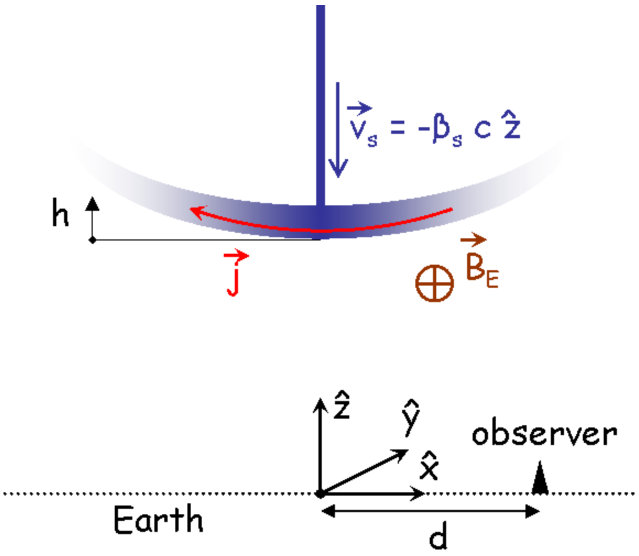

Figure 2.6: Sketch of the studied shower configuration. In this vertical geometry, the particle shower front travels at a speed $\beta_s c$ to the ground, and is characterised by a thickness h. The observer is located at a distance d from the core. Taken from [161].

In [161] the authors study a simplified vertical EAS description as depicted in Figure 2.6. The electron/positron density is written as function of the distance h behind the shower front

$$\rho(x,y,z,t) = \int \tilde{\rho}(x,y,z,t,h)\, \mathrm{d}h \ , \tag{2.15}$$

where $\tilde{\rho}(x,y,z,t,h)$ is expressed as a combination of the temporal longitudinal development $f_t(t)$, the NKG lateral shower front density $\rho_{\mathrm{NKG}}(x,y)$ (see Equation 2.1) and the particle front thickness density $\rho_p(h)$

$$\tilde{\rho}(x,y,z,t,h) = N_e \delta(z + \beta_s ct + h) \times f_t(t) \rho_{\mathrm{NKG}}(x,y) \rho_p(h) \ . \tag{2.16}$$

The charged current can then be described as

$$j(x,y,z,t) = \int \langle v_d q \rangle \, e \tilde{\rho}(x,y,z,t,h) \, \mathrm{d}h \ , \tag{2.17}$$

with $\langle v_d q \rangle$ the averaged drift velocity (to take into account positron and electron opposite drifts). Before re-injecting Equation 2.17 in Equation 2.13, the observer distance $R\Big(1 - \vec{\beta} \cdot \vec{u}\Big)\big|_{\mathrm{ret}}$ can be rewritten explicitly in terms of the retarded time t_r, the shower velocity β_s in unit of c and the pancake thickness h

$$\begin{aligned} \mathcal{D} = R\Big(1 - \vec{\beta} \cdot \vec{u}\Big)\Big|_{\mathrm{ret}} &= \frac{c}{n}(t - t_r) - n\beta_s(h - c\beta_s t_r), \\ &= \sqrt{(-c\beta_s t + h)^2 + (1 - \beta_s^2 n^2) d^2} \ . \end{aligned} \tag{2.18}$$

This leads to the reduced expression of the vector potential to the x component only (since the current density is only along the x component, in this simplified, vertical, configuration)

$$A^x(t,d) = J \int \mathrm{d}h \, \frac{\rho_p(h) f_t(t_r)}{\mathcal{D}} \ , \tag{2.19}$$

with $J = \langle v_d q \rangle N_e e / 4\pi\epsilon_0$. The dominant component of the electric-field derivative is given by

$$\vec{E}(t,d) = -\partial_0 \vec{A}(t,d) \ , \tag{2.20}$$

because the spatial derivative only describes a dipole effect which is subdominant as explained by the authors [161]. Finally the electric-field is given by

$$\vec{E}(t,d) = -J \int_0^\infty \mathrm{d}h \, \frac{f_t(t_r)}{\mathcal{D}} \beta \frac{\mathrm{d}\rho_p(h)}{\mathrm{d}h} - J \int_0^\infty \frac{\rho_p(h)}{\mathcal{D}} \frac{\mathrm{d}f_t(t_r)}{\mathrm{d}h} \ , \tag{2.21}$$

where the collective effects of the EAS on the electric-field are described through the derivative of the temporal longitudinal development $f_t(t_r)$ and the pancake thickness $\rho_p(h)$. This emission description will be used later in Section 3.2 for a derivation of the shower induced electric-field in simplified conditions, for the study of the radiation wavefront.

Additional emission mechanisms exist, which are not relevant for this work but are highly interesting. We may cite in particular the atmospheric electric-field acceleration [162], which becomes dominant during thunderstorm (or even heavy rains), the transition radiation [163], which comes at play when the emission travels from one medium to another, the particle plasma reflection emission [164], which are promising for in-ice experiments.

2.1.3 Simulations of EAS radio emission: ZHAireS

The simulation of EAS radio signals can be achieved following either a macroscopic or a microscopic description. Semi analytical macroscopic approaches have been developed (see in particular the MGMR method [161]), with the advantages of fast computational times and transparency in the emission mechanisms. However the assumptions to disentangle the various emission mechanisms assumed in these simulation models are not always realistic [165]. Microscopic approaches rely on the superposition effect of individual radiating charges (as described in Section 2.1.2.3). Therefore, all the coherence mechanisms are automatically taken into account thanks to a careful phase shift treatment. Such an approach is used in the ZHAireS [166] and CoREAS [167] codes, where the stochastic interactions of billions of charged particles inside the EAS are described via a Monte-Carlo model (respectively Aires [168] and Corsika [169]) based on hadronic interaction models (for instance Sybill [170] or EPOS [171]). Then, the radio emissions of all the simulated particles are computed via an emission formalism derived from first principles, respectively the *ZHS* [172] and *EndPoint* [165] formalisms.

In the following subsections, I present the ZHAireS simulation code used for this work. In particular, I briefly present the emission formalism and then focus on the atmosphere model and refraction index computation.

2.1.3.1 The Radio emission computation: *ZHS* formalism

The *ZHS* formalism consists in computing the Liénart-Wiechert electric-field from the subdivision of particles tracks. Along each of these tracks, the speed and direction remain constant. The superposition of all these tracks naturally takes into account any radio interferences resulting from particle deflection, scattering, creation or annihilation.

However the electric-field computation relies on the Fraunhofer approximation for each individual tracks. Consequently for each track of length l, located at a distance R for the observer and with a viewing angle θ between the track and the line of sight of the observer, the following condition must be fulfilled

$$\frac{l^2 \sin(\theta)^2}{R} < \frac{c}{2\pi f} \ , \tag{2.22}$$

where f is the observation frequency. This condition is verified for frequencies up to 300 MHz [166] and even higher for very inclined EAS, which develop further away from the observer (see Section 2.1.1.2).

2.1.3.2 The Atmosphere model in Aires

The atmosphere model is obviously of primordial importance as it is the medium through which the particles propagate and interact and through which the radiation propagates. Therefore, it strongly impacts the longitudinal shower development, thus the X_{max} value but also the refractive index and therefore the shape of the electromagnetic pulse (including Cerenkov effect, propagation time, coherence, etc.). The inhomogeneity of the atmosphere density varies of about six orders of magnitude between 0 km to 100 km altitude and another six orders of magnitude between 100 km to 300 km altitude.

The Aires atmospheric model uses the *US standard atmosphere* [173] by default, but other models can be used. The atmosphere is described as spherically symmetric layers of few hundreds of kilometers thick centered on the Earth. In this description, all relevant quantities are computed as a function of their local vertical altitude. The implemented atmosphere is based on the *Linsley* model, with an upper atmospheric altitude extending up to $h_{\text{max}} = 420\,\text{km}$. Any higher altitude is assumed to result in a null density, which is justified, since the shower development only takes place in the last 50 km above ground. The chemical composition of the atmosphere is assumed to be constant, which deviates from reality only for altitudes higher than 90 km. The chemical composition is modelled as *air-atoms* with $Z_{\text{eff}} = 7.3$ and $\langle Z_{\text{eff}}/A_{\text{eff}} \rangle = 0.5$ to match the measurements best.

Finally the *Linsley* parameterisation is a function of the vertical atmosphere depth $X_v(h)$, following a similar definition as in Equation 2.2 and from which the density is given by

$$\rho(h) = -\frac{\mathrm{d}X_v(h)}{\mathrm{d}h} \ . \tag{2.23}$$

The atmosphere is divided in L layers and each layer i corresponds to a vertical altitude h_i, with $h_0 = 0$ and $h_{L+1} = h_{\text{max}}$. The atmospheric layer depth is expressed as [168]

$$X_v(h) = \begin{cases} a_i + b_i e^{(-h/c_i)} \ \ h_i < h < h_{i+1} \ i = 1, ..., L-1 \ , \\ a_L - b_L(h/c_L) \ \ h_L < h < h_{L+1} \ , \\ 0 \ \ h > hL + 1 \ , \end{cases} \tag{2.24}$$

in Aires, $L = 5$ and the coefficient a, b and c are adjusted so that the model fits the data (see Figure 2.7).

2.1.3.3 The refraction index model ZHAireS

In ZHAireS, the variation of the index of refraction with altitude is modelled through an exponential description of the refractivity $\mathcal{R}$

$$\mathcal{R}(h) = \mathcal{R}_S \, e^{(-K_r \, h)} \ , \tag{2.25}$$

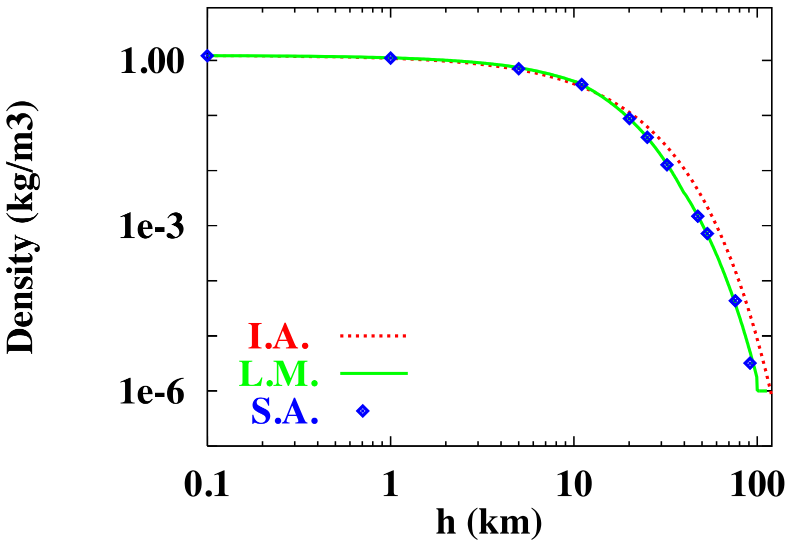

Figure 2.7: Air density for different vertical altitudes. The US standard atmosphere data [173] in dots, the *Linsley* model with a green line, and the classic isothermal model $\rho(h) = \rho_0 e^{(-gMh/RT)}$ with a red line, where g is the gravitational acceleration, $M = 28.966\,\mathrm{g/Mol}$ is the mean molecular mass, $R = 8.32$ the ideal gas constant, $T = 288\,\mathrm{K}$ the local temperature, and $\rho_0 = 1.225\,\mathrm{kg/m^3}$. Taken from [168].

where the refractivity is linked to the index of refraction $n(h)$ via $\mathcal{R}(h) = [n(h) - 1] \times 10^6$, and $\mathcal{R}_S = 325$ corresponds to the refractivity at $h = 0$ and $K_r = 0.1218\,\mathrm{km}^{-1}$. These values are chosen to describe the refractivity at low altitudes with less than 1% of error [174], taking into account humidity effects with altitudes up to 20 km. Above this altitude, the model slightly over-estimates the refractivity, which remains a minor issue since most of the shower development takes place below this altitude. It is worth mentioning that the humidity, hence the refractivity, undergoes seasonal and daily variations which strongly depend on the location on Earth. Consequently, a monitoring of the local atmosphere would be required in order to reproduce at best these effects for a given experiment.

It has been shown that the refraction effects on the time structure of the electromagnetic pulses is negligible in the atmosphere [166]. Therefore, straight optical paths are assumed between the observer location and the emission point. However the effect of the refractive index on the propagation time is taken into account through the computation of an effective refraction index as an integral over the radiation paths

$$n_{\text{eff}} = 1 + \mathcal{R}_{\text{eff}} \times 10^{-6} \ , \tag{2.26}$$

$$\mathcal{R}_{\text{eff}} = \frac{1}{R} \int_0^R \mathcal{R}(h)\, \mathrm{d}l \ \ , \tag{2.27}$$

with dl a small increment along the path between the observer and the emission, and R the total distance between the emission point and the observer location.

Finally, it is interesting to note that since no refraction (light bending) of the propagation path is modelled, the relevant refraction index of the Cerenkov effect is the refractive index located at the emission altitude, since it is the one appearing in the denominator of Equations 2.8 and 2.9.

2.1.4 Detection of EAS

EAS can be detected either by directly collecting their particles or by measuring the radiations they emit. In the first case, the detection principles rely on the tracks left by the ultra-relativistic particles when traveling through an instrumented target. One can cite for instance scintillation for charged particles crossing conductive materials or fluorescence light produced by the ionising particles in the atmosphere and Cerenkov light, often used in water tanks.

Among the EAS particle detectors, it is worth mentioning the Pierre Auger Observatory, dedicated to the study of the UHE cosmic rays, located in the altiplano in Argentina.

In this section I focus on the detection of the emitted radiations via radio techniques. Radio detection relies on the conversion of the EAS-induced electromagnetic field into a potential difference between two antenna arms. The detection of EAS radio emissions benefits in particular from the long-lasting experience of the radio telecommunication and radio astronomy fields, which I will not detail here (see e.g [175] for a complete review).

Below are presented a few experiments which contributed to the development of EAS radio detection. See e.g. [176, 153] for a more complete review.

The first observations of EAS induced radio emission were achieved in the 1960s [177, 178, 157] but the technique was abandoned due to technological limitations, in particular in the recording of the prompt antenna signal, and also because particle detectors were achieving better performances. The renewal of the radio technique took place with the first digital generation of radio arrays, CODALEMA [179] and LOPES [180], in 2003. CODALEMA is located in the Nançay Radio Observatory and benefits from a clean radio background and radio astronomy expertise. LOPES was colocated with the Kascade-Grande particle detector profiting from the particle detection technology and expertise.

Following the feasibility of the digital technology in radio arrays, a number of next generation detectors were deployed all over the world. Some were built in Antartica, where the background noise level is much lower, thanks to the restricted presence of humans and therefore human-made radio noise. These experiments focused on the detection of in-ice particles cascades, such as the ANITA experiments [181] (four generation of instruments, launched separately), consisting in a set of airborne antennas (thanks to a long duration –atmospheric– balloon) monitoring the emissions coming from interaction inside the ice. This radically different concept allowed for the observation of an unprecedented volume of neutrino target. The ANITA successor is foreseen to be the PUEO experiment [182]. Alternatively, the ARA [183] and ARIANNA experiments [184] (also merged under the RNO concept [185]), deployed antennas directly inside the ice. These experiments allowed for a strong gain of experience in the radio technique, the deployment and the maintenance of arrays in hostile environments. They also led to an increase of our understanding of the ice as medium of the particle interactions and radiation propagation [186, 187].

In less hostile environments and focusing on air particle cascades, the AERA [28] and LOFAR [188] experiments, were deployed respectively at the Pierre Auger Observatory in Argentina and in the Netherlands. While LOFAR's primary goal was radio-astronomy, the high density of antennas and the extremely accurate time resolution enable the study of the principles and the physics of the EAS-induced radio emissions. On the other hand, AERA experimented the sparse and large covering area array configurations, needed to reach the UHE cosmic rays detection, with almost $20\,\mathrm{km}^2$ of collecting area. Both experiments allowed for significant progress in the reconstruction of the events, now competitive with other techniques. However the autonomous radio detection of EAS remains a challenging task even though pioneering efforts were carried out by AERA [189, 190], and in TREND [29], an experiment located in China and focusing on that aspect.

Nevertheless, the nearly perfect transparency of the atmosphere to radio waves, combined with the strong relativistic beaming of the radio emission in the forward direction [191] make it possible to detect radio signals from air showers at large distances from their maximum of development $X_{\max}$: a $2 \times 10^{19}\,\mathrm{eV}$ shower was for example detected by the AERA with a $X_{\max}$ position reconstructed beyond 100 km from shower core [26]. This is obviously an important asset in favour of radio-detection of neutrino-induced air showers.

In conclusion, the progress achieved by radio-detection of EAS in the last 15 years [180, 22, 192, 25, 193, 194] combined with the possibility to deploy these cheap, robust detectors over large areas opens the possibility to build giant radio arrays designed to hunt for neutrino-induced EAS as proposed by the GRAND project [23, 195].

Giant Radio Array for Neutrino detection (GRAND) This experiment is a planned large scale observatory for UHE particles (cosmic rays, neutrinos and gamma rays). Thanks to its large exposure at EeV energies, its sensitivity and sub-degree angular resolution, it will achieve an unprecedented detection and reconstruction of UHE EAS. GRAND consists in 20 clusters of 10 000 antennas installed in favourable locations, over the world, with a kilometric antenna step, totalling a collecting surface of 200 000 km^2, an area required to reach the UHE neutrino frontier. In addition, the large number of antennas and the large field of view make it a competitive instrument in the transient domain of radio astronomy (see Section 5.3).

GRAND is being conceived thanks to years of progress in the radio technique, achieved by all the previous experiments mentioned earlier. However, in order to validate the key technical aspects of the project, a staged approach is planned, with the construction of prototypes focusing on specific aspects, but also able to achieve scientific goals. In that purpose, GRANDProto300 (GP300) is a 300 antenna prototype, designed to develop and validate the autonomous radio detection and reconstruction of very inclined EAS. In the mean time, GP300 will also study cosmic rays physics and astrophysics as well as gamma rays and radio astronomy [196].

Apart from the technical challenges of radio detection which will be addressed in GP300, preparatory work for GRAND includes a dedicated study of the peculiar geometry of EAS induced by Earth-skimming neutrino, and the effect of topography on their detection efficiency. Indeed the strong beaming of the radio signal implies that the topography of the ground surface may play a key role in the detection probability of the induced EAS. I was deeply involved in the dedicated study carried out on this topic within the GRAND collaboration using a simplified toy-model topography for the radio array. I therefore detail this work below: in Section 2.2 we present the general principle of our study, in Section 2.3 we detail the implementation of the simulation chain used in this study, and finally in Section 2.4 we discuss the results.

2.2 Optimisation of a kilometric-size radio array: general principles

2.2.1 End-to-end simulation

In order to study the impact of a non-flat topography on the detection of neutrino-induced EAS, we have implemented an end-to-end simulation chain, from the entrance in the Earth of the tau neutrino to the subsequent shower detection by a radio array with a simplified geometry (ideal toy-model geometry - Figure 2.8).

The simulation chain consists of three independent steps:

- We produce a fixed number of tau decays induced by cosmic tau-neutrinos (ν_τ) interacting in a spherical Earth. This is done for two neutrino energies ($E_\nu = 10^9$

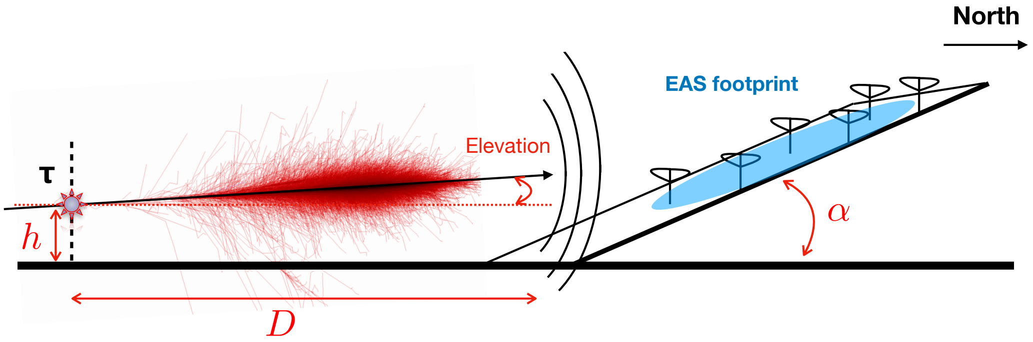

Figure 2.8: Layout of the toy-model considered in this study. A tau particle decays at a location represented as a star, producing an air shower. The radio signal emitted by the shower impinges the detector plane, tilted of an angle α from the horizontal. The intersection between the detector plane and the horizontal plane is set at a horizontal distance D from the decay point, the parameter D is therefore a measurement of the amount of free space in front of the detector.

and 10^{10} GeV) with a dedicated Monte-Carlo engine: DANTON [197, 198], further described in Section 2.3.1.

- We compute the EAS radio footprint on the detector for the showers induced by these tau decays. It is achieved with two independent methods: a microscopic simulation and a semi-analytical simulation.
- We determine the number of detected showers, corresponding to a minimal number of five antennas with voltage above a specific threshold. This threshold value is either twice (aggressive scenario) or five times the noise level (conservative scenario).

The *microscopic* treatment corresponds to a full simulation of the EAS development and of the associated electromagnetic radiation using the ZHAireS [166] simulation code (see Sections 2.1.2.3 and 2.1.3 for details). The voltage induced by the radio wave at the antenna output is computed using a modelling of the GRAND HorizonAntenna [23] performed with the NEC4 [199] code. If the peak-to-peak amplitude of the output voltage exceeds the defined threshold for five antennas or more, then the neutrino is considered as detected (see Sections 2.3.3 and 2.3.4 for more details).

The simulation of the electric field requires significant computational resources (the CPU time is mainly proportional to the number of simulated antennas and can last up to $\approx$ 792 h.HS06 on one core for 1000 antennas given our simulation parameters), but provides the most reliable estimate of the detection probability of a shower. It is thus used as a benchmark in this work. An alternative simulation chain uses the so-called *Radio Morphing* method [156] instead of ZHAireS. *Radio Morphing* performs a very fast, semi-analytical computation of the electric field (see Section 2.3.2.2 for details). The antenna response and the trigger computation are simulated in the same way as for the *microscopic simulation* chain. The gain in computation times allows to study a larger number of configurations than with the *microscopic* approach.

2.2.2 Cone Model

A third method is used in this study. It is based on a geometric modelling of the volume inside which the electromagnetic field amplitude is large enough to trigger an antenna. We give to this volume the shape of a cone, oriented along the shower axis, with its apex placed at the $X_{\max}$ position, half-angle Ω and height H. Values of Ω and H depend on shower energy, and are adjusted from ZHAireS simulations (see Section 2.3.5 for details). A shower is considered as detected if at least five antennas are within the cone volume. A similar *Cone Model* was used to compute the initial neutrino sensitivity of the GRAND detector [200]. Being purely analytical, this method produces results in a very short amount of CPU time.

2.2.3 Toy-model detector

The detector considered here (Figure 2.8) is a rectangular grid with a step size of 1000 m between neighbouring antennas. This large step size is a distinct feature of the envisioned radio array dedicated for the detection of neutrino-induced air showers, such as GRAND [191]. It is a compromise between the need for very large detection areas imposed by the very low event rates expected for one part, and the instrumental and financial constraints which limit the number of detection units on the other hand. The exact value of this antenna spacing will be assessed by future optimisation studies.

In our study we use a simplified, toy-model topography: the detector is deployed over a plane of infinite width, inclined of an adjustable angle α (also called "slope" in the following) with respect to the horizontal. For simplicity, all showers propagate towards North and the detector plane faces them. The horizontal distance D between the tau decay point and the basis of the detector, can be understood as the amount of free space in front of the detector over which the shower can develop and the radio signal propagate. It is therefore closely related to the topography of the detection site. The reference ground elevation is chosen to be 1500 m above see level (a.s.l.) A maximum altitude of 4500 m a.s.l. is set for the antennas, as larger elevation differences are unrealistic. The vertical deviation due to Earth curvature can be estimated by $2\delta h \approx R_{\text{earth}}(L/R_{\text{earth}})^2$ km, where $L << R_{\text{earth}}$ is the longitudinal distance between the development of the shower maximum and the observer. For $L = 50\,\mathrm{km}$, we find $\delta h < 100\,\mathrm{m}$. A flat Earth surface is therefore assumed in this toy-model.

The slope α and the distance D are the two adjustable parameters of the study. Values of α vary from 0 to 90° and D ranges between 20 and 100 km, covering a wide variety of configurations. Larger values of D are not considered because most showers then fly over the detector. The Earth curvature would also start playing a role, reducing even further the chance for a shower to hit the detector.

For each pair of values (α, D), we process the two sets of tau decays of energies $E_\nu = 10^9\,\mathrm{GeV}$ and $E_\nu = 10^{10}\,\mathrm{GeV}$ with the three methods *microscopic*, *Radio Morphing* and *Cone Model*. We then use the fraction of tau decays inducing a trigger by the detector to perform a relative comparison between (α, D) configurations. This will allow to evaluate how the ground topography affects the detection efficiency of neutrino-induced air showers by a radio array: the purpose of this chapter.

2.3 Computational methods

We present in the following the implementation of the methods described in Section 2.2.1 and 2.2.2.

2.3.1 Production of the shower progenitors

The production of the shower progenitors was performed with the DANTON software package [197, 198]. DANTON simulates interactions of tau neutrinos and tau energy losses. It produces results compatible with similar codes [201]. Additionally DANTON offers the possibility to run simulations in backward mode (i.e. from tau decay upwards, with appropriate event weight computations), an attractive feature for massive simulations, and it also allows us to take into account the exact topography of the Earth surface [202]. It is however operated here in forward mode, i.e. as a classical Monte-Carlo. The primary neutrino source is set as mono-energetic and isotropic. A spherical Earth is used with a density profile given by the Preliminary Reference Earth Model (PREM) [203], but with the sea layer replaced by Standard Rock [204]. The characteristics of the tau lepton resulting from the interaction of the neutrino with the Earth and of all the particles produced during the decay of the tau in the atmosphere are also computed: decay position, list of products and their associated momenta.

For this study one million primary neutrinos were simulated per energy value. Those inducing tau decays in the atmosphere were then selected if the total particle energy in the subsequent showers was above 5×10^7 GeV, because lower values can hardly lead to detection for such a sparse array [22, 176]. In Figure 2.9, we show the distribution in energy, elevation angle and height of the two sets of tau decays. Among the surviving set, 100 were randomly chosen for each energy. This value is a good compromise between computation time and statistical relevance.

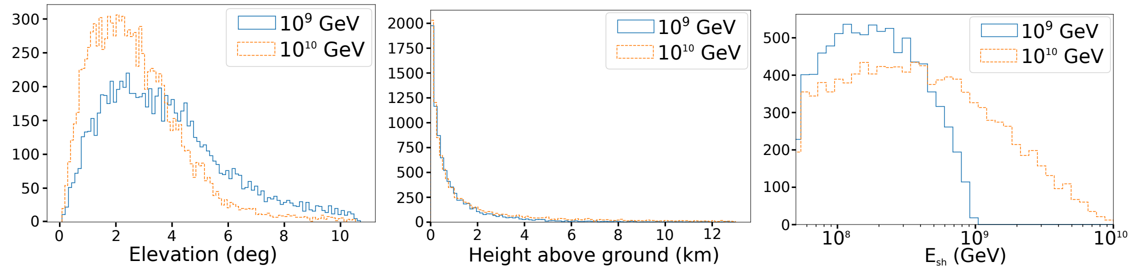

Figure 2.9: Distributions of tau decay elevation angles of particle trajectory measured with respect to the horizontal (*left*), height above ground at tau decay point (*center*) and shower energy (*right*) for the two sets of primary ν_τ energy considered in this study.

2.3.2 Simulation of the electric field

2.3.2.1 Microscopic method

In the *microscopic* method, the extensive air showers initiated by the by-products of the tau decay, and the impulsive electric field induced at the antenna locations were simulated using the ZHAireS software (see Sections 2.1.2.3 and 2.1.3). To allow for geometries where cascades are up-going and initiated by multiple decay products, we implemented a dedicated module called RASPASS (Radio Aires Special Primary for Atmospheric Skimming Showers) in the ZHAireS software.

2.3.2.2 Radio Morphing

Radio Morphing [156] is a semi-analytical method for a fast computation of the expected radio signal emitted by an air shower. The method consists in computing the radio signal of any *target* air shower at any target position by simple mathematical operations applied to a single *generic* reference shower. The principle is the following:

- The electromagnetic radiation associated with the *generic* shower is simulated using standard microscopic tools at positions forming a 3D mesh.
- For each *target* shower, the simulated signals are scaled by numerical factors which values depend analytically on the energy and geometry of the *target* and *generic*

showers.

- The *generic* 3D mesh is oriented along the direction of propagation of the target shower.
- The electromagnetic radiation expected at a given *target* position is computed by interpolation of the signals from the neighbouring positions of this 3-D mesh.

This technique lower the required CPU time of at least two orders of magnitude compared to a standard simulation tool like ZHAireS, while reproducing its results within $\sim 25\%$ error in amplitude [156].

2.3.3 Antenna response

In order to compute the voltage generated at the antenna output for both *microscopic* and *Radio Morphing* methods, we choose in this study the prototype antenna for the GRAND project: the HORIZONANTENNA [23]. It is a bow-tie antenna inspired from the *butterfly antenna* [205] developed for the CODALEMA experiment [206], later used in AERA [207] and adapted to GRANDProto35 [208]. As for GRANDProto35, three arms are deployed along the East-West, South-North and vertical axes, but the radiating element is half its size to better match the $50 - 200$ MHz frequency range considered for GRAND (see Figure 2.10 for a picture). As the *butterfly antenna*, the HORIZONANTENNA is an active detector, but in the present study, we simply consider that the radiator is loaded with a resistor $R = 300\,\Omega$, with a capacitor $C = 6.5 \times 10^{-12}$ F and inductance $L = 1\,\mu$F in parallel. The HORIZONANTENNA is set at an height of 4.5 m above ground in order to minimise the ground attenuation of the radio signal. The equivalent length $\vec{l}^{k}_{eq}$ of one antenna arm k (where k = EW, NS, Vert) is derived from NEC4 [199] simulations as a function of wave incoming direction $(\theta,\ \phi)$ and frequency ν. The voltage at the output of the resistor R loading the antenna arm is then computed as:

$$V^k(t) = \int \vec{l}^{k}_{eq}(\theta, \phi, \nu) \cdot \vec{E}(\nu) e^{2i\pi\nu t} d\nu \tag{2.28}$$

where $\vec{E}(\nu)$ is the Fourier transform of the radio transient $\vec{E}(t)$ emitted by the shower.

The equivalent length was computed for a vertical antenna deployed over a flat, infinite ground. The ground slope of the toy-model setup can then be accounted for by a simple rotation of this system by an angle α, which translates into a wave effective zenith angle $\theta^* = \theta - \alpha$, to be used in Equation 2.28. This treatment however implies that the antenna pole is always considered as perpendicular to the ground in our treatment, which is probably not a practical choice in reality.

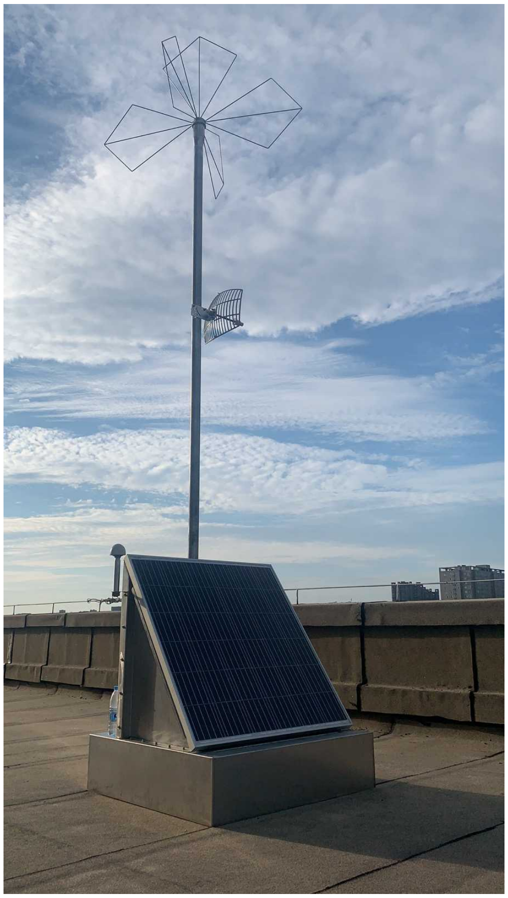

Figure 2.10: Picture of the HorizonAntenna detection unit, taken at Xi'an University. The bow-tie antenna design of the HorizonAntenna is placed on top of a 4 m long pole. At the bottom of the pole, the solar panel covers a triangular box where the electronics are stored. In the middle of the pole a WiFi antenna is placed for the data transfert. Credit: Zhang PengFei.

2.3.4 Trigger

The last step of the treatment consists in determining whether the shower could be detected by the radio array. For this purpose, we first apply a Butterworth filtering[2] of order 5 to the voltage signal in the $50 - 200\,\mathrm{MHz}$ frequency range. This mimics the analog system that would be applied in an actual setup in order to filter out background emissions outside the designed frequency range.

Then the peak-to-peak amplitude of the voltage V_{pp} is compared to the level of stationary background noise $\sigma_{\mathrm{noise}} = 15\,\mu\mathrm{V}$, computed as the sum of Galactic and ground contributions (see [23] and [194] for details). If $V_{\mathrm{pp}} \geq N\sigma_{\mathrm{noise}}$, then we considered that the antenna has triggered. Here $N = 2$ in an aggressive scenario, which could be achieved if innovative triggering methods [210, 211] were implemented, and $N = 5$ in a conservative one.

If at least five antennas trigger on a same shower, then we consider it as detected.

2.3.5 Cone Model

The *Cone Model* allows for a purely analytical computation of the radio footprint on ground, based on a conical modelling of the volume inside which the electromagnetic radiation is strong enough to trigger radio antennas. It is implemented as follows:

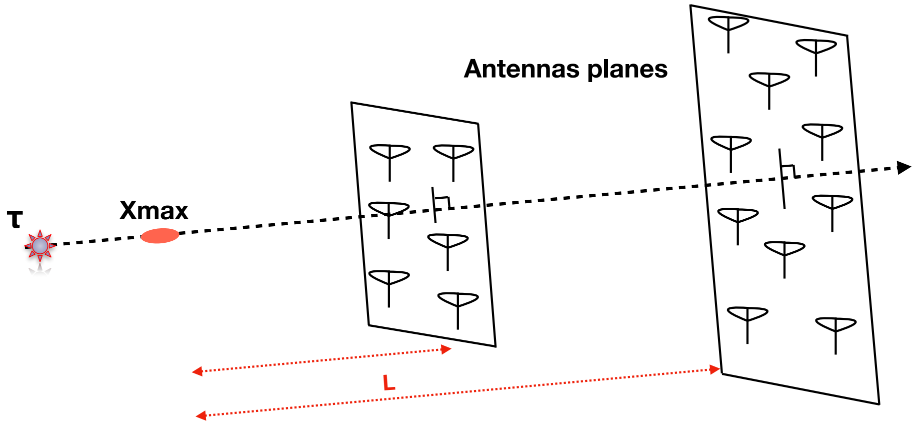

Figure 2.11: Position of the planes used to parametrize the *Cone Model*. These are placed perpendicular with respect to the shower axis, at various longitudinal distances L from X_{max}. See Section 2.3.5 for details.

---

[2] From the British engineer and physicist Stephen Butterworth who designed this type of frequency filters (1930) with a frequency response as flat as possible in the passband [209].

- We simulate with the ZHAireS code the electric field from one shower at different locations set at fixed longitudinal distances L from the X_{max} position (see Figure 2.11 for an illustration). Values of $L > 100\,\mathrm{km}$ are not simulated because the maximal value $D = 100\,\mathrm{km}$ chosen in our study for the distance between the tau decay point and the basis of the detector (see Section 2.2.3) makes it unnecessary. As the X_{max} position is reached $\sim 15\,\mathrm{km}$ after the decay, a distance L = 100 km allows to simulate radio signals over a detector depth of 15 km at least. This is, in the majority of cases, enough to determine if the shower would be detected or not.

- In each of these antenna planes, identified by an index j in the following, we compute the angular distance between the antennas and the shower core from the tau decay point. We determine the maximal angular distance to the shower core Ω^j beyond which the electric field drops below the detection threshold, set to 2 (aggressive) or 5 (conservative) times the value of E_{rms}, the average level of electromagnetic radiation induced by the galaxy is computed as:

  $$E_{\mathrm{rms}}{}^2 = \frac{Z_0}{2} \int_{\nu_0}^{\nu_1} \int_{2\pi} B_\nu(\theta, \phi, \nu) \sin(\theta) d\theta d\phi d\nu \tag{2.29}$$

  where B_ν is the spectral radiance of the sky, computed with GSM [212] or equivalent codes, $Z_0 = \mu_0\, c = \sqrt{\mu_0/\epsilon_0} = 376.7\,\Omega$ the impedance of free space, and $[\nu_0, \nu_1]$ the frequency range considered for detection. Here we choose $\nu_0 = 50\,\mathrm{MHz}$ and ν_1=200 MHz, the frequency range of the HorizonAntenna. The factor 1/2 arises from the projection of the (unpolarized) Galactic radiation along the antenna axis. We find $E_{\mathrm{rms}} = 22\,\mu\mathrm{V/m}$. Defining a detection threshold on the electric field amplitude as done here —rather than the voltage at antenna output as usual— allows to derive results that do not depend on a specific antenna design. It is however not precise: by construction, the details of a specific antenna response and its dependency on the direction of origin of the signal are neglected here, and only the average effect is considered. The *Cone Model* is therefore only an approximate method.

  The distribution of the electric field amplitudes as a function of the angular distance to the shower axis is shown for illustration in Figure 2.12 for the plane j located at a longitudinal distance $L = 59\,\mathrm{km}$. As the Cherenkov ring induces an enhancement in the amplitude profile for $\Omega \sim 1^\circ$, we actually compute two values of the angle Ω^j: Ω^j_{min} and Ω^j_{max}, thus defining the angular range inside which the electric field amplitude is above the detection threshold.

- The value of Ω^j does not vary significantly with L (see Figure 2.13). This validates the choice of a conical model for the trigger volume and allows to derive a single set of values $(\Omega_{\mathrm{min}};\Omega_{\mathrm{max}})=(\langle\Omega^j_{\mathrm{min}}\rangle;\ \langle\Omega^j_{\mathrm{max}}\rangle)$ for one specific energy.

- A similar procedure is applied to determine the cone height H, set to be equal to the longitudinal distance L up to which the signal is strong enough to be detected.

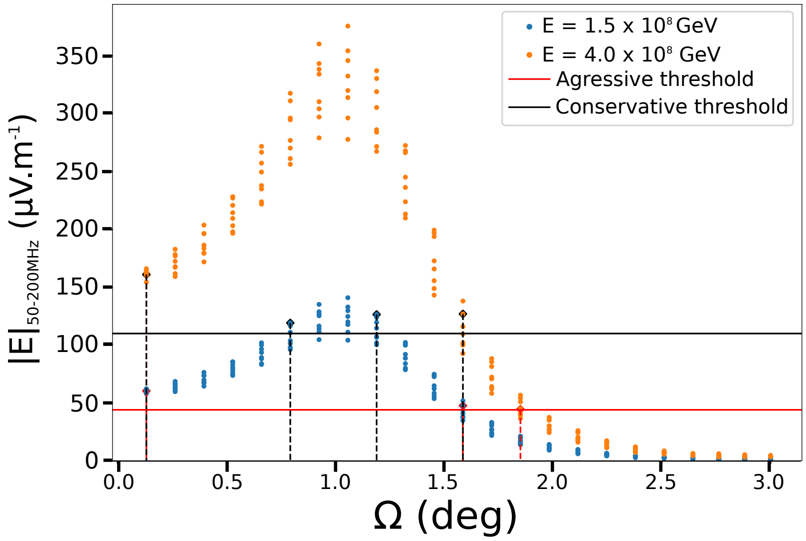

Figure 2.12: Distribution of the electric field amplitude as a function of Ω, the angular distance to the shower axis, for antennas located at a longitudinal distance of 59 km from $X_{\max}$. The amplitude dispersion at a given Ω value is due to interplay between Askaryan and geomagnetic effects leading to an azimuthal asymmetry of the signal amplitude. Here we find $(\Omega^j_{\min}; \Omega^j_{\max}) = (0.1°; 1.7°)$ in the aggressive case, $(0.8°; 1.2°)$ in the conservative one. For a shower energy $E = 1.5 \times 10^8$ GeV.

- We repeat the treatment for various shower energies $E_{\rm sh}$ by rescaling the signals amplitudes and thus obtain the distributions $\Omega(E_{\rm sh})$ and $H(E_{\rm sh})$ shown in Figures 2.14 and 2.15. We fit these distributions for shower energies larger than 3×10^7 GeV with analytical functions given by

$$H|_{50-200\mathrm{MHz}} = \quad a \, + \, b \left(\frac{E_{\rm sh}-10^{17}\mathrm{eV}}{10^{17}\mathrm{eV}}\right), \tag{2.30}$$

$$\Omega|_{50-200\mathrm{MHz}} = \quad c \, + \, d \log\left(\frac{E_{\rm sh}}{10^{17}\mathrm{eV}}\right). \tag{2.31}$$

  with $E_{\rm sh}$ expressed in eV in the formulas. Numerical values of a, b, c, d are given in Table 2.1.

  The three parameters $\Omega_{\min}$, $\Omega_{\max}$ and H allow us to define a hollow cone, with an apex set at the shower $X_{\max}$ location and oriented along the shower axis. Any antenna located inside this volume is supposed to trigger on the shower according to the *Cone Model*.

  As mentioned in the introduction, the interplay between the geomagnetic effect and the charge excess induces an asymmetry on the electric field amplitude as a function

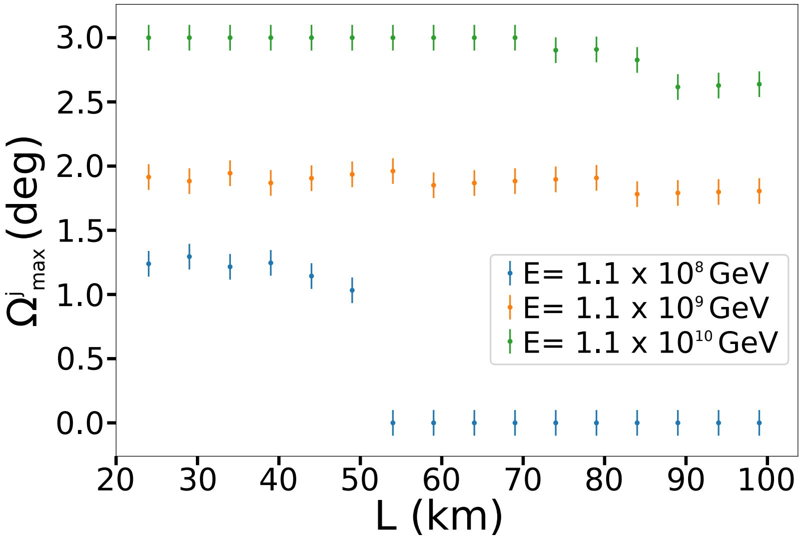

Figure 2.13: Angular distances Ω^j_{max} (conservative case) as a function of longitudinal distance for various shower energies. The angle value varies marginally over the full range of longitudinal values considered for shower energies $E = 1.1 \times 10^9$ and 1.1×10^{10} GeV, validating the choice of a cone model for the trigger volume modeling. For $E = 1.1 \times 10^8$ GeV, Ω drops to 0 for $L > 50$ km because the cone height H is equal to this value in the conservative case (see Figure 2.15). Note that the error bars of 0.1° correspond to the geomagnetic asymmetry.

of antenna angular position w.r.t. the shower core. This can be seen on Figure 2.12, for instance, where the dispersion in field strength at a given angular distance is the exact illustration of this phenomenon. The *Cone Model* however assumes a rotation symmetry around the shower axis and thus neglects this asymmetry. This is still acceptable if we are only interested in the average number of triggered antenna by the shower —which is the case here— and not by the amplitude pattern of the radio signal.

- The *Cone Model* is applied to the selected set of tau decays: the cone parameters are computed for the energy and geometry of each shower and the intersection between the resulting cone volume and the detection area is calculated. If at least five antennas fall within this intersection, then the shower is considered as detected.

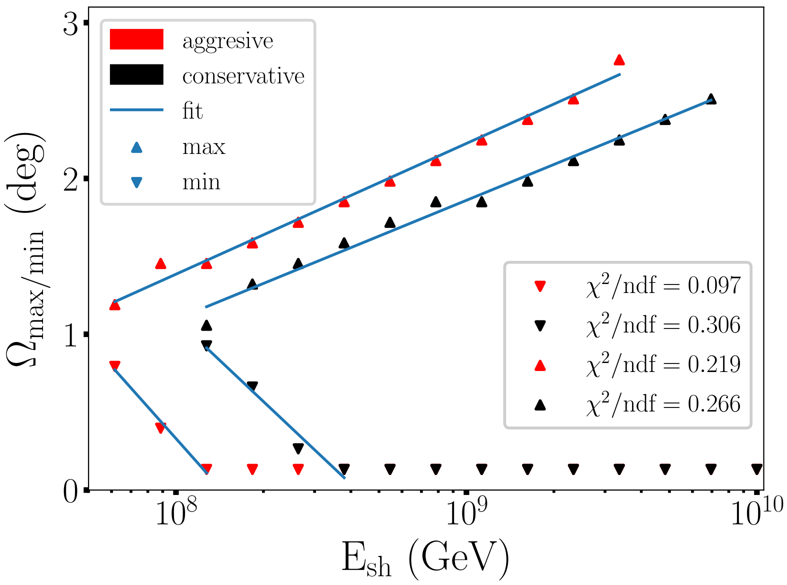

Figure 2.14: Angles Ω_{max} and Ω_{min} as a function of shower energy E_{sh} and fit by Equation 2.31. At the highest energies, Ω_{min} drops down to 0°, implying that the radio signal is above the detection threshold for all angular distances $\Omega \leq \Omega_{\mathrm{max}}$.

2.4 Results

We have computed the detection efficiency for our toy-model through the three independent simulation chains presented in Section 2.2. Detection efficiency is defined here as the ratio of the number of showers detected to the total of 100 selected tau decays. The parameters ranges explored initially are distances $D = \{20, 30, 40, 60, 80, 100\}$ km and slopes $\alpha = \{0, 5, 10, 15, 20, 45, 90\}$ degrees. This coarse step is mainly motivated by computation time and disk space considerations for the *microscopic* simulation.

We first show a relative comparison of the different methods before discussing the effects of the topography on the detection efficiency.

2.4.1 Relative comparison

Figure 2.16 shows that the *Radio Morphing* treatment induces trigger efficiencies at most 15% higher than *microscopic* simulations. This qualifies the *Radio Morphing* chain as a valid tool for the study presented in this article. Taking advantage of the factor ∼100 gain in computation time of *Radio Morphing* compared to *microscopic* simulations [156] we then

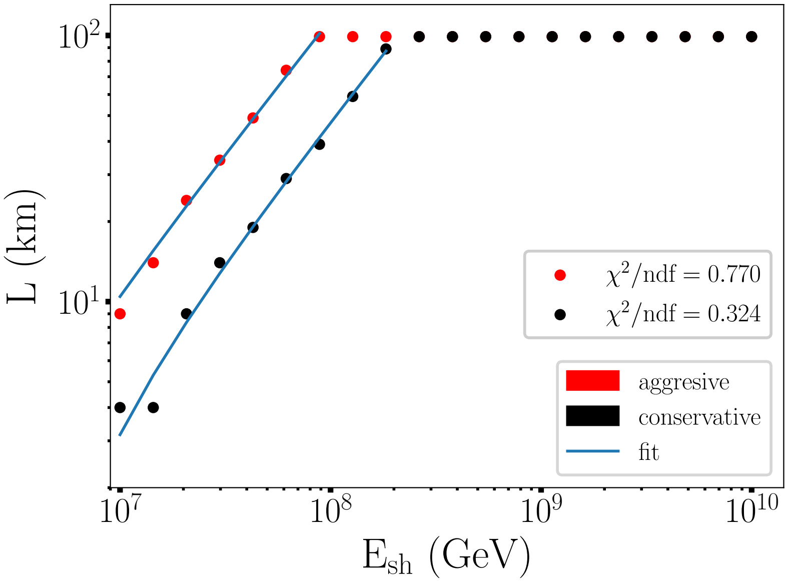

Figure 2.15: Cone height H as a function of shower energy E_{sh} and fit by Equation 2.30. Cone height saturates at values $H = 100\,\mathrm{km}$, because the antenna planes used to parametrize the *Cone Model* do not extend beyond this value (see text for details). It is therefore extrapolated from the fit given in Equation 2.30 beyond this value.

decrease the simulation step size down to 2° for slope α and 5 km for the distance to decay D, allowing for a more detailed study of the effect of topography on the array detection efficiency.

This refined analysis is presented in Figure 2.17, where results of the *Cone Model* are also shown. The distribution of the *Cone Model* detection efficiency in the (α,D) plane follows a trend similar to the *Radio Morphing* one. One of the differences is a flatter distribution as a function of slope for the conservative trigger hypothesis, which results in an over-estimation for $\alpha > 30°$ for the *Cone Model* (see also Figure 2.18). Discrepancies are not surprising since *Cone Model* is an approximate method as already pointed out in Section 2.3.5. It should however be noted that the offset with the *Radio Morphing* results remains in any case below 50% and that it produces detection efficiencies below those of the *Radio Morphing* approach for realistic slope values $\alpha < 30°$. The *Cone Model* can thus safely be used to provide a rough, conservative estimate of the neutrino sensitivity for realistic topographies. This result also provides an *a posteriori* validation of the initial computation of the GRAND array sensitivity [200], even though the cone was then parametrized from showers simulated in the 30-80 MHz frequency range.

Table 2.1: Parameters for the fitting functions given in Equations 2.30 and 2.31, for aggressive and conservative thresholds and maximal and minimum Ω angles. Parameters a and b are in km, c and d in degrees.

threshold	a	b	Ω	c	d
aggressive	109 ± 15	116 ± 3	min	0.20 ± 0.02	-2.4 ± 0.2
			max	1.3 ± 0.2	1.00 ± 0.02
conservative	42 ± 7	48 ± 1	min	1.2 ± 0.2	-2.2 ± 0.2
			max	1.0 ± 0.3	0.80 ± 0.03

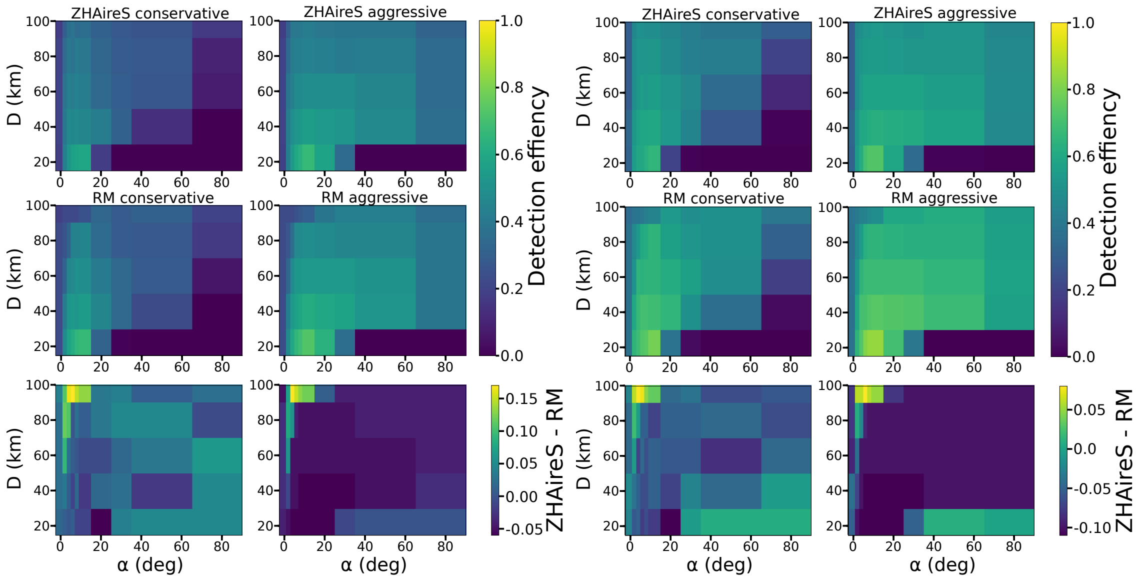

Figure 2.16: *Left:* Detection efficiency as a function of the distance D and slope α for the simulation set with a primary neutrino energy of 10^9 GeV. Comparison between ZHAireS and *Radio Morphing* (respectively top and middle plots, while the difference is plotted at the bottom) and conservative thresholds (*left*) and aggressive thresholds (*right*). *Right:* Same for a primary neutrino energy of 10^{10} GeV.

2.4.2 Toy-model discussion

Below we study how the topography affects the detection potential of neutrino-induced air showers by a radio array. To do that, we use the results of the *Radio Morphing* chain, which provide at the same time good reliability and fine topography granularity as explained in the previous section.

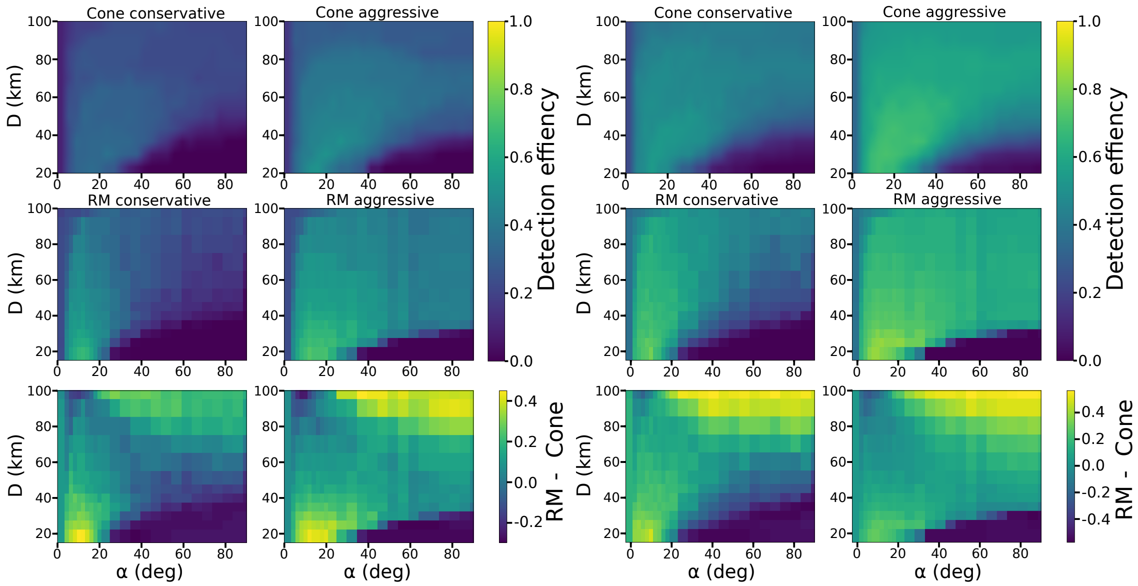

Figure 2.17: *Left:* Detection efficiency as a function of distance D and slope α for the simulation set with a primary neutrino energy of 10^9 GeV. Results are plotted for the *Cone Model* (up) and *Radio Morphing* (middle), as well as the difference (Radio Morphing - *Cone Model*) (bottom). Conservative (*left*) and aggressive (*right*) threshold hypothesis are also considered (*right*). *Right:* Same for a primary neutrino energy of 10^{10} GeV.

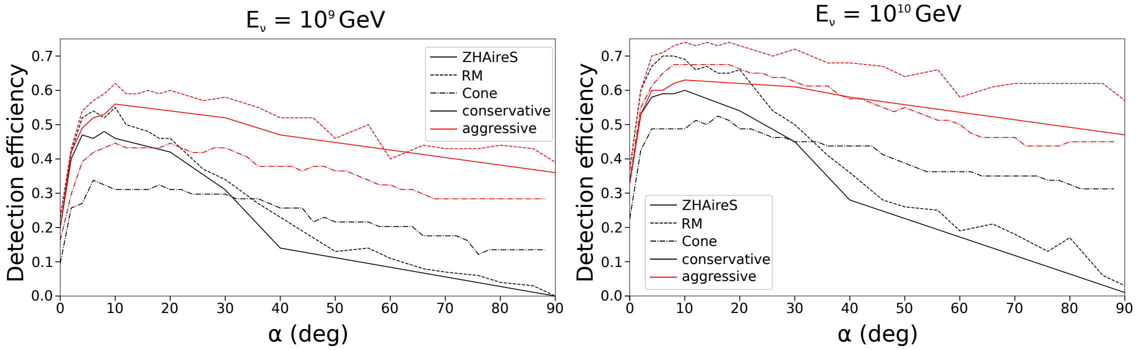

Figure 2.18: Detection efficiency as a function of slope α for a distance $D = 40$ km for neutrinos energies of 10^8 (*left*) and 10^9 GeV (*right*). Comparisons between the microscopic (solid lines), *Radio Morphing* (dashed lines) and *Cone Model* (dash-dotted lines), for conservative (black lines) and aggressive (red lines) threshold hypothesis.

Four striking features can be singled-out from Figures 2.17 and 2.18:

- A significant increase of the detection efficiency for slopes varying from 0 degree up to few degrees: the detection efficiency for a flat area is reduced by a factor 3 compared to an optimal configuration $(\alpha, D) \approx (10^\circ, 25\,\text{km})$. This result is consistent with the study presented in [23], where the effective area computed for a real topography on a mountainous site was found to be four times larger than for a flat site.
- Limited variation of the detection efficiency for slopes between $\sim 2^\circ$ and $\sim 20^\circ$.
- An efficiency slowly decreasing for slopes larger than $\sim 20^\circ$. This is in particular valide for distances D shorter than 40 km, where the detection efficiency is nearly null.
- A slow decrease of the detection efficiency with increasing value of D.

To interpret these results, we may first consider that two conditions have to be fulfilled to perform radio-detection of showers: first the radio beam must hit the detector, then enough antennas (five in this study) have to trigger on the corresponding radio signal. In order to disentangle these two factors —one mostly geometrical, the other experimental—, we display in Figure 2.20 the fraction of events reaching the detector as a function of the parameters (α, D). These events are defined by a non-null intersection between the detector plane and a 3° half-aperture cone centered on the shower trajectory, a conservative and model-independent criterion (see sketches of Figure 2.19).

It appears from Figure 2.20 that the large fraction —around 90%— of showers flying above the detector is the main cause of the limited efficiency of a flat detection area. As a corollary, the steep rise of detection efficiency with increasing slope is clearly due to the increasing fraction of intercepted showers. Figures 2.17 and 2.20 however differ significantly for configurations corresponding to $\alpha > 20^\circ$ and $D < 40\,\text{km}$: the fraction of intercepted events varies marginally with α at a given D, while the detection efficiency drops. This means that the first condition for detection —detector inside the radio beam— is fulfilled for these configurations, but the second —sufficient number of triggered antennas— is not, because the tau decay is too close, and the radio footprint at ground consequently too small. The situation may be compared —with a 90° rotation of the geometry of the problem— to the radio-detection of "standard" air showers with zenith angle $\theta < 60^\circ$, which suffers limited efficiency for sparse array [194]. A larger density of detection units would certainly improve detection efficiency, but the need for large detection areas, imposed by the very low rate of neutrino events, discards this option.

Finally the slow decrease in efficiency with increasing value of D is mostly due to geometry, as the fraction of intersecting events diminishes with D in similar proportion.

Yet, one could argue that the limit set to the detector elevation in our toy-model (3000 m above the reference altitude, see Section 2.2.3) implies that a detector deployed over mild slopes is larger than one deployed over steeper ones. For example $\alpha = 10^\circ$ allows for a detector depth of $3/\sin(\alpha) \sim 17\,\text{km}$, but $\alpha = 70°$ implies a value six times smaller. Equal detection efficiencies for different slopes may therefore yield a significantly larger event number for a detector deployed on a steep slope, compared to one of similar size deployed on a milder slope. A reliable answer to this question would require a complete Monte-Carlo simulation. This is beyond the scope of this study, and would be useful only if real topographies were taken into account.

It is however possible to get a hint on this issue by studying how the *constant area detector efficiency* ($\mathcal{E}(\alpha)$) varies with slope. This quantity is computed by weighting the efficiency averaged over the full range of D with a factor $\sin(\alpha)$:

$$\mathcal{E}(\alpha) = \frac{1}{N_D} \sum_{\mathrm{D}}^{N_D} \epsilon_D(\alpha) \times \sin(\alpha) \ , \tag{2.32}$$

where $\epsilon_D(\alpha)$ is the efficiency of one array configuration of parameters (α, D) and N_{D} is the total number of distances D used in this study. As D measures the amount of empty space in front of the detector (see Section 2.2.3), averaging the efficiency over all values of D allows us to take into account all possible shower trajectories for a given slope value. The factor $\sin(\alpha)$ corrects for the variation of the detector area with slope. The *constant area detector efficiency* can therefore be understood as a proxy for the event rate per unit area one could expect with a detector deployed on a plane of slope α, with infinite flat ground in front of it. The *constant area average efficiency* computed from the *Radio Morphing* results is displayed as a function of slope on Figure 2.21.

Beyond a certain threshold ($\sim 20°$ for the conservative case, $\sim 30°$ for the aggressive one), there is no significant variation of its value with α, because the poor performance of steep slopes for close-by showers (i.e. small values of D) compensates for the larger area factor $\sin(\alpha)$. Figure 2.21 also confirms the clear gain of a slope —even mild— compared to a detector deployed over flat ground.

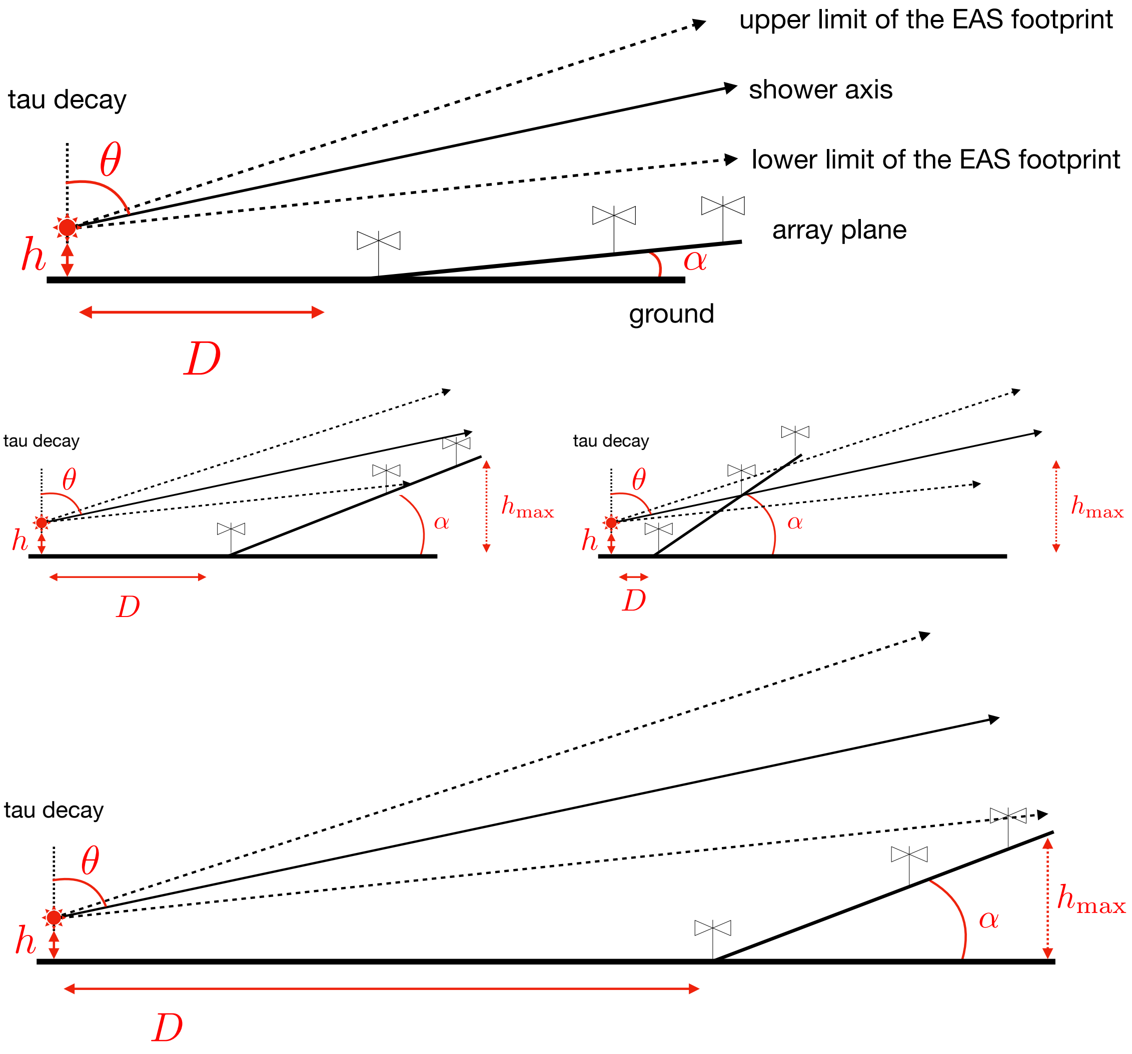

Figure 2.19: Various illustrative sketches of the impact of the toy-model topography on the detection of an up-going EAS. Four scenarii are considered here: *Top:* A low inclination results in a total loss of the signal as the emission flies above the array. *Middle left:* A sufficient inclination leads to a detection of the signal as several antennas intercept the emission. *Middle right:* A close-by detector from the tau decay point intercepts the emission, however the footprint on the array is too small to contain enough antennas to issue a trigger. *Bottom:* A detector far away from the tau decay point misses the signal since no interception of the emission can be achieved due to the altitude limitation of the array. As illustrated here, an optimal parameter set for the topography of the detector lies in arrays inclined of a few degrees and distant of a few tens of kilometers from the tau decay point.

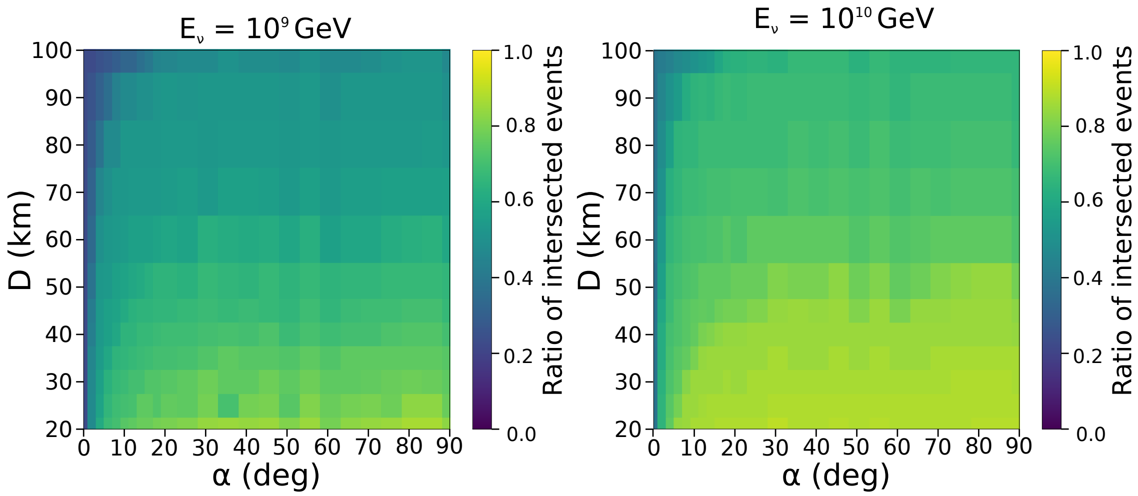

Figure 2.20: *Left:* Fraction of events intersecting the detection area as a function of distance D and slope α for the simulation set with a primary neutrino energy of 10^9 GeV. *Right:* Same for a primary neutrino energy of 10^{10} GeV.

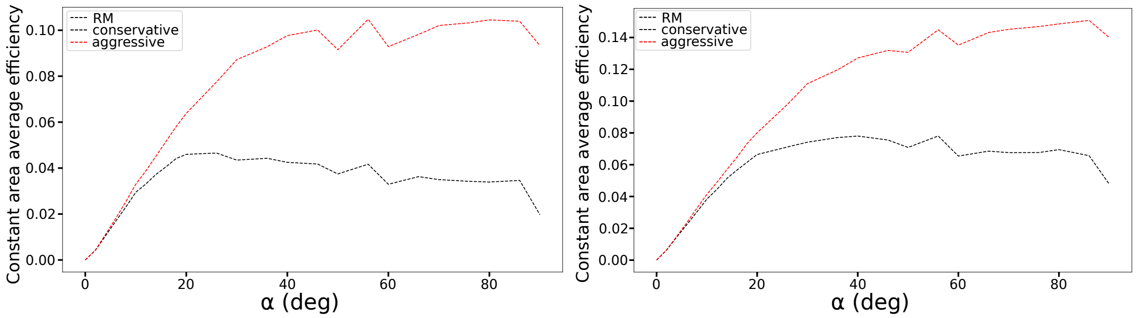

Figure 2.21: *Left:* Average detection efficiency over a constant detector area as a function of slope for the simulation set with a primary neutrino energy of 10^9 GeV. *Right:* Same for a primary neutrino energy of 10^{10} GeV. In both cases values are computed with the *Radio Morphing* treatment.

2.5 Conclusion

We have studied the impact of the topography for radio-detection of neutrino-induced Earth-skimming air showers. For this purpose, we have developed a toy-model with a simplified topography for the detector, depending on two parameters: the distance between the air shower injection point and the detector array, and the ground slope of the detector array. We have computed the neutrino detection efficiency of this toy-model detector through three computation chains: a microscopic simulation of the shower development and its associated radio emission, a radio-signal computation using *Radio Morphing* and an analytical treatment based on a *cone model* of the trigger volume.

The comparison of these three independent tools proves that *Radio Morphing* is a reliable method in this framework, while the *Cone Model* offers a fast, conservative estimate of the detection efficiency for realistic topographies.

More importantly, the results presented here show that ground topography has a great impact on the detection efficiency, with an increase by a factor $\sim$3 for angles of just a few degrees compared to a flat array. This boost effect is very similar for any slope value ranging between 1° and 20°. The other noticeable result of this study is the moderate effect of the distance on the detection efficiency, with comparable values for tau decays taking place between 20 and 100 km from the detector.

This study highlights the necessity of taking into account the ground topography when estimating the potential of a radio array for the detection of neutrino-induced air showers. It is the seed for an ambitious effort initiated in the framework of the GRAND project to include detailed Earth topographic information in the computation of the detector effective area. This will allow to find the optimal sites on Earth where the $\mathcal{O}(10)$ sub-arrays composing the GRAND array could be deployed to optimize its neutrino detection efficiency.

Chapter 3

Cosmic neutrino signals: reconstruction of radio detected astroparticles induced extensive air showers

3.1 Introduction

Determining precisely the arrival direction of the signal is key to achieve neutrino astronomy. Unlike cosmic rays, neutrinos point back directly to their source. Their detection thus opens the way to a new era of HE astronomy, as illustrated by the recent detection of TXS0506+056 [8], probing the high energy processes of the Universe (see Section 1 or [213]). An angular resolution of 0.1° would allow to discriminate between close by sources [135]. Fortunately, the arrival direction of the EAS is directly linked to the arrival direction of the neutrino, thanks to the strong Lorentz boost of the particle (see for instance Figure 3.1).

In addition, the reconstruction of the arrival direction is also one of the key ingredients to determine EAS characteristics, such as the nature and energy of the primary particle. The determination of the arrival direction indeed allows us to set the general geometry of the EAS, a parameter required in order to determine the $X_{\max}$ position or the radiated energy of the shower [153, 176].

Finally, the angular resolution will be a crucial tool to directly discriminate between EAS induced by neutrinos from those induced by cosmic rays or gamma rays, as none of the latter are expected to originate below the horizon.

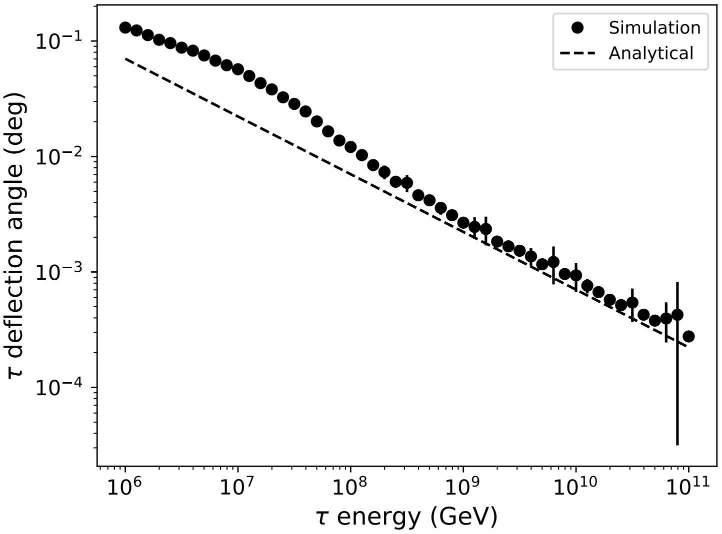

Figure 3.1: Deflection angle of a tau lepton produced by a charged-current interaction of a cosmic neutrino underground with respect to the primary neutrino direction, for a 1° emerging angle from the Earth surface with standard rocks ($2.65\,\mathrm{g.cm}^{-3}$). These data were computed by Valentin Niess with the DANTON simulation code [198].

The method described in this work consists in determining the arrival direction of the shower using the timing information contained in the radio signal. We will use as a starting point for our study the pioneering works on shower radio wavefronts of the LOPES and LOFAR experiments. This is detailed in Section 3.2.2. Before that, we will first introduce a general definition of the wavefront for EAS radio signals. In the third part we present my work on the study of the wavefront shape for the GRAND configuration.

3.2 General study of the wavefront: time information

3.2.1 Wavefront: physical interpretation and practical definition

The wavefront of an EM emission is formally defined as the set of electric-field locations on a same phase at a given time, or the set of points reached simultaneously by the emission. As seen in Section 2.1.2, the emitting region of an EAS, the so-called "pancake", is a few meters thick, to be compared to observation distances of several kilometers to hundreds of kilometers. In addition, the source moves at a speed close to the speed of light in vacuum c, while the electromagnetic radiation propagates at a similar speed c/n, where n is the refraction index of the atmosphere. This leads to a sharp and clean wavefront of the radiation, with duration varying from a few nanoseconds to hundreds of nanoseconds, depending on the variation of the refractive index (see in particular the Cerenkov cone effect in Section 3.3.2) and the location of the observer. For the purpose of illustration, Figure 3.2 (left column) displays simulated electric-field traces (see Section 3.2.3.1 for details on the simulation setup) for different antenna locations within the footprint.

For very inclined and up-going EAS, the geometrical configuration places us in Fraunhofer conditions: given by $S/L\,\lambda \ll 1$, where S is the surface of the the emitting region, L is the observer distance to the emitting region and λ is the wavelength at which the observation is done. In our case the surface of the emitting region is given by the lateral extension of the pancake with $S \sim 10\,\mathrm{m}$ (see Sections 2.1.1 and 2.1.2), $L \sim 20 - 400\,\mathrm{km}$ and $\lambda \sim 1.5 - 6\,\mathrm{m}$ (corresponding to 200 MHz and 50 MHz), leading to $S/L\,\lambda \sim 4\times10^{-5} - 3\times10^{-3}$. Therefore, at first order, we consider the radiation wavefront as a plane. Nevertheless, we expect the collective interactions between all charged particles inside the EAS to imprint the global shape of the wavefront and so to lead to an intrinsic curvature or deviation from this standard plane wavefront emission, as will be shown in Section 3.2.2.

Finally, from a practical point of view, the wavefront time is defined in this study as the instant of the detected signal maximum. This choice is purely arbitrary and is totally independent of the technical method used to define the signal maximum as well as its associated time, which will be detailed in Section 3.2.3.1.

3.2.2 Previous works

The very ambitious goal set for the angular resolution (see Section 3.1), implies that a precise description of the wavefront will be necessary to correctly reconstruct the arrival direction of the emission. For this purpose, it is first necessary to define the correct wavefront model. In this section, I present the previous works done by the LOPES and LOFAR experiments on that matter.

LOPES is, together with CODALEMA [179], a pioneering first-generation digital antenna array (see Section 2.1.4), operating in the frequency range $30 - 80\,\mathrm{MHz}$, between 2003 and 2013. The LOPES collaboration (see [214]) analysed the arrival times measured by the radio array and, thanks to the colocated particle detector, reconstructed the shower geometry from particles information, allowing to compare the results from true measurements with simulated events. The analysis method first consists in correcting the arrival times by those of the *propagation plane* (called "shower plane" in the LOPES study), perpendicular to the shower direction and propagating at a speed $v = c/n$ (see the left panel of

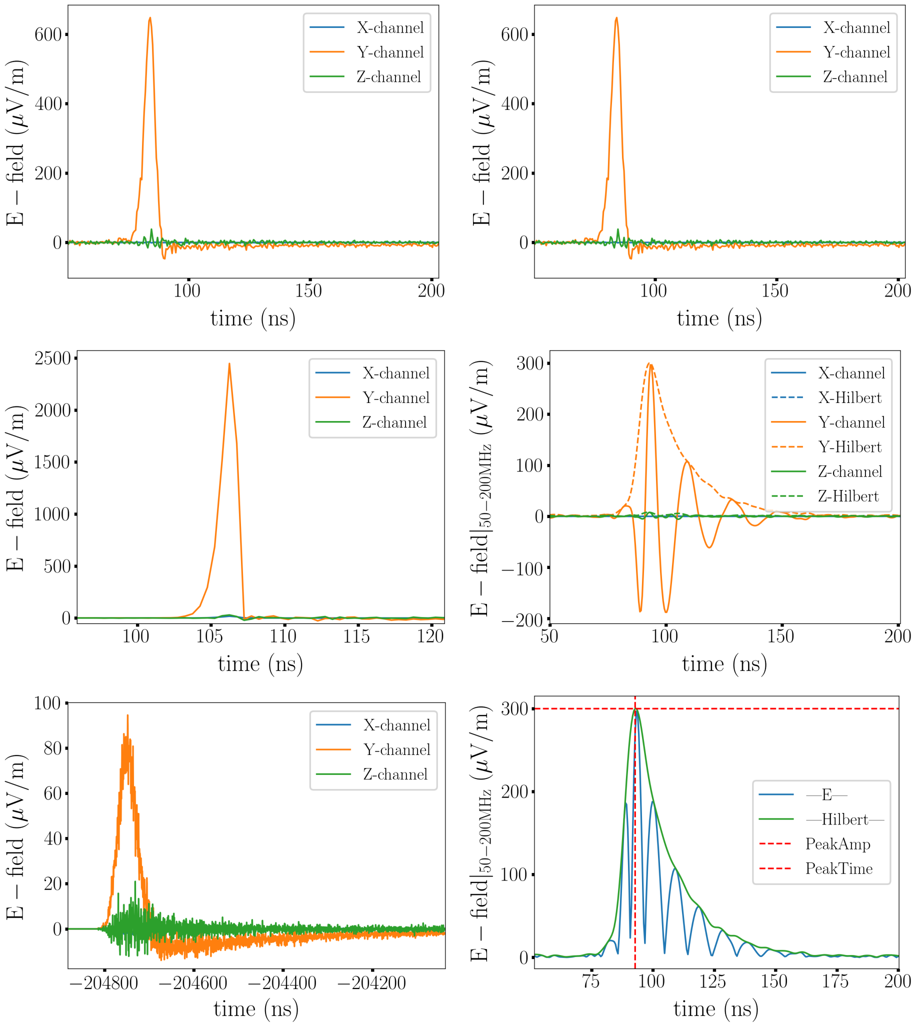

Figure 3.2: *Left column:* Exemples of simulated electric field traces for various locations inside the footprint (note here the different time and amplitude scales). *Top:* inside the Cerenkov cone (2.9 km from the shower core). *Middle:* at the Cerenkov cone (3.4 km from the shower core). *Bottom:* Outside the Cerenkov cone (61.7 km from the shower core). As it can be clearly seen, closer to the Cerenkov cone the signal amplitude rises while the time width of the signal tightens. The signals were simulated for a proton induced EAS of energy 3.94 EeV, azimuth 180° and zenith 92.92°. *Right column:* Exemple of ZHAireS simulated signals as seen by an antenna. *Top:* Raw electric-field signal at the antenna location. *Middle:* Filtered electric-field and Hilbert envelope of each channel (see Section 3.2.3.1). *Bottom:* Modulus of the electric field and of the Hilbert envelope. The maximum of the Hilbert envelope is used as a definition of the trigger time and peak-amplitude in our study. For a proton induced EAS of energy 3.94 EeV, azimuth 180° and zenith 92.92°.

Figure 3.3). The resulting time values thus describe the deviation of the intrinsic wavefront from the plane wavefront. In a second step, the authors fitted different wavefront models to study the deviation from the plane wavefront. In particular a hyperbolic wavefront model defined as (following their notations)

$$c\tau_{\mathrm{proj}}(d) = \sqrt{(d\sin(\rho))^2 + (c \cdot b)^2} + b\ , \tag{3.1}$$

where τ_{proj} is called by the authors the projected time in the propagation plane. Here d is the lateral distance to the shower axis, ρ is the asymptotic angle of the hyperbola with respect to the propagation plane and b is the offset between the hyperbola and the asymptotic cone. The authors found that the hyperbolic wavefront shape was the best model to describe the arrival time deviation from the plane as illustrated on the right panel of Figure 3.3. Those pioneering results are however limited by the low sensitivity, the large radio backgrounds of the experiment and the small extension of the array [214], resulting in particular in large statistical uncertainties in the results.

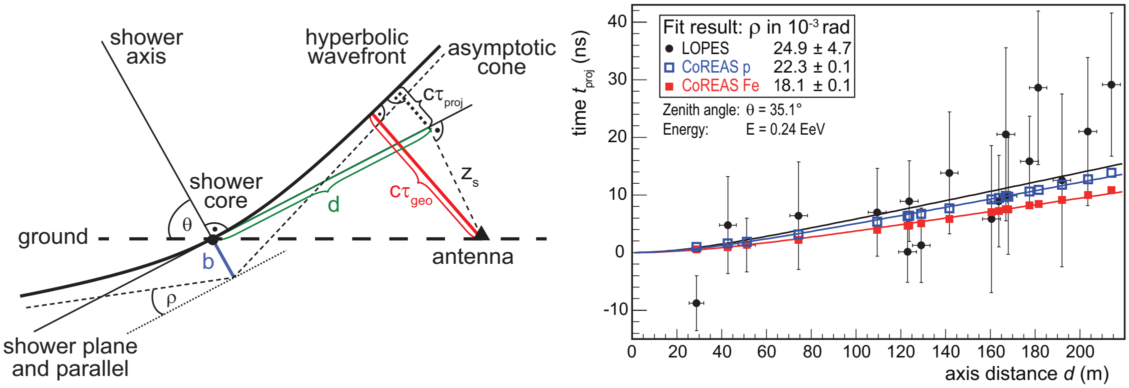

Figure 3.3: *Left:* Sketch of the hyperbolical wavefront model. The model is described for times τ_{proj} with respect to the shower plane (called *propagation plane* in our study) and characterised by an asymptotic cone angle ρ and an offset b in the continuity of the core location. *Right:* Illustrative result of the LOPES experiment: the projected arrival times as a function of the lateral distance to the shower axis are best fitted with an hyperbolic model for both the real event and the simulated one. Taken from [214], and using their naming conventions.

LOFAR is a radio telescope (see Section 2.1.4) composed of two sets of antennas: a low frequency array called LBA (low-band antennas) operating between 10 − 90 MHz and a high frequency array called high-band antennas (HBA) operating between 110 − 240 MHz. Thanks to the large density of antennas (see for instance one of the LOFAR cores on Figure 3.4 left panel), it is one of the most precise radio telescopes in the world in this frequency range, with extremely accurate timing measurements (see Figure 3.4) right panel).

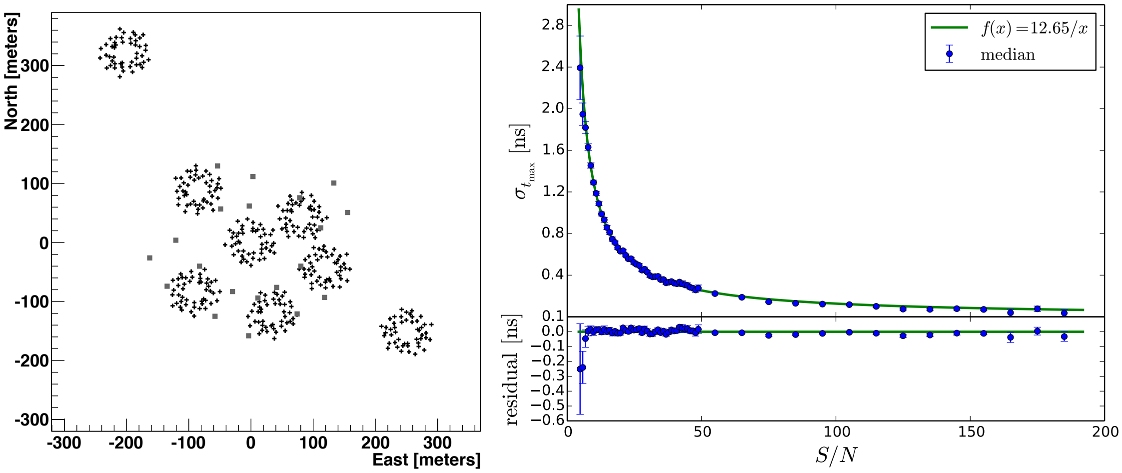

Figure 3.4: *Left:* Layout of the LOFAR stations used for the study, each "+" symbol representing one of the LBA antenna and the grey squares the particles detectors. All the analysed events have been detected in at least four of the core stations (rings of antenna). *Right:* Time resolution of the analysed events as a function of the signal to noise ratio (SNR) of the events (blue dots are the median over all the bins of the event). Taken from [24].

For the EAS radio wavefront study, only the LBA array in beamforming mode was used and re-filtered in the $30 - 80\,\mathrm{MHz}$ bandwidth to reduce the amount of radio frequency interferences. In their study (see [24]) the arrival times measured by LOFAR are analysed for a subset of high quality events, detected in at least four LOFAR core stations to ensure a high sampling of the wavefront. The method follows the same approach as LOPES: first computing the arrival times plane and then testing different fits of wavefront models to study the deviation from a plane wavefront. Two models were tested in particular: a spherical wavefront model and a hyperbolic wavefront model defined with respect to the propagation plane as (following their notations)

$$ct_{\mathrm{sph}}(r) = \sqrt{R^2 + r^2} - R \ , \tag{3.2}$$

$$ct_{\mathrm{hyp}}(r) = -a + \sqrt{a^2 + b^2 r^2} \ , \tag{3.3}$$

where R is the sphere radius, r the lateral distance to the shower axis and a and b are the parameters of the hyperbola. Figure 3.5 illustrates the results for the two wavefront models fitted to the data. These results show that the hyperbolic model is favoured with a χ^2 value roughly twice smaller than for the spherical model, for the 161 other events of the study.

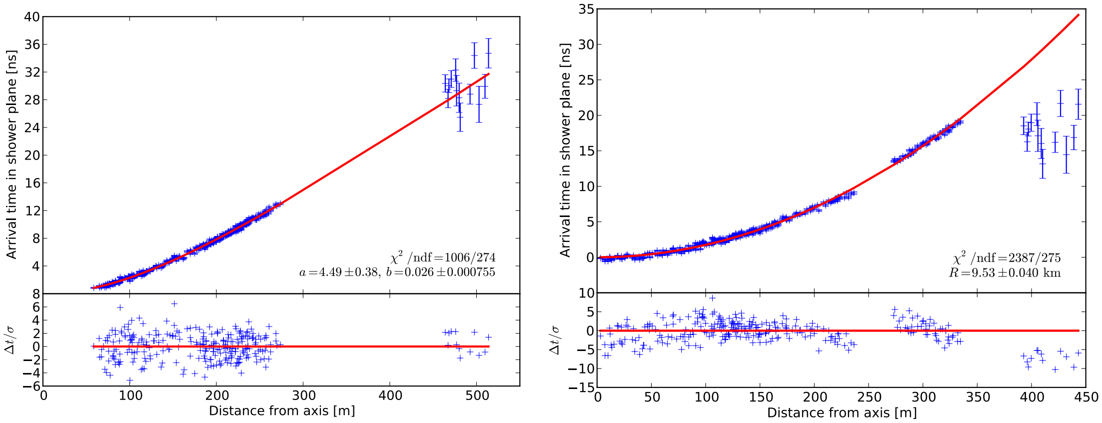

Figure 3.5: LOFAR results of the fit procedure on the arrival times in the shower plane as a function of the lateral distance to the shower axis, for one of the events used in the analysis. *Left:* Hyperbolic wavefront model. *Right:* Spherical wavefront model. The hyperbolic model is favoured in the minimisation with a χ^2 value two times smaller than for the spherical case. Taken from [24].

Results of LOPES and LOFAR show that the measured wavefront is hyperbolic: close to the axis, the curvature is quasi-spherical, but far from it, the behaviour tends to be conical. This result can be explained by comparing the ratio of the emission region size to the distance to the detector. Depending on the configuration of the EAS and detector location, three scenarii can indeed be considered (see Figure 3.6): in the first case, the emission region is much smaller than the propagation distance. The detected wavefront emission will then appear spherical. When the emission region is comparable to the propagation distance to the detector, the curvature induced by the physical extension of the emission region then leads to a hyperbolic wavefront emission. Finally when the emission region is much larger than the propagation distance, one should expect a conical wavefront emission. In light of this model, it seems reasonable to detect hyperbolical wavefronts with LOPES and LOFAR, since the nearly vertical configuration of the detected EAS places the emission region at distances of few kilometers from the detector, which is comparable to the size of the emission region.

3.2.3 Our work

In this section I present the study of the wavefront shape performed in the framework of the arrival direction reconstruction for GRAND. I first present the technical details related to the simulation sets and trigger time conventions. Then I discuss the study of the wavefront shape in the configuration of the GRAND experiment, in the perspective of two wavefront

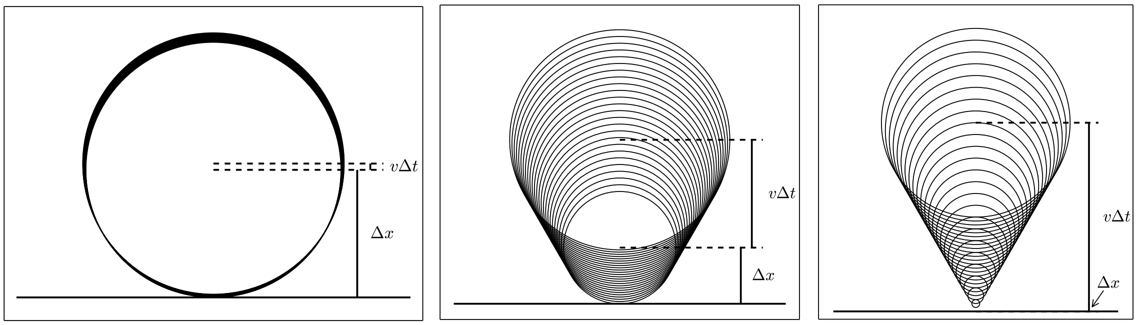

Figure 3.6: LOFAR wavefront models. Each of them corresponds to a specific configuration of emission region of size $\sim v\delta t$ compared to propagation distance Δx. *Left:* Spherical wavefront model corresponding to $v\delta t \ll \Delta x$. *Middle:* Intermediate case where the emission region extension $v\Delta t \sim \Delta x$ creates a deviation from the spherical wavefront i.e. hyperbolical curvature. *Right:* Extreme case where the emission region $v\Delta t \gg \Delta x$ dominates the propagation distance leading to a conical wavefront emission detected. Taken from [24].

models: hyperbolic and spherical.

3.2.3.1 Simulation sets and trigger conditions

In this analysis, we have used two distinct simulation sets. The first one is the *ToyModel* simulations, corresponding to up-going neutrino induced EAS already used in Section 2.2.3 with about 5000 events. The second set is called *Star-Shape* simulations, corresponding to about 2000 events of cosmic-ray and gamma-ray induced EAS. As the goal of this study is to properly describe the shower front, the nature of the primary is not critical and cosmic ray showers are valid tools as well as neutrinos. The simulated array follows a star-shaped array layout, where the antennas are placed at regular angular steps from the shower direction, resulting in an ellipsoidal star-shape on ground by projection (see Figure 3.7). For the *Star-Shape* set, the energies range from 0.0251 EeV to 3.94 EeV with a logarithmic step. Azimuth values corresponds to South-North ($\phi = 0°$), North-South ($\phi = 180°$) and East-West ($\phi = 270°$) trajectories. The zenith angles range from $\theta = 92.92°$ to $\theta = 141.8°$ in $1/\cos(\theta)$ logarithms bins. Primaries are Protons, Iron nuclei and Gamma rays. The altitude of 1086 m and magnetic field values of $\phi_{\mathrm{B}} = 0.36°$ and $\theta_{\mathrm{B}} = 60.8°$ of the simulation site corresponds to one of the potential GP300 sites (see [23]), in Gansu province, Western China. In both *ToyModel* and *Star-Shape* set, we use ZHAireS Monte-Carlo simulations (see Section 2.1.3 for more details).

Each of these sets allows us to study specific effects in the process of reconstruction. The *ToyModel* simulation allows us to easily play and study the interplay between the topo-

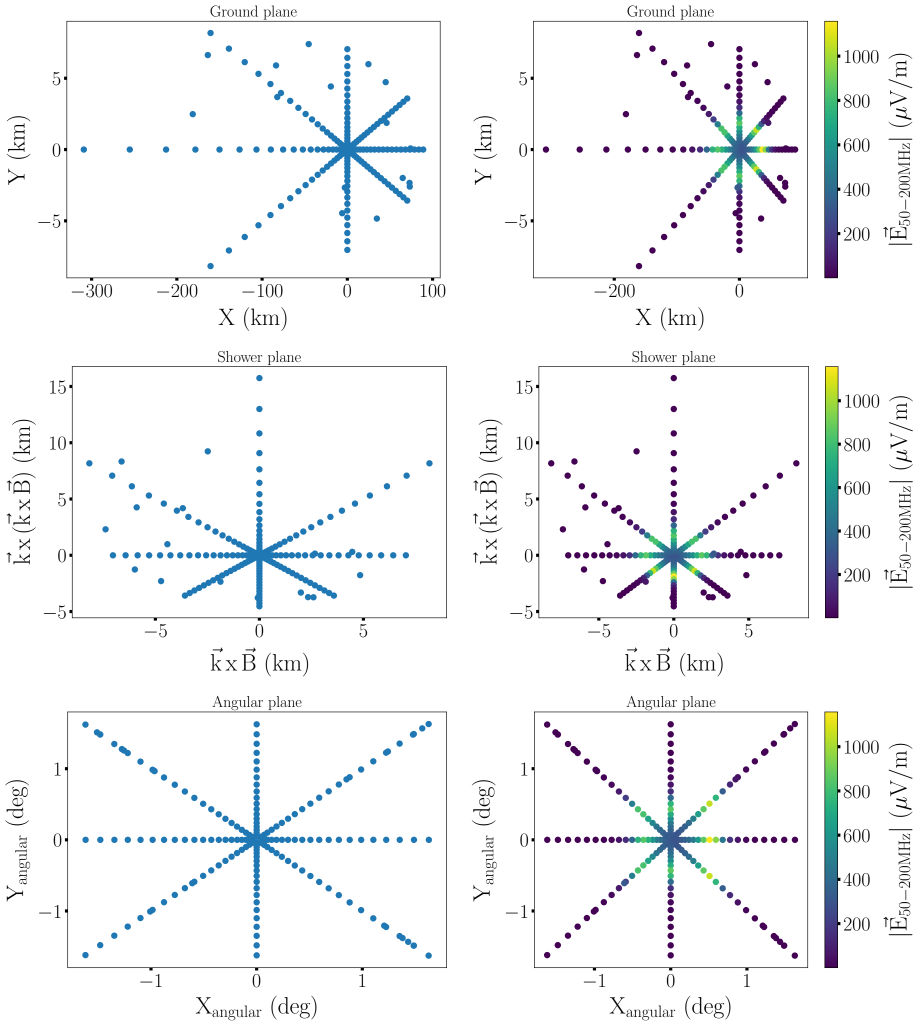

Figure 3.7: *Left column: Star-Shape* antenna layout. Antennas are placed at regular angles from the shower direction (here flying towards the South, azimuth= 180°) along the star-shape pattern. The x-axis and y-axis stand respectively for the South-North and East-West directions. This layout results in an stretched ellipsoidal star-shape along the shower direction on ground (*Top*) and therefore also in the shower plane (*Middle*). However in the angular plane (*Bottom*) the star-shape is by definition a symmetric circle, which makes this frame convenient for the study of inclined EAS (see Figure 3.8 for a sketch). *Right column:* Illustration of the signal amplitude distribution on ground of a *Star-shape* EAS simulation for azimuth 180° flying towards decreasing values of the x-axis, zenith= 92.92° and primary proton energy 3.98 EeV. *Top:* In the array plane. One can see the clear ellipse pattern. *Middle:* In the shower plane. The amplitude pattern is still an ellipse event though the projection attenuates it. *Bottom:* in the angular plane, where all projection effects are naturally corrected. Some antennas have been randomly placed outside the star shape for verification purposes when the simulation set was produced. We keep these antennas for the following study.

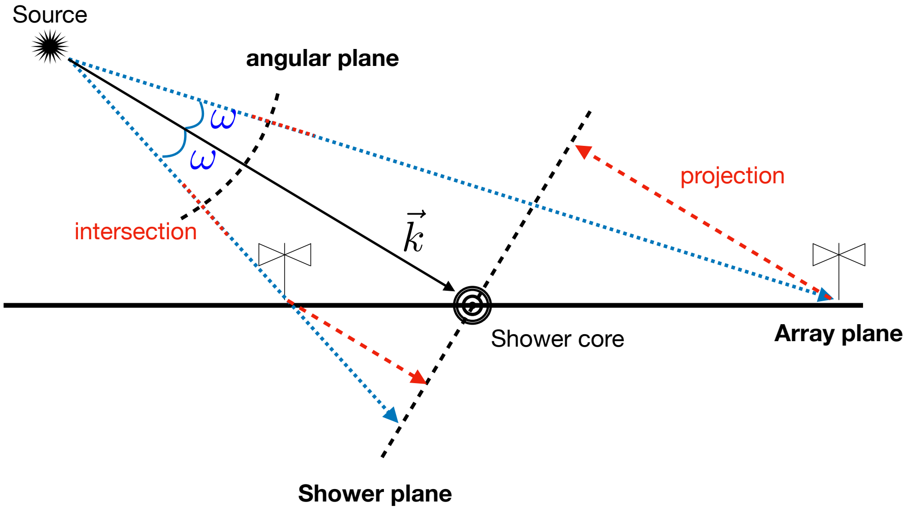

Figure 3.8: Sketch of the three possible representations of the antenna array. The array plane corresponds to the geographical plane where the antennas are placed on the ground. The shower plane is defined as the projection of the antennas position into a plane perpendicular to the shower axis and set at the shower core location. Finally, the angular plane displays the angular positions of the antenna with respect to the shower axis.

graphical parameters and the reconstruction, while the rectangular array layout allows for a good sampling of the wavefronts of up-going EAS. The *Star-Shape* simulations set, on the other hand, enables a good sampling of the shower radiation and in particular of the amplitude pattern with the various signal asymmetries contained (see Section 3.3).

The trigger conditions (and subsequent selection of antennas) are the same as in Section 2.3.4. The maximum of the signal is computed as the maximum of its Hilbert envelope, and the trigger time is defined as the time of the maximum of the Hilbert envelope. The Hilbert envelope is derived as the modulus of the Hilbert transform, which allows for the computation of the analytic form of the signal. It is commonly used in the community for the determination of the maximum of the signal [215]. On Figure 3.2, from left to right, one can see the different steps between the direct raw electric field signal at the antenna location, then the filtered ($50 - 200\,\mathrm{MHz}$) signal and finally the comparison between the modulus of the electric field and the Hilbert envelope. It can be clearly seen that both definitions of the trigger time in this case are quite similar and will not impact too much our study of the wavefronts. At some stage of the study (see Section 3.4.2), the trigger time is randomised with a gaussian distribution of $\sigma_t = 5\,\mathrm{ns}$, mimicking the GRAND nominal timing resolution.

3.2.3.2 Wavefront study

A proper description of the shape of the detected wavefronts is a critical issue, as it will drive the achieved angular precision in GRAND. It is not however a trivial question, since the results of earlier work, presented in Section 3.2.2, may not be directly applicable to GRAND. Indeed, the showers targeted by GRAND (very inclined and up-going), as well as the detector itself (sparse and very extended) differs significantly from the LOFAR and LOPES experiments. As an immediate consequence, the parameter space explored will be quite different. For example the distance to the shower axis in LOPES and LOFAR extends to about hundreds of meters (see Figures 3.3 and 3.5) while we expect for GRAND extensions of up to few kilometers (see for instance Figure 3.9). It is an excellent opportunity to explore the wavefronts shape at large distances from the core with an unprecedented lever arm. Finally, the very inclined trajectory, combined with the large extension of the array will allow us to sample the longitudinal propagation of the emission for very inclined EAS, unlike standard arrays which are only detecting an instantaneous snapshot of the radiation.

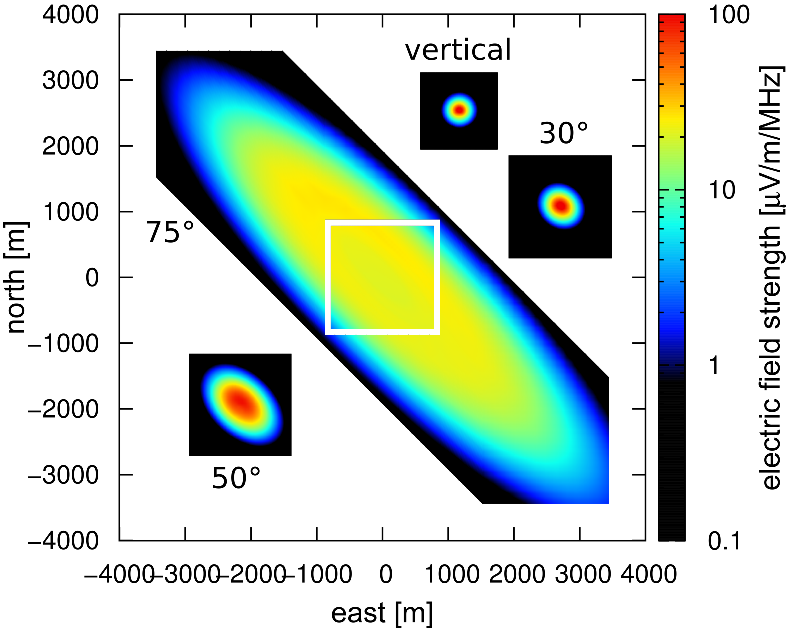

Figure 3.9: Sizes of simulated footprints on ground for various zenith inclinations (cosmic-ray conventions). The footprint grows strongly with the zenith inclination up to kilometer-size areas. For showers close to 90°, footprints even extend to several tens of kilometers. Taken from [176].

We led a dedicated study of the wavefront in the framework of GRAND, starting with a similar approach to the one presented in Section 3.2.2. There again, the first step consists in correcting the trigger times of the propagation times corresponding to a plane wave emission. The resulting delay gives us the intrinsic curvature of the wavefront emission. In our study, we formally define this plane as the plane perpendicular to the shower propagation at the antenna location and so the corrected times are simply given by

$$c\,t_{\mathrm{corr},i} = c\,t_{\mathrm{trigger},i} - n\,\vec{k}\cdot\vec{x}_i\ , \tag{3.4}$$

where $\vec{k}$ is the unit direction vector of the shower, $\vec{x}_i$ the antenna position taken from the X_{max} location and n is the refractive index.

The second step consists in finding the best wavefront model to describe the corrected delays. We consider both a hyperbolic model (see Section 3.2.3.3) and a spherical (see Section 3.2.3.4) model since in our configuration, the source extension is expected to be small compared to the observation distance (i.e. $v\delta t \ll \Delta x$ as shown on the first panel of Figure 3.6).

3.2.3.3 Hyperbolic model

The hyperbola can be described as a sphere with an additional curvature in the axis direction, or more accurately a sphere is a peculiar case of hyperbola where the parameters are degenerated. This additional curvature breaks the isotropy of the sphere and defines a preferred direction, which is in our case the shower propagation direction. We choose to write the hyperbolic model as follows

$$ct_i - n\,\vec{k}\cdot\vec{x}_i = \sqrt{a^2 + b^2 r_i^2} - a\ , \tag{3.5}$$

where t_i is the triggering time of the antenna A_i, $\vec{x}_i$ its position, r_i its lateral distance to the shower axis, and $a\,[m]$ and $b\,[m^{-1}]$ are adjustable parameters.

Before evaluating this model in the case of GRAND, let us first search for a physical explanation from first principles to the hyperbolic wavefront shape. Under a macroscopic description of the EAS emission mechanism (as detailed in Section 2.1.2), we can describe the time varying electric field as the derivative of the vector-potential $A^{\mu}(t,\vec{x})$ created by the charged current $J^{\mu}(t,\vec{x})$ induced by the motion of the charged particles in the EAS.

We follow here the electric-field derivation done in [161]. The authors studied a vertical shower described as in Figure 2.6 under some simplifying hypothesis called the *limiting case*, where the thickness of the particle front (pancake) can be ignored ($h \approx 0$), the shower velocity β_s in units of c and the refractive index are close to one. Consequently, the distance between the observer and the emitting source can be derived from Equation 2.18

$$\mathcal{D} = c\beta_s t \ + \mathcal{O}\big(1 - \beta_s^2 n^2\big) \ . \tag{3.6}$$

The retarded time (see Section 2.1.2) of the radiation emission can be defined through this general relation

$$ct - ct_r = c\Delta t = nc\sqrt{r^2 + (z+h)^2} \ , \tag{3.7}$$

from which one can obtain

$$ct_r = \frac{ct - n^2\beta_s h - n\sqrt{(-c\beta_s t + h)^2 + (1 - \beta_s^2 n^2) r^2}}{1 - \beta_s^2 n^2} \ , \tag{3.8}$$

as shown in particular in the Appendix B of [161]. Finally, in the limiting case, it reduces to

$$ct_r = \frac{ct}{1 + \beta_s} - \frac{r^2}{2c\beta_s t} \ + \mathcal{O}\big(1 - \beta_s^2 n^2\big) \ , \tag{3.9}$$

where the first term denotes the emission propagation with the shower displacement along the shower axis and the second term describes the additional time delay for an off-axis observer. The electric field can then be written as a function of the time of observation t and the lateral distance r

$$E_x(t, r) = -J \frac{n^2 \Delta}{c\mathcal{D}^2} \frac{\mathrm{d}f_t(t_r)}{\mathrm{d}t_r} + J f_t(t_r) \frac{c\beta_s^2 t}{\mathcal{D}^3} \ , \tag{3.10}$$

where $J = \langle v_\mathrm{d} q \rangle \, N_\mathrm{e} e / 4\pi\epsilon_0 \, c$ is the magnitude of the charged current expressed as a function of the mean drift velocity of the particles in the atmosphere $\langle v_\mathrm{d} \rangle$, their charge q, the electron number N_e in the EAS, e the electron charge, and ϵ_0 is the vacuum permittivity. As already said, the refractive index n, is assumed to be constant here.
$\Delta = \sqrt{r^2 + c^2 \beta_s^2 t_r^2}$ represents the geometrical distance between the observer and the emission source at the retarded time, D is the distance between the observer and the emission source at the observer time, $f_t(t_r)$ is the particle longitudinal profile as function of the retarded time t_r for an observer time t.

We investigate the resulting radiation wavefront induced by this electric-field description. To be consistent with our definition of the wavefront time as the maximum of the electric field (given in Section 3.2.1) for any given observer location, wavefront times are the roots of the first order derivative of the electrical field

$$\frac{\mathrm{d}E_x(t, r)}{\mathrm{d}t} = 0 \ . \tag{3.11}$$

Using Equation 3.10, we find this general expression

$$\begin{aligned}
&-\frac{\mathrm{d}^2 f_t(t_r)}{\mathrm{d}t_r^2}\frac{n^2 t\Delta}{c\beta_s}\left[\frac{1}{1+\beta_s}+\frac{1}{\beta_s}\left(\frac{r}{ct}\right)^2\right] \\
&+\frac{\mathrm{d}f_t(t_r)}{\mathrm{d}t_r}\left\{\frac{2n^2\Delta}{c\beta_s}+\left[\frac{1}{1+\beta_s}+\frac{1}{\beta_s}\left(\frac{r}{ct}\right)^2\right]t\left(1-\frac{n^2 c\beta_s t_r}{\Delta}\right)\right\} \\
&-2f_t(t_r)=0\ .
\end{aligned} \tag{3.12}$$

For the particle profile $f_t(t_r)$, a first approximation and a convenient choice is a gaussian distribution (see Figure 3.10)

$$f_t(t_r) \propto e^{\frac{(t_r-t_0)^2}{2\sigma^2}}\ , \tag{3.13}$$

where t_0 corresponds to the time of maximum shower development ($X_{\max}$) and σ is the standard deviation of the full time profile of the shower.

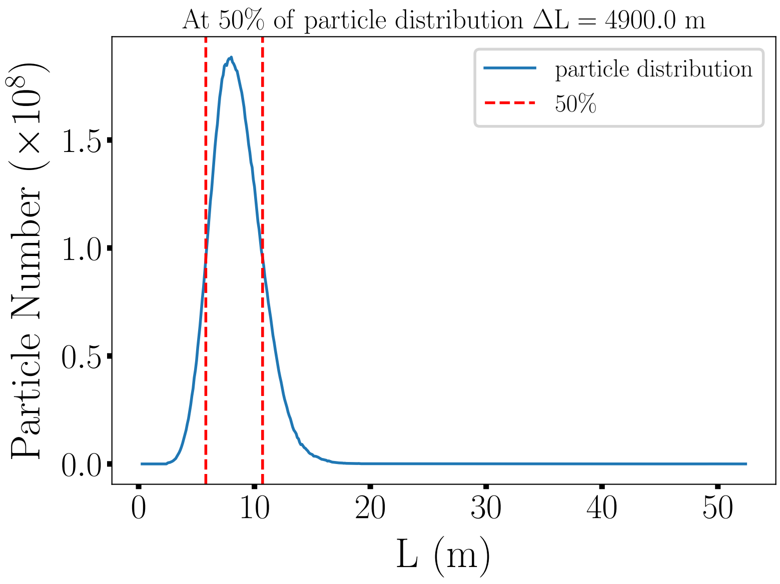

Figure 3.10: Particle distribution along the longitudinal axis for an up-going 10 EeV neutrino induced EAS with zenith $\theta = 87.9$ and $\phi = 0°$.

Injecting Equation 3.13 in Equation 3.12, we find the following second order polynomial

$$\begin{aligned}&\frac{t^2}{1+\beta_s}\frac{l}{\beta_s c\sigma^2}\left\{\frac{ln^2\Delta}{\beta_s^2c^2\sigma^2}+\left[1-\frac{n^2(l-l_{X_{\max}})}{\Delta}\right]\right\}\\&+2t\left(1+\frac{n^2l\Delta}{c^2\beta_s^2\sigma^2}\right)\\&+\frac{lr^2}{\beta_s^2c^3\sigma^2}\left\{\frac{ln^2\Delta}{\beta_s^2c^2\sigma^2}+\left[1-\frac{n^2(l-l_{X_{\max}})}{\Delta}\right]\right\}=0\ ,\end{aligned} \tag{3.14}$$

where we define for convenience $l = c\beta_s(t_r - t_0)$ as the longitudinal distance traveled between the starting time of the emission t_0 and the retarded time t_r, and $c\beta_s t_0 = l_{X_{\max}}$ is the longitudinal distance from $X_{\max}$ to the shower core at ground. We also define

$$\tau = \frac{lr^2}{\beta_s^2c^3\sigma^2}\ , \tag{3.15}$$

$$\delta = \frac{ln^2\Delta}{\beta_s^2c^2\sigma^2}\ , \tag{3.16}$$

$$\chi = 1-\frac{n^2(l-l_{X_{\max}})}{\Delta}\ , \tag{3.17}$$

$$T = \frac{l}{\beta_s c\sigma^2}\ , \tag{3.18}$$

where τ = [Time], T = [Time^{-1}] and δ and χ are dimensionless. Then Equation 3.14 becomes

$$\frac{t^2}{1+\beta_s}T + 2t\frac{1+\delta}{\chi+\delta}+\tau = 0\ . \tag{3.19}$$

Finally the canonical roots of this equation can be expressed as

$$t = -\frac{(1+\beta_s)(1+\delta)\pm\sqrt{(1+\beta_s)^2(1+\delta)^2 - T\tau(\delta+\chi)(1+\beta_s)}}{T(\delta+\chi)}\ , \tag{3.20}$$

which can be written as

$$t = -\frac{(1+\beta_s)(1+\delta)}{T(\delta+\chi)}\mp\sqrt{\frac{(1+\beta_s)^2(1+\delta)^2}{T^2(\delta+\chi)^2}-\frac{\tau(1+\beta_s)}{T(\delta+\chi)}}\ , \tag{3.21}$$

to identify it to a hyperbola under the form of Equation 3.5, if a and b are given by

$$a = \frac{(1+\beta_s)(1+\delta)}{T(\delta+\chi)}\ , \tag{3.22}$$

$$b = \frac{(1+\beta_s)}{T(\delta+\chi)}\frac{l}{\beta_s^2c^3\sigma^2}\ . \tag{3.23}$$

From this computation, we can plot the evolution of the wavefront time delay t as function of the lateral distance r (or distance to the shower axis). In the following, we examine the impact of the physical parameters of the air shower on the wavefront shape by using test-set values for the different parameters (see Table 3.1).

$l\,(\mathrm{m})$	$l_{X_{\max}}\,(\mathrm{m})$	$\sigma\,(\mathrm{s})$	n	β
10^5	10^4	3×10^{-6}	1	1

Table 3.1: Set of test parameters. By default the following parameters are used for the different plots.

From Figure 3.11 (top-right panel) we can see that the wavefront shape tends to flatten as longitudinal distance increases. This can be interpreted as the ageing of the shower emission. Similarly, a more distant $X_{\max}$ (middle-right panel) position along the shower axis also tends to flatten the wavefront shape.

Figure 3.11 also displays the effects of particle shower distribution on the wavefront shape (top-left and bottom panels). The time extension σ of the particle shower seems also to play an important role in the wavefront shape (for our range of values, which has to be more constrained). The bulk velocity of the particles in the shower seems to have a subdominant impact here. Finally the effect of the refractive index seems to be negligible for air (middle-left panel).

Finally, this simple model shows that under simplifying assumptions on the radiation emission and source characteristics, a hyperbolic wavefront shape naturally arises. The hyperbolic features of the wavefront are closely linked to the shower geometry, but also to its particle profile. However this model requires a large number of parameters not easily accessible from the radio emission information only. In addition, the assumptions made to derive this results are rather strong, in particular concerning the constant index of refraction which is obviously not valid in the general case. This is why for this study, we will restrain ourselves to the standard formulation of Equation 3.5.

Besides, the LOFAR model suggests that for our configuration (i.e. showers developing far away from the observer), we may expect a nearly spherical shower wavefront. Consequently, if indeed the observed wavefront is close to a sphere, then the hyperbolic model given by Equation 3.21 would have difficulties in converging to the correct result without falling into degenerated cases similar to spheres. All of the above leads us to consider closely the case of a spherical wavefront.

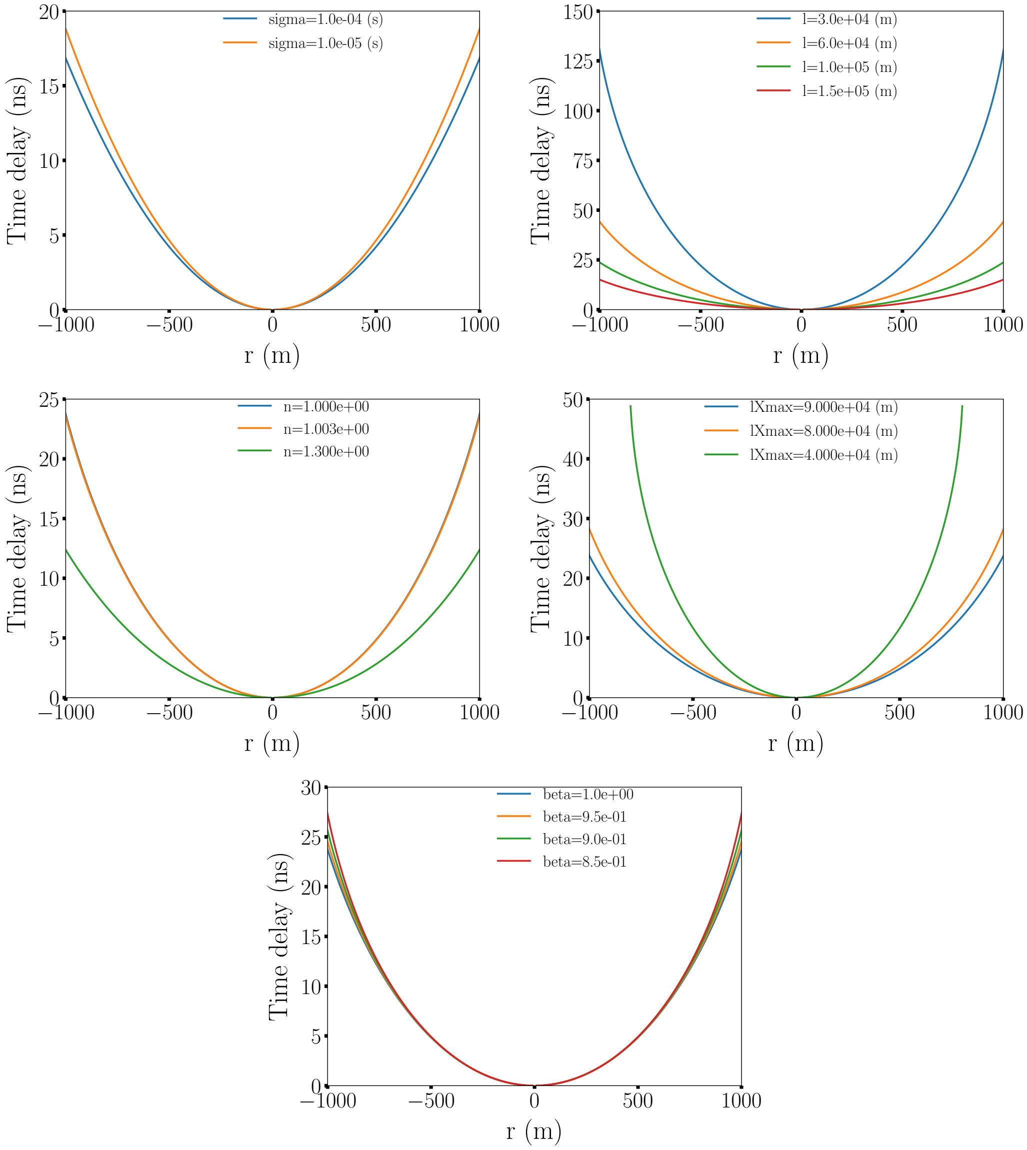

Figure 3.11: Evolution of the wavefront shape as a function of the distance to the shower axis. *Top-left:* For various values of σ in the particle distribution $f_t(t_r)$. *Middle-left:* different air refraction index. *Bottom:* For various particle velocity. *Top-right:* For various longitudinal distances or shower development. *Middle-right:* for different $X_{\max}$ positions along the shower axis.

3.2.3.4 Spherical model

A sphere is a particular case of degenerated hyperbola. The spherical model can be formally written in terms of antenna radial distance R_i or in terms of longitudinal distance l_i and lateral distance r_i of the antenna as depicted on the left panel of Figure 3.12. The model simply gives the causal relation between the source emission and the observer (antenna)

$$ct_i = n_i R_i = n_i \sqrt{l_i^2 + r_i^2} \ . \tag{3.24}$$

The two formulations are of course equivalent. Note that the refractive index n_i given in this equation, corresponds to an effective value: it is the integral of the refractive index values along the line of sight of the antenna A_i from the source. Its typical variations are of the order of 10^{-5}. In the case of very inclined (and up-going) EAS, the distances traveled by the radiation are so large (above hundreds of kilometers) that the small variations of the air refractive indices will delay significantly the signals. Let us consider for illustration purposes, a very inclined geometry. The X_{max} location is at altitude $H \approx 13\,\text{km}$ above ground and the zenith is 94° (see right panel of Figure 3.12).

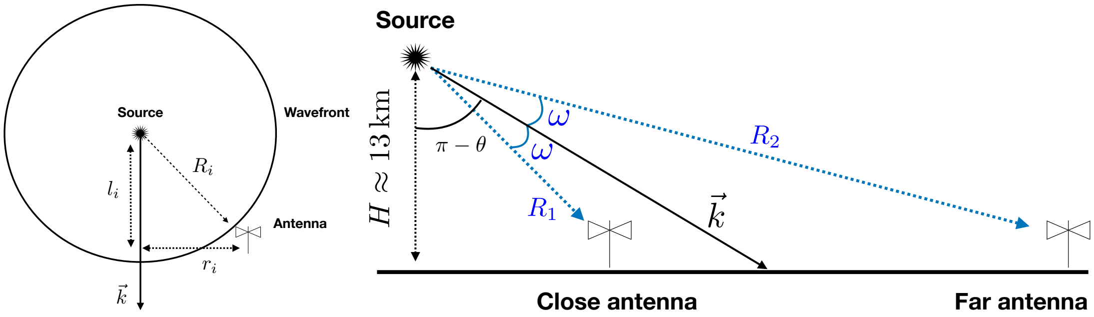

Figure 3.12: *Left:* Sketch of the spherical emission model. The time of the wavefront can easily be described as a function of the radial distance R_i of the antenna A_i or as a function of the longitudinal distance l_i (or propagation distance) and the lateral distance r_i. *Right:* Illustrative sketch of a very inclined cosmic-ray with two antennas at the same angular position from the shower direction but at very different radial position from the source.

Now let us look at two antennas located on the ground at a same angle ω from the shower direction so that one is closer to X_{max} and the other one is farther away. In this simple configuration, the distance from X_{max} to the first antenna is given by $R_1 = H/\cos(\pi - \theta - \omega)$ and the other antenna is at $R_2 = H/\cos(\pi - \theta + \omega)$. Since the radiation reaching the farthest antenna will have to cross more atmosphere depth, its effective refractive index will be larger $n_2 = n + \Delta n$ and equivalently for the closer antenna $n_1 = n - \Delta n$ (we assume for simplicity here the same variation of effective refractive index Δn). The relative timing delay between these two antennas will be $c\Delta t = R_1(n - \Delta n) - R_2(n + \Delta n)$. For $n = 1$, $\Delta n \approx 10^{-5}$ and $\omega \approx 3^\circ$ we then obtain $\Delta t \approx 30\,\mathrm{ns}$. Such systematic offsets are significantly larger than the expected time resolution of GRAND, hence they need to be taken into account for very inclined EAS. It can also be noticed that the difference of effective refractive index will scale with the traveled distance. A simple way to see this is to assume an isothermal atmosphere model. The refractive index in this case is an exponential function of the altitude: the larger the distance traveled by the emission, the larger the resulting integral along the line of sight. So for very inclined EAS, where the difference of traveled emission between different antennas of the array is larger, the effective refractive index difference will be larger and so will be the systematic offset.

3.2.4 Results

In this section I will present the results of the wavefront shape study and in particular the results from the fit by the two wavefront models, discussed in the previous section.

3.2.4.1 GRAND wavefront shape

On the right panel of Figure 3.13 are displayed the wavefront time delays (i.e. the trigger times with respect to the propagation plane, following Equation 3.4) as a function of the lateral distance to the shower axis, for a *ToyModel* simulation. The first striking features are, as already said in Section 3.2.3.2, that the distance to the shower axis spans over kilometers instead of hundreds of meters for less inclined EAS. Similarly, the time delays are in the range of hundreds of nanoseconds instead of tens of nanoseconds.

Finally the propagation distances extends to hundreds of kilometers instead of few kilometers as expected for nearly vertical EAS. Regarding the variations of the time delays as a function of the distance to the shower axis, we clearly see that the wavefront curvature depends on the propagation distance. In the case of very inclined EAS detected by GRAND, the longitudinal development of the shower clearly imprints on the trigger times at ground, while detection of vertical showers only allows for an instantaneous snapshot (see Figure 3.13). From Figure 3.15 it appears clearly that the curvature increases with the distance to the source, giving a clear illustration of the radiation propagation.

A similar result can be seen on Figure 3.16 for a proton primary cosmic-ray of energy 3.94 EeV propagating South (azimuth 180°) and with a zenith angle 94.2°, in the *Star-Shape* simulation set. In this case the star-shaped array gives a less dense sampling of the footprint but the trend is the same. A distinct change of wavefront curvature is observed between the closest antennas of the array and the farthest ones.

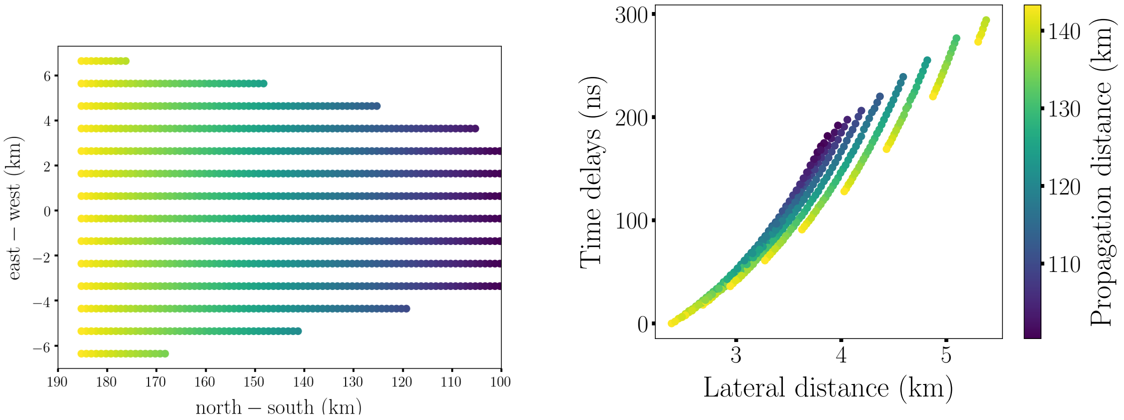

Figure 3.13: Triggered antennas of a *ToyModel* simulation with azimuth = 0°, zenith = 87.9° and primary neutrino energy 10 EeV. *Left:* Seen in the geographical plane (North-South, East-West). Note that the shower propagates from South to North hence from right to left on this figure. *Right:* Time delays as a function of the distance to the shower axis (or lateral distance r). For both plot, the colour code shows the propagation distance to the antennas from the $X_{\max}$ position (or longitudinal distance l). Due to the alignment between the shower propagation direction and the antenna grid, for a given string of antennas, the closest antennas to the shower axis are the farthest in propagation distance (see Figure 3.14). This results in the jumps observed for each string in the *ToyModel* time delays.

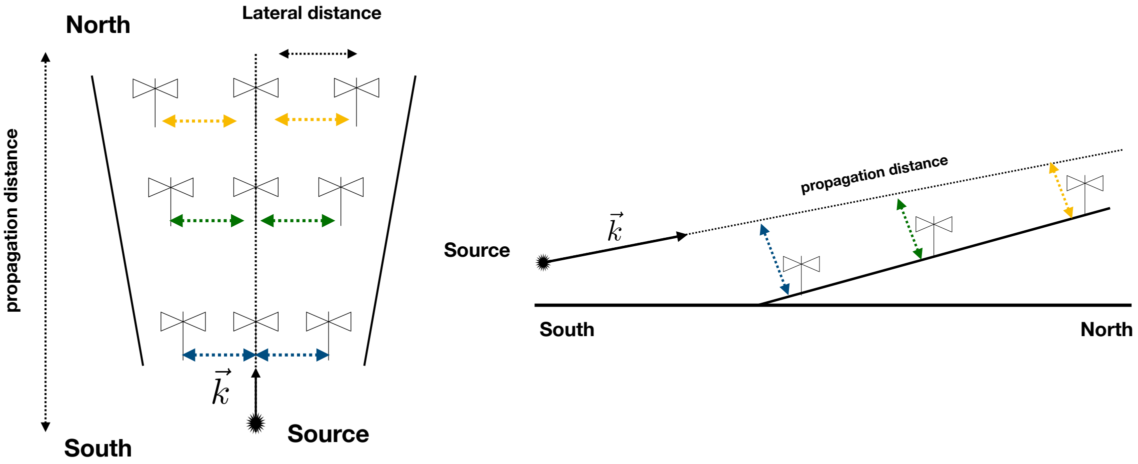

Figure 3.14: Sketch of the *ToyModel* array configuration with an up-going EAS.

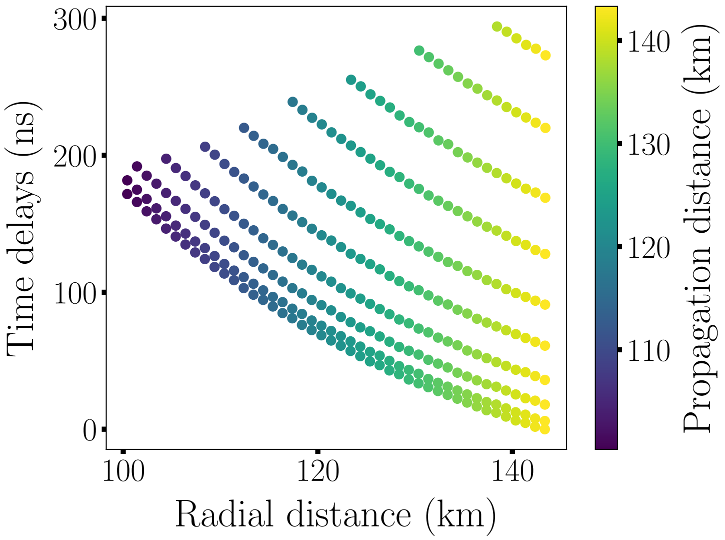

Figure 3.15: Time delays as a function of distance of the antennas from $X_{\max}$ (or radial distance R, defined in Equation 3.24), for a *ToyModel* simulation with the antenna array of the left panel of Figure 3.13 (azimuth= 0°, zenith= 87.9° and primary neutrino energy 10 EeV). For larger radial distances the time delay decreases, showing the flattening of the radio wavefront.

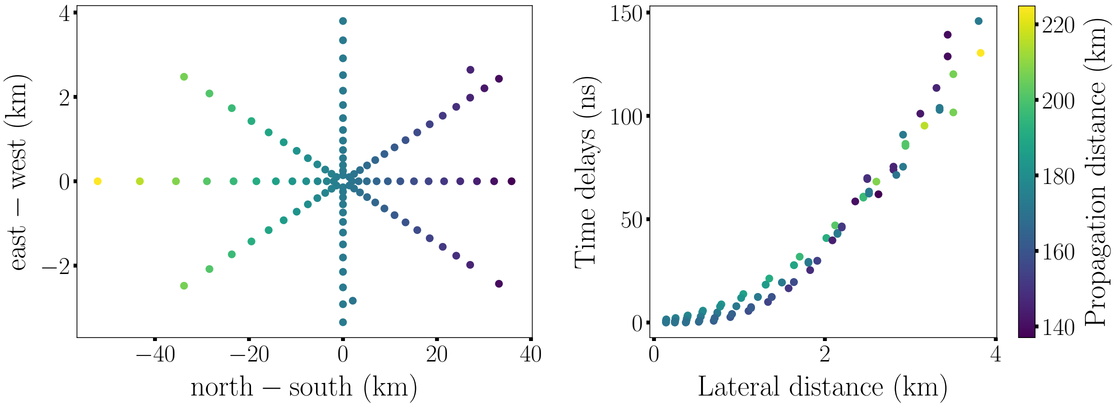

Figure 3.16: Same as Figure 3.13 for a cosmic-ray *Star-Shape* simulation (proton, azimuth = 180°, zenith = 94.2° and primary energy 3.94 EeV)

The next step is to find the best wavefront shape model to accurately reproduce this effect.

3.2.4.2 Hyperbolic model

Figure 3.17 shows the time delays as a function of the distance to shower axis. A standard hyperbolic fit to these point is performed. The true shower direction $\vec{k}$ is considered, and only a and b from Equation 3.5 are adjusted. As one would have expected, this fit fails to describe the antenna distribution in the plane (triggering time, distance to the shower axis), because the wavefront cannot be described by a single hyperbola, as its shape evolves with the propagation distance. In order to take into account this effect, we apply the same fit on distinct slices of array corresponding to different ranges of longitudinal values (see Figure 3.18). Each individual fit reproduces in a more accurate way the curvature of its slice (see the residuals from this fit on Figure 3.19).

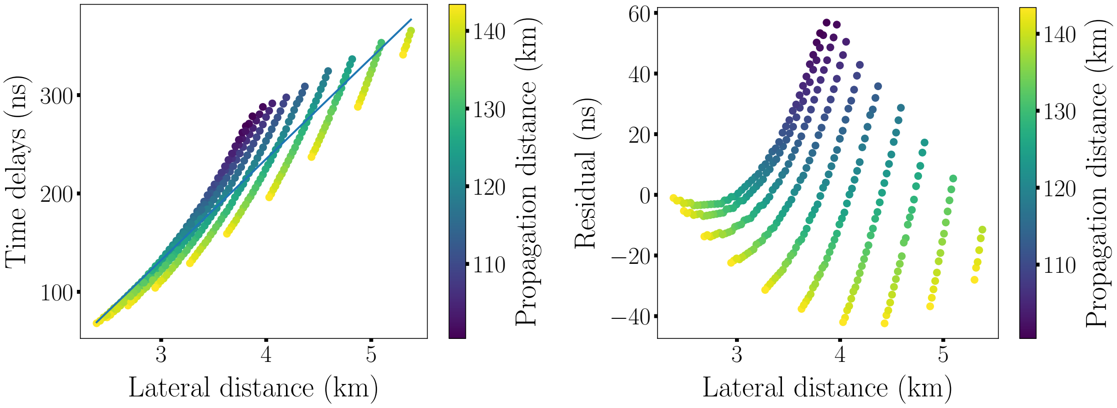

Figure 3.17: *Left*: Illustrative hyperbolic fits, performed on the same simulation as Figure 3.13. *Right:* Corresponding residuals from this fit.

Figure 3.20 represents the evolution of the stacked hyperbolic parameters of Equation 3.5 for different simulations slices. The simulations used correspond to identical showers (same direction and energy) but to different array configurations. Specific trends are visible for each parameter, but fail to clearly describe the flattening with longitudinal distance, as can be seen on Figure 3.17.

However the ratio of b^2/a, clearly shows a trend as a function of the longitudinal distance. Under this conditions, the hyperbolic wavefront model from Equation 3.5 simply reduces to (since $b^2/a \ll 1$)

$$ct_i - n\,\vec{k}\cdot\vec{x}_i \approx \frac{1}{2}\left(b^2/a\right) r_i^2 \ . \tag{3.25}$$

This corresponds to a wavefront shape proportional to a distance, with the term b^2/a describing the wavefront curvature with longitudinal propagation. This term can be naturally

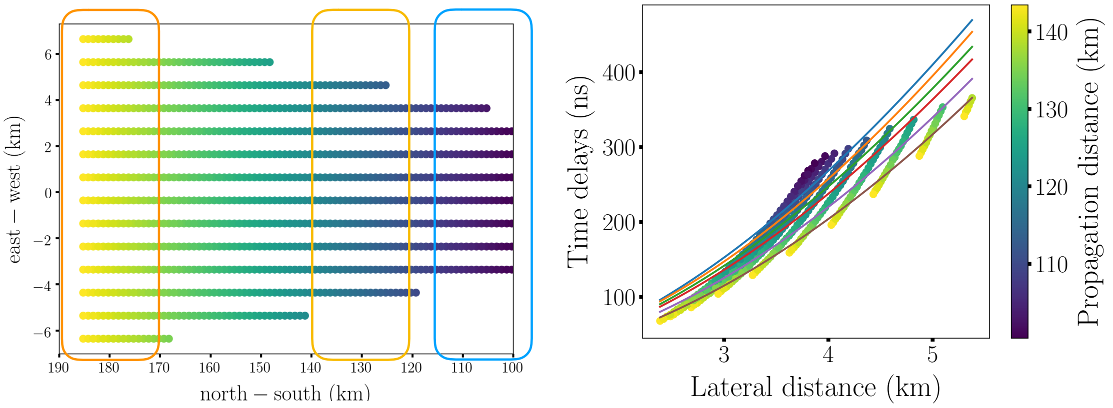

Figure 3.18: *Left:* Illustrative sliced array. Groups of antennas at similar longitudinal distances are fitted with different hyperbola. *Right:* Corresponding hyperbolic fits to array slices.

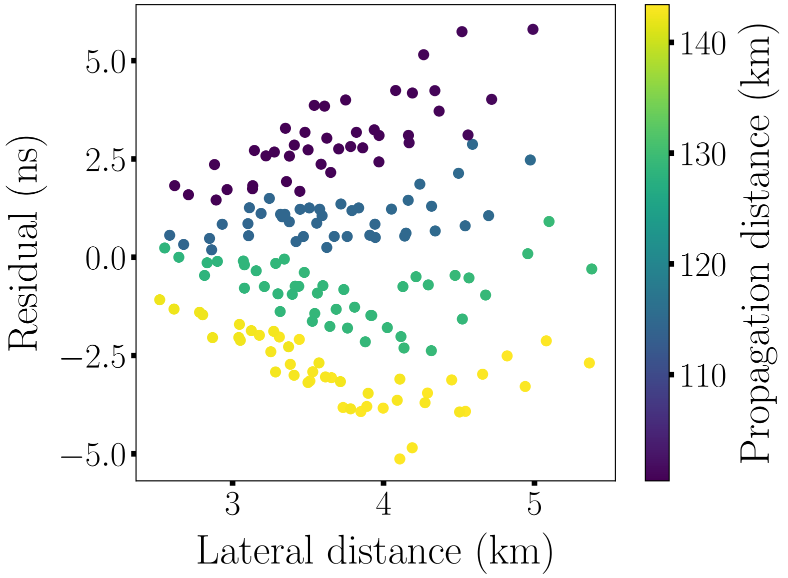

Figure 3.19: Residuals of the difference between the simulation data and the sliced hyperbolic fit of Figure 3.18.

interpreted as the curvature radius of the emission, which decreases inversely proportionally to the longitudinal distance l_i. Indeed, if we link Equation 3.25 to Equation 3.24 in terms of l_i and r_i, we can easily identify the time curvature of the fitted hyperbolic model

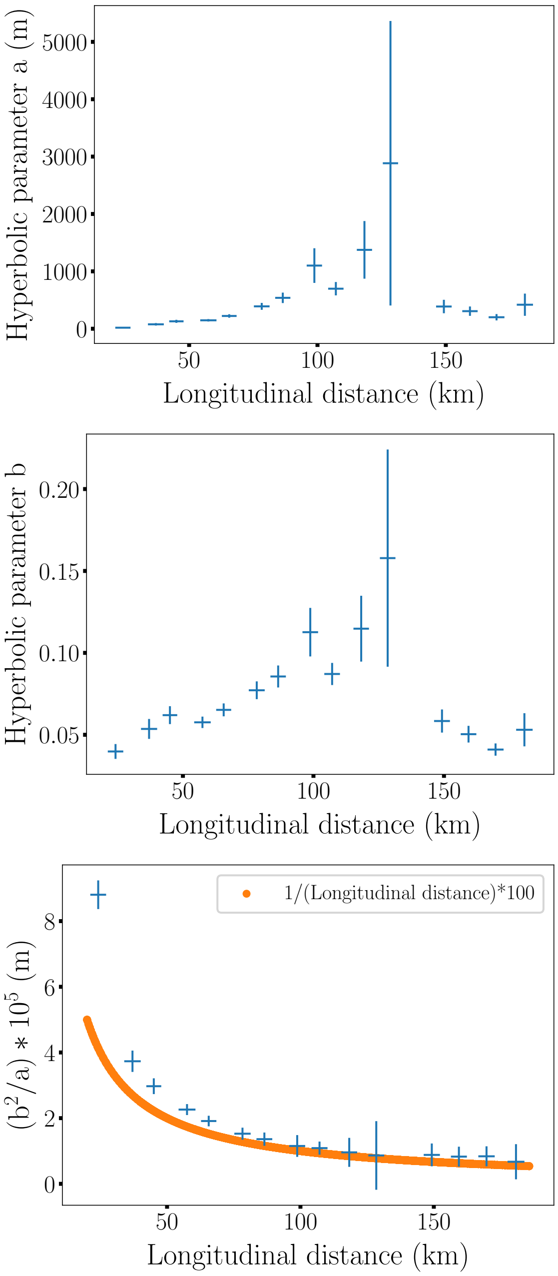

Figure 3.20: Evolution of the hyperbolic fit parameters with longitudinal distance. For stacked simulations: in order to cover a larger parameter space, the same EAS is simulated for different array configurations as detailed in Section 2.2.3. The ratio b^2/a shows a trend close to the one expected for the curvature radius of a sphere of radius equal to the propagation distance.

to a spherical model in the particular case where $l_i \gg r_i$

$$ct_i - n_i l_i \approx \frac{1}{2}(1/l_i)r_i^2 \ , \tag{3.26}$$

with $n_i l_i$ the time delay. From these fits, it is clear that in our specific case of distant emission, the hyperbolic fit may be reduced to a spherical fit far away from the emission source. This is tested in the next section.

3.2.4.3 Spherical model

The left panel of Figure 3.21 shows the times associated with the spherical model reproduced on top of the simulation results (again as time delay as a function of lateral distance). The spherical model naturally gives a wavefront evolution as an expanding sphere, which matches well with the evolution of the simulated data. On the right panel of Figure 3.21, the residuals confirms the good agreement between the simulation data and the analytical model. The mean residual is about 0.4 ns and the standard deviation is about 1.7 ns, below the GRAND experimental timing accuracy of $\sim$ 5 ns. Finally, displayed on Figure 3.22 one can see the average values and the standard deviation of the residuals between the spherical model and the simulation for the whole *ToyModel* simulation set. The averaged residuals remain below 20 ns and the standard deviation rarely exceeds 10 ns. Given those results, it appears that for a GRAND detector configuration and for very inclined EAS, the detected wavefront can be efficiently described with a spherical wavefront model.

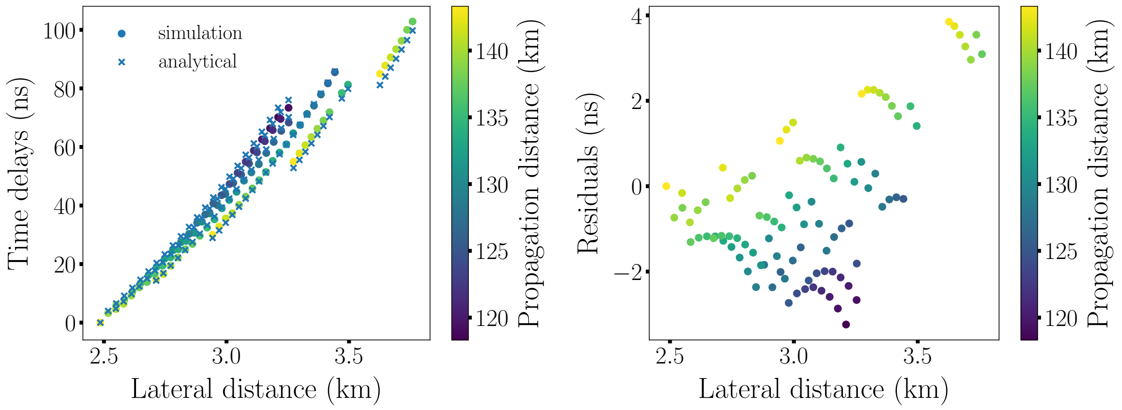

Figure 3.21: *Left:* Trigger times with respect to the propagation plane, as a function of the distance to shower axis. The time delay computed for the analytical spherical model are shown as blue crosses. *Right:* Residuals of the difference between the simulation data and the spherical model.

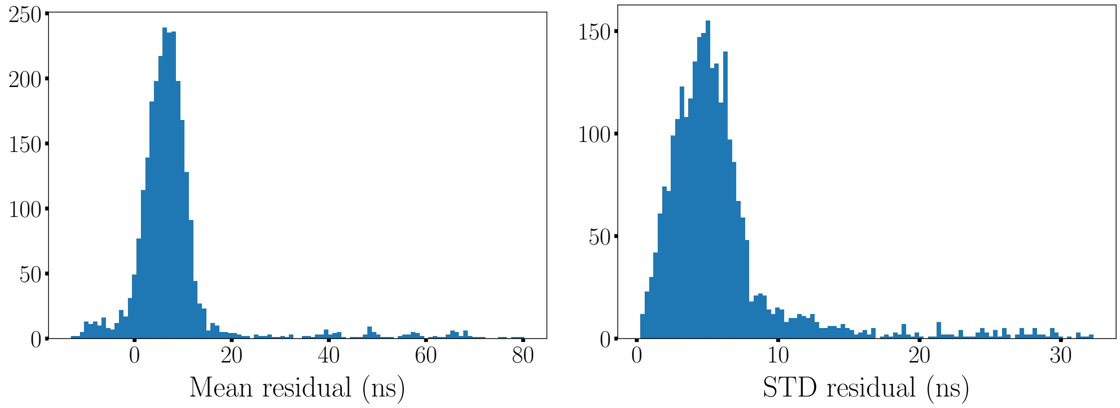

Figure 3.22: Mean residuals (*Left*) and standard deviations(*Right*) of the spherical model on the whole *ToyModel* set. Each value corresponds to the average of all antennas from one simulation.

In Figure 3.23 we can see a similar result for a *Star-Shape* simulation. However it can be noticed that the dense sampling close to the shower core reveals a deviation of the model for lateral distances below 2 km. This is a signature of the additional curvature close to the shower core as in the hyperbolic model but it is unfortunately undetectable (below 5 ns). This confirms that, the wavefront is indeed hyperbolic, but the deviation from a spherical model will remain undetectable for a sparse array like GRAND and a timing resolution of 5 ns.

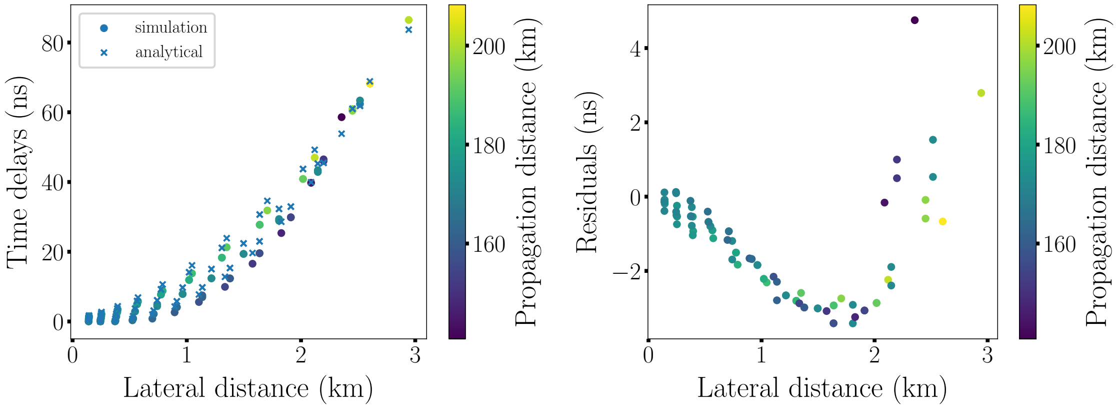

Figure 3.23: Same as Figure 3.21 for a *Star-Shape* simulation.

One last point concerns the fitting procedure, the spherical model appears to correctly describe the evolution of the wavefront shape, using all the antennas, unlike the hyperbolic model which requires a slicing of the array. This means that the efficiency and the accuracy of the fitting procedure will be much more degraded for the hyperbolic procedure than for the spherical one. Furthermore the hyperbolic model requires the adjustment of two extra parameters (a and b, see Equation 3.5) in addition to the shower direction. Finally low energy events are statistically detected with less antennas than high energy events, in particular for sparse arrays. This would make the reconstruction of the arrival direction impossible for the low energy events. All in all, it therefore appears that the spherical model is more suitable for the reconstruction of the arrival direction in the case of GRAND.

3.2.5 Conclusion

This detailed study shows that a spherical model is accurate enough, to describe the wavefront of the radio emission in GRAND. This choice has two main implications:

The first one is the impossibility to reconstruct the arrival direction of the radiated EAS, being in the case of a spherical emission, every direction are equivalent. A straightforward argument to support this, lies in Equation 3.24, where for a given radial distance R_i of the antenna A_i, any direction $\vec{k}$ will verify $R_i = \sqrt{l_i^2 + r_i^2}$ (see left panel of Figure 3.12).

The second implication is that since the emission is considered point like, it is possible to reconstruct the position of the emission source. There are two main arguments in favour of such an assertion. As Equation 3.10 shows, the electromagnetic emission scales with the number of particles in the EAS, which itself peaks at the X_{max} position (see Figure 3.10). Therefore it is not unreasonable to relate the maximum of the signal we detect to a region close to the X_{max} position. The second argument stems from the beaming effect. Since the emission is beamed into the shower direction due to its relativistic motion, the emission region appears more compact. An additional argument (although related) stems from the Cerenkov cone. Due to the large distance from the EAS emission region to the detector, the resulting footprint on ground results only from the Cerenkov cone emission. This emission is a geometrical feature of a radiating particle moving faster than the radiated emission in a given medium. It results in a compressed signal, containing high frequencies and more importantly, a large fluency content i.e. it produces large signal amplitudes. The antennas inside this Cerenkov cone (the most likely to trigger) will see the emitting part of the EAS at the same time due to the relative delay between each radiation track (due to the refractive index of the atmosphere). Hence the antenna sees the emission region as a condensed point-like source.

The conclusion of this study is that, in the case of a GRAND-like detector and for very inclined EAS, the wavefront seen by the array can be well model by a spherical description. This description does not allow us to reconstruct the arrival direction of the emission but it gives access to the emission source, which in our configurations behaves as a point-like source. In order to reconstruct the arrival direction, we will thus need a second point along the EAS path. A natural choice is the shower core, which can be reconstructed using the amplitude distribution.

3.3 General study of the footprint pattern: amplitude information

In this section We present the study of the amplitude distribution in the radio footprint, starting with the method and tools, with a specific focus on the regime of very inclined EAS, followed by the results.

The following study was performed on the *Star-Shape* simulation set only. The efficient sampling of its amplitude pattern makes it a tool well suited to study and disentangle the various asymmetries at play. Nevertheless the tools and conclusion developed below can be fully applied to the *ToyModel* set. Indeed, the following study remains valid for showers observed with a high inclination with respect to the array position i.e. far away from the emission region.

3.3.1 Method and tools

We detail in this section, the main asymmetries of the EAS signal: the geomagnetic vs charge-excess effect, the early-late effect, and an additional asymmetry, poorly documented yet and briefly mentioned in [27], which impacts the observed position of the Cerenkov angle at ground. As detailed below, this is a key parameter to describe the signal distribution of the EAS. Consequently, we developed a method to study this new asymmetry and model its effects on the signal. The last subsection gathers all the previous effects in a handy model to describe the amplitude signal distribution in the footprint.

3.3.1.1 Angular description vs shower plane description

A well established method in the community consists in displaying the signal amplitude distribution through a projection of all the information in the so-called shower plane, defined by the vector basis $\{\vec{k} \times \vec{B}, \vec{k} \times \left(\vec{k} \times \vec{B}\right), \vec{k}\}$, with $\vec{k}$ the shower direction and $\vec{B}$ the geomagnetic field direction (see Figure 3.8). It is a natural basis considering that, the geomagnetic emission polarisation is aligned with the $\vec{k} \times \vec{B}$ axis and inside the array, the emission triggers the antennas (from the first one: “early” to the last one “late”) along the $\vec{k} \times \left(\vec{k} \times \vec{B}\right)$ axis. This projection allows us to disentangle the main asymmetry effects detailed in Sections 3.3.1.2 and 3.3.1.3.

However, the intersection of the Cerenkov cone with the ground plane for instance results in an ellipse (see Figure 3.7); with an elongation increasing with zenith angle and shower axis lying at one focus. Its projection in the shower plane remains an ellipse (see Figure 3.24), which induces a distortion of the amplitude pattern, and makes it modelling more complex.

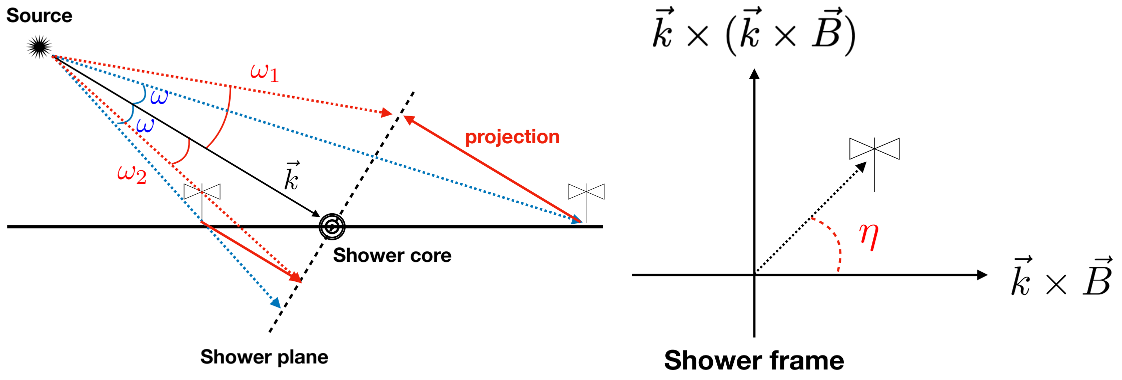

Figure 3.24: *Left:* Sketch of the projection into the shower plane of two antennas at the same ω angle with respect to the shower direction. The resulting angles to the shower plane are different $\omega_1 \neq \omega_2$. The projection does not conserve the angles. *Right:* The η angle describes the position of the antenna with respect to this axis and goes from 0°, when aligned with the positive direction of the $\vec{k} \times \vec{B}$ axis, to 180° when aligned with the negative direction. In addition, one can already see the disentangling of the geomagnetic asymmetry.

In our opinion, this issue can be overcome in a more elegant way by simply referring to the antenna locations through their angles ω measured from $X_{\max}$ with respect to the shower direction. It is a more natural choice for very inclined EAS as the projection effects of the footprint on ground are then avoided, since the angle does not depend on the array location. Furthermore the Cerenkov cone is then a circle of angular distance ω_C to the axis.

For illustrative purposes, Figure 3.25 displays the angular distribution of the signal amplitude for a given shower. Here, the amplitude is computed as the maximum of the Hilbert envelope (in a similar way as the trigger time see Section 3.2.3.1). Note that as expected, the two sets of simulations present similar signal amplitude distributions and hence we do not restrict our study by only focusing on the *Star-Shape* set. The peaks corresponding to the Cerenkov effect can be observed at two symmetrical positions $\omega = \pm\omega_C$ from the center at first order. The shower core lies, by construction, at the center where $\omega = 0$. In order to ease reading, the sign of the ω angle is given with respect to the position of the antenna along the $\vec{k} \times \vec{B}$ axis (see the sketch on the right panel of Figure 3.24).

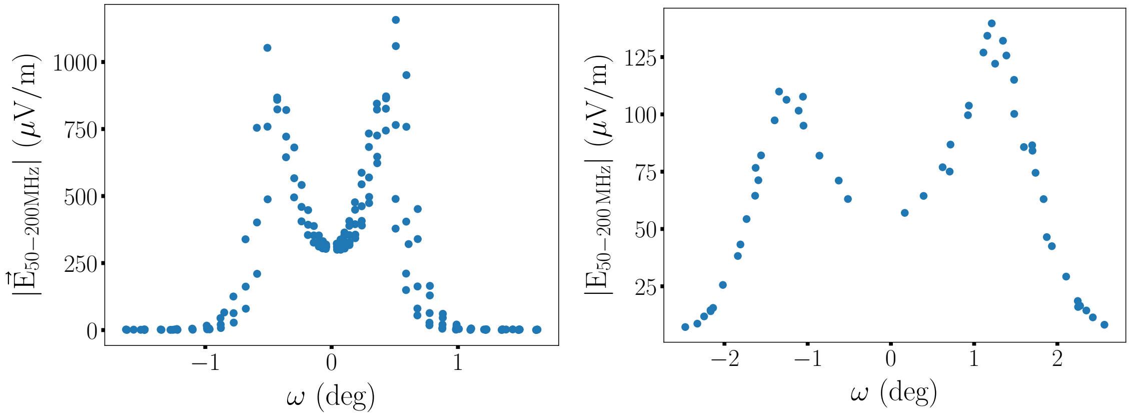

Figure 3.25: Angular distributions of the signal amplitude as defined in Figure 3.2. *Left:* for a *Star-Shape* simulation: azimuth 180°, zenith 92.92° and a proton primary energy of 3.94 EeV. *Right:* For a *ToyModel* simulation: azimuth 0°, zenith= 87.9° and primary neutrino energy 10 EeV. Both distributions follow the same trend and the difference in the position of the peaks, corresponding to the Cerenkov cone, is due to the difference of geometrical configuration (down-going and up-going trajectories) thus of refractive index.

3.3.1.2 Geomagnetic asymmetry

The geomagnetic asymmetry is the consequence of the interplay between the charge excess and the geomagnetic emission. In Section 2.1.2, we presented how these two different emission processes contribute to the shower emission. The Askaryan (or charge-excess) process results in a radial emission signature pointing towards the shower axis, and the geomagnetic process results in an electric-field pointing towards the $\vec{k} \times \vec{B}$ direction (see Figure 3.26). In the atmosphere, the latter emission process is dominant, and as a consequence, the signal amplitude distribution presents a slight asymmetry along the $\vec{k} \times \vec{B}$ axis, with a higher amplitude for $\vec{k} \times \vec{B} > 0$ compared to $\vec{k} \times \vec{B} < 0$. This effect has already been extensively studied, in particular in [216]. Naturally, in order to accurately describe the angular distribution function of the amplitudes, this effect needs to be taken into account (see Section 3.3.3).

3.3.1.3 Early-late asymmetry

The early-late asymmetry results from the dilution of the signal energy with the propagation distance L. From an energy conservation point of view, the radiated energy density decreases as $1/L^2$ where L is the propagation distance, since the radiated energy is constant over the surfaces perpendicular to the signal propagation (see Figure 3.27). Consequently,

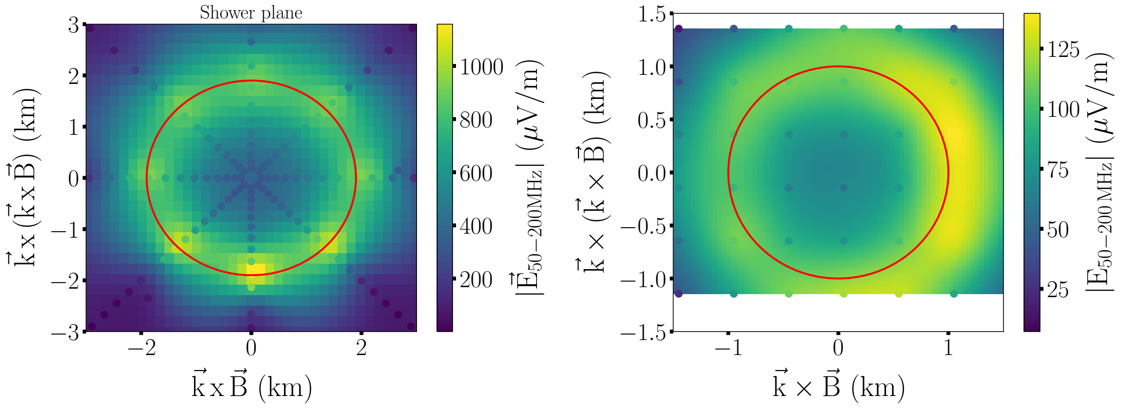

Figure 3.26: Signal amplitude distribution in the shower plane. *Left:* For a *Star-Shape* simulation: azimuth 180°, zenith 92.92° and a proton primary energy of 3.94 EeV. *Right:* For a *ToyModel* simulation: azimuth 0°, zenith= 87.9° and primary neutrino energy 10 EeV. The array plane in this *ToyModel* simulation is vertical with respect to the ground and allows us to see the full signal, since the EAS is nearly horizontal, it is somehow equivalent to a vertical shower seen by flat array (if we neglect the refractive index effects). One can see the small signal amplitude excess along the positive $\vec{k} \times \vec{B}$ axis, called geomagnetic asymmetry.

the amplitude of the signal varies as $1/L$. For inclined (and very inclined) EAS, this results in a differential energy repartition between the antennas of the array closer (hereafter called early antennas) to the source and the antennas farther away (hereafter called late antennas). The global output is a larger signal amplitude observed for early antennas than for late ones. This dilution effect has been well studied in particular in [217]. In Section 3.3.3 we detail how this effect is handled in our model.

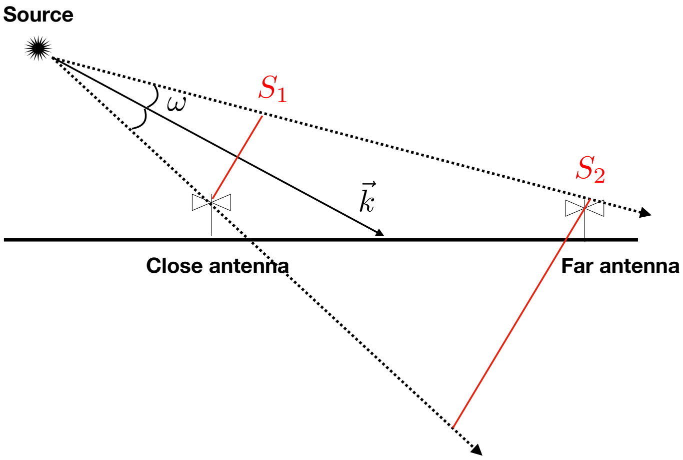

Figure 3.27: Illustration of the early-late effect. Two antennas at the same angle with respect to the shower direction, will not receive the same energy as the energy density is diluted along the propagation of the radiation. This is easily understandable as the surfaces perpendicular to the shower direction inside the beamed cone are given by $S = \pi(L\tan(\omega))^2$, with L the shower propagation. Consequently the energy density will be diluted as $1/L^2$.

3.3.2 Cerenkov asymmetry

3.3.2.1 An unexpected asymmetry

If, at first order, the Cerenkov ring lies at positions $\omega = \pm\omega_C$, an asymmetry in the positions of the signal amplitude peaks in the angular distribution is however observed for very inclined EAS, as displayed the right panel of Figure 3.28.

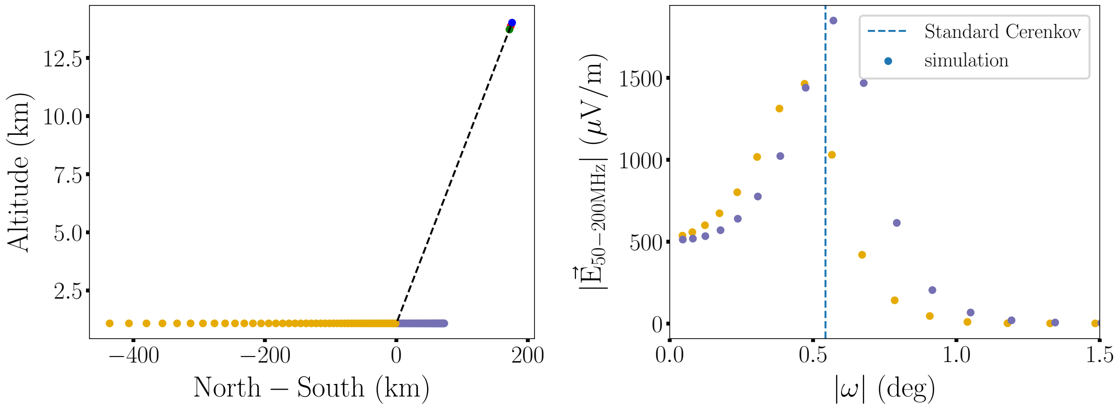

Figure 3.28: Left: Configuration set up of antennas along the shower direction (azimuth = 180° and zenith = 94.2°) with the *early* antennas in purple and the *late* antennas in brown. The shower axis is shown with a dotted line and the X_{max} as a blue point. Right: Angular Distribution Function of the simulated electric-field amplitude in the $50-200$ MHz frequency bandwidth. It can be clearly seen that early antennas have a larger Cerenkov angle than late ones. The vertical blue dotted line represents the expected Cerenkov angle value for the refractive index at the X_{max} altitude.

Early antennas (purple) are observed with a slightly larger Cerenkov angle than late antennas (brown). In a homogeneous medium, the Cerenkov cone angle is given by

$$\omega_{\text{C}} = \text{acos}\,(1/n)\ , \tag{3.27}$$

where n is the refractive index. The expected result would be two peaks at the same angle (corresponding to the Cerenkov angle) with respect to the shower direction ($\omega = 0$). However, the right panel of Figure 3.28, shows two peaks at two distinct angles. Furthermore the Cerenkov angle computed with Equation 3.27 from the refractive index at X_{max} position, fails to reproduce any of these two peaks angle positions.

3.3.2.2 Hypothesis and physical interpretation

From an observer point of view, the definition of the Cerenkov cone can be interpreted as the position where the signals of all the emitting points of the EAS arrive with the shortest relative delay, which leads to a compression effect, maximal at the Cerenkov angle (see Section 2.1.2). Our hypothesis is that, for inclined EAS this position is no longer symmetrical with respect to the shower axis in ZHAireS simulations. Indeed, the optical paths are no longer equivalent as early antennas do not observe the emitting region under the same viewing angle as late antennas. This hypothesis can be easily tested thanks to a toy model presented below.

3.3.2.3 Toy-model description

In our toy model, we choose two emission points along the EAS track, placed around the maximum of development of the shower, separated by a distance $\Delta \sim 1-2\,\mathrm{km}$ (see a sketch on Figure 3.29 and note that this value is chosen accordingly to the particle distribution displayed in Figure 3.10), and we compare for various observer positions (defined by their ω angles) how the signal reception delay varies between these two emission points. Note that due to the comparison between the two emission points, the exact value (in a reasonable range) of Δ does not matter and does not changes the results. Finally, the effective refraction index of each observer's line of sight is taken into account.

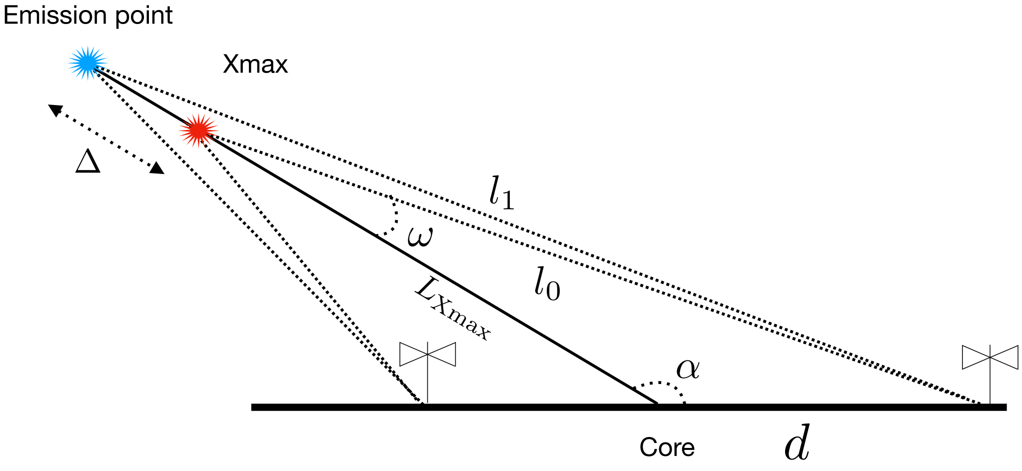

Figure 3.29: Sketch of the toy model used to study the Cerenkov angle deviation and asymmetry. The idea is to consider a two-points emission along the shower propagation. The points where those two emissions reach the ground with the shortest delays define the Cerenkov angle.

It is possible to compute numerically the time delays between these two points, using the same atmosphere model as ZHAireS for the computation of the refractive index and signal propagation time. The Cerenkov angle can then be associated to the angle value for which the time delays equals zero (from the definition presented in Section 3.3.2.2). Figure 3.30 displays the time delay values for various observer positions for the same EAS as Figure 3.28. The values of the Cerenkov angle (for which time delays are null) clearly differ for early and late antennas.

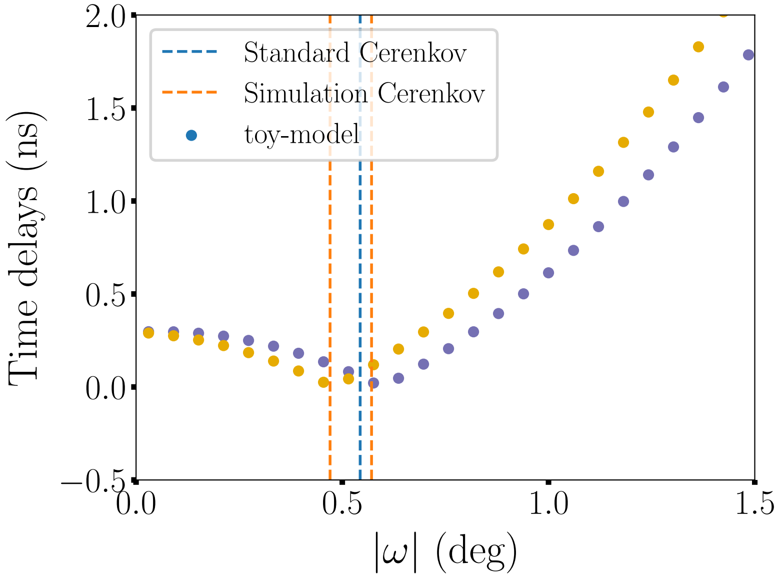

Figure 3.30: Time delays as a function of observer position, computed from the two emission points of the toy model for the same EAS as Figure 3.28. We can clearly see two Cerenkov angles for early and late antennas (same color code). Again the expected Cerenkov angles from the refractive index at the altitude of the two emission points fails to reproduce the exact Cerenkov values as well as the asymmetry between early and late observers.

This simple toy model therefore allows us to reproduce the asymmetry effect between early and late antennas. The next step is to develop an analytical model allowing us to quantitatively compute this effect for various shower configurations and so to extract the Cerenkov angles values for any shower geometry.

3.3.2.4 Analytical model

Let us consider the time delay between the optical path from a given point (taken above the $X_{\max}$ position) to an observer position ω and the one from $X_{\max}$ to that same observer position ω. Note that $\omega < 0$ corresponds to early antennas and $\omega > 0$ to late antennas. To each line of sight l_1 and l_0 corresponds a given effective index of refraction n_1 and n_0, defined respectively at the emission point and at the $X_{\max}$ altitude, or as the integral of the refractive index along the line of sight. The time delay can then be written

$$c\delta t = n_0 l_0 - n_1 l_1 + \Delta \ , \tag{3.28}$$

where l_0 is given by the solution of

$$l_0^2 = L_{X_{\max}}^2 + d^2 - 2L_{X_{\max}} d \cos(\alpha) \ , \tag{3.29}$$

$$d^2 = L_{X_{\max}}^2 + l_0^2 - 2L_{X_{\max}} l_0 \cos(\omega) \ , \tag{3.30}$$

where d is the distance between the core and the observer position, leading to

$$l_0 = \frac{L_{X_{\max}} \sin(\alpha)}{\sin(\alpha - \omega)} \ . \tag{3.31}$$

After solving a second order polynomial in l_0 and few simplifications in terms of sine and cosine (or via the Al-Kashi theorem directly), we obtain

$$l_1 = \sqrt{l_0^2 + \Delta^2 + 2\Delta l_0 \cos(\omega)} \ . \tag{3.32}$$

The Cerenkov angle position is the solution to $c\delta t \approx 0$ or equivalently $c^2 \frac{\mathrm{d}(\delta t)^2}{\mathrm{d}\omega} = 0$. In the latter case the derivative of Equation 3.28 squared is given by

$$c^2 \frac{\mathrm{d}(\delta t)^2}{\mathrm{d}\omega} = 2(n_0 l_0 - n_1 l_1 + \Delta)\left(n_0 \frac{\mathrm{d}l_0}{\mathrm{d}\omega} - n_1 \frac{\mathrm{d}l_1}{\mathrm{d}\omega}\right) \ , \tag{3.33}$$

which only cancels out for $n_0 l_0 - n_1 l_1 + \Delta = 0 = c\delta t$, since the time delays are strictly growing functions of ω, we end-up in the first case.

In the first case, we can either try a limited expansion of Equation 3.32 in terms of $\Delta/l_0 \ll 1$ inside Equation 3.28, which gives

$$l_0(n_0 - n_1) + \Delta(1 - n_1 \cos\omega) = 0 \ , \tag{3.34}$$

replacing l_0 by its expression of Equation 3.31 yields

$$L_{X_{\max}} \sin(\alpha)(n_0 - n_1) + \Delta(1 - n_1 \cos\omega) \sin(\alpha - \omega) = 0 \ . \tag{3.35}$$

The equation is satisfied for $\omega = \omega_{\mathrm{Cerenkov}}$, and can not be solved analytically.

Since a numerical solution is needed for the approximative expression, let us look for an exact computation. It can be achieved by looking at the square of Equation 3.28

$$(n_0 l_0 + \Delta)^2 = (n_1 \, l_1)^2 \ , \tag{3.36}$$

leading to

$$l_0^2\big(n_0^2 - n_1^2\big) + \Delta^2\big(1 - n_1^2\big) + 2l_0\Delta\big(n_0 - n_1^2\cos(\omega)\big) = 0 \ . \tag{3.37}$$

Replacing l_0 by its expression of Equation 3.31 yields

$$L_{X_{\max}}^2 \sin(\alpha)^2\big(n_0^2 - n_1^2\big) + \Delta^2\big(1 - n_1^2\big)\sin(\alpha - \omega)^2 + 2l_0\Delta\big(n_0 - n_1^2\cos(\omega)\big)\sin(\alpha - \omega) = 0 \ . \tag{3.38}$$

This equation hides a quartic polynomial, which can be developed as a function of $t = \tan(\omega/2)$, under the form

$$\begin{aligned} -t^4 \ \sin(\alpha)&\big[2l_0n_0\Delta + n_1^2\big] \\ &- t^3\, 2\cos(\alpha)[2l_0n_0\Delta + n_1] \\ &+ t^2 \ \sin(\alpha)\big[n_1^2\big(2 + \Delta^2 - L^2\big) + n_0^2L_{X_{\max}}^2 - \Delta\big] \\ &+ t\, 2\cos(\alpha)\big[n_1^2\big(1 + \Delta^2\big) - \Delta^2 - 2l_0n_0\Delta\big] \\ &+ \sin(\alpha)\big[2l_0n_0\Delta + \Delta^2 - n_1^2\big(\Delta^2 + 1 + L_{X_{\max}}^2\big) + L_{X_{\max}}n_0^2\big] \\ &= 0 \ , \end{aligned} \tag{3.39}$$

with no obvious solutions (see Figure 3.31). At this stage a numerical solution is needed, following for example a basic dichotomy search. This treatment allows us to determine a numerical value for the Cerenkov position from the shower geometry only. This will allows for a treatment of this asymmetry in the modelling of the amplitude distribution. Note that an independent treatment of this asymmetry was published after this work was carried out [218], however it was performed on less inclined events that in this study.

3.3.3 Phenomenological description of the Angular Distribution Function

Thanks to all the previous asymmetry descriptions, we can build a phenomenological model to describe the angular distribution function (ADF) of the signal amplitude within the footprint.

Our model can be decomposed as

$$f^{\mathrm{ADF}}(\omega, \eta, \alpha, l; \delta\omega, \mathcal{A}) = \frac{\mathcal{A}}{l} f^{\mathrm{GeoM}}(\alpha, \eta, \mathcal{B}) \ f^{\mathrm{Cerenkov}}(\omega, \delta\omega) \ , \tag{3.40}$$

where $\mathcal{A}$ is a free parameter adjusting the amplitude, l is the antenna longitudinal propagation distance and $f^{\mathrm{GeoM}}(\alpha, \eta, \mathcal{B})$ is given by

$$f^{\mathrm{GeoM}}(\alpha, \eta, \mathcal{B}) = 1 + \mathcal{B}\sin(\alpha)^2\cos(\eta) \ , \tag{3.41}$$

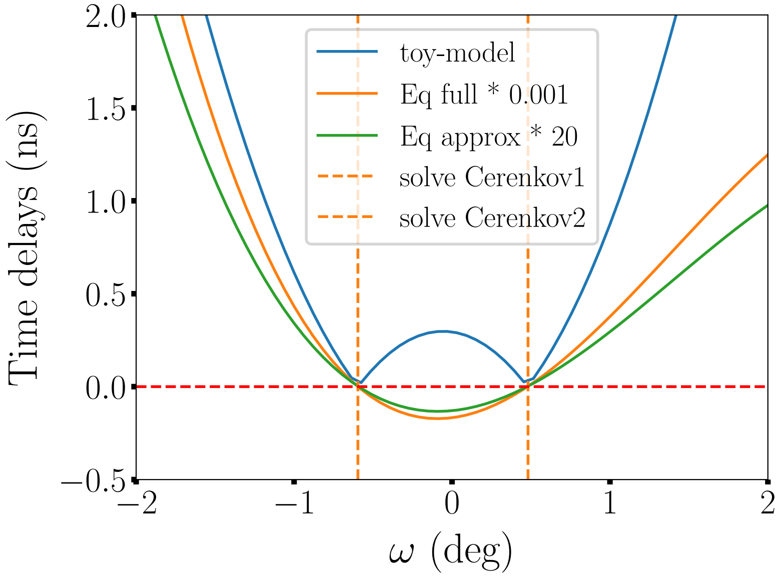

Figure 3.31: In blue, the toy-model time delays, in orange, Equation 3.38 and in green Equation 3.35. From the figure we can infer a quartic polynomial for Equation 3.38 and Equation 3.35 the roots of which exactly match the minima of the time delays. Vertical lines are the solutions of Equation 3.38 found by a basic dichotomy search.

where $\mathcal{B} \sim 0.005$ is the geomagnetic asymmetry strength (adjusted from simulations and in the range of expected value, see Section 2.1.2), α is the angle between the shower direction and the magnetic field, η is the antenna angle with respect to the $\vec{k} \times \vec{B}$ axis, introduced in Section 3.3.1.1.

We choose to model the Cerenkov pattern with a Lorentzian distribution, as for inclined showers it describes best the sharp rise observed close to the Cerenkov angle. The expression of $f^{\text{Cerenkov}}(\omega, \delta\omega)$ is given by

$$f^{\text{Cerenkov}}(\omega, \delta\omega) = \frac{1}{1 + 4\left[\frac{(\tan(\omega)/\tan(\omega_{\text{C}}))^2 - 1}{\delta\omega}\right]^2} \,, \tag{3.42}$$

where ω is the antenna angle from the shower direction, ω_{C} is a the Cerenkov angle computed from the model presented in Section 3.3.2.4 and $\delta\omega$ is a free parameter describing the width of the Cerenkov cone.

All the variables used in this model can be written explicitly as a function of the shower direction $\vec{k}$

$$\begin{aligned}
\omega_i &= \mathrm{acos}\left(\vec{k}\cdot\vec{x}_i\right) \ , \\
l_i &= \vec{k}\cdot\vec{x}_i \ , \\
\eta_i &= \mathrm{atan}\left(\vec{y}_i^{\,\mathrm{sp}}/\vec{x}_i^{\,\mathrm{sp}}\right) \ , \\
\alpha &= \mathrm{acos}\left(\vec{k}\cdot\vec{B}\right) \ ,
\end{aligned} \tag{3.43}$$

where $\vec{x}_i$ is the antenna position with respect to the shower source and $\vec{x}_i^{\,\mathrm{sp}}$, $\vec{y}_i^{\,\mathrm{sp}}$ are the antenna coordinates in the shower plane defined as the projections on $\vec{k}\times\left(\vec{k}\times\vec{B}\right)$ and $\vec{k}\times\vec{B}$. Note however, that the ADF model does not depend on the shower core position, which makes it usable as well for up-going EAS with no core on the ground. Therefore, it provides a great handle for the reconstruction of the shower direction of propagation.

3.3.4 Validation

In this section I present the comparison between the ADF model and the amplitude distribution from simulated data. This treatment is performed with the array configuration of Figure 3.32, where each branch of the star shape is given for clarity a specific colour corresponding to an angle η. The *Star-Shape* layout allows us to detail each asymmetry effect on the data with the corresponding model component.

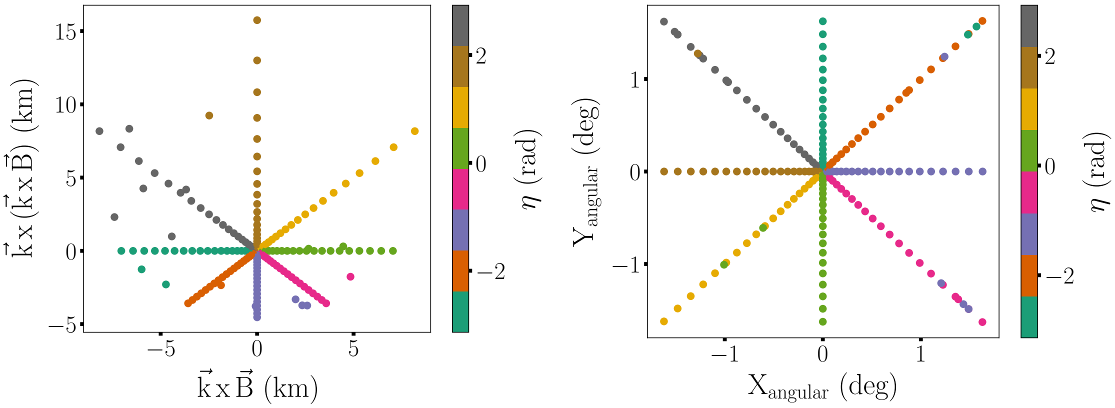

Figure 3.32: *Star-Shape* array configuration with a colour code for each branch. *Left:* Shower plane, the ellipsoid shape is due to the high inclination of the studied EAS: azimuth 180°, zenith 92.92°, primary proton of energy 3.94 EeV. *Right:* Angular plane, by definition of the *Star-Shape* array, the antennas position are symmetrical within a circular pattern.

Here only the amplitude term $\mathcal{A}$ and the Cerenkov width $\delta\omega$ are adjusted so that the model matches the data best, while the true direction is used, and $X_{\max}$ taken as the emission point source.

3.3.4.1 Geomagnetic correction

Figure 3.33 displays the results of the signal amplitude distribution model along the $\vec{k} \times \vec{B}$ axis. Along this specific axis, the geomagnetic excess is expected to create an asymmetry between antennas of positive and negative η values. The model takes this effect into account via Equation 3.41. The relative amplitude difference between positive and negative η values is slightly larger in the model (see right panel of Figure 3.33). Which shows that the geomagnetic effect is slightly over-estimated. The absolute difference between data and model is commented in Section 3.3.4.3.

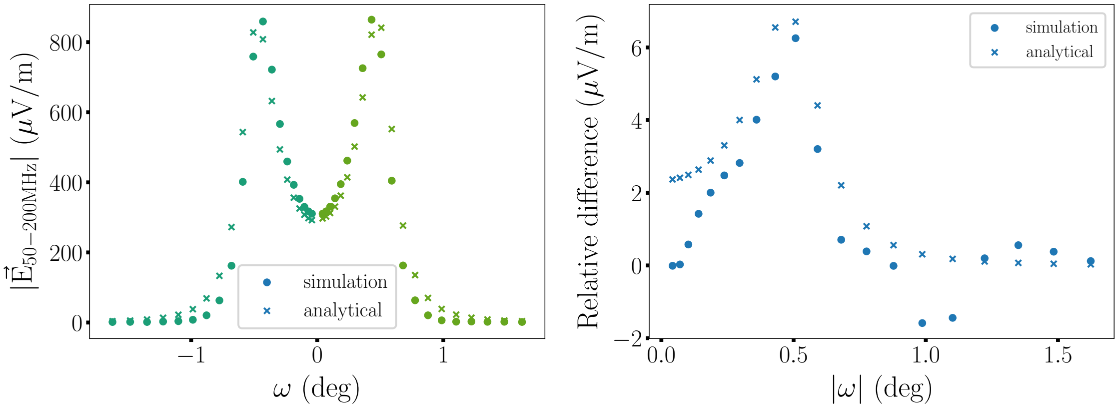

Figure 3.33: *Left:* Illustration of the signal amplitude distribution model for antennas along the $\vec{k} \times \vec{B}$ axis. *Right:* Relative amplitude difference between antennas with positive and negative η values, displayed as a function of the absolute ω value to ease the reading. Due to the geo-magnetic asymmetry antennas with same $|\omega|$ value, have different amplitudes. Signals computed for a EAS with azimuth 180°, zenith 92.92°, primary proton of energy 3.94 EeV.

3.3.4.2 Early-late correction

Figure 3.34 shows the signal amplitude distribution along the $\vec{k} \times \vec{k} \times \vec{B}$ axis, where the early-late effect is expected to be the strongest for inclined configurations. In our model this asymmetry is described through the $\mathcal{A}/l$ term in Equation 3.40. The maximal amplitude of the early peak is clearly larger than the late one and this asymmetry is correctly reproduced with our model. The absolute difference between the model and the data is commented in Section 3.3.4.3.

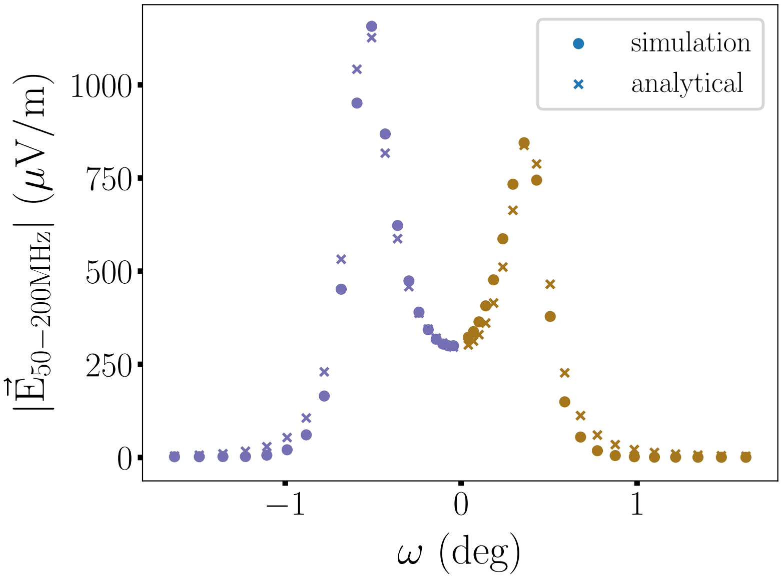

Figure 3.34: Illustration of the early-late effect. Purple antennas are considered as early since they receive the signal before the brown late antennas. The early antennas display a larger signal amplitude than the late ones. The effect is correctly reproduced by the model. Signals computed for a EAS with azimuth 180°, zenith 92.92°, primary proton of energy 3.94 EeV.

3.3.4.3 Cerenkov correction

Figure 3.35 displays the signal amplitude distribution along the $\vec{k} \times \left(\vec{k} \times \vec{B}\right)$ axis. As for the early-late effect we expect the Cerenkov asymmetry to be the strongest along this axis, since the difference of optical path between early and late antennas is then maximal. The red dotted vertical lines correspond to the standard Cerenkov angle computed as in Equation 3.27 and the purple and brown dotted vertical lines corresponds to the Cerenkov angle computed with the model described in Section 3.3.2.4. The standard Cerenkov angle computation fails to accurately reproduce both the early and the late angle values, but the model presented in Section 3.3.2.4 does reproduce correctly the Cerenkov angles. However, it clearly appears in the simulated data that the width of the Cerenkov cone is asymmetric with larger width for early antennas. This effect is not reproduced by the model as we use the same parameter $\delta\omega$ for all antennas, see Equation 3.42. This effect is the main cause of

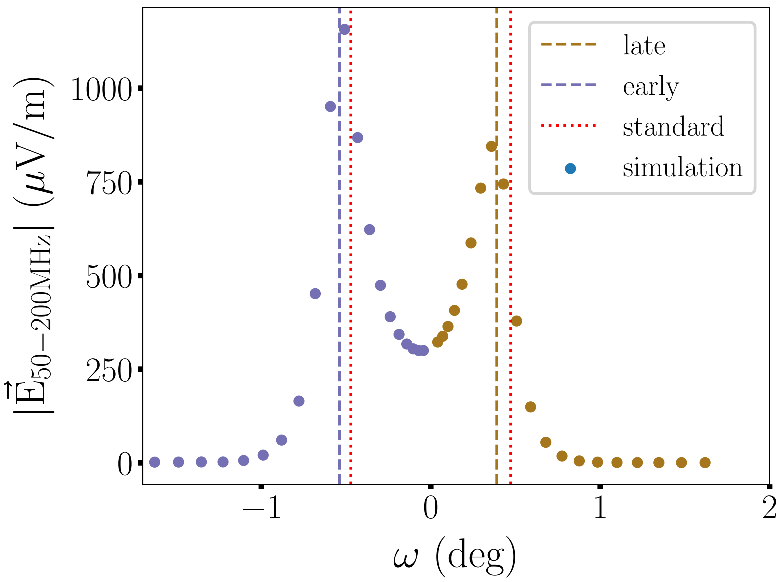

Figure 3.35: Cerenkov asymmetry effect, where early antennas corresponds to $\omega < 0$ and late antennas correspond to $\omega > 0$. The standard Cerenkov angle (red dotted vertical lines) does not match the positions, corresponding to the maxima of the signal amplitude distribution. However, the Cerenkov model of Section 3.3.2.4, reproduces accurately the position of the Cerenkov angles. Signals computed for an EAS with azimuth 180°, zenith 92.92°, primary proton of energy 3.94 EeV.

absolute difference between the model and the data, and will require further studies.

3.3.4.4 Global fit

Finally Figure 3.36 (left panel) shows the signal amplitude distribution for the whole array (dots) with the model from Section 3.3.3 (crosses). We can see that the model does not exactly reproduce the positions of each data point but the general trend is correctly described (see the right panel of Figure 3.36 for an estimation of the difference simulation/model). The main source of error stems from the angular description of the Cerenkov pattern of Equation 3.42. In particular in this model the width of the angle is taken as a free parameter and is symmetrical with respect to the Cerenkov angles, which is obviously not the case in the simulated data. This effects has not been investigated yet, although it is likely linked (as the peak positions) to the different refractive indices for early and late paths.

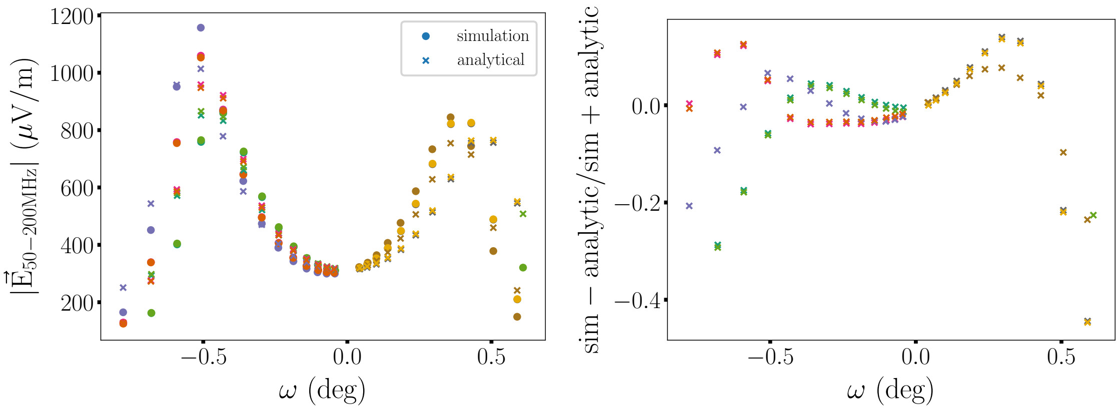

Figure 3.36: *Left:* Illustration of the full signal amplitude distribution for antennas above $5\sigma_{\mathrm{Amp}} = 110\,\mu\mathrm{V/m}$ as in the simulation trigger conditions. The model correctly describes the general trend but fails to accurately reproduce the exact value of the simulation data. Signals computed for a EAS with azimuth 180°, zenith 92.92°, primary proton of energy 3.94 EeV. *Right:* Display of the residuals computed as (simulation − model)/(simulation − model).

We developed an analytical model called ADF to describe the signal amplitude distribution in the footprint as a function of the angular positions of the antennas with respect to the shower direction. Even though the model does not exactly reproduce the data points, it allows us to correctly describe the trend of the signal amplitude for very inclined EAS, taking into account all asymmetries effects.

3.4 Reconstruction procedure

In Section 3.2 we have seen how the position of the emission point along the shower axis can be extracted from the wavefront shape. In Section 3.3 we have seen how the amplitude pattern can be described with a model depending highly on the direction of propagation of the shower. I present in this section how these two models are implemented in a general reconstruction process, which allows us to determine the arrival direction.

3.4.1 Principles

The reconstruction of the arrival direction consists in determining a point (the source emission) on the EAS path and a vector along this path (the shower direction), determined from the shower core. In practice, the reconstruction follows three steps: first a plane wave reconstruction is used in order to reduce the parameter space, then the emission source position is determined within the spherical reconstruction and finally, the amplitude profile is fitted with the ADF model. In this study, we focus on the development of a working reconstruction procedure for very inclined EAS. Details regarding the optimisation and the treatment of calibration errors and systematics are not considered here. Therefore all antennas have identical errors for timing and amplitude. Finally all the minimisation processes are achieved numerically.

3.4.1.1 The plane wave reconstruction

The plane wave reconstruction relies on a plane wavefront model of the trigger times. It is an approximate description of the wavefront (see Section 3.2) but it is fast to reconstruct. This reconstruction is used to efficiently reduce the parameter space from all the directions on the sphere down to a cone of a few square degrees.

The procedure relies on the comparison of the relative trigger times from one antenna to another. The minimisation function is given by

$$f(\theta,\phi) = \sum_{i,j}^{N_{\mathrm{antenna}}} \left[\frac{c}{n}(t_i - t_j) - \vec{k}(\theta,\phi)\cdot(\vec{x}_i - \vec{x}_i)\right]^2 , \tag{3.44}$$

where θ and ϕ are the zenith and azimuth of the shower direction, N_{antenna} is the total number of antennas of the array, t_k is the trigger time of the antenna A_k and $\vec{x}_k$ its position. There are only two free parameters in this reconstruction. With this reconstruction we reduce the parameter space of the zenith down to $\theta_{\mathrm{true}} \in [\theta_{\mathrm{plan}} - 2°, \theta_{\mathrm{plan}} + 2°]$ and the azimuth $\phi_{\mathrm{true}} \in [\phi_{\mathrm{plan}} - 1°, \phi_{\mathrm{plan}} + 1°]$. The range is computed so as to correspond roughly to 10 standard deviations on the azimuth and zenith error. The reduced parameter space is smaller for azimuth angle than for zenith because the large lateral extension of the footprint provides an excellent handle, while the zenith is constrained by the smaller difference of elevation among the antennas.

3.4.1.2 The spherical wave reconstruction

The spherical reconstruction detailed in Section 3.2.3.4 describes an isotropic emission originating from a point-like source.

The reconstruction procedure determines the best position of the point-source through the minimisation of the following function:

$$f(\theta, \phi, \rho, t_{\text{source}}) = \sum_{i}^{N_{\text{antenna}}} \left(\frac{c}{n_i}(t_i - t_{\text{source}}) \right. \\ \left. - \sqrt{(x_i - x_{\text{source}})^2 + (y_i - y_{\text{source}})^2 + (z_i - z_{\text{source}})^2} \right)^2 , \qquad (3.45)$$

with

$$x_{\text{source}} = \rho \cos(\phi) \sin(\theta) , \qquad (3.46)$$

$$y_{\text{source}} = \rho \sin(\phi) \sin(\theta) , \qquad (3.47)$$

$$z_{\text{source}} = \rho \cos(\theta) , \qquad (3.48)$$

where the values of ρ range from 1 km to 600 km. Thanks to the plane wave reconstruction, the reduced parameter space can be used to efficiently find the source emission position with the free parameters ρ, θ, ϕ and t_{source}.

The spherical wave reconstruction allows us to find one point along the direction of the shower axis. In order to reconstruct the arrival direction we need to find the direction along the shower path, which is provided by the signal amplitude distribution.

3.4.1.3 The ADF reconstruction

The final part of the reconstruction consists in fitting the amplitude profile of the EAS radiation footprint with the ADF model. For this purpose, we present the signal amplitude distribution in the frame defined in Section 3.3.1.1). The exact model of the angular amplitude distribution is based on the phenomenological approach detailed in Section 3.3.3. The reconstruction procedure starts from the point source reconstructed with the spherical wavefront model. Then the procedure optimises the arrival direction to minimise the difference between the ADF model and the amplitude pattern. The minimisation function reads

$$f(\theta, \phi, \delta\omega, \mathcal{A}; x_{\text{s}}, y_{\text{s}}, z_{\text{s}}) = \sum_{i}^{N_{\text{antenna}}} \left[A_i - f_i^{\text{ADF}}(\theta, \phi, \delta\omega, \mathcal{A}; x_{\text{s}}, y_{\text{s}}, z_{\text{s}}) \right]^2 , \qquad (3.49)$$

where $f_i^{\text{ADF}}(\theta, \phi, \delta\omega, \mathcal{A}; x_{\text{s}}, y_{\text{s}}, z_{\text{s}})$ is given by Equation 3.40 with all the angles computed with respect to the reconstructed position $(x_{\text{s}}, y_{\text{s}}, z_{\text{s}})$.

The free parameters of the minimisation are: the arrival direction θ, ϕ, the amplitude coefficient $\mathcal{A}$ related to the total shower energy and $\delta\omega$ the Cerenkov width.

This full reconstruction chain allows us to compute the arrival direction as well as the emission point of the EAS. The three subsequent reconstruction procedures extract the information contained inside the wavefront and the signal amplitude distribution.

3.4.2 Performances

I will present in this section the reconstruction performances obtained on the *Star-Shape* simulation set. Three experimental scenarii are investigated[1]: a scenario where the data from simulations are directly used for the reconstruction (labelled *NoNoise*), a second scenario (labelled *Aggressive*) where a random gaussian error with a standard deviation of $\sigma_\mathrm{t} = 5\,\mathrm{ns}$ is added on the trigger times and signal amplitudes randomised with a gaussian distribution of $\sigma_\mathrm{A} = 10\%$. This mimics the experimental uncertainties of the calibration of the setup. Finally we implement a third scenario (labelled *Conservative*), similar to *Aggressive* but with a $\sigma_\mathrm{A} = 20\%$ gaussian standard deviation error on the signal amplitudes, corresponding to a worst case scenario for the amplitude calibration.

Similarly to the study presented in Section 2.2, the simulations of the *Star-Shape* set requires at least 5 antennas to be selected with a signal amplitude above $5\,\sigma_\mathrm{A} = 5{\times}22\,\mu\mathrm{V/m}$, where the noise is computed as in Section 2.3.

The accuracy of the reconstruction of the arrival direction is measured in terms of angular distance between the true direction and the reconstructed one and given by

$$\cos(\psi) = \cos(\theta_\mathrm{rec})\cos(\theta_\mathrm{true}) + \cos(\phi_\mathrm{rec} - \phi_\mathrm{true})\sin(\theta_\mathrm{true})\sin(\theta_\mathrm{rec})\ , \tag{3.50}$$

where ψ is the angular distance, θ_rec is the reconstructed zenith, θ_true is the true zenith, ϕ_rec is the reconstructed azimuth and ϕ_true is the true azimuth.

3.4.2.1 Parameter space reduction: plane reconstruction

For the plane wave reconstruction (see Section 3.4.1.1), only the trigger times and the antenna coordinates (in the ground frame) are provided as input for the reconstruction.

We present in Figure 3.37 histograms of the angular distance ψ. The good angular accuracy achieved is due to the layout: a star-shaped layout symmetrical around the shower core. The main issue with the plane wave model is that the reconstruction only fits a part of the wavefront curvature. With this array layout, the wavefront curvature is fully symmetrical, thus avoiding the asymmetrical bias inherent for plane reconstruction. Tests performed on the *ToyMode*l layout have shown for example, that such level of performances

---

[1] The models for the experimental noises and systematics are preliminary and only represent a first step in the development of the reconstruction method. Further dedicated studies are needed and envisioned.

cannot be achieved with the plane reconstruction on a realistic layout. Apart form that, a small degradation of the accuracy is observed for *Aggressive* and *Conservative* scenarii, as expected.

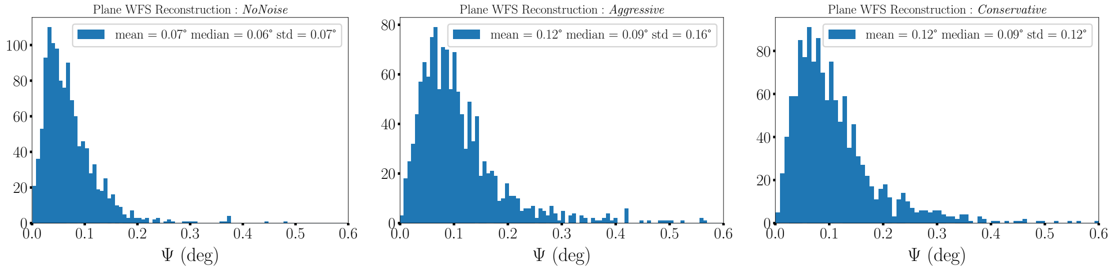

Figure 3.37: Histograms of the angular distances ψ plane wave reconstruction for the *Star-Shape* simulation set. *Left:* for the *NoNoise* scenario. *Middle:* for the *Aggressive* scenario. *Right:* for the *Conservative* scenario.

The performances achieved by the plane reconstruction does not allow us to reach a sufficient accuracy on the arrival direction but the simplicity of the method and the fast execution of the procedure provides an efficient parameter space reduction. Although for more realistic array layouts, a larger parameter space may need to be defined for the next stages of the reconstruction.

3.4.2.2 Longitudinal and lateral source position: spherical reconstruction

For the spherical reconstruction (see Section 3.4.1.2), we use the outputs of the plane wave reconstruction (see Section 3.4.1.2) in addition to the trigger times and antenna coordinates (similarly to the plane wave reconstruction).

Figure 3.38 (left column) displays the distributions of the lateral error (i.e. error on the distance in the orthogonal direction to the true shower axis) on the reconstructed source position with respect to the $X_{\max}$ position. The lateral positions for all experimental scenario are extremely well reconstructed with average errors of few tens of meters.

Figure 3.38 (right column) shows the distributions of the longitudinal error (i.e. error along the shower axis) on the reconstructed source position, again using the $X_{\max}$ position as a reference. The longitudinal positions are less accurately reconstructed, with an average error of $\sim -20\%$ and a standard deviation of $\sim 20\%$ in the *ideal* case. This discrepancy can be explained by the sensitivity of the model to a lateral deviation compared to a longitudinal one.

To illustrate this, let us consider a configuration where a vertical radiation from an EAS

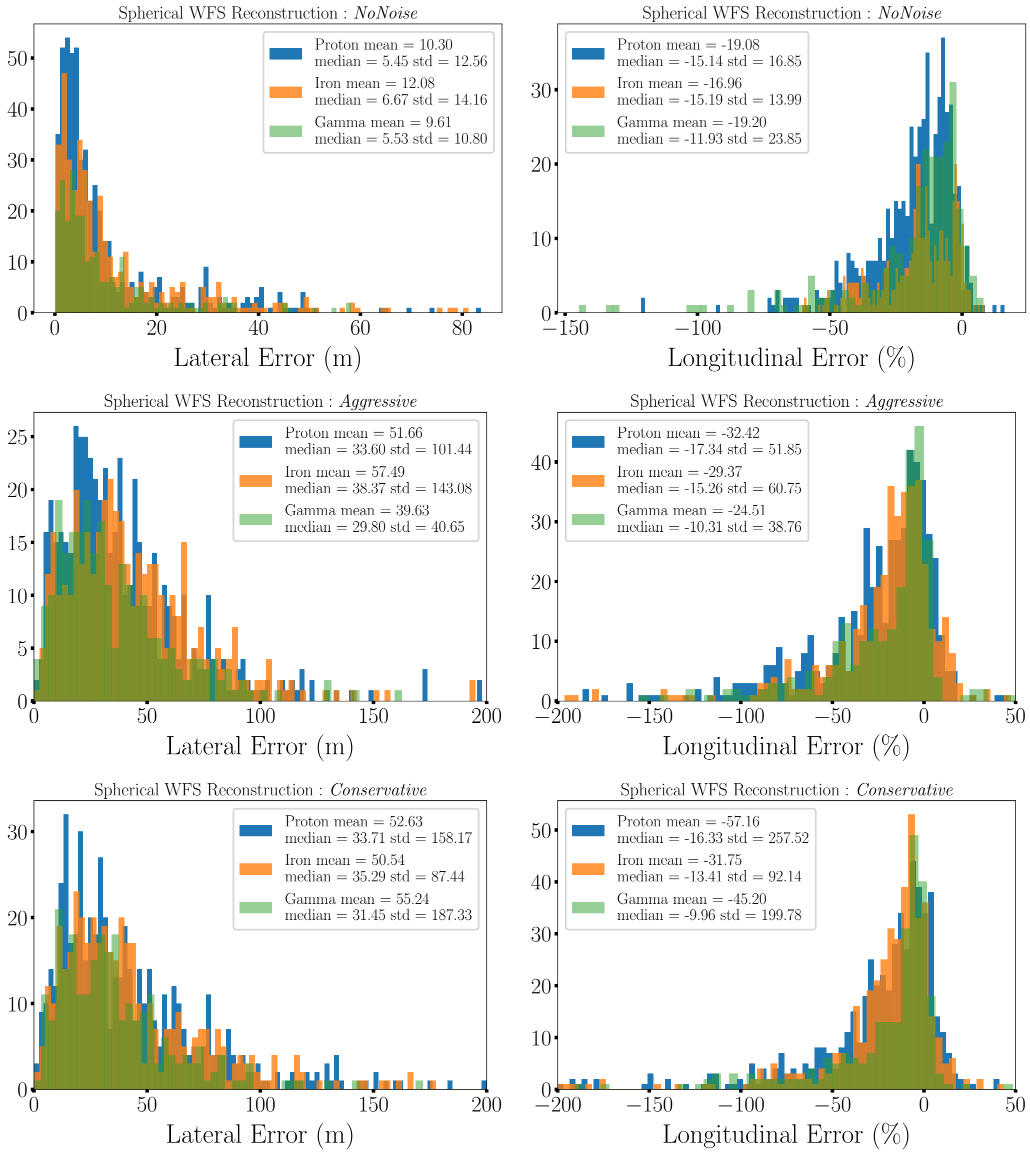

Figure 3.38: *Left column:* Distributions of the lateral error on the reconstruction of the source position. *Right column:* Distributions of the relative longitudinal error on the reconstruction of the source position. For the *Star-Shape* simulation set and with a reference set at $X_{\max}$. *Top:* For the *NoNoise* scenario. *Middle:* For the *Aggressive* scenario. *Bottom:* For the *Conservative* scenario.

hits the ground after a propagation of $l_0 = 60\,\mathrm{km}$ as depicted on Figure 3.39, with an antenna 1 located on the shower core and a second antenna 2, located 3 km away.

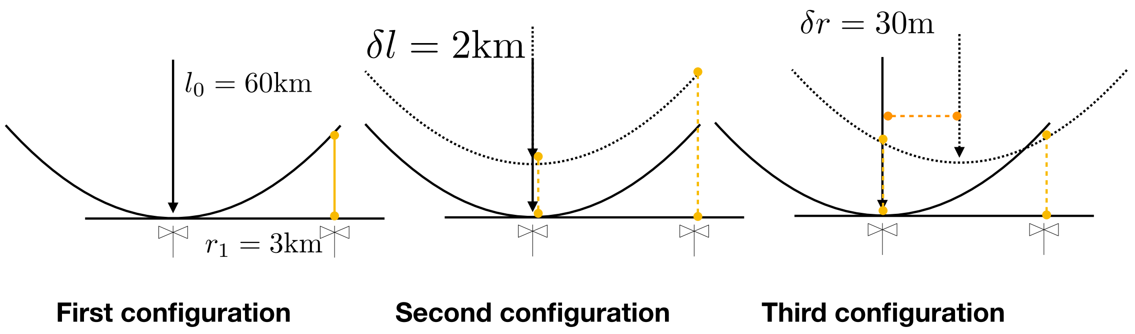

Figure 3.39: Sketch of the effect on the wavefront of a longitudinal and lateral deviation of the source, with respect to the first configuration.

In the point-like source emission, the trigger times t_i of the antennas are given by

$$t_0 = \frac{n}{c} l_0 \ , \tag{3.51}$$

$$t_1 = \frac{n}{c}\sqrt{r_1^2 + l_0^2} \ , \tag{3.52}$$

where r_i is the lateral distance to the shower axis and n is assumed to be identical for the two paths for this demonstration, since in this configuration, the optical paths are similar ($l_0 \gg r_1$ meaning that $l_1 = \sqrt{l_0^2 + r_1^2} \approx l_0 + \mathcal{O}(75\,\mathrm{m})$). The relative time delay between these two antennas then reads

$$\delta t = t_1 - t_0 = \frac{n}{c}\left(\sqrt{r_1^2 + l_0^2} - l_0\right) \approx 250\,\mathrm{ns} \ . \tag{3.53}$$

Let us now consider a second configuration where the emitting point is 2 km farther from ground. The time delay is then given by

$$\delta t = t_1 - t_0 = \frac{n}{c}\left[\sqrt{r_1^2 + (l_0 + \delta l)^2} - l_0 - \delta l\right] \approx 242\,\mathrm{ns} \ , \tag{3.54}$$

This offset between these two values is 8 ns only, just above the GRAND timing resolution of 5 ns. Finally, the third configuration is given for an emission laterally translated by $\delta r = 30\,\mathrm{m}$, resulting in a time delay of

$$\delta t = t_1 - t_0 = \frac{n}{c}\left[\sqrt{(r_1 + \delta r)^2 + (\delta r^2 + l_0^2)} - \sqrt{\delta r^2 + l_0^2}\right] \approx 255\,\mathrm{ns} \ , \tag{3.55}$$

again comparable to the initial delay within the GRAND timing resolution of 5 ns. Consequently a 30 m lateral offset in the source position induces a similar time difference

(5 ns) plausible as a 2 km longitudinal offset. From this simple example, it seems that the observed difference between the lateral reconstruction and the longitudinal one in Figures 3.38, originates from a similar effect and that, by construction, a better resolution on the longitudinal position of the source is hardly achievable.

Another interesting feature on Figure 3.38 is the negative offset in the mean longitudinal reconstructed position. The source emission appears to be reconstructed systematically further away from the detector than the X_{max} position. This is expected in the emission models, as the electric-field is related to the derivative of the vector-potential which, for typical particle profiles of EAS, are larger before the X_{max} position (see Sections 2.1.1 and 2.1.2).

Figure 3.40 (left column) displays the absolute longitudinal error as a function of the number of antennas N_{ant}, where a dispersion of the absolute longitudinal error is observed for events with a low number of antennas, below $N_{\text{ant}} = 15$. This effect comes from the minimisation procedure which is less accurate for a low number of antennas. Besides, events with a low number of antennas are often low energy events hence those events have a higher numerical noise that can impact the computation of the trigger time, i.e. shift the Hilbert envelope.

Similarly, Figure 3.40 (right column) also shows the relative longitudinal error as a function of the zenith angle of the shower. The reconstruction of less inclined events, in particular above $\theta = 115°$, leads to a larger relative longitudinal error. This is expected, since less inclined events are closer (see Figure 3.41 left column) hence at equivalent absolute longitudinal error, those less inclined events present a larger relative error. In addition, less inclined events are more difficult to model with a point-like emission, implying that the wavefront will appear more hyperbolical than spherical. Regarding the reconstruction of the arrival direction, the relative longitudinal error is more critical than the absolute error, as the computation of the ADF will be proportional to the absolute error since it is an angular description (see Section 3.3.3).

Figure 3.41 (right column), shows the evolution of the relative longitudinal error as function of the primary energy. The fact that we are able to reconstruct quite accurately events with $\gtrsim 15$ antennas only, indicates that we are able to reconstruct low energy events. Otherwise, no peculiar trend is observed with energy.

In the following, we define two quality cuts: an antenna number lager than $N_{\text{ant}} = 15$ and events below $\theta = 115°$, the percentage of events passing the cuts is about $\sim 57\%$. Figure 3.42, shows the lateral error and relative longitudinal error, after these quality cuts have been applied. The cuts efficiently reject the badly reconstructed events for both lateral and longitudinal distances but the impact on the average and standard deviation of the lateral error is rather limited. On the other hand, it reduces the average relative longitudinal error by a factor of two almost.

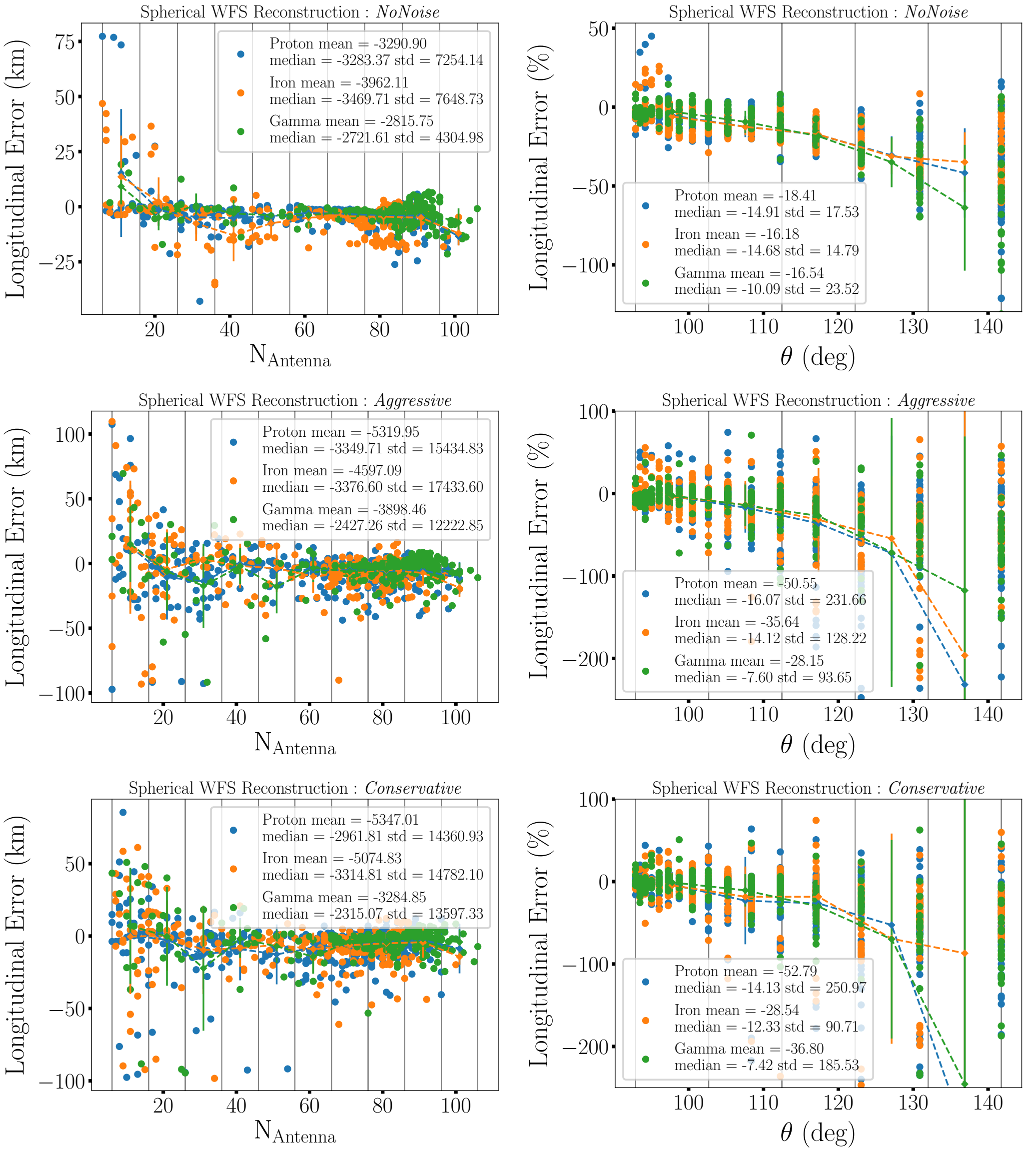

Figure 3.40: *Left column:* Absolute longitudinal error on the reconstruction of the source position as function of the number of antennas N_{ant}. *Right column:* Relative longitudinal error on the reconstruction of the source position as function of the zenith angle θ. For the *Star-Shape* simulation set and with a reference set at $X_{\max}$. *Top:* For the *NoNoise* scenario. *Middle:* For the *Aggressive* scenario. *Bottom:* For the *Conservative* scenario.

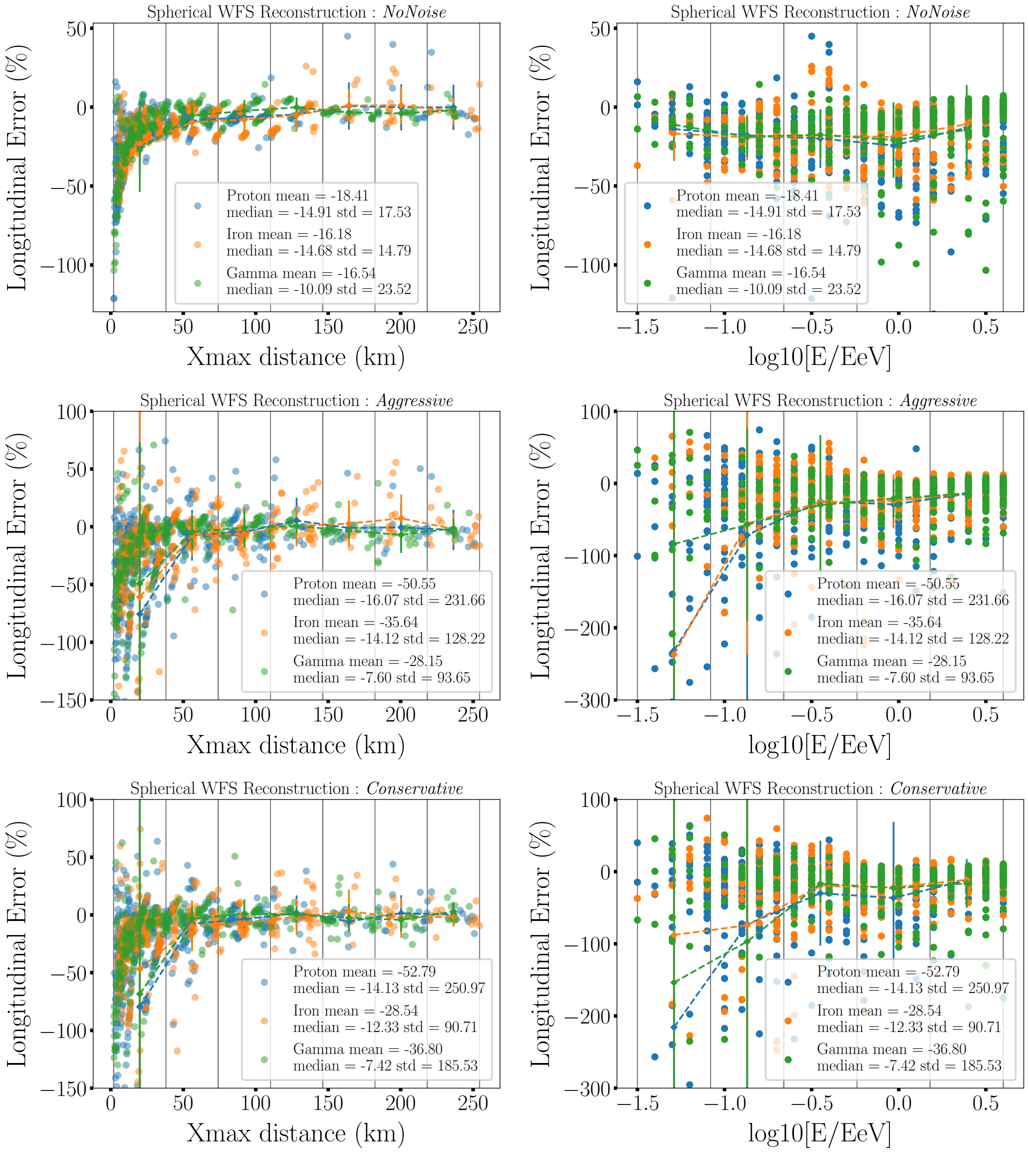

Figure 3.41: *Lef column:* Relative longitudinal error on the reconstruction of the source position as function of the $X_{\max}$ distance to the shower core. *Right column:* Relative longitudinal error on the reconstruction of the source primary energy. For the *Star-Shape* simulation set and with a reference set at $X_{\max}$. *Top:* For the *NoNoise* scenario. *Middle:* For the *Aggressive* scenario. *Bottom:* For the *Conservative* scenario.

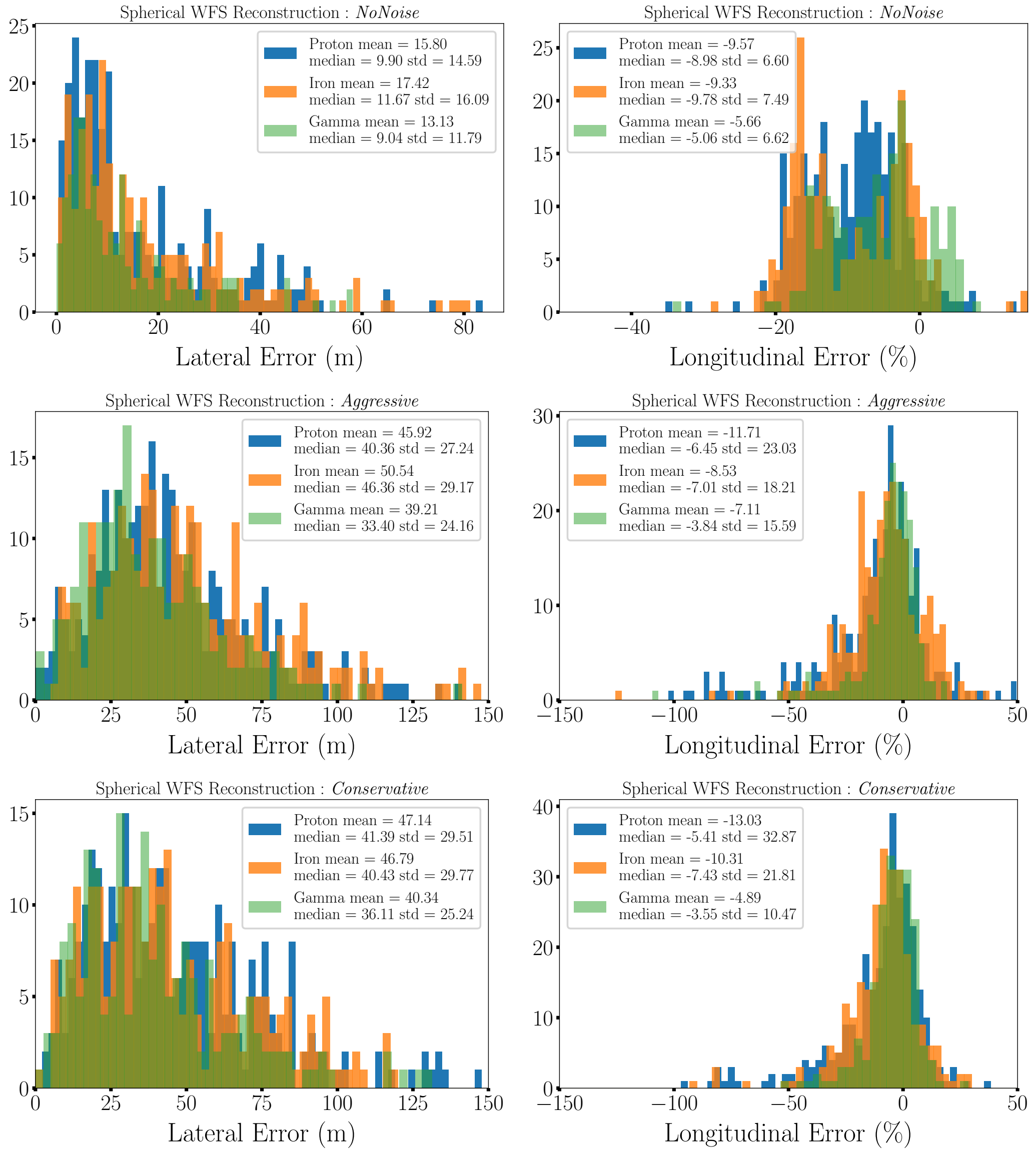

Figure 3.42: Same as Figure 3.38, with the quality cuts: $N_{\mathrm{ant}} > 15$ and $\theta < 115°$. In the *NoNoise* scenario, 711 events out of 1242 triggered events pass the cuts, corresponding to a percentage of 57.2%. In the *Agressive* scenario, 744 events out of 1307 triggered events pass the cuts, corresponding to a percentage of 56.9%. And finally, in the *Conservative* scenario, 749 events passes the cuts out of 1329 triggered events, corresponding to a percentage of 56.4%.

In conclusion to this paragraph, the spherical reconstruction has proven to be extremely accurate on the reconstruction of the lateral position of the source. Even though the results on the reconstruction of the longitudinal position are less accurate, this statement has to be mitigated by taking into account the long propagation distances, up to more than 450 km, for the more inclined events, limiting the relative errors within $10 - 20\,\%$.

3.4.2.3 Arrival direction: ADF reconstruction

For the ADF reconstruction, the reconstruction outputs of the plane wave fit and the spherical fit are provided, in addition to the amplitude maxima and the antenna coordinates. Unlike the plane wave reconstruction output, which is solely used to reduce the parameter space for the fitting procedure, the spherical output is a key ingredient. Indeed, the accuracy of the ADF reconstruction will depends on the accuracy of the source reconstruction. The following results are all obtained with the quality cuts defined in Section 3.4.2.2: $N_{\mathrm{ant}} > 15$ and $\theta \leqslant 115°$, for which about $\sim 43\%$ of the events are rejected. Additionally convergence criteria are also applied, rejected about $\sim 30\%$ of the remaining events.

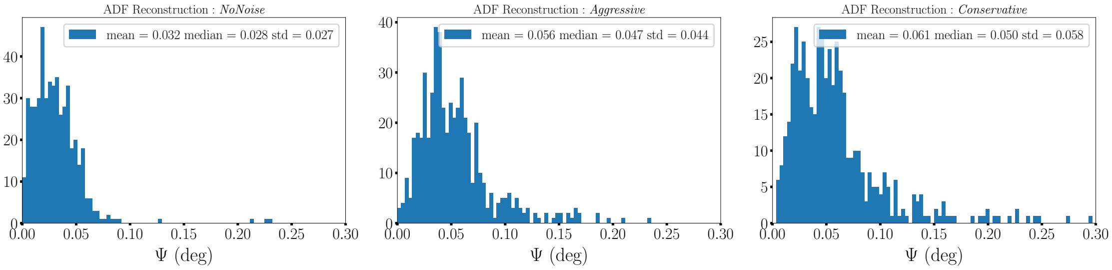

Figure 3.43: Distributions of the angular distance ψ for the *Star-Shape* simulation set. *Left:* for the *NoNoise* scenario. *Middle:* For the *Aggressive* scenario. *Right:* For the *Conservative* scenario.

Figure 3.43 presents the distribution of the angular distance ψ. The good accuracy on the reconstruction of the arrival direction, with an average error of $\langle\psi\rangle = 0.032 - 0.061°$ and a standard deviation $\mathrm{STD}(\psi) = 0.027 - 0.058°$ between the three experimental scenarii, proves that the ADF model enables us to reach an arc-minute level. A small, regular and expected degradation of the results is observed within the the *Aggressive* and *Conservative* experimental scenarii, yet well below the initial target.

Figure 3.44 shows, the angular distance as function of the residuals squared res^2 and the zenith angle θ of the shower. No specific trend is observed, within the parameter ranges set by the quality cuts, showing a rather stable reconstruction method.

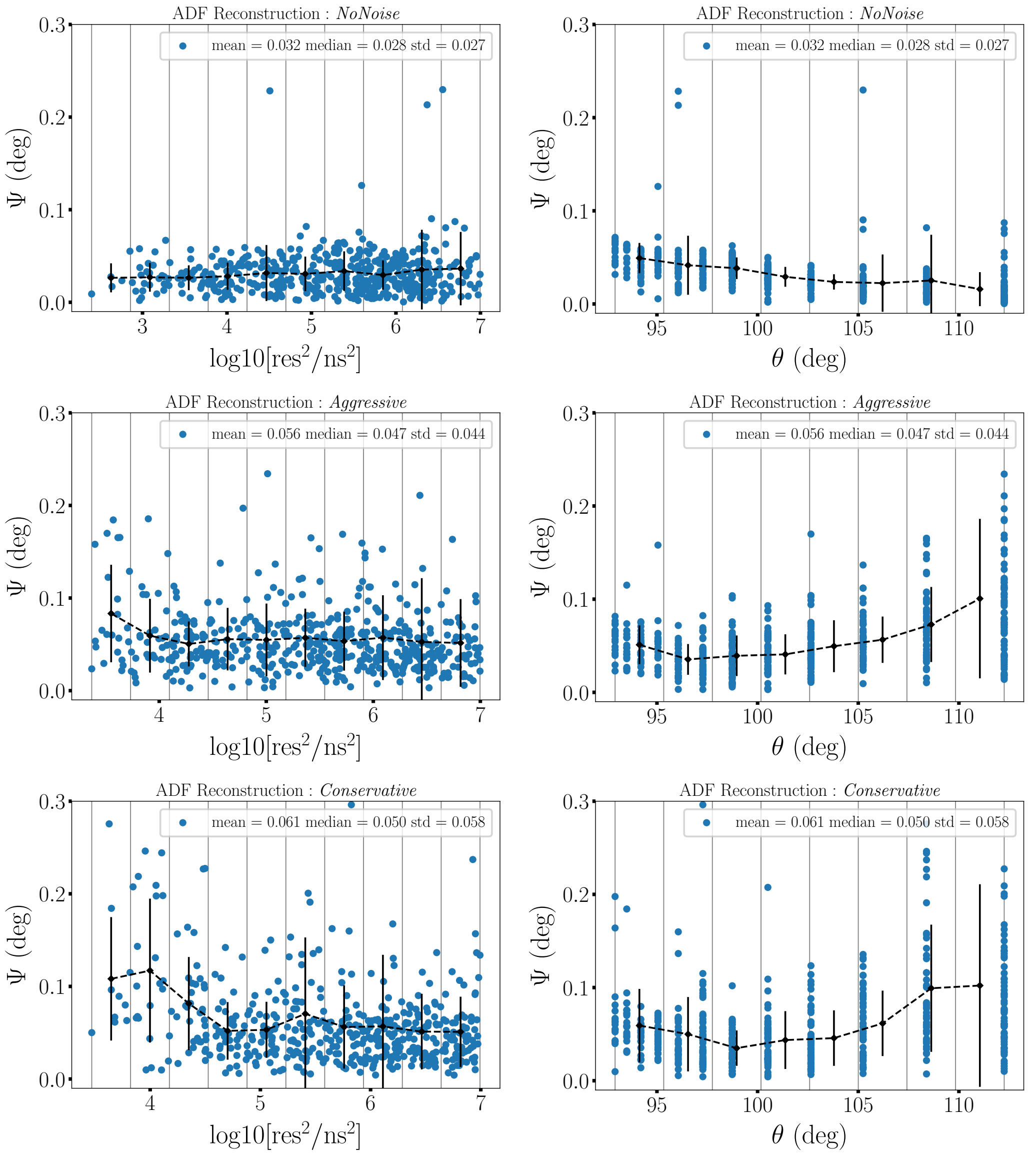

Figure 3.44: Angular distances ψ for the Star-Shape simulation set. *Left column:* As a function of the residuals. *Right column:* As a function of the zenith angle θ. *Top:* For the *NoNoise* scenario. *Middle:* for the *Aggressive* scenario. *Bottom:* For the *Conservative* scenario.

The ADF reconstruction achieves a resolution on the reconstruction of the arrival direction better than the targeted resolution of 0.1°. It however has to be noted that these results are obtained on the *Star-Shape* simulation set, which corresponds to an ideal layout. This encouraging results is validated on realistic array layouts in the next section.

3.4.2.4 Reconstruction on the GP300 layout

GP300 is an engineering array planned in the staged approach of the GRAND project (see Section 2.1.4 for more details). It is designed for the detection of very inclined EAS (from 95° to 110°), hence it is a benchmark for the reconstruction of these very inclined showers. In this part, I present the performances of our reconstruction methods on a set of simulated EAS, on the GP300-like layout.

Layout and simulation set: Figure 3.45 displays the GP300-like layout with the real topography of one of the candidate sites in Western China. The array is characterised by a hexagonal layout pattern of 215 antennas with a 1 km spacing and an infill of 72 antennas with a 500 m step, allowing for the detection of EAS at a lower energy than the usual energy targeted by GRAND. The simulation set consists in about 1500 simulated EAS, induced by Protons, Iron nuclei and Gamma rays with energies ranging between 0.1 EeV and 3.98 EeV with logarithmic bins, and the arrival directions are set with a random azimuth angle (ϕ) (comprised between 0° to 360°) and a zenith angle (θ) between 92.92° and 117°, with logarithm bins in $1/\cos(\theta)$. The shower core positions are randomly drawn over an area larger than the array.

Emission point reconstruction: Figure 3.46, shows the histograms of the lateral error and the longitudinal error on the reconstruction of the source emission, with respect to the X_{max} position. The reconstructed lateral position, presents on average an error of about 125 m (a median of about 45 m) with a standard deviation of about 150 m, for all three primaries. These large values results from sub-populations of events with lateral errors around 200 m and 400 m. On the other hand, the reconstruction of the longitudinal position, appears much less dispersed, with a relative average error of about 3% and a standard deviation of about 9%, for all three primaries.

The large dispersion of the results of the lateral reconstruction clearly depends on the distance to the source. Figure 3.47 (left column) shows the evolution of the lateral error with the distance to X_{max}, the sub-population observed in the left column of Figures 3.46, is explained here by the distance of the source, where far away events are much less accurately reconstructed. It is worth noting that the largest lateral errors, remain however below

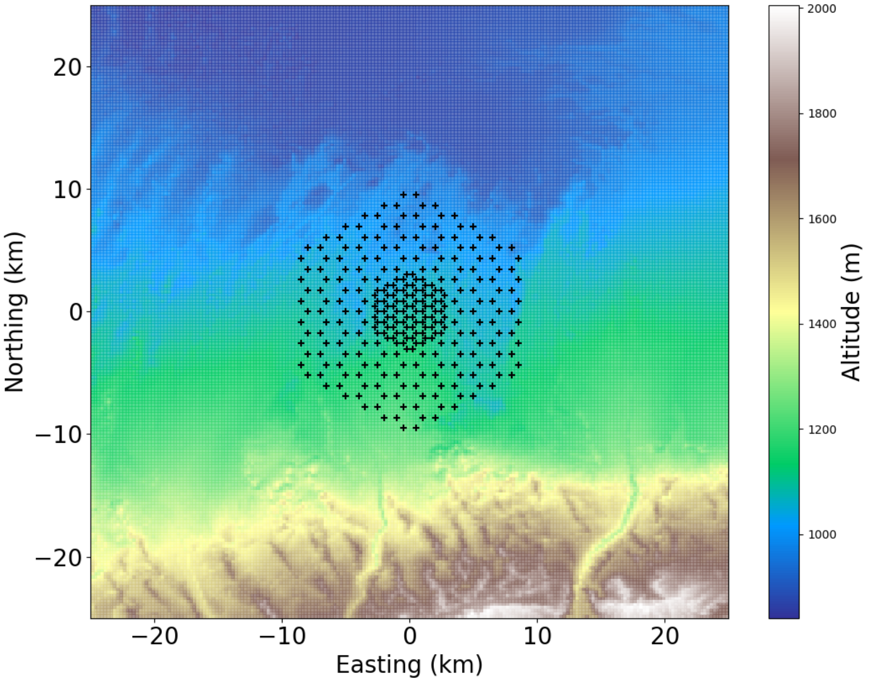

Figure 3.45: Layout of a GP300-like array taking into account the topography at one of the selected site, located in Western China. Hexagonal layout pattern of 215 antennas with a 1 km step and an infill of 72 antennas with a 500 m step.

~ 750 m for event seen at distances up to 250 km, which corresponds to an overall relative error of about $\sim 0.3\%$.

The longitudinal reconstruction accuracy depends much less on the distance to $X_{\max}$ than the lateral reconstruction, as displayed on Figure 3.47 (right column), however, the scattering appears to reduce with the distance to $X_{\max}$. The global trend is rather identical as the one displayed for the *Star-Shape* simulation set (see Figure 3.41 left column).

Figure 3.48 (left column), presents the evolution of the longitudinal error as a function of the number of triggered antennas. No dispersion as large as in the *Star Shape* simulation set is observed. This is due to the fact that the low energy events, with fewer antennas, are much less detected since the layout is not centered on the shower core. Without these low energy events, the dispersion at low antenna number is suppressed.

Finally, Figure 3.48 (right column), also present the longitudinal error dependency on the

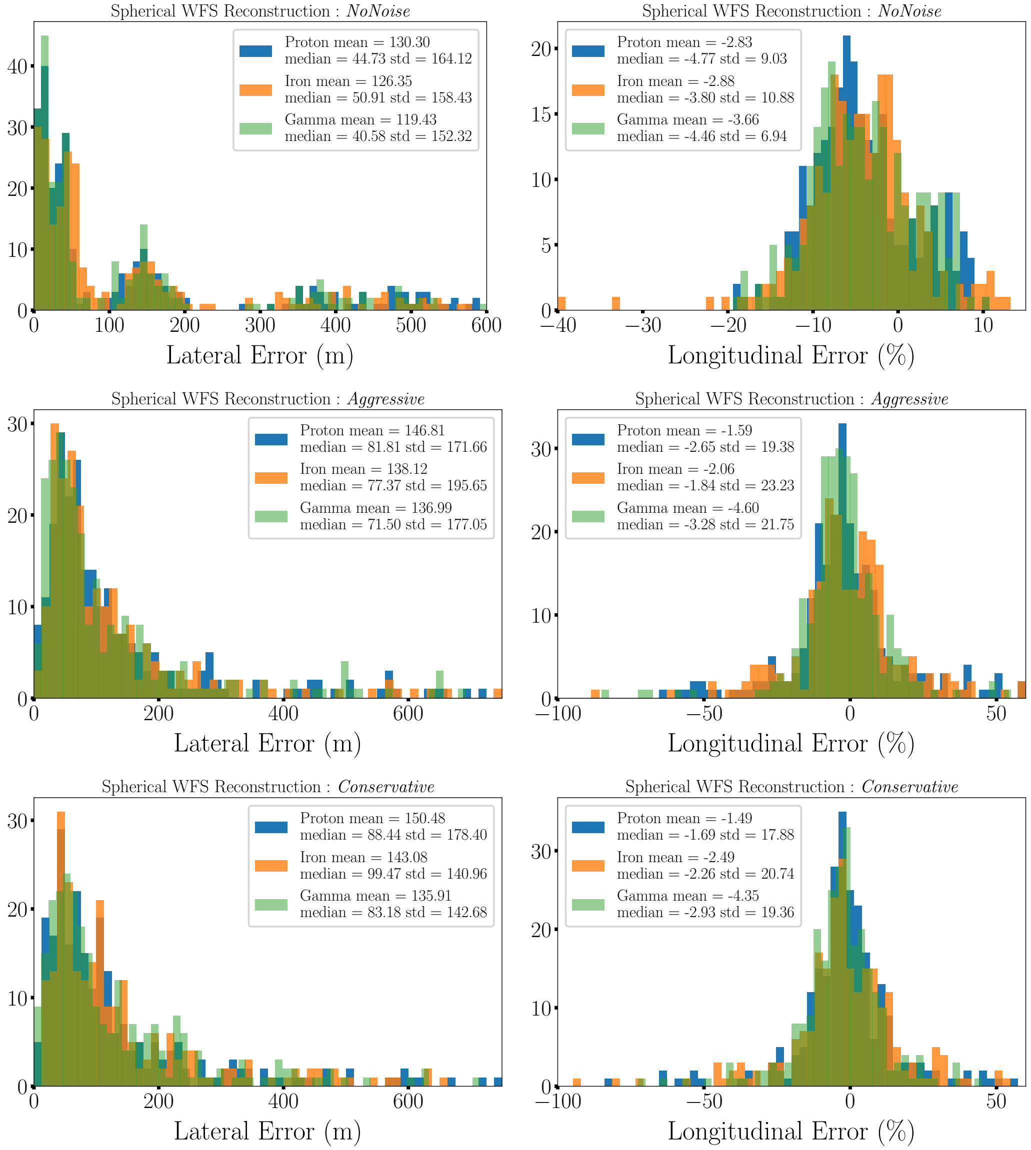

Figure 3.46: *Left column:* Distributions of the lateral error on the position of the emission source. *Right column:* Distributions of the longitudinal error on the position of the emission source. *Top:* For the *NoNoise* scenario. *Middle:* For the *Aggressive* scenario. *Bottom:* For the *Conservative* scenario. For the GP300-like layout.

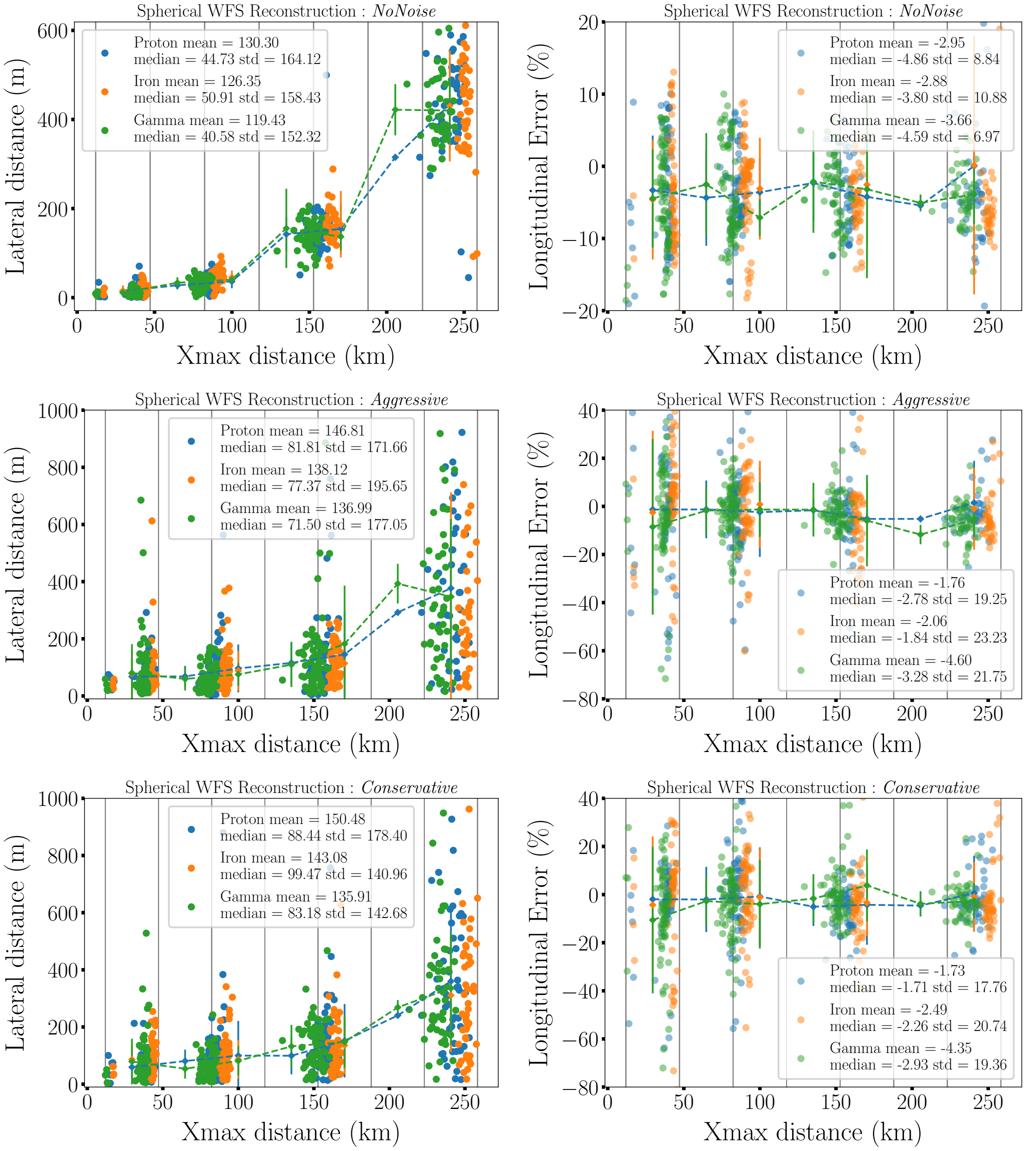

Figure 3.47: *Left column:* Lateral distance to the shower axis as function of distance to $X_{\max}$. A clear degradation of the lateral reconstruction accuracy is seen at large distance to $X_{\max}$, however this absolute lateral error remains below 700 m for events seen more than 250 km away. *Right column:* Longitudinal error as a function of the distance to $X_{\max}$. *Top:* For the *NoNoise* scenario. *Middle:* For the *Aggressive* scenario. *Bottom:* For the *Conservative* scenario. For the GP300-like layout. The $X_{\max}$ distance values cluster around positions related to the original set of zenith values.

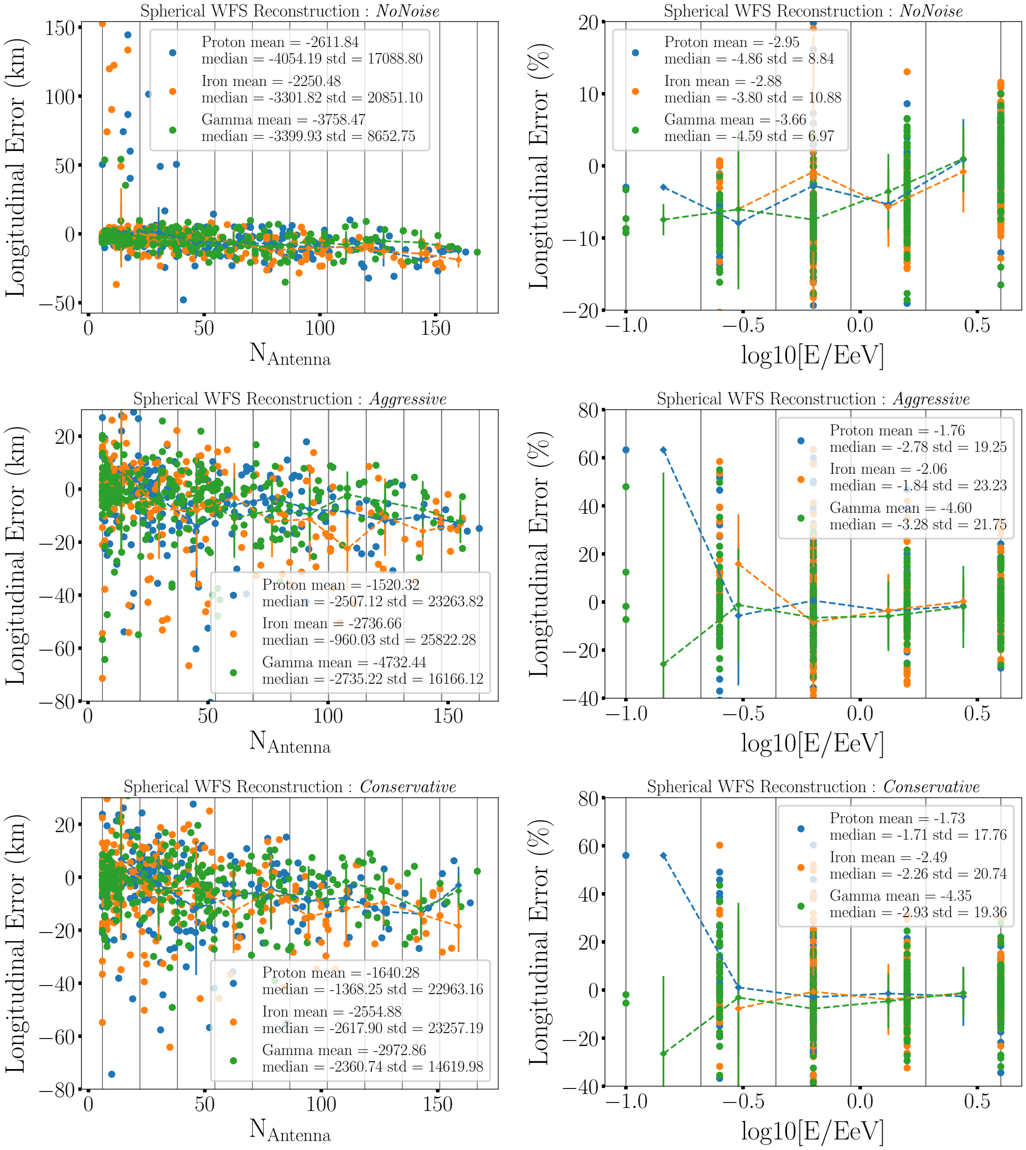

Figure 3.48: *Left column:* Distribution of the relative longitudinal error as a function of the number of antenna triggered. *Right column:* Distribution of the relative longitudinal error as a function of the shower energy. *Top:* For the *NoNoise* scenario. *Middle:* For the *Aggressive* scenario. *Bottom:* For the *Conservative* scenario. For the GP300-like layout.

shower energy, where a similar trend as in the *Star Shape* simulation set is observed (see Figure 3.41 right column).

Arrival direction reconstruction: Figure 3.49 presents the histogram of the angular distance between the reconstructed and the true arrival direction of the shower, with on average an error $\langle\psi\rangle = 0.088 - 0.1°$, with a standard deviation of about $\mathrm{STD}(\psi) = 0.06 - 0.081°$.

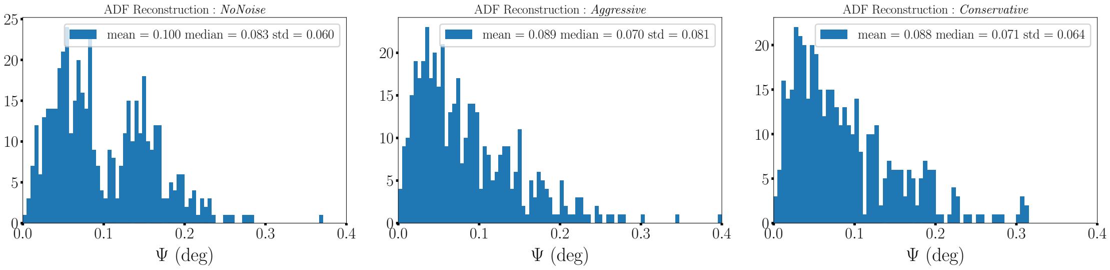

Figure 3.49: Distributions of the angular distances ψ for the GP300-like layout. *Left:* For the *NoNoise* scenario. *Middle:* For the *Aggressive* scenario. *Right:* For the *Conservative* scenario.

In the *NoNoise* scenario, two populations of errors are visible in this histogram, one at an error of about 0.05° and another one at roughly 0.15°. These two populations stem from the sub-populations observed for the lateral error (see Figure 3.46 left column).

Similarly a dependance to the distance to X_{max} can be found, as displayed on Figure 3.50 (left column), hence on the zenith angle (see Figure 3.50 right column). Contrarily to the *Star-Shape* array, where the layout is centered on the events and fully contains the footprint, these very inclined events appear not to be fully contained in the GP300 layout which also translate into a large number on average of antenna, as presented on Figure 3.51 (left column).

Figure 3.51 (right column), also shows the energy dependancy on the angular accuracy. No particular trend can be seen: the reconstruction remain stable regarding this parameter.

The reconstruction performances on the realistic GP300 array layout, overall matches the expectations with an angular accuracy of about 0.1° on average. Some degradations are observed as expected when increasing the level of realism, in particular for the point emission reconstruction and will be investigated in further works. Note that these last results are preliminary.

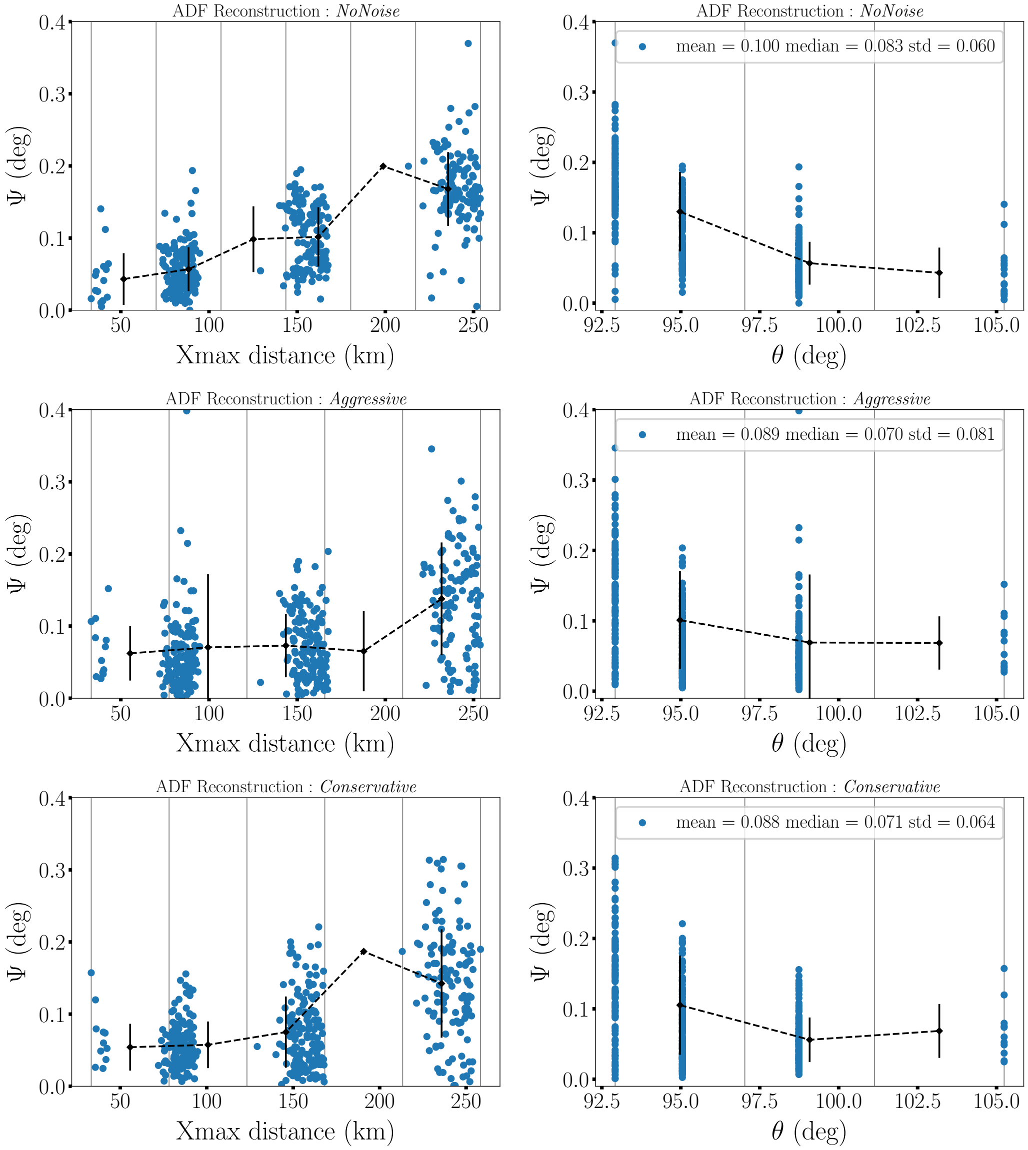

Figure 3.50: *Left column* Angular distance ψ as a function of the distance to $X_{\max}$. *Right column:* Evolution of the angular distance ψ with the zenith angle θ. *Top:* For the *NoNoise* scenario. *Middle:* For the *Aggressive* scenario. *Bottom:* For the *Conservative* scenario. For the GP300-like layout.

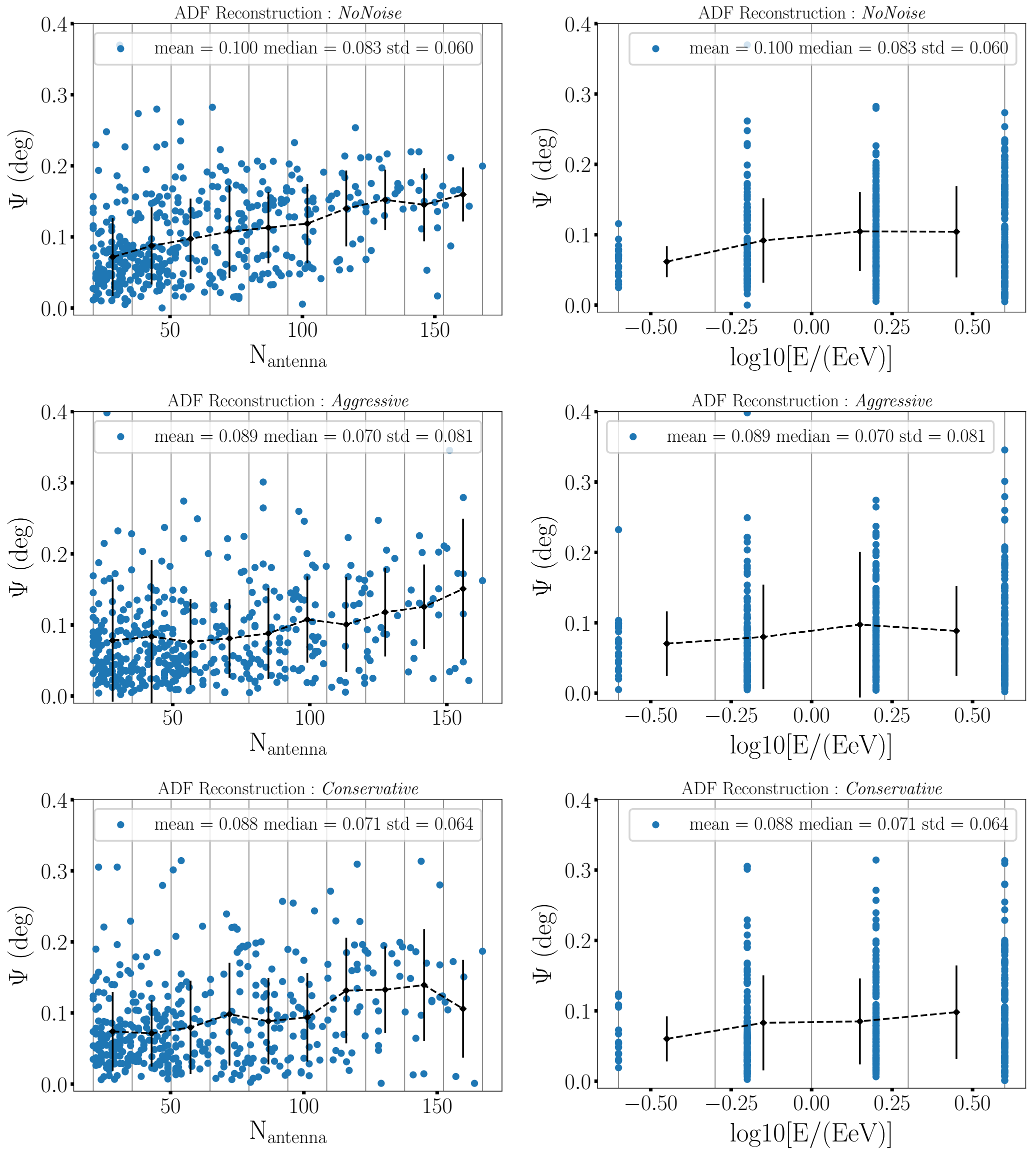

Figure 3.51: *Left column:* Angular distance ψ as a function of the number of triggered antennas N_{ant}. *Right:* Energy dependancy of the angular distance ψ. *Top:* For the *NoNoise* scenario. *Middle:* For the *Aggressive* scenario. *Bottom:* For the *Conservative* scenario. For the GP300-like layout.

3.5 From source position to X_{max} reconstruction

With the spherical model, we can reconstruct the position of the emission source with a high accuracy on the lateral position and a precision between $10-20\,\%$ on the longitudinal position with respect to X_{max}. The translation of these performances in terms of X_{max} reconstruction naturally follows. In a first step we study this reconstruction on the *Star-Shape* simulation set and then apply the same method to the realistic layout of the *GP300* simulation set.

It is straightforward to compute the equivalent grammage from the physical position of the source emission, if we possess enough information on the local atmosphere. Starting from the reconstructed position, we integrate the density value along the propagation direction up to the injection point following Equation 2.24. The injection point can be written as function of the shower zenith θ and azimuth ϕ in the X_{max} referential as

$$x_{\mathrm{injection}} = -L_{\mathrm{injection}} \cos(\phi) \sin(\theta) \ , \tag{3.56}$$

$$y_{\mathrm{injection}} = -L_{\mathrm{injection}} \sin(\phi) \sin(\theta) \ , \tag{3.57}$$

$$z_{\mathrm{injection}} = -L_{\mathrm{injection}} \cos(\theta) = 100\,\mathrm{km} \ , \tag{3.58}$$

where $L_{\mathrm{injection}}$ is the longitudinal distance between the X_{max} position and the injection point, given by

$$L_{\mathrm{injection}} = (R_{\mathrm{Earth}} + z_{X_{\mathrm{max}}}) \cos(\theta) + \sqrt{\Delta} \ , \tag{3.59}$$

$$\text{with } \Delta = (R_{\mathrm{Earth}} + z_{X_{\mathrm{max}}})^2 \cos(\theta)^2 + (100\,\mathrm{km} - z_{X_{\mathrm{max}}})(100\,\mathrm{km} + z_{X_{\mathrm{max}}} + 2R_{\mathrm{Earth}}) \ , \tag{3.60}$$

with R_{Earth} the Earth radius and $z_{X_{\mathrm{max}}}$ the altitude of the X_{max} point, we recall that the atmosphere begins at an altitude of 100 km in Aires (see Section 2.1.3.2 and sketch on Figure 3.52).

Figure 3.53 shows the histograms of the reconstructed grammage. Interestingly, a distinction can be made between the different primaries. In particular the expected trend between the average grammage of Gamma, Proton and Iron primaries is observed for the energy ranges considered here: the deepest average X_{max} corresponds to the Gamma primaries with $\langle X_{\mathrm{max}} \rangle \approx 740\,\mathrm{g.cm}^{-2}$, then follow the Proton primaries with $\langle X_{\mathrm{max}} \rangle \approx 630\,\mathrm{g.cm}^{-2}$ and finally the Iron primaries with $\langle X_{\mathrm{max}} \rangle \approx 530\,\mathrm{g.cm}^{-2}$, as expected.

Figure 3.54 (left column) displays the histograms of the difference between the true grammage from simulations and the reconstructed grammage called here *grammage error*. We observed an average difference of $\sim 120\,\mathrm{g.cm}^{-2}$ and with a standard deviation of about $\sim 70\,\mathrm{g.cm}^{-2}$ in the ideal case, mostly dominated by the outliers of the distribution. This offset may be explained by the fact that we do not reconstruct the particle $X_{\mathrm{max}}^{\mathrm{particle}}$ but

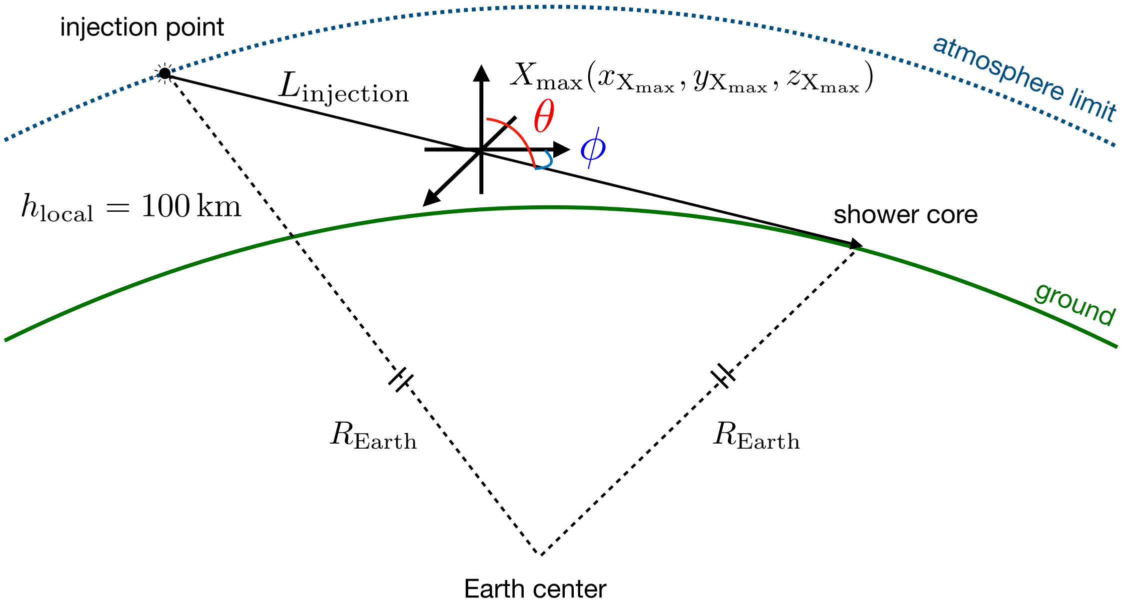

Figure 3.52: Sketch of the computation of the injection length $L_{\text{injection}}$, defined as the distance between the injection point at the upper limit of the atmosphere (100 km above ground) to the $X_{\max}$ location. In this computation the curvature of the Earth must be accounted for, since in the Aires simulations, the atmospheres is described as curved layers (see Section 2.1.3.2).

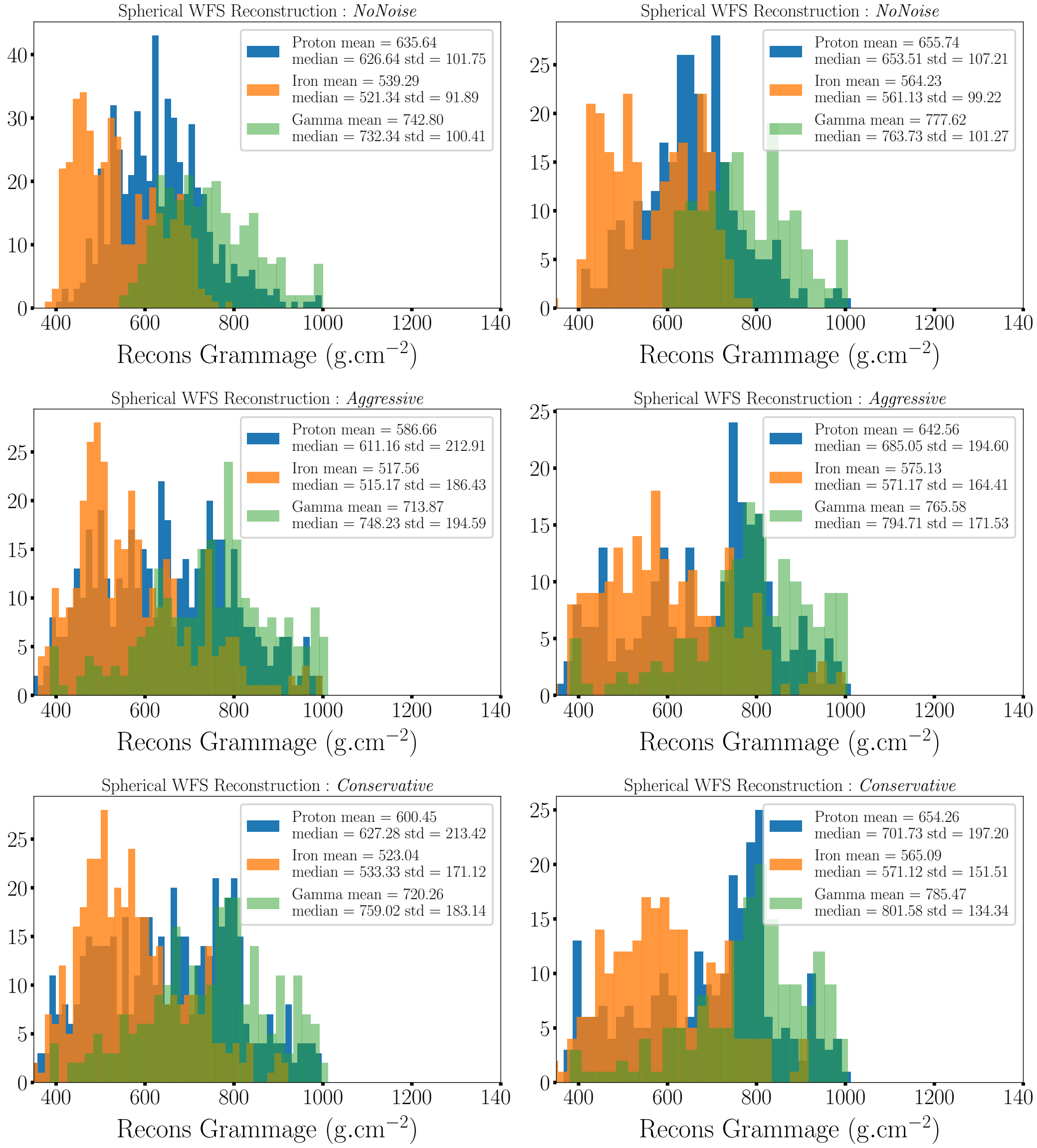

Figure 3.53: Distributions of the reconstructed grammage. *Left column:* without quality cuts. *Right column:* with quality cuts ($N_{\rm ant} > 15$ units and $\theta < 115°$). For the *Star-Shape* simulation set. *Top:* For the *NoNoise* scenario. *Middle:* For the *Aggressive* scenario. *Bottom:* For the *Conservative* scenario.

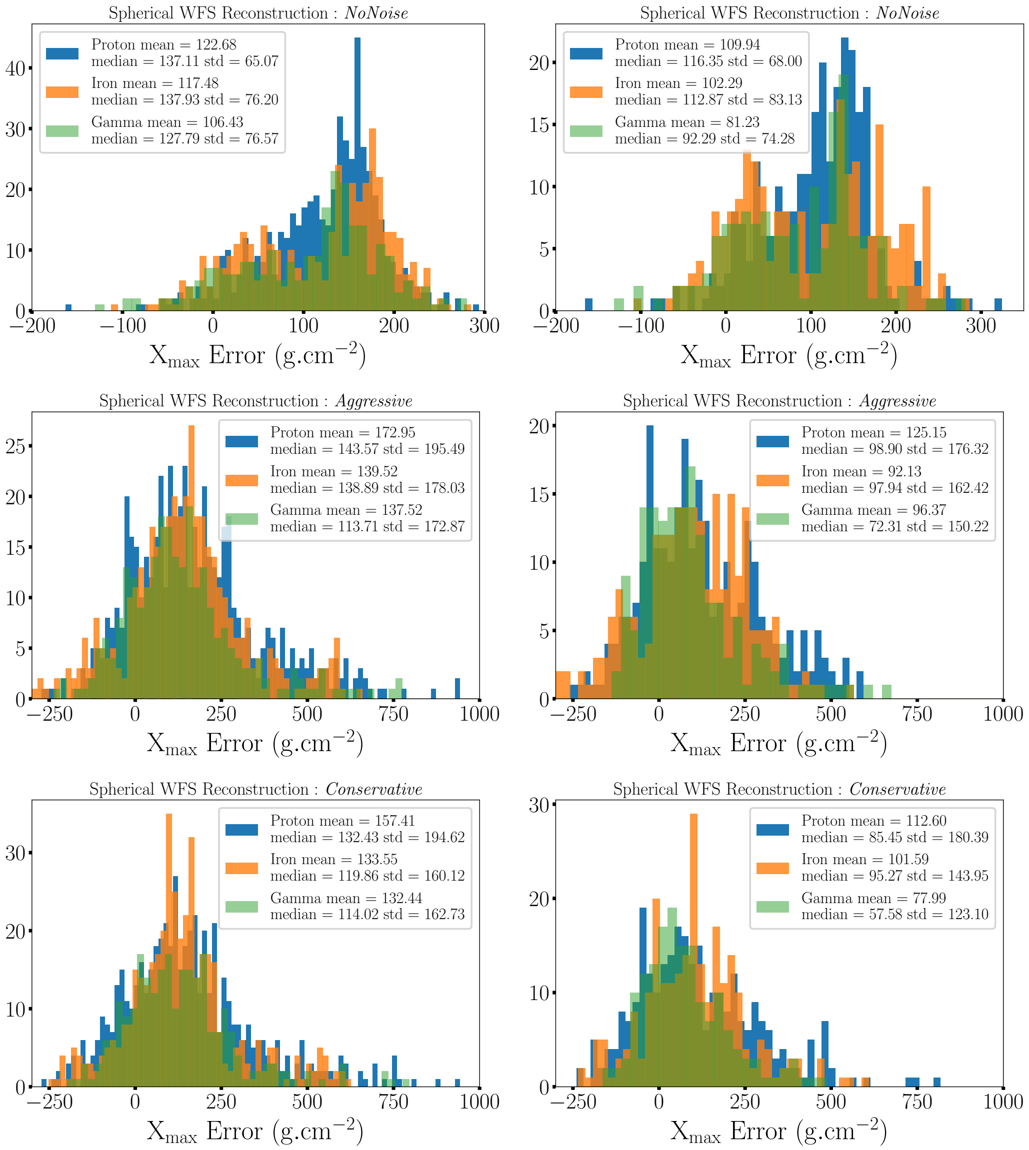

Figure 3.54: Distribution of the grammage error computed as the difference between the true grammage (from the simulation) and the reconstructed grammage. *Left column:* without quality cuts. *Right column:* with quality cuts ($N_{\text{ant}} > 15$ units and $\theta < 115°$). For the *Star-Shape* simulation set. *Top:* For the *NoNoise* scenario. *Middle:* For the *Aggressive* scenario. *Bottom:* For the *Conservative* scenario.

the radio $X_{\mathrm{max}}^{\mathrm{radio}}$, which from classical electrodynamics considerations can be expected to occur before the maximum of the particle is reached, when the derivative of the particle number is maximal (see Section 2.1.2 and in particular Equation 2.21). Figure 3.54 (right column) also displays the grammage error but with quality cuts applied, as defined in the previous Section 3.4.2.2 ($N_{\mathrm{ant}} > 15$ units and $\theta < 115°$). No changes is observed, except for the *Aggressive* and *Conservaitve* scenarii, where an improvement of both the average error and standard deviation is observed.

Figure 3.55, displays the reconstructed grammage as function of the energy. The results show the expected elongation rate with energy, in particular in the right column with the quality cuts where only the best reconstructed source positions are visible.

The spherical reconstruction allows us to estimate the source location of the radio emission. The X_{max} reconstruction from a direct comparison to the true X_{max} grammage, presents a resolution of $70\,\mathrm{g.cm^{-2}}$, with a significant bias of $\approx 120\,\mathrm{g.cm^{-2}}$ at best on the *Star-Shape* simulation set and need to be confirmed on a realistic layout.

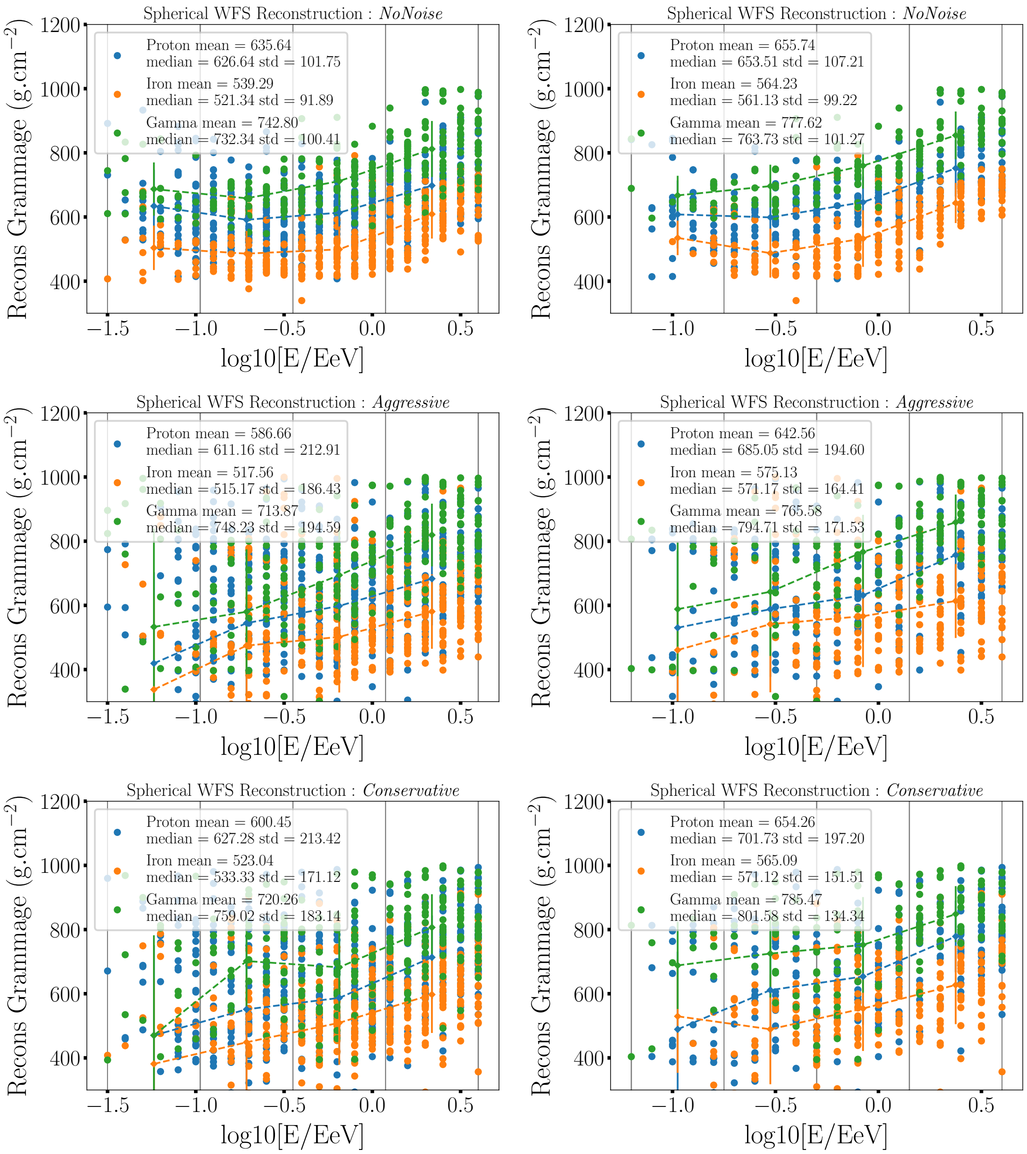

Figure 3.55: Reconstructed grammage as function of the primary energy. *Left column:* without quality cuts. *Right column:* with quality cuts ($N_{\text{ant}} > 15$ units and $\theta < 115°$).. or the *Star-Shape* simulation set. *Top:* For the *NoNoise* scenario. *Middle:* For the *Aggressive* scenario. *Bottom:* For the *Conservative* scenario.

3.5.1 GP300 $X_{\max}$ study

A similar analysis can be conducted on the GP300 simulation set.

Figure 3.56 (left column) presents the reconstructed grammage for the three primaries (protons, Iron nuclei and gamma rays). On average the three primaries can be distinguished, with mean reconstructed grammage values of $\sim 675\,\mathrm{g.cm^{-2}}$ for the Protons, $\sim 590\,\mathrm{g.cm^{-2}}$ for the Iron nuclei and $\sim 760\,\mathrm{g.cm^{-2}}$ for the gamma rays. However the large standard deviation does not allow for a robust statistical distinction. This is also confirmed with the comparison of the reconstructed grammage to the true grammage, as also displayed in Figure 3.56 (right column), with standard deviations above $100\,\mathrm{g.cm^{-2}}$.

However, it is interesting to note that the energy dependancy of the reconstructed grammage follows a trend consistent with the expected elongation rate (see Figure 3.57).

These results show that on a realistic GP300 layout, the grammage reconstruction is not accurate enough to conduct a precise primary composition study on GP300. However these results are preliminary and a detailed analysis on a realistic GRAND layout needs to be performed. In particular the level of precision could be sufficient to give an additional handle to discriminate between neutrino-induced EAS and cosmic-ray.

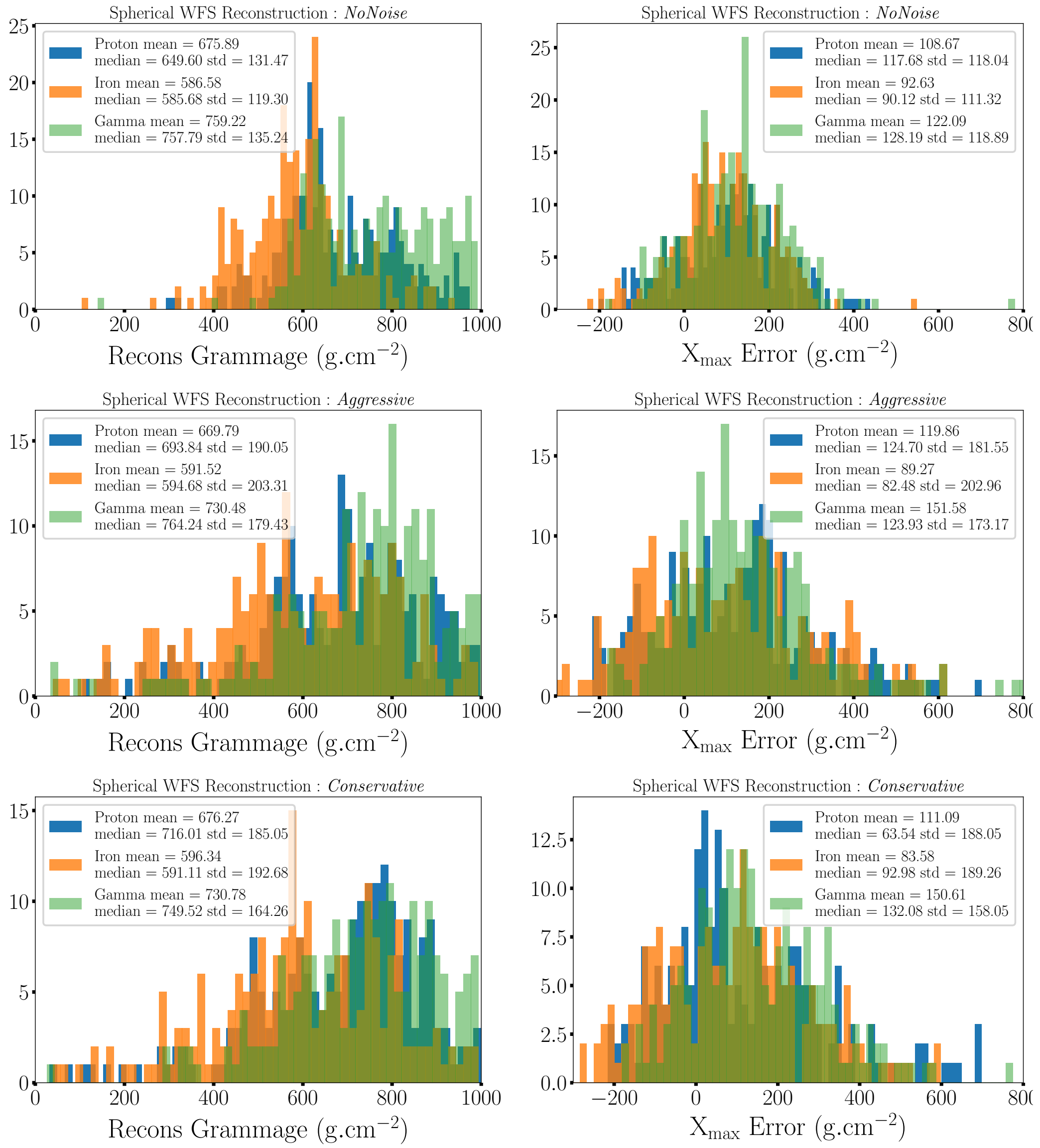

Figure 3.56: *Left column:* Distributions of the reconstructed grammage. *Right column :* Distributions of the grammage error, computed as the difference between the true gramme minus the reconstructed grammage. For the GP300-like layout. *Top:* For the *NoNoise* scenario. *Middle:* For the *Aggressive* scenario. *Bottom:* For the *Conservative* scenario.

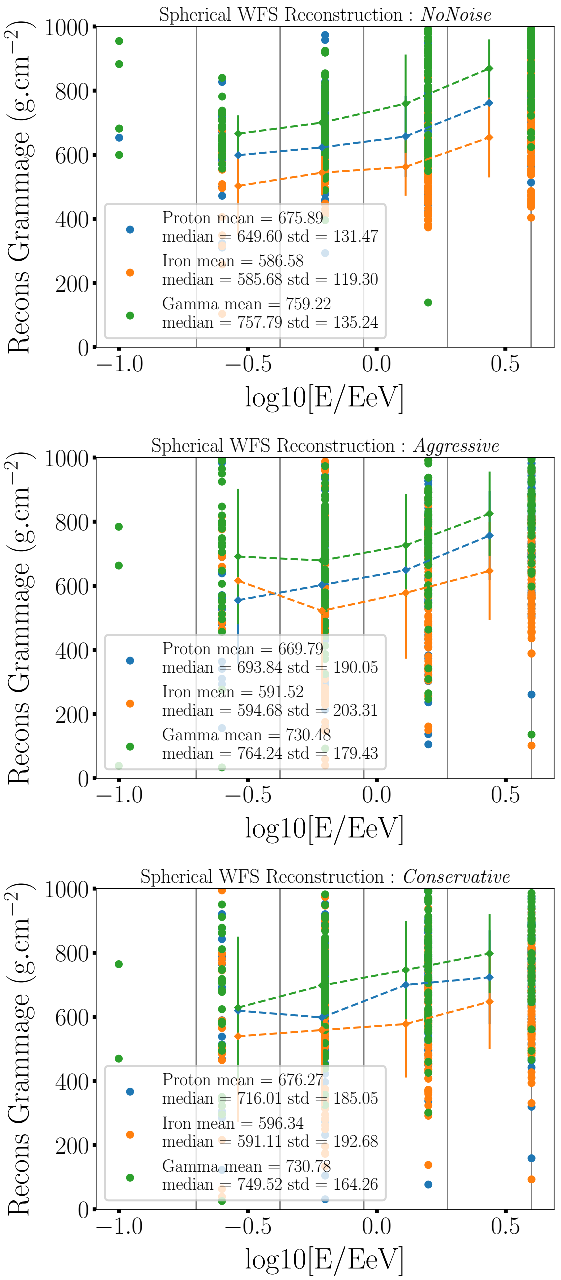

Figure 3.57: Energy dependancy on the reconstructed grammage, for the GP300-like layout. The increasing behaviour with energy, is expected as the elongation rate. *Top:* For the *NoNoise* scenario. *Middle:* For the *Aggressive* scenario. *Bottom:* For the *Conservative* scenario.

3.6 Conclusion

In this chapter, I have presented a study on the reconstruction of the arrival direction of EAS observed with GRAND-like radio arrays. We have first studied in detail the wavefront shape of the radio emission. Our work has shown that in the case of GRAND-like arrays the wavefront emission can be satisfyingly described with a spherical model. Even though the true wavefront shape is hyperbolic, the time and spatial resolution of the GRAND array on the curvature of the EAS are not high enough, due to the fact that the actual source of emission is remote from the detector. However the spherical model allows us to reconstruct the position of the source with a satisfactory resolution. We then developed a model describing the signal amplitude distribution as a function of the angular distance to this source of emission. This model allows us to reconstruct the direction of propagation of the signal from its amplitude information, with an angular resolution better than 0.1°.

As an additional bonus from this study, the emission source reconstruction seems to be a promising method for the identification of the nature of the primary, through the reconstruction of the radio X_{max} grammage value.

This reconstruction procedure shows the great advantage of combining different information from the detected electric-field. In this token, it opens the way to a coherent description of all electric-field information directly as a vectorial model. Such a description would be in my opinion the most robust and elegant way to directly reconstruct all the quantity we seek to measure, with the full power of a vectorial information without information losses due to the projection onto scalar quantities.

Part II

Fast Radio Bursts

Chapter 4

Fast Radio Burst repeaters produced via Kozai-Lidov feeding of neutron star-black hole systems

My work in the Fast Radio Burst field started with the GRAND project: for several reasons, detailed in Section 5.3, GRAND envisions to also detect these radio transients events. The nature of these phenomena (unknown source, highly energetic, transient events, see Section 4.1) immediately triggered my interest for this field. Therefore when Philippe Zarka who conducted the preliminary studies of FRB detection with GRAND offered me the opportunity to perform with him a dedicated observational program on the NenuFAR telescope (Section 5), I gladly accepted. The motivation for this project was to explore the detection possibility and challenges of FRBs at low frequency with the NenuFAR instrument, typically around the GRAND frequency bandwidth, and see how this could be applied to GRAND. Later, Joseph Silk proposed to work on a theoretical model of FRB source, in order to explore a possible source model for FRBs via gravitational perturbations of asteroids trajectories around a compact object (see Section 4). Connections between my studies on UHE neutrino and FRB were obvious. In both cases, I worked on the question of the sources, and the underlying theoretical mechanisms of emissions, and in both cases I also worked on the detection challenges. Furthermore the FRB project gave me the opportunity to work on data analysis, which of course was not possible yet with GRAND, and therefore complemented the panel of methods and tools I learned during my Ph.D.

4.1 Introduction:

Fast Radio Bursts are astrophysical radio transient phenomena, discovered by Lorimer during searches of fast single pulses in pulsar surveys in 2007 [219]. They are characterised by short radio pulses (bursts) of millisecond duration, over a broad frequency range of several hundreds of MHz.

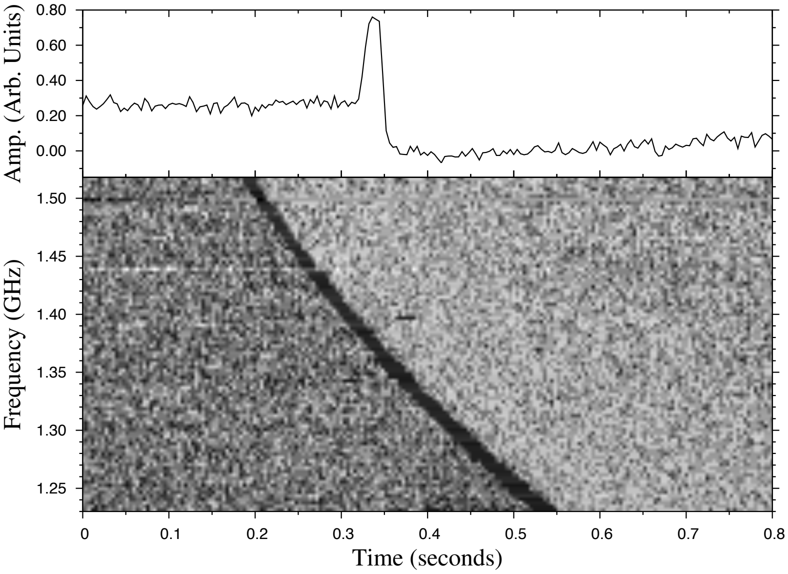

Figure 4.1: The Lorimer burst, the first detected FRB in 2007. *Top:* Waterfall plot (projection along the temporal dimension of the dynamical spectrum of the de-dispersed signal) of the pulse, integrated along the frequencies. *Down:* Dynamical spectrum of the pulse. The pulse can be characterised as a milliseconds pulse over a broad band frequency range. Furthermore the large time delay between the high frequencies and the low ones clearly shows a signal with a high DM. Taken from [219].

Figure 4.1 displays the so-called Lorimer burst, the first FRB ever detected. The dynamical spectrum represents the time evolution of the frequency content of a radio emission. An example of this dynamical spectrum is given on the lower panel. It is characterised by a high dispersion of the arrival times between the high frequencies and the low ones. This results from the propagation of the emission through a plasma between the source and the observer. The electromagnetic wave induces a charge displacement, which translates into a variation of the group velocity of the emission, which depends on the frequency. This time delay can be expressed as a function of the Dispersion Measure (DM) and reads

$$\Delta t(\nu_1, \nu_2) = 4.15 \times 10^3 [\mathrm{DM}] \left(\nu_1^{-2} - \nu_2^{-2}\right) \text{ s} , \tag{4.1}$$

where $\Delta t(\nu_1, \nu_2)$ is the dispersed arrival time between two frequencies ν_1 and ν_2 in MHz. The DM represents the total electron column density crossed by the emission (in $\mathrm{pc.cm^{-3}}$) and therefore can be written as

$$\mathrm{DM} = \int_0^d n_e \,\mathrm{d}l \ , \tag{4.2}$$

where n_e is the electron density and d is the emission distance traveled before reaching the detector. The distance of the emission can therefore be inferred from the FRB measurements, thus providing information about the electron density along the path (Milky Way, circum-galactic medium, extra-galactic medium and host galaxy). Detected FRBs present DM values ranging from $\sim 100\,\mathrm{pc.cm^{-3}}$ up to $\sim 2000\,\mathrm{pc.cm^{-3}}$. The typical time delay between two low frequencies can therefore last several minutes, as for example, between 200 MHz and 100 MHz, we have

$$\Delta t(200 - 100\,\mathrm{MHz}) \approx 0.3 \times [\mathrm{DM}]\ \mathrm{s}\ . \tag{4.3}$$

These DM values usually correspond to cosmological distances. For illustration purposes, a DM $= 100\,\mathrm{pc.cm^{-3}}$ corresponds to roughly $\sim 200\,\mathrm{Mpc}$ and a DM $= 2000\,\mathrm{pc.cm^{-3}}$ to $\sim 5\,\mathrm{Gpc}$ (the exact value depends on the galactic longitude and line of sight of the observation).

Another interesting feature that appears at lower frequencies is the broadening of the emission (see Figure 4.2), resulting from the multi-paths scattering of small scales fluctuation in the electron density. This scattering is related to the source emission mechanisms and therefore provides a probe of its surrounding environment. However this is an important limiting factor in the detection of FRBs at low frequencies as it results in the dilution of the signal intensity.

The extra-galactic origin is further confirmed by the isotropic distribution of FRBs over the sky. They are distributed in particular at high galactic latitude, hence outside the galactic plane (see Figure 4.3). So far, FRBs have been detected with fluences ranging from sub-Jansky[1] up to more than 400 Jy, with steep energy spectra [222]. Consequently, the isotropic energy equivalent of a FRB is more than ten billions times larger than the galactic pulsar emissions, with in addition, spectra that are radically different from most of the radio sources known. The recent detection of two intense radio bursts coincident with X-ray bursts and localised at the position of SGR1935+2154 (a galactic magnetar known for its X-ray flares), points towards the magnetars hypothesis as source of FRBs [30, 31]. This might however apply to a subset of the population only, since the equivalent luminosity of the radio bursts from SGR1935+2154 seems to be 40 times dimmer than the dimmest FRB.

---

[1] One Jansky (1 Jy) corresponds to an electric field of amplitude 25 nV/m approximatively.

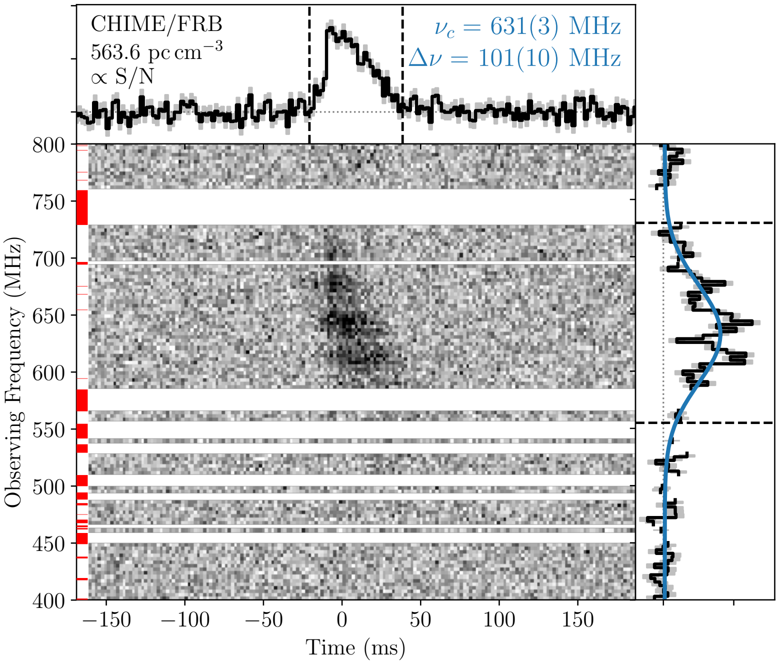

Figure 4.2: Dynamic spectrum (*Center*) and waterfall plots along the time (*Up*) and frequency dimension (*Right*) for the Arecibo repeater FRB121102, observed for the first time around 600 MHz with the CHIME telescope. A clear frequency broadening effect can be observed towards the low frequencies, which is not present at the Arecibo observatory frequency. Taken from [220].

In addition, a fraction of FRBs appears to repeat, i.e. multiple bursts distant of a few seconds to months can be observed at the same location. This implies that FRBs could belong to two distinct populations: repeaters and non repeaters. Among the hundred of events published yet, about 21 appear to repeat, mostly with no apparent periodicity (even though one has been reported to be periodical [223]). A large fraction of these FRBs and in particular the repeating FRBs have been discovered by the CHIME instrument in Canada, operating around 400 MHz. The absence of real differences in their spectra however suggests that the two populations may originate from the same sources. Also the event rate, extrapolated from current observations (necessarily limited in observation time and field of view), suggests that FRBs occurs at an extraordinarily high rate of thousands per day, implying that the objects at the origin of these emissions must be numerous in the Universe.

Besides the unknown origin of FRB, many observational unknowns remains, partly due to the very recent discovery of these events. Technological challenges also play a role in this.

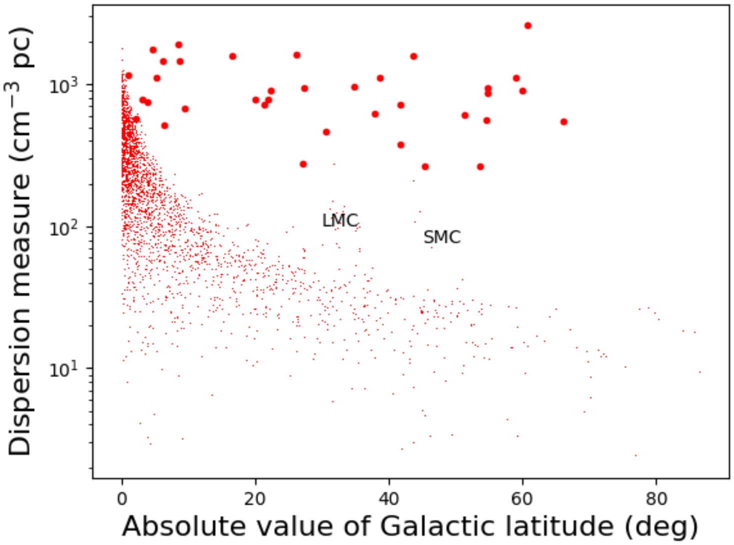

Figure 4.3: DM distribution of the FRBs (big red dots) and galactic pulsars (small red dots) as function of the galactic latitude. The pulsar population mostly lies in the galactic plane and the high DM can be accounted by the galactic bulge, while FRB are isotropically distributed over the sky with high DM. LMC and SMC stands for Large Magellanic Cloud and Small Magellanic Cloud. Taken from [221].

Among these unknowns, it can be noticed that some pulse profiles seems to present complex substructures and even drifting frequencies features. DM fluctuations have been observed from event to event, as well as scattering times fluctuations, but the small statistics prevents any consensual conclusion. Finally, detection have only been achieved between 8 GHz, down to 111 MHz by the Pushchino observatory in Russia. However, only few polarisation measurements has been made (except very recently in the ASKAP survey [224]). Therefore the existence of FRBs at low frequencies below 111 MHz as well as the population rate and spectra remain totally unexplored and would provide some of the strongest constraints on many existing source models (see Chapter 5).

A vast amount of emission models exists, from exotic Alien signals to cosmic strings, and can be found in these catalogues [225, 226]. Since it is not the purpose of this work to present all the possible emission models, I focus here on one of these emission models called Alfvén wings mechanism, directly used in our FRB model and presented in this chapter. It relies on a high coherence plasma instability, as for example the cyclotron maser instability, operating in the Alfvén wing and emitted from the magnetic wake of a body immersed in a pulsar wind [227] (see Figure 4.4 for an illustration).

In the following, I will summarise the key ingredients leading to these Alfvén wings emissions and then I will present how this mechanism can be coupled to gravitational instabilities of asteroids in binary systems such as neutron star-black hole (NS-BH) and lead to FRB rates which are interestingly consistent with the observed ones.

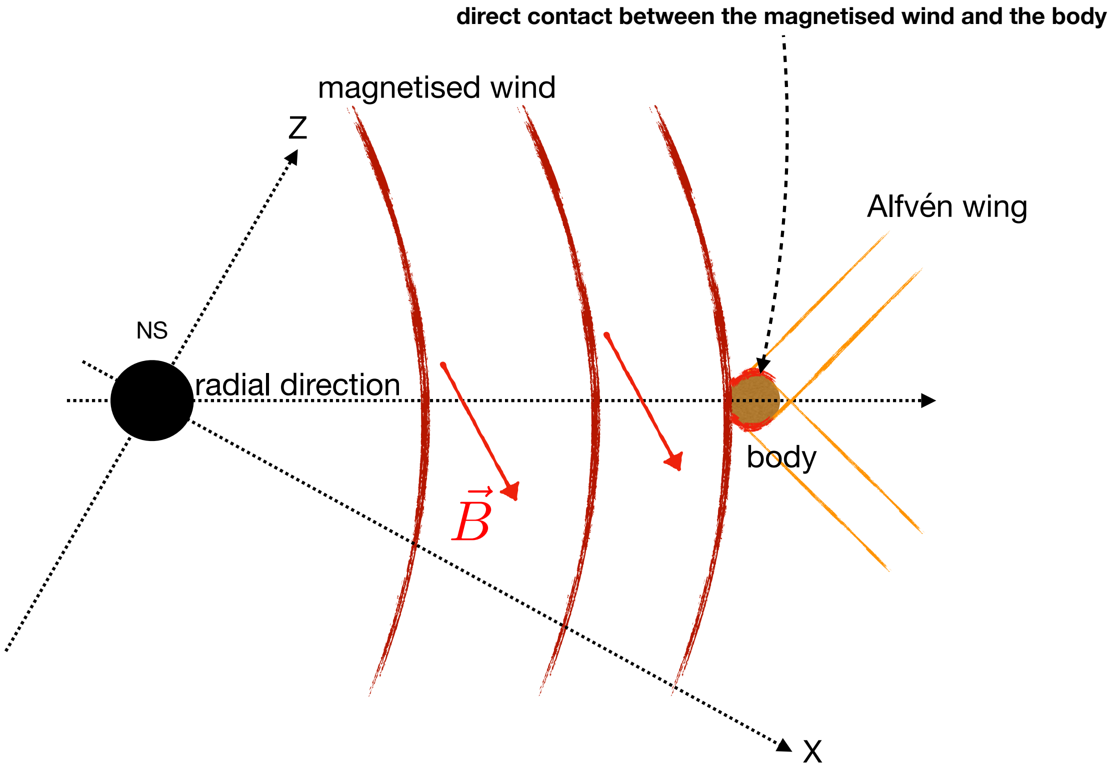

Figure 4.4: Sketch of the general principle leading to the creation of Alfvén wings. A companion body of a pulsar is immersed in the magnetised wind of that pulsar. The direct contact of the magnetised wind with the body leads to the creation of two current sheets called Alfvén wings. The plasma crossing these current sheets can be destabilised and leads to high coherence emission mechanisms.

4.2 Alfvén wings emissions

Reference [227] presents the extension of the Alfvén wing theory (see e.g. [228]) to relativistic winds induced by pulsar and interacting with a companion body (e.g. planet, comet, asteroid, etc.). The emission mechanism can be summarised in three steps: first the relativistic and magnetised wind enters in direct contact with the orbiting body, creating a magnetic coupling. This direct contact induces a current sheet called Alfvén wing, extending from the body far into space. Finally, the interaction of the outflow plasma crossing the Alfvén wing results in radio emissions through coherent mechanisms such as the cyclotron maser instability (CMI).

4.2.1 Magnetic coupling

Pulsars are rapidly rotating and highly magnetised neutron stars. The electromagnetic coupling to their rotation momentum leads to significant energy losses, resulting in their so-called spin-down. The high rotation speed and high magnetic field induce an outflow composed of a relativistic high energy radiation wind from the magnetosphere and a Poynting flux-dominated component called pulsar wave. Close to the neutron star, the energy outflow is assumed to be Poynting flux-dominated, while farther away, a relativistic particle component is expected to be dominant (see e.g. [229]).

Small bodies are expected to be found around pulsars, in particular in binary systems since accretion discs are expected to form in these configurations. Small bodies systems can form inside the accretion disc at typical distances of several hundreds of light cylinders $r \sim 100\, r_{\rm LC}$.

At these distances, the plasma flow induced by the neutron star is radial and the magnetic field energy density dominates largely the plasma kinetic energy as $B^2 \gg \mu_0\, \rho\, \gamma\, c^2$, where B is the pulsar magnetic field, μ_0 is the vacuum permeability, ρ is the flow density, γ is the Lorentz boost of the flow and c is the vacuum speed of light. Consequently, the wind is Poynting flux dominated, with in addition, the azimuthal component B_ϕ of the magnetic field dominant over the poloidal component $B_{\rm poloidal}$ leading to $B \sim B_\phi \gg B_{\rm poloidal}$.

In these conditions, any body orbiting the pulsar ($r \sim 100\, r_{\rm LC}$) is in direct contact with the wind, resulting into a magnetic coupling [230] at the origin of an electric field at the position r of the orbiting body

$$E_b = v^2 B_b^\phi = B_b^2 \Omega r \ , \tag{4.4}$$

with v the flow velocity, Ω the angular rotation of the neutron star and B_b the magnetic field at the body location, given by

$$B_b^{\phi} = \frac{B^2 \Omega^2 R^3}{r\, c^2} \ , \tag{4.5}$$

where R is the neutron star radius. Consequently a potential drop is induced due to the finite conductivity of the body

$$U = 2 R_b E_b \ , \tag{4.6}$$

where R_b is the orbiting body size. Naturally this potential drop leads to an induced electric current I_A extending in space and carried by an Alfvénic wing structure

$$I_A \sim 4 \frac{(E_b - E_s) R_b}{\mu_0\, c} \ , \tag{4.7}$$

where E_s is the electric field carried by the surface finite conductivity of the orbiting body. For instance, considering a 1 ms rotation pulsar and an asteroid-like companion of $R_b \sim 100\,\mathrm{km}$, at a distance $r \sim 0.2\,\mathrm{UA}$ leads to an induced current of 3.8×10^5 A.

This Alfvén wing structure forms an angle δ with the radial direction (see Figure 4.5), which can be derived in the case of a simple pulsar wind model [229]. In this model, the magnetic dipole axis of the pulsar is aligned with its rotation axis and the wind is described with two parameters, the mass flux f and the neutron star magnetic flux Ψ, given by

$$f = \gamma \rho v^r r^2 \ , \tag{4.8}$$

$$\Psi = r^2 B_b^r \ , \tag{4.9}$$

where $v^r \sim v_b$ is the radial velocity of the flow and B_b^r is the radial magnetic field.

The Alfvén wings angles can then be derived following the theory of incompressible Alfvén waves (see the derivation in [230]) which gives, with respect to the local magnetic field

$$\delta_s = s\,\mathrm{atan}\left[\frac{x}{\gamma\left(\sqrt{1+x^2} - s\right)}\right] \ , \tag{4.10}$$

where $s = \pm 1$ corresponds to the two resulting symmetrical Alfvén wings with respect to the radial direction (see Figure 4.5) and $x = r/(\gamma r_{\mathrm{LC}})$ is a dimensionless parameter. Note that, if $x \gg 1$ and $\gamma \gg 1$ then $\delta_s \sim s\gamma^{-1}$.

These two Alfvén wing structures can lead to radio emission, thanks to the plasma interaction with the current induced wings.

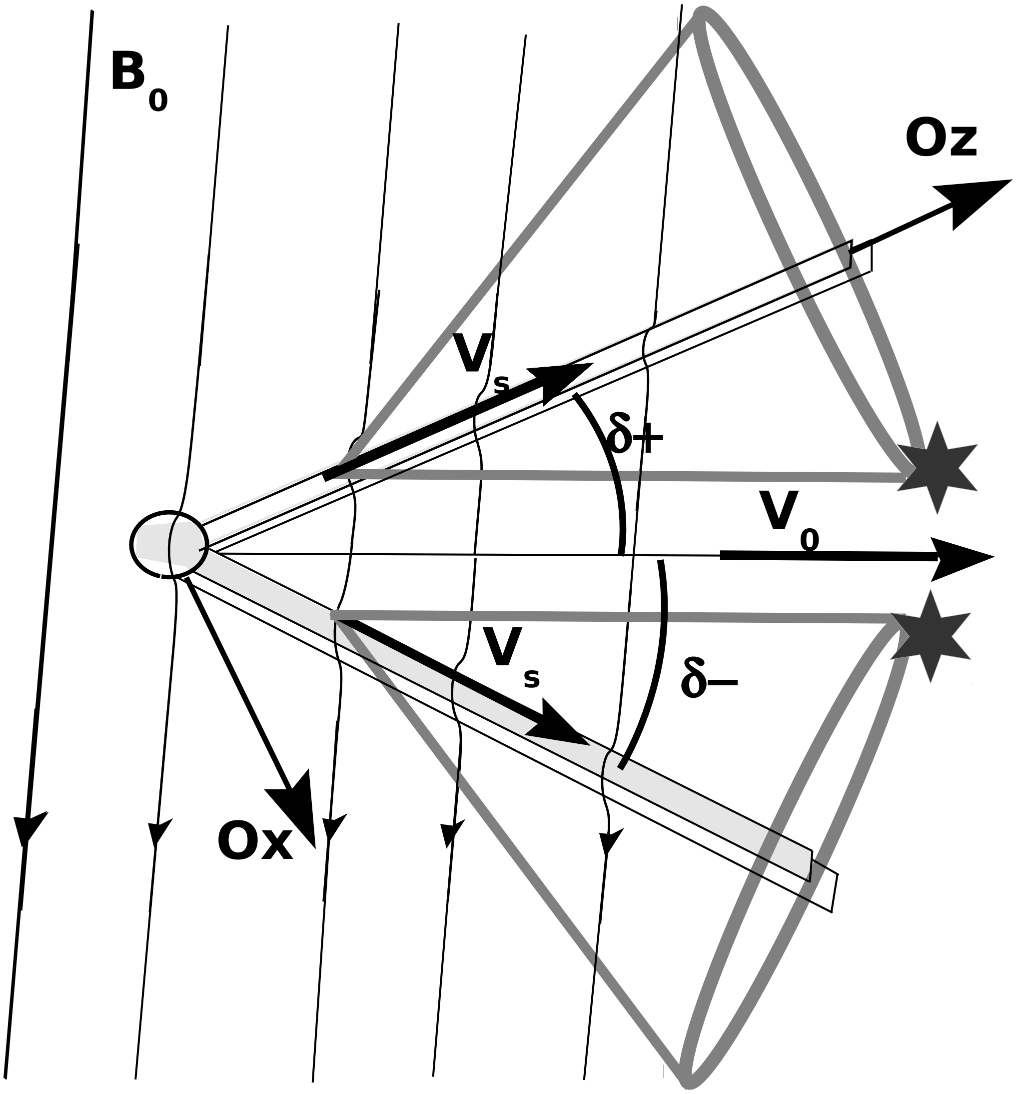

Figure 4.5: Alfvén wings attached to the pulsar companion, immersed in the pulsar magnetic field. Each wing forms an angle $\delta_\pm$ with respect to the radial direction (i.e radial outflow velocity). The velocity of the source regions $\vec{v}_s$ is assumed to be along the Alfvén wings. From which, the cones represented by the thick grey lines, describe the radio emission directions. The two stars show the highest emission intensity directions of each wing. Taken from [227].

4.2.2 Radio emissions

Emissions can be produced from the companion body or from the co-rotating plasma as it is the case for the magnetic coupling between Io and Jupiter. However these emission are not detectable at distances larger than 1 pc, and therefore will not be considered here.

Various coherent emission mechanisms can take place in the destabilised plasma of the wind. Following [227], we focus on the Cyclotron Maser Instability (CMI) emission. This emission takes place in the crossing of the plasma wind with the Alfvén wings far from the companion body. Therefore in the observer frame, the source is convected within the relativistic wing and moves at a relativistic speed given by

$$v_s = \frac{v_b}{\cos\delta} \sim c^2\left(1-\gamma^{-2}\right)\left(1+\delta^2\right) \; . \tag{4.11}$$

From relativistic principle, $v_s < c$ which imposes that $\delta^2 < \left(\gamma^2-1\right)^{-1}$ and therefore $x \gg 1$ (introduced in Equation 4.10) for the two wings or $x \ll 1$ only for the δ_- wing.

The CMI emission features in our framework can be summarised as follow (the detailed argumentation can be found in [227] and is not reproduced here)

- In the source frame, the resulting CMI induced electromagnetic waves are emitted along a cone of aperture $\alpha_s = 85 - 90°$ [231] parallel to the magnetic field.
- The intensity of the emitted electromagnetic wave depends on its direction of propagation inside the cone and are maximal when aligned with the Alfvén wings (see sketch of Figure 4.5)
- Due to purely relativistic effect, in the observer frame, the aperture of the emission cone is reduced to a factor $\sim 1/\gamma$, with γ the Lorentz factor the wind, and similarly the intensity is amplified by a factor γ^2.
- The emitted CMI frequency is close to the local electron gyro-frequency, which yields in the source frame to

  $$f_{c,s} = \frac{eB\Omega R^3}{2\pi m c^2 r^3}\sqrt{1+\left(\frac{r}{\gamma r_{\mathrm{LC}}}\right)^2} \; , \tag{4.12}$$

  where e is the electron charge and m its mass.

Finally, the maximum power inside an Alfvén wing is given by [230, 232]

$$\dot{E} = \frac{\pi\, c}{\mu_0} R_b^2 B_b^\phi = \frac{\pi\, c}{\mu_0 c^3} R_b^2 r^{-2} R^6 B^2 \Omega^4 \; . \tag{4.13}$$

Studies of the Io-Jupiter radio emissions show that the emitted power scales with the Poynting flux, with a constant of proportional factor $\epsilon \sim 2 - 10^{-3}$. Therefore, the radio emitted power is expressed as

$$P_{\text{radio}} = \epsilon \dot{E} \ . \tag{4.14}$$

This leads to an average emission flux observed at a distance D, with a frequency-range spectrum of emitted waves Δf of

$$\begin{aligned}\left(\frac{\langle S\rangle}{\text{Jy}}\right) =& 2.7 \ \times 10^{-3}\left(\frac{\gamma}{10^5}\right)^2\left(\frac{\epsilon}{10^{-3}}\right)\left(\frac{R_b}{10^7\text{m}}\right)^2\left(\frac{1\text{AU}}{r}\right)^2\left(\frac{R}{10^4\text{m}}\right)^6\left(\frac{B}{10^5\text{T}}\right)^2 \\ &\times\left(\frac{10\text{ms}}{T}\right)^4\left(\frac{\text{Mpc}}{D}\right)^2\left(\frac{1\text{GHz}}{\Delta f}\right) ,\end{aligned} \tag{4.15}$$

where γ is the Lorentz factor of the wind, ϵ is efficiency conversion from pointing flux to radio power, R_o is the pulsar companion radius, r its distance to the pulsar, R the pulsar radius, B the pulsar magnetic field, T the pulsar period, D the observer distance and Δf the frequency bandwidth. The $\langle S\rangle$ translates the non isotropic emission, resulting from the CMI mechanism and the beaming effect.

The Alfvén wing radio emission is one of the possible mechanisms at the origin of FRBs. In addition to describing a millisecond coherent emission as observed, it provides a strong enough signal to match observations. Interestingly, this scenario does not involve cataclysmic events, and does not require an extreme release of energy, which makes it relevant for repeating FRBs. Furthermore the ingredients to power the emission are well known and very common in the Universe (pulsars and small bodies). This promising scenario could explain the large rate of FRB observed in the sky.

4.3 Neutron-star black hole systems as source of FRBs ?

The emission mechanisms presented above (Section 4.2) are promising for the explanation of the FRB signals. However the rate of these emissions is bound to the motion of the pulsar companion. Therefore in a standard celestial configuration, we expect the orbits of the companion to be stable, hence periodical. Such configurations should lead to a periodical repetition of the bursts, which appears to be a marginal behaviour so far (see Section 4.1). Furthermore this kind of systems cannot describe the population of non repeater FRBs, thus implying a distinct origin between these two populations. Consequently, it appears that the dynamics of the pulsar companion is a key parameter in the burst rate of FRBs.

We examine this question under a novel angle, by studying the effect of the *Kozai-Lidov* mechanism on a triple system consisting of a central neutron star, a companion black hole, and sizeable bodies orbiting nearby, such as an asteroid belt around the neutron star. Bodies perturbed by gravitational effects leave their orbits and fall onto the central object [233]. For instance in the Solar System, the Kozai-Lidov mechanism (see Section 4.5) is responsible for the Kirkwood gap in the asteroid belt, under the influence of Jupiter [234]. The first discovery of earth-mass exoplanets was indeed around a millisecond pulsar [235]. The existence of asteroid belts around millisecond pulsars has been invoked to explain various timing variations and other observational features [236, 237, 238, 239, 240].

The infall of bodies onto a compact object should have numerous consequences. It could clean out the neutron-star environment, but also lead to observable electromagnetic signals. In particular, via the Alfvén wing emission mechanism presented in Section 4.2, this emission could be the source of FRBs. Other authors have proposed that FRBs result from the impact of asteroids and comets on central compact objects [241, 242, 243]. Such scenarii require however both a large number of progenitors, and an efficient infall mechanism into the neutron-star Roche lobe. The Kozai-Lidov effects applied to the numerous neutron star-black hole binary systems naturally provide such a framework. Interestingly, the above models could naturally lead to repeating signals, as long as small bodies, such as asteroids, pass by the star at a rate corresponding to the observations. Furthermore, it provides a natural explanation to the dichotomy between repeater and non repeater FRBs.

Although the number of FRB detections is growing fast, the observational constraints remain limited. The key observables at this stage, beside the energy budget and time variability, are the rates of bursts and of repeating events. In our framework, these quantities are directly related to the asteroid fall rate.

The object of our study are binary NS-BH systems, with an asteroid belt orbiting the neutron star. In a sense, this study is very similar to the one presented in [244], where the authors discuss the possible FRB emission from the interaction between an asteroid belt and a pulsar. This is why we will often refer to their work regarding the radio emission mechanism. However, our work focuses on the orbital dynamic of the asteroids inside the belt. In that perspective, we first present the FRB emission model and the parameter-sets required for the signal to be observed. We then compute the Kozai-Lidov time-scales for our binary system (Section 4.5) and discuss the implications in terms of FRB rates, taking into account the binary population rates (Section 4.6). We simulate the Kozai-Lidov effect on a mock solar-like asteroid belt in Section 4.7. Finally, we discuss the broader applications of this calculation in Section 4.8.

4.4 FRB emission from asteroids orbiting a pulsar

Asteroid belts close to neutron stars have been previously proposed to explain observational timing and radio features [236, 237, 238, 239, 240, 245]. No asteroid belt has yet been observed at distances larger than 1 A.U., but this is likely due to observational bias. Asteroid belts could be the remains of planetary objects destroyed by the supernova that led to the formation of the neutron star, or result from the supernova fallback itself [246, 247]. The aggregation of the debris to form a planet depends mostly on external conditions [248]. In particular, the presence of Jupiter prevents the formation of planets in the Solar belt. The perturbations produced by an outer black hole at $\gtrsim$ few A.U. with a mass of $10\,\mathrm{M}_\odot$ would be several orders of magnitude more intense than the influence of Jupiter on the Solar system belt. Therefore it is likely that no planet would form inside this asteroid belt.

For an asteroid of radius R_ast orbiting at distance a_ast of a pulsar located at distance D from the observer, the average flux density of radio waves inside the cone of emission of opening angle $1/\gamma$, with γ the Lorentz factor of the wind, reads (as in Equation 4.15):

$$\begin{aligned}\langle S\rangle &= 0.43\,\mathrm{Jy}\,\frac{\epsilon_\mathrm{w}}{10^{-2}}\,A_\mathrm{cone}\\ &\times\left(\frac{\gamma}{3\times10^{6}}\right)^{2}\left(\frac{R_\mathrm{ast}}{30\,\mathrm{km}}\right)^{2}\left(\frac{a_\mathrm{ast}}{10^{-2}\,\mathrm{A.U.}}\right)^{-2}\\ &\times\left(\frac{R_\star}{10^{6}\,\mathrm{cm}}\right)^{6}\left(\frac{B_\star}{10^{13}\,\mathrm{G}}\right)^{6}\left(\frac{P_\star}{0.1\,\mathrm{s}}\right)^{4}\\ &\times\left(\frac{D}{100\,\mathrm{Mpc}}\right)^{-2}\left(\frac{\Delta f}{1\,\mathrm{GHz}}\right)^{-1},\end{aligned} \tag{4.16}$$

but with different numerical values. Here Δf is the spectral bandwidth of the emission, ϵ_w the wind power conversion efficiency, and $R_\star$, $P_\star$, $B_\star$ the pulsar radius, rotation period and dipole magnetic field strength. $A_\mathrm{cone} = 4\pi/\Omega_A \geq 1$ is an anisotropy factor, with Ω_A the solid angle in which the radio-waves are emitted in the source frame. For an isotropic emission, $A_\mathrm{cone} = 1$ and if, the instability triggering the radio emissions is the cyclotron maser instability, $A_\mathrm{cone} \sim 100$ [244].

It is interesting to note that in this radio emission mechanism model, magnetar-like objects with a strong magnetic field could power FRB emission of hundreds of Jansky as observed in the ASKAP survey (see Section 4.1). Such phenomena are also suggested by the recently observed double radio bursts from the magnetar SGR1935+2154 [31], also coincident with X-ray bursts [30].

In light of this emission equation, we discuss below the parameters required for the pulsar and the asteroids in order to produce an observable FRB.

4.4.1 Pulsar parameters

In a majority of NS-BH and BH-NS systems (depending on which forms first), the neutron star is born with normal pulsar characteristics. Various evolutionary studies show indeed that it is difficult to form recycled pulsars in these systems and their low inferred rates are compatible with their non-detection in radio so far [249, 250, 251, 252] .

In our model, the FRB emission will happen in the first $\lesssim 10^4$ yrs of the birth of the pulsar, and for compact binaries, even within the first 10 yrs (see Section 4.6). The relevant pulsar parameters are hence those at birth. It is commonly accepted that the dipole magnetic field strength of the pulsar experiences little decay, with an average initial value of $10^{12.65}$ G [253]. Recent simulations show that the initial spin period could be as low as 20 ms [254] and typically below $P_\star < 150\,\mathrm{ms}$ [255].

The numerical values of Equation 4.16 demonstrates that such fiducial normal pulsar parameters suffice to produce an observable radio emission at Jansky level, provided that the asteroid presents specific characteristics, which we detail below.

4.4.2 Asteroid size

The radio emission depends crucially on the radius R_{ast} and orbital distance a_{ast} of the asteroid. One can infer from Equation 4.16 that large asteroids with radius $R_{\mathrm{ast}} \gtrsim 3\,\mathrm{km}$ are favored to power observable FRBs. From simple fragmentation arguments, it can be shown that the asteroid size distribution roughly follows a power-law [256]

$$N_{\mathrm{ast}} \sim 10^3 \;(R_{\mathrm{ast}}/30\,\mathrm{km})^{-2} \;. \tag{4.17}$$

Larger, less numerous asteroids could produce intense bursts, at a lower rate. Conversely, mJy emissions, detectable with current instruments, could be produced by smaller ($3-10\,\mathrm{km}$), more numerous asteroids.

4.4.3 Asteroid belt distance

Equation 4.16 shows that short distances from the central neutron star are required for the body to be immersed in strong magnetic fields. Although mJy emission can be produced at a distance $a_{\mathrm{mJy}} \sim 0.1\,\mathrm{A.U.}$ fom the neutron star, shorter orbital distances are required to power more intense bursts.

The shortest possible distance corresponds to the Roche limit. Indeed, it represents the distance beyond which the internal cohesion of an object, gravitationally bound (such as an asteroid) is not ensured anymore, eventually leading to its disruption. The Roche limit for an asteroid falling onto a neutron star is

$$
\begin{aligned}
d_{\rm NS}^{\rm Roche} &= 2R_{\rm ast}\left(\frac{M_{\rm NS}}{M_{\rm ast}}\right)^{1/3} &(4.18)\\
&\sim 9.2\times10^{-3}\,\text{A.U.}\left(\frac{2\,\text{g}\,\text{cm}^{-2}}{\rho_{\rm ast}}\right)^{1/3}\left(\frac{M_{\rm NS}}{1.4\,M_\odot}\right)^{1/3} &(4.19)
\end{aligned}
$$

with $R_{\rm ast}$ the asteroid radius, $M_{\rm ast}$ its mass, $\rho_{\rm ast}$ its density, and $M_{\rm NS}$ the central compact object mass.

Asteroids could penetrate deeper than the Roche lobe if the so-called plunging factor is taken into account [257], allowing for shorter $a_{\rm ast}$ to be reached at maximum eccentricities. This would enable smaller ($R_{\rm ast} \sim 3 - 10\,\text{km}$) – more numerous ($N_{\rm ast} \sim 10^{4-5}$) – asteroids to emit Jansky-level bursts.

Note that even at these close distances, small objects like asteroids are in general not evaporated via induction heating by the winds of the central neutron star [258]. Their size is indeed shorter than the typical wind electromagnetic wavelength, in the framework of the Mie theory. The effects of non-sphericity, as is the case for asteroids, are $\lesssim 30\%$ on light absorption coefficients [259].

The required short orbital distances imply that, unless most asteroid belts are already created in this emission zone delimited by $d_{\rm Roche}$ and $a_{\rm mJy}$, the process of Mottez & Zarka [227, 244] can work only if asteroids actually fall close enough to the central object. We propose here that this can happen via the Kozai-Lidov effect. We set our fiducial asteroid belt distance to $a_{\rm ast} = 1\,\text{A.U.}$ in the following.

We note that observations of pulsars show that there might be asteroid belts at $\sim R_\odot$ [236, 240, 245]: these do not need to undergo infall in order to produce FRBs, as they are already deep into the strong wind region to produce Alfvén wing emissions. The signals from such belts could present some periodicity due to the regular orbits as observed for FRB180916, which presents a $\sim 16.35\,\text{days}$ periodicity [223]. Indeed for favorable configurations, the alignment between the asteroid periodical motion and the observer line of sight could result in a periodical observations of bursts. However, turbulence effects in these inner wind regions along the observer's line of sight may play a role in modifying such periodicities, an effect that we do not address here. Note also that [260] shows that infrared emission limits the inner radius of an asteroid belt to a factor that is two or three times larger than $\sim R_\odot$.

4.4.4 Reconciling the emission beaming with the observed FRB rate

FRB emission would be observed when the radio beam of the Alfvén wings crosses the observer's line of sight. This probability is diminished by the narrow emission beam (of opening angle $1/\gamma \sim 10^{-6} - 10^{-5}$) produced by the Alfvén wave mechanism of Ref. [227], but compensated by the large number of orbits achieved by the asteroids before reaching the Roche limit. The exchanges of momentum leading to the shrinking of the orbits to its final eccentricity are secular effects, happening on long period of time and slowly achieved orbits after orbits. The time-scale for the asteroid eccentricity to shift from $a_{\rm mJy} \sim 0.1\,{\rm AU}$ to the Roche Limit in the emission zone (due to Kozai-Lidov effects) would be $\sim 10^4\,{\rm yr}$, yielding a number of Keplerian orbits performed in the emission zone of up to $N_{\rm orb} = 10^6 - 10^7$. The large number of orbits can thus compensate for the strong beaming and lead to more than one emission burst per asteroid, as we assume in the rest of our discussion. Other asteroids can also enter the emission zone, leading to repetitions of bursts.

In addition, turbulence effects, wind fluctuations and asteroid proper motions will also randomly affect the beam position and orientation. From [244] the authors derive a conservative value of the emission source velocity, due to the wind intrinsic oscillations, of about $v_s \sim 0.01c \ll v_{\rm wind}$, equivalent to an angular velocity of about $\dot{\omega} \sim 10^{-4}\,{\rm rad/s}$. Consequently, the emission beam wander over an area proportional to the time of observation $t_{\rm obs}$ and the Keplerian orbital pulsation of the asteroid $n_{\rm ast} = \sqrt{GM_{\rm NS}/a_{\rm ast}^3} = 2\pi/T_{\rm ast}$, with the Keplerian orbital period $T_{\rm ast} \sim 1.6\,{\rm days}(M_{\rm NS}/1.4\,M_\odot)\big(a/10^{-2}\,{\rm U.A.}\big)$, assuming the orbital motion is in the same plane as the observer line of sight for simplification. This area can be described with an opening angle $\alpha_{\rm w} = n_{\rm ast}t_{\rm obs} \sim 10^{-1}\,{\rm rad}\ (M_{\rm NS}/1.4M_\odot)\big(a/10^{-2}{\rm U.A.}\big)(t_{\rm obs}/1\,{\rm h}) \gg \alpha_{\rm beam} \sim \gamma^{-1}$ and defines the probable detection region. During the observation time $t_{\rm obs}$, multiple bursts can be observed if the beam crosses several times the observer line of sight. Another consequence of the beam wandering motion is the burst duration, which result from the sweep time of the beam across the observer line of sight, given by

$$\begin{aligned}\tau_{\rm burst} =& \frac{\alpha_{\rm beam}}{n_{\rm ast} + \dot{\omega}}\ , \\ \sim& 7\,{\rm ms}\ \left(\frac{\gamma}{3\times 10^6}\right)\left(\frac{M_{\rm NS}}{1.4M_\odot}\right)\ \left(\frac{a_*}{10^{-2}{\rm U.A.}}\right)^{3/2}\ . \end{aligned} \tag{4.20}$$

Finally the number of bursts observed and their durations depend on the position of the asteroids when the emission is produced, but also on the pulsar characteristics, which make possible configuration as diverse as the observed FRB bursts durations and repetitions.

Our final picture corresponds to an emission zone filled with asteroids whose Alfven wings randomly cross the observer's line of sight during the large number of orbits achieved to reach the Roche limit, where the asteroid disruption occurs. During the disruption, complex tidal-induced fragmentation could happen, especially for large asteroids, leading to a multitude of sub-emission components over short time-scales. Such events could explain the observations of FRB 121102, from which ~ 90 bursts were detected during a five hour period (half falling within 30 minutes) [261].

4.5 Kozai-Lidov time computation

Let us consider a binary system consisting of a neutron star and a companion black hole (as depicted on Figure 4.6). We will study in this section the gravitational influence of such a system on an asteroid orbiting the neutron star.

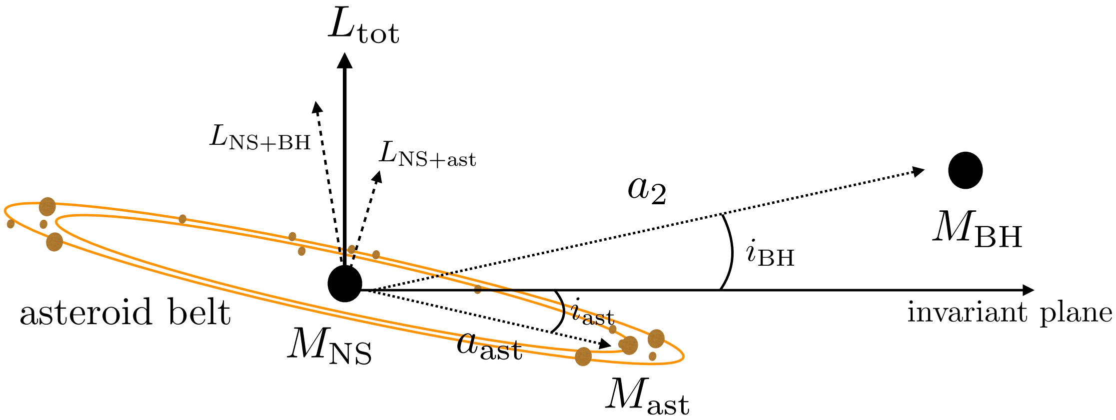

Figure 4.6: Sketch of the NS-BH system. The NS is surrounded by the asteroid belt, and the BH orbits at a larger distance. All objects are represented by their distance to the NS (for instance $a_{\rm ast}$ and $a_{\rm BH}$) and their inclination (for instance $i_{\rm ast}$ and $i_{\rm BH}$) with respect to the invariant plane.

The Kozai-Lidov effect is characterised by a periodic exchange between the eccentricity and the inclination of the inner orbital body –in our case an asteroid. The projection of its orbital momenta along the total orbital momenta of the system (which defines the invariant plane) is constant and given by

$$L_z = \text{Constant} = \sqrt{1-e^2}\cos i \ , \tag{4.21}$$

where L_z is the z-component of the inner body momentum, e is its eccentricity and i its total inclination. From this equation, it is clear that any increase of eccentricity results in a decrease of the inclination (and vice versa). The left panel of Figure 4.7 presents the initial and final configurations of one asteroid under the Kozai-Lidov perturbation. The right panel of Figure 4.7 displays the final configuration of one asteroid orbit reaching the Roche limit.

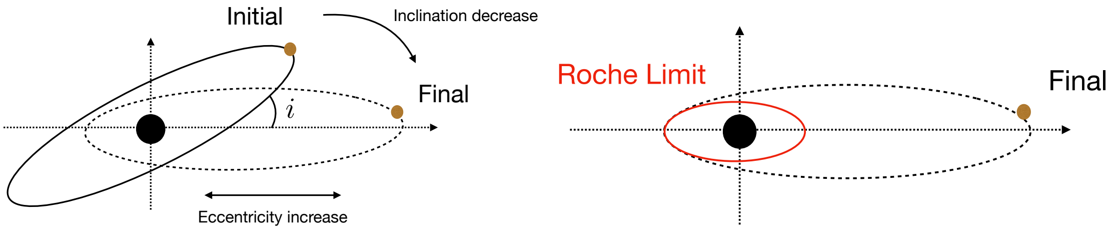

Figure 4.7: *Left:* Sketch of the initial and final configurations of an asteroid orbit under Kozai-Lidov perturbations. The exchange of orbital momenta inside the three body system leads to a decrease of the inclination and an increase of the eccentricity. *Right:* Final configuration of the asteroid orbit reaching the Roche Limit. While the orbit is an ellipse, the Roche limit can be viewed as circular area (inside the orbital plane) beyond which the gravitational cohesion of the asteroid (or any object) is no longer ensured. This leads eventually to the disruption of the asteroid.

4.5.1 Classical derivation

For an asteroid with initial inclination i_{ast} and a black hole with orbital inclination i_{BH}, one can derive the maximal eccentricity value of the asteroid, resulting from Kozai-Lidov oscillations, as

$$e_{\mathrm{max,KL}} = \sqrt{1-(5/3)\cos^2 i} \ , \tag{4.22}$$

where $i = i_{\mathrm{ast}} + i_{\mathrm{BH}}$. The periastron of an elliptical orbit with semi-major axis a_{ast} is given by $r_{\mathrm{ast}}^{\mathrm{periastron}} = a_{\mathrm{ast}}(1-e_{\mathrm{ast}})$. If the periastron crosses the Roche limit (Equation 4.18), the following equation is verified:

$$a_{\mathrm{ast}}(1-e_{\mathrm{ast}}) = 2R_{\mathrm{ast}}\left(\frac{M_{\mathrm{NS}}}{M_{\mathrm{ast}}}\right)^{1/3} \ . \tag{4.23}$$

The Kozai-Lidov oscillations can drive an asteroid to disruption inside the Roche limit if the following condition is fulfilled:

$$\sqrt{1-5/3\cos^2 i} \geqslant 1 - 2\frac{R_{\mathrm{ast}}}{a_{\mathrm{ast}}}\left(\frac{M_{\mathrm{NS}}}{M_{\mathrm{ast}}}\right)^{1/3} \ . \tag{4.24}$$

Namely, we require the maximal Kozai-Lidov eccentricity to be larger than the required eccentricity for the periastron to cross the Roche limit. Any asteroid, with orbital parameters matching the above equation, will be disrupted by the central neutron star on a time-scale larger than the orbital period of the asteroid.

The general expression of the Kozai-Lidov time, over which the maximum eccentricity is reached, is [233]:

$$
\begin{aligned}
t_{\rm KL} &= \frac{16}{15}\frac{a_{\rm BH}^3}{a_{\rm ast}^{3/2}}\left(1-e_{\rm BH}^2\right)^{3/2}\frac{1}{\sqrt{G}}\frac{\sqrt{M_{\rm NS}+M_{\rm ast}}}{M_{\rm BH}} \qquad (4.25)\\
&\sim 2\times 10^4\,{\rm yr}\left(\frac{a_{\rm ast}}{\rm A.U.}\right)^{-3/2}\left(\frac{a_{\rm BH}}{100\,{\rm A.U.}}\right)^{3}\\
&\quad\times\left(\frac{M_{\rm BH}}{10\,M_\odot}\right)^{-1}\left(\frac{M_{\rm NS}}{1.4\,M_\odot}\right)^{1/2}\,, \qquad (4.26)
\end{aligned}
$$

where $a_{\rm BH}$ is the semi-major axis of the orbiting black hole, $e_{\rm BH}$ its eccentricity and $M_{\rm BH}$ its mass. The numerical estimate assumes a null eccentricity $e_{\rm BH}$.

Another relevant time-scale is the relative Kozai-Lidov time between two *consecutive* asteroid disruptions, which can be compared to the burst frequency for repeating FRBs. This time-scale can be computed from Equation 4.25, assuming a fixed asteroid mass and a fixed position for the outer black hole:

$$
\Delta t_{\rm KL} \approx \frac{16}{15}\frac{a_{\rm BH}^3}{a_{\rm ast}^{5/2}}\Delta a_{\rm ast}\left(1-e_{\rm BH}^2\right)^{3/2}\frac{1}{\sqrt{G}}\frac{\sqrt{M_{\rm NS}}}{M_{\rm BH}} \qquad (4.27)
$$

where $\Delta a_{\rm ast}$ is the difference in semi-major axis between two asteroids consecutively undergoing Kozai-Lidov oscillations in the asteroid belt.

Assuming that the initial distribution of $a_{\rm ast}$ in the belt follows a Normal distribution with mean $\langle a_{\rm ast}\rangle$ and width $\sigma_a = \varepsilon_{\rm ast}\langle a_{\rm ast}\rangle$, the mean distance between two consecutively falling asteroids can be estimated statistically as $\langle \Delta a_{\rm ast}\rangle \approx \sigma_a/N_{\rm ast,KL}$, with $N_{\rm ast,KL}$ the number of asteroids meeting the Kozai-Lidov criterion. One can express $N_{\rm ast,KL} = f(i_{\rm BH})\,N_{\rm ast}$, with $N_{\rm ast}$ the total number of asteroids in the belt and $f(i_{\rm BH})$ the fraction of asteroids meeting the Kozai-Lidov criterion.

The fraction $f(i_{\rm BH})$ of asteroids meeting the Kozai-Lidov criterion depends on the inclination $i_{\rm BH}$ as

$$
f(i_{\rm BH}) = \int_{i_{\rm ast}=0}^{\pi/2}\mathcal{N}_{\langle i_{\rm ast}\rangle}^{\sigma_i}\int_{a_{\rm ast}=0}^{a_{\rm ast,KL}}\mathcal{N}_{\langle a_{\rm ast}\rangle}^{\sigma_a}(a_{\rm ast}){\rm d}a_{\rm ast}\,{\rm d}i_{\rm ast}\ , \qquad (4.28)
$$

where $\mathcal{N}_{\langle x\rangle}^{\sigma_x}(x)$ is the normal distribution function of mean $\langle x\rangle$ and variance σ_x^2. The Kozai-Lidov maximum semi-major axis to reach the Roche limit reads

$$
a_{\rm ast,KL}(i_{\rm BH}) = \frac{2R_{\rm ast}\left(M_{\rm NS}/M_{\rm ast}\right)^{1/3}}{1-\left[1-(5/3)\cos^2\left(i_{\rm ast}+i_{\rm BH}\right)\right]^{-1/2}}\ . \qquad (4.29)
$$

Figure 4.8 presents the values of $f(i_{\rm BH})$ in the classical derivation (blue). However, we will see in the next paragraph that in our regime, General Relativity (GR) effects dominate and lead to lower $f(i_{\rm BH})$.

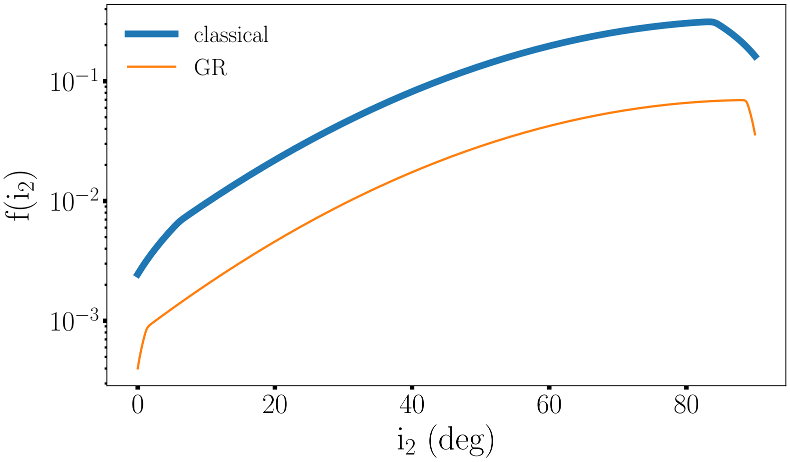

Figure 4.8: Fraction of asteroids reaching the Roche limit via the Kozai-Lidov effect in the classical calculation (blue) and in the general relativity case (orange), as a function of the black hole inclination $i_{\rm BH}$. Its mass is set to $M_{\rm BH} = 10\,M_{\odot}$. The density of the asteroids are set to $\rho_{\rm ast} = 2\,{\rm g.\,cm^{-3}}$ and their semi-major axes follow a Normal law with mean semi-major axis $\langle a_{\rm ast} \rangle = 1\,$A.U. and standard deviation $\sigma_a = 0.15\,\langle a_{\rm ast} \rangle$.

4.5.2 GR corrections

General Relativity (GR) can suppress high eccentricity excitations $e_{\rm KL,max}$ for inner orbits, when the ratio between the inner orbit GR precession time-scale and the Kozai-Lidov time-scale [233, 262]

$$\frac{t_{\rm GR,inner}}{t_{\rm KL}} = \epsilon_{\rm GR}^{-1}(1 - e^2_{\rm max,GR}) < 1 \ , \tag{4.30}$$

where we define

$$\epsilon_{\rm GR} = \frac{3G(M_{\rm NS} + M_{\rm BH})^2 a_2^3 (1 - e^2_{\rm BH})^{3/2}}{a^4_{\rm ast} c^2 M_{\rm ast}} \ . \tag{4.31}$$

The maximal eccentricity reachable taking into account GR effects $e_{\rm GR,max}$ satisfies the following equation

$$\epsilon_{\rm GR}\left(\frac{1}{j} - 1\right) = \frac{9}{8}\frac{e^2_{\rm GR,max}}{j^2}\left[j^2 - \frac{5}{3}\cos^2 i\right] \ , \tag{4.32}$$

with $j = (1 - e^2_{\rm max,GR})^{1/2}$. For $\epsilon_{\rm GR} \ll 1$, this yields $j \approx (15^{1/2}/3)\cos i = (15^{1/2}/5)(1 - e^2_{\rm KL,max})^{1/4}$. Figure 4.9 displays the maximal eccentricities computed in the classical and general relativistic frameworks. The GR corrections tend to reduce the maximal eccentricity reachable and therefore implies a lower fraction of asteroids capable of reaching the Roche limit as shown in Figure 4.8. As demonstrated also in Ref. [262], GR effects on the

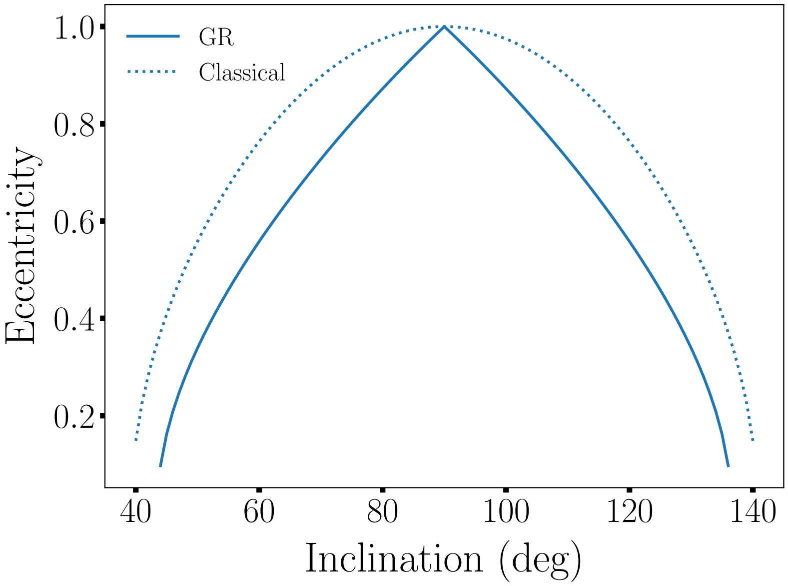

Figure 4.9: Maximal eccentricity reachable via Kozai-Lidov perturbations as a function of the inclination, for the classical computation (dotted line) and the general relativistic corrections (straight line). The GR corrections tend to reduce the maximal eccentricity reachable.

maximum eccentricity reached will be stronger for higher inclinations.

The Kozai-Lidov oscillations in the GR regime can drive an asteroid to disruption inside the Roche limit if the following condition is fulfilled

$$a_{\mathrm{ast,KL,GR}}(i_{\mathrm{BH}}) = \frac{2R_{\mathrm{ast}}(M_{\mathrm{NS}}/M_{\mathrm{ast}})^{1/3}}{1-\sqrt{1-16/25\sqrt{(5/3)\cos^2(i_{\mathrm{ast}}+i_{\mathrm{BH}})}}}\ . \tag{4.33}$$

This maximum semi-major axis replaces $a_{\mathrm{ast,KL}}$ in Equation 4.28, leading to a reducing of $f(i_{\mathrm{BH}})$ by a factor ~ 3, as can be seen in Figure 4.8. Numerically, including GR corrections, $f(i_{\mathrm{BH}} = 45°) \sim 0.02$, leading to $N_{\mathrm{ast,KL}} = f(i_{\mathrm{BH}} = 45°)(N_{\mathrm{ast}}/1000) \sim 20$.

In this calculation, we have neglected the tidal and rotation terms, which can also affect the maximum eccentricity reached by the body. These terms are negligible compared to the GR term in our model. Note that the quadrupole approximation leads to a good analytical estimate of the orbital evolution, even when the octupole effects are strong [262].

The mean relative Kozai-Lidov time between two consecutive asteroid disruptions can then be estimated as

$$\begin{aligned}\langle \Delta t_{\rm KL} \rangle \quad & \sim 150\,{\rm yr}\left[\frac{f(i_{\rm BH})N_{\rm ast}}{20}\right]^{-1}\frac{\varepsilon_{\rm ast}}{0.15}\left(\frac{\langle a_{\rm ast}\rangle}{\rm A.U.}\right)^{-3/2} \\ & \times\left(\frac{a_{\rm BH}}{100\,{\rm A.U.}}\right)^{3}\left(\frac{M_{\rm BH}}{10\,M_\odot}\right)^{-1}\left(\frac{M_{\rm NS}}{1.4\,M_\odot}\right)^{1/2}\ , \end{aligned} \tag{4.34}$$

where we have assumed $e_{\rm BH} = 0$ for the numerical estimate. Here, we have used the parameters values explained in the following section. The value of $\varepsilon_{\rm ast}$ is chosen so as to fit the parameters of the solar belt (see Section 4.7).

Figure 4.10 displays the evolution of the Kozail-Lidov time $t_{\rm KL}$ and relative delay $\Delta t_{\rm KL}$ as a function of the outer perturbing body semi major axis a_2. A clear distinction between compact and wide systems can be made based on the typical delay, the first ones, present relative delay on day-scales while the other ones have relative delay of several tens of years.

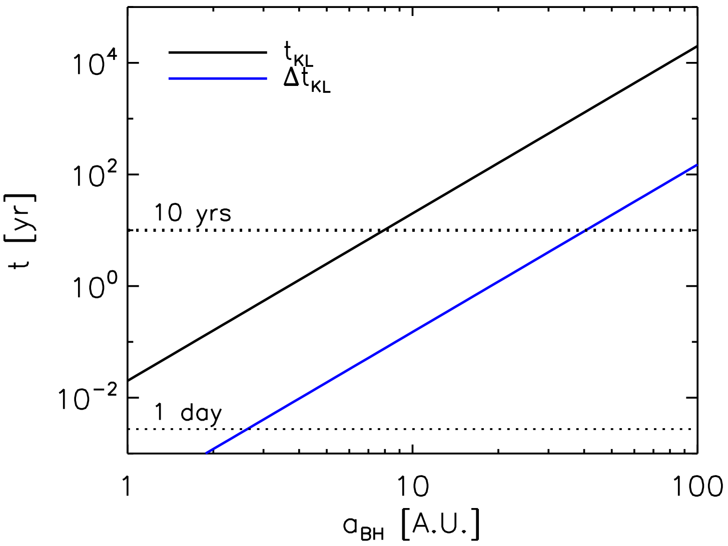

Figure 4.10: Mean Kozai-Lidov time $\langle t_{\rm KL}\rangle$ (Equation 4.25) and relative time delay $\langle \Delta t_{KL}\rangle$ (Equation 4.34) as a function semi-major axis $a_{\rm BH}$ of the outer perturbing black hole semi-major axis.

4.6 FRB rates for compact and wide NS-BH binaries

We will consider for our systems, masses of $M_{\rm NS} = 1.4\,M_\odot$ (since it is the minimal masse required to produce a NS) for the neutron star, and $M_{\rm BH} = 10\,M_\odot$ for the black hole. The latter is a typical value in NS-BH systems [252]. Larger black hole masses would lead to higher asteroid infall rates. We have also set our primordial asteroid belt at distance $\langle a_{\rm ast}\rangle = 1\,$A.U.. Closer belts would again lead to higher asteroid infall rates.

The effects of $M_{\rm BH}$ and $a_{\rm ast}$ are however marginal and it appears from Equation 4.34 that the main parameter governing the infall rate via Kozai-Lidov effect is the orbital separation between the neutron star and the black hole $a_{\rm BH}$. Recent simulations show that most NS-BH binaries are compact, with $a_{\rm BH} \lesssim$ few 10 A.U. [252]. Up to ten percent of the binary population could be wider binaries [252, 263, 264].

Interestingly, compact binaries and wide binaries are expected to be observed as different types of FRB sources for our model. Indeed, for $a_{\rm BH} \gtrsim 40\,$A.U., $\Delta t_{\rm KL} \gtrsim 10\,$yrs, leading to non-repeating sources. For $a_{\rm BH} \lesssim 40\,$A.U., $\Delta t_{\rm KL} \lesssim 10\,$yrs, sources could be observed as repeating, with various frequencies. Within the compact population, simulations indicate that the binary population peaks around $a_{\rm BH} \sim 0.1 -$ few A.U., which lead to $\Delta t_{\rm KL} \lesssim$ day. In our scenario however $a_{\rm BH} =$ few A.U. is a lower limit, in order to allow for the existence of a stable disk between the two compact objects leading to the formation of asteroids [265]. Therefore, much higher falling frequencies are not expected, even though we discussed in Section 4.4.4 that fragmentation of single asteroids could lead to sub-bursts with higher frequencies.

Therefore, in this scenario, compact binaries would produce day-repeaters and wide binaries non-repeaters. It is interesting to notice that in the current analysis [266, 267], day to few day periods seem to be favoured among repeaters. This could be consistent with the dichotomy between the signatures from compact and wide binaries.

These two populations present another major difference in terms of typical belt lifespan, $t_{\rm KL}$. While wide binaries have $t_{\rm KL} \gg 10\,$yrs and can be viewed as long-lived FRB sources, compact binaries have $t_{\rm KL} < 10\,$yrs and should be considered as short-lived FRB transients. This dichotomy reflects in the calculation of the FRB rates from each of these categories.

Compact binaries, the most frequent among the NS-BH population, can be day-repeater FRBs during $t_{\rm KL} < 10\,$yrs. Their rate density is hence directly linked to the birth rate of NS-BH, estimated to be $0.6 - 13\,{\rm Myr}^{-1}$ in the Galactic disk [251, 128, 268]. The local density of galaxies is $0.02\,{\rm Mpc}^{-3}$, which yields a crude approximation of neutron star-black hole birth rate density of $\dot n_{\rm NSBH} \sim 0.2\,{\rm Mpc}^{-3}\,{\rm Myr}^{-1}$, assuming a birth rate of $10\,{\rm Myr}^{-1}$

per galaxy. The rate density of day-repeater FRB sources then reads

$$\dot{n}_{\rm FRB,rep} \sim 200\,{\rm Gpc^{-3}\,yr^{-1}}\frac{\epsilon_{\rm rep}\,\dot{n}_{\rm NSBH}}{0.2\,{\rm Mpc^{-3}\,Myr^{-1}}}\ , \tag{4.35}$$

where $\epsilon_{\rm rep} < 1$ is a source efficiency factor.

For wide binaries, the rate of FRBs expected to be sourced by infalling asteroids can be estimated by convolving the mean infall rate $1/\langle\Delta t_{\rm KL}\rangle$ with the number of contributing asteroids $N_{\rm ast,KL}$, the typical lifespan of the asteroid belt in its primordial configuration, $t_{\rm KL}$, and the birth rate of wide neutron star-black hole systems $\epsilon_{\rm wide}n_{\rm NSBH}$, with $\epsilon_{\rm wide}$ the fraction of wide systems among NS-BH binaries. It yields

$$\dot{n}_{\rm FRB,non-rep} \sim N_{\rm ast,KL}\frac{t_{\rm KL}}{\langle\Delta t_{\rm KL}\rangle}\epsilon_{\rm non-rep}\,\epsilon_{\rm wide}\,\dot{n}_{\rm NSBH} \tag{4.36}$$

$$\sim 5.3\times10^4\,{\rm Gpc^{-3}\,yr^{-1}}\,\frac{f(i_{\rm BH})N_{\rm ast}}{20} \times\frac{t_{\rm KL}}{2\times10^4\,{\rm yr}}\,\frac{150\,{\rm yr}}{\langle\Delta t_{\rm KL}\rangle}\,\frac{\epsilon_{\rm non-rep}\,\epsilon_{\rm wide}\,\dot{n}_{\rm NSBH}}{0.02\,{\rm Mpc^{-3}\,Myr^{-1}}}\ , \tag{4.37}$$

with $\epsilon_{\rm wide} = 0.1$ [252, 263, 264] and $\epsilon_{\rm non-rep} < 1$ a similar source efficiency factor as in Equation 4.35. These calculations assume that these binaries undergo a flat source emissivity evolution, out to redshift $z \sim 1$ [127]. For a star-formation type evolution, the number of sources would increase by a factor of ~ 2.

As the gravitational-wave merger time-scale is

$$t_{\rm GW} \sim 6\times10^{14}\,{\rm yr}\,[(M_{\rm NS}+M_{\rm BH})/10\,M_\odot]^{-3}(a_{\rm BH}/10\,{\rm A.U.})^4(1-e_{\rm BH}^2)^{7/2}\ , \tag{4.38}$$

the survival of both compact and wide binary systems over the age of the Universe is mostly guaranteed for a circular orbit ($e_{\rm BH} = 0$). For large eccentricity, the merger can however happen on a shorter time-scale, down to $\sim 10^4$ years [269]. In any case, these timescales are shorter than $t_{\rm KL}$ and do not need to be considered here.

The factor $N_{\rm ast,KL} = f(i_{\rm BH})N_{\rm ast}$ corresponds to the number of asteroids which experience the Kozai-Lidov effect, as in Equation 4.34. Higher $i_{\rm BH}$ can boost the FRB rates estimated above by $1-2$ orders of magnitude, due to a larger $f(i_{\rm BH})$. Larger $N_{\rm ast}$ and higher $i_{\rm BH}$ would also shorten $\langle\Delta t_{\rm KL}\rangle$, consequently increasing the event rates.

The rate estimated in Equation 4.36 can be directly compared with the cosmological FRB rates found in the literature, of order $\dot{n}_{\rm FRB} \sim 2\times10^3\,{\rm Gpc^{-3}\,yr^{-1}} \ll \dot{n}_{\rm FRB,non-rep}$. The inferred source efficiency can thus be of order $\epsilon_{\rm non-rep} \lesssim 4\,\%$. This number leaves room for binary systems which do not fulfil the criteria to undergo Kozai-Lidov mechanisms: e.g., systems without asteroid belts, orbital inclinations, etc.

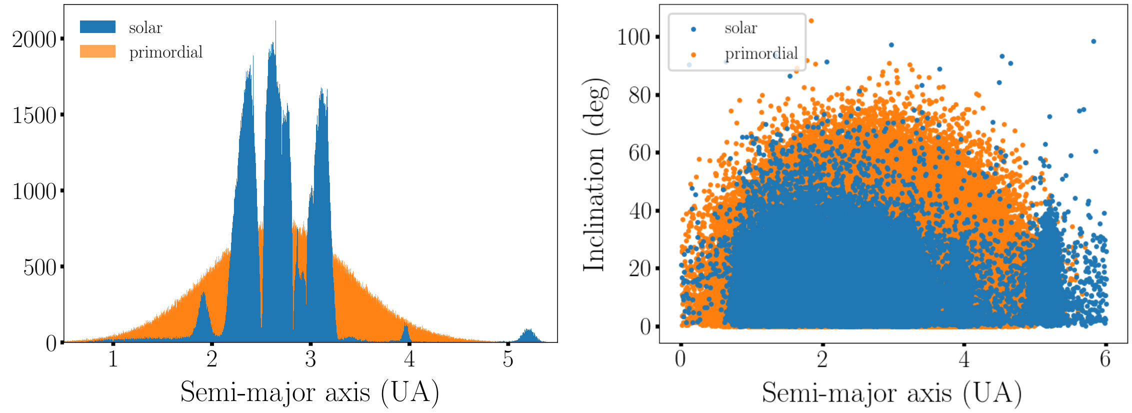

Figure 4.11: Asteroids distributions inside the Solar asteroid belt (blue) and the reconstructed primordial model belt (orange). *Left:* Asteroids semi major axes distribution. *Right:* Asteroids eccentricities as a function of the semi major axes. In both panels, the Kirkwood gaps are clearly visible for the Solar asteroid belt. Data have been obtained thanks to the IAU Minor Planet Center [256]

More than 700 FRBs have been observed as of today, among which 21 are repeaters [270, 267], yielding a ratio of $\sim 3\%$. This is one order of magnitude higher than the ratio estimated here: $\dot{n}_{\rm FRB,rep}/\dot{n}_{\rm FRB,non-rep} \sim 0.4\%\, \epsilon_{\rm rep}/\epsilon_{\rm non-rep}$. Given that most of the NS-BH binaries are compact systems leading to repeaters, it is likely that the ratio $\epsilon_{\rm rep}/\epsilon_{\rm non-rep} > 1$. We will also see in Section 4.7.3 that many of these repeaters could also be explained as being the tail of the asteroid falling rate distribution in wide binaries.

4.7 Application to a solar-like belt

In this section, we calculate the Kozai-Lidov effects from a compact binary system on a *primordial* asteroid belt (without any gapes such as the Kirkwood gapes of the solar system), modelled by analogy with the solar asteroid belt.

4.7.1 Computing the primordial solar-like asteroid belt

We model the distribution of the orbital parameters of the current solar belt using the data from the IAU Minor Planet Center [256]. A total number of 792041 asteroids of the solar belt are inventoried in these data.

Numerous asteroids sensitive to the Kozai-Lidov effect are missing from the distribution of orbital elements of the current solar asteroid belt, influenced by giant planets such as Jupiter. The Kirkwood gaps for instance, illustrate this effect. These features motivate the construction of a synthetic asteroid belt for our model, filling most of the gaps and mimicking the primordial population of the belt (see Figure 4.11).

The synthetic belts follow a gaussian distribution fitting the general trend of the current solar belt. We use for the semi-major axis a standard deviation of $\sigma_a = 0.15\langle a_{\rm ast}\rangle$, with the mean semi-major axis $\langle a_{\rm ast}\rangle$ left as a free parameter. For the inclinations, we follow the solar belt distribution with mean inclination $\langle i_{\rm ast}\rangle = 0^\circ$ and standard deviation $\sigma_i = 30^\circ$. The eccentricities are not relevant to our computation and are not modeled. This simple method allows us to construct a more generic asteroid belt, although it is restricted to our knowledge of the solar system.

4.7.2 Falling rates for a solar-like belt

We draw asteroid parameters by Monte-Carlo calculations, following the computed asteroid distributions. We select asteroids sensitive to Kozai-Lidov oscillations and compute the associated time of inclination to eccentricity transfer, leading to a crossing of the periastron and the Roche limit, as described in the previous section.

Figure 4.12 shows the distribution of the relative time delays for asteroids falling onto the central neutron star, for a current (green) and primordial solar-like belt for black-hole inclinations $i_{\rm BH} = 5^\circ$ (orange) and $i_{\rm BH} = 45^\circ$ (blue). The central neutron star has mass $M_1 = 1.4\,M_\odot$ and the outer black hole $M_2 = 10\,M_\odot$. The initial number of asteroids is set to $N_{\rm ast} = 10^3$. We examine the case of a wide system with black hole distance $a_{\rm BH} = 100\,$A.U. and mean asteroid belt distance $\langle a_{\rm ast}\rangle = 1\,$A.U. (left panel) and of a compact system with $a_{\rm BH} = 10\,$A.U. and $\langle a_{\rm ast}\rangle = 1\,$A.U. (right panel). For the wide system, the infall rates span days to millions of years, with a maximum around $\langle\Delta t_{\rm KL}\rangle \sim 1 - 100\,$years, depending on the inclination $i_{\rm BH}$. For compact systems, the rates are of order day-scales.

The comparison between the current solar belt and the primordial belt shows that the lack of Kirkwood gaps induces a drastic increase of short time-scales in the asteroid infall rate, and depending on the inclination, a factor of a few to an order of magnitude more events in total. Larger inclinations $i_{\rm BH}$ lead to shorter time-scales, and to higher event rates since the shifting time-scales due to inclination $i_{\rm BH}$ is dominant over the $1/f(i_{\rm BH})$ effect. Systems with larger inclinations $i_{\rm BH}$ and with higher rates ($\Delta t_{\rm KL} \sim 10\,$yr) will thus dominate in the sky.

Furthermore, one can notice the tail distribution at large time-scales for the solar belt in the right panel of Figure 4.12. It results from the Kirkwood gaps, where groups of asteroids with lower inclinations can reach the Roche limit due to the closer position of the outer

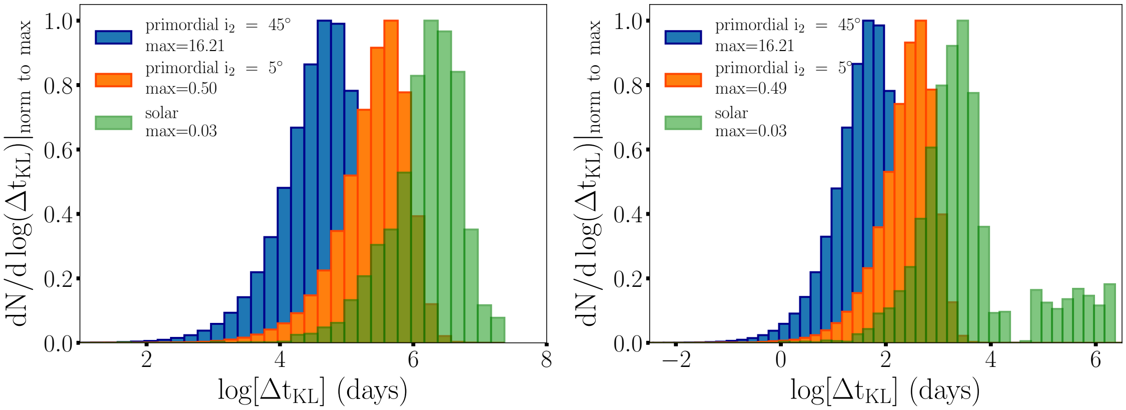

Figure 4.12: Distribution of relative time differences $\Delta t_{\rm KL}$ of falling asteroids in the Roche lobe of the central compact object due to Kozai-Lidov oscillations, for the current solar asteroid belt (green) and the primordial belt, for an inclination of the outer black hole plane $i_{\rm BH} = 5°$ (orange) and $i_{\rm BH} = 45°$ (blue), and initial asteroid number $N_{\rm ast} = 10^3$. We consider a wide system (*left*) with $a_{\rm BH} = 100\,$A.U. and $\langle a_{\rm ast}\rangle = 1\,$A.U., and a compact system (*right*) with $a_{\rm BH} = 10\,$A.U. and $\langle a_{\rm ast}\rangle = 1\,$A.U. Each histogram is normalised to the maximal distribution, i.e., divided by $\max({\rm d}N\,/\,{\rm d}\log{(\Delta t)})$.

black hole 10 AU (rather than 100 AU in the left panel). However, their lower inclinations result in larger time-scales.

4.7.3 Connection with FRB observations

The rates obtained here can be directly compared to observed FRB rates. The expected observed FRB rate can be obtained by multiplying the mean rate densities $\dot{n}_{\rm FRB,non-rep}$ obtained in Section 4.5 with the fraction of events observed with $\Delta T_{\rm obs} = 10\,$yr. Figure 4.12 yields an expected observable rate of $\sim 10 - 100\%$ ($\sim 0 - 2\sigma$) of the maximal rate in the distribution, depending on $i_{\rm BH}$ and $N_{\rm ast}$. Hence, with $N_{\rm ast} \sim 10^3$ and $\langle \Delta t_{\rm KL}\rangle \sim 10^2\,$yrs as in Figure 4.12, one can easily accommodate the observed FRB rate of $\dot{n}_{\rm FRB,obs} \sim 2\times 10^3\,{\rm Gpc}^{-3}\,{\rm yr}^{-1}$.

Among all observed FRBs, a fraction of sources are found bursting with irregular short periods, ranging from days to month-time-scales. These bursts would correspond to the left-hand tail of distributions such as the one shown in Figure 4.12. For example, the fraction of sources that would repeat at $\lesssim$month-time-scales can be estimated from the fraction of events with $\langle \Delta t_{\rm KL}\rangle < 1\,$month out of the fraction of events with $\langle \Delta t_{\rm KL}\rangle = 10\,$yr. From the distribution of Figure 4.12, this corresponds to the population at $\sim 2 - 4\sigma$ from the mean $\langle \Delta t_{\rm KL}\rangle$ depending on $i_{\rm BH}$ and the total number of asteroids $N_{\rm ast}$, corresponding to about $\sim 0.1 - 10\%$ of the total event rate, and to $\sim 1 - 30\%$ of the observed rate. This happens to match the current observations: more than 700 FRBs have been observed as of today, among which 21 are repeaters [270, 267]. The numbers could however also be accommodated with the tail of the distribution of different NS-BH systems, in particular for less wide binaries, larger inclinations, more numerous asteroids, all leading to shorter FRB rates.

One should note that these repetitions would be highly irregular, and would not be sustained over time, as they are statistically rare.

FRB121102 could be a good candidate for this tail scenario. Activity periods have been reported for hour scale periods, day scale periods and monthly periods (Table 2 in [271]). Such an erratic behavior could well be explained as a tail of the asteroid falling rate distribution. This source also presents sub-structure in the signal, with fainter pulses arriving at shorter intervals [261]. These could be explained by the fragmentation of asteroid during the disruption in the Roche lobe, as mentioned in Section 4.4.4.

Finally, the compact system presented in Figure 4.12 (right panel) illustrates the possibility of having a population of short-lived repeaters, with day-scale periods. These sources will appear less numerous than the wide systems due to their short active timescale, which is consistent with the low percentage of repeaters observed so far.

4.8 Conclusion

Fast Radio Bursts can be produced if asteroids pass close to the Roche limit of a compact object with an electromagnetic wind [227, 244], or if they undergo collisions with this object [242, 243]. The infall of asteroids from standard belts onto the central compact object can be triggered by Kozai-Lidov oscillations, in the presence of an outer black hole.

The asteroid dynamic described by our model is able to reproduce the overall observed ratio of repeating to non repeating FRBs and motivates an explanation to unify the two observed population under one simple mechanism, already observed in the Solar system. By modelling the population of asteroids in a Solar-like belt, we calculate that the observable FRB rate is of order $\sim 10 - 100\%$ of the maximal rate in the distribution, depending on the inclination and the initial number of asteroids considered. The dichotomy between compact and wide systems allows us to account for the various burst dynamics observed within the repeating population. As illustrated by the erratic bursts behaviour between month-time scale and day-time scale, and predicted in the tail of the falling rate distribution of wide systems, and observed for FRB121102. The same approach allows us to predict a rate of day-repeaters (corresponding to compact systems) corresponding to $1 - 30\%$ of this observed rate. These numbers match the observations. Furthermore, these systems should not last too many years as the asteroids belt should be depleted rapidly. This would be a way to assess the validity of our model.

Finally, a large number of dynamical configurations of binary systems exists and can lead to a great flexibility in the bursts dynamics, hence in the observables. For instance, in the case of non-circular orbits, we expect that the outer black hole will be drawn closer to the central compact object, over some tens of thousands of years for large eccentricities. This migration will change the dynamics of the system and enable the infall of new asteroids from the belt. The belt can hence be totally wiped out while the outer black hole converges to the central object, and finally merges. FRBs can hence constitute an electromagnetic counterpart to binary black hole [35] and neutron star-black hole mergers.

The present study can be applied to other compact binary systems, provided that the central object generates a magnetised wind. As already proposed in [35], binary black hole systems could also lead to similar scenarios, as well as binary neutron stars or neutron star-white dwarf systems. We illustrate the case of a neutron star-white dwarf binary in Figure 4.13 One can see that the burst arrival periods are short (day-scale), as expected for a compact system. Binary neutron star and neutron-star white dwarf systems are particularly interesting because of their extremely large population rates. However, these systems are also usually very compact. In our scenario, this implies that these sources will be only emitting for an extremely short period of time, and cannot be necessarily considered as long-lived repeaters.

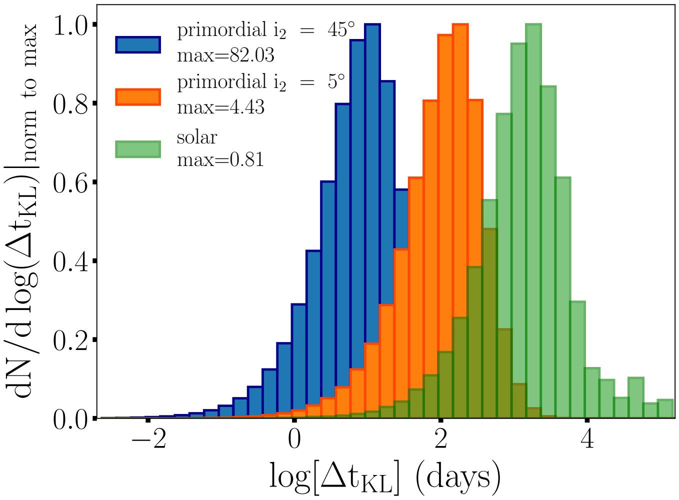

Figure 4.13: Same as Figure 4.12, for a NS-WD (neutron star-white dwarf system) with $M_{\mathrm{WD}} = 1\,M_{\odot}$, $a_{\mathrm{WD}} = 2\,\mathrm{A.U.}$ and $\langle a_{\mathrm{ast}} \rangle = 0.2\,\mathrm{A.U.}$ The initial asteroid number is $N_{\mathrm{ast}} = 10^3$.

Chapter 5

Fast Radio Burst observation: the very low frequency quest

5.1 Introduction

The young FRB community is in a similar situation to the GRB community 50 years ago. In spite of the fast-growing number of FRB detection, the community still lacks observational constraints. Many models have been developed (see Section 4 and [225]), which can hardly be discriminated against the current data. One major unknown which remains is the existence and the behaviour of FRBs below the uGMRT and Pushchino lowest frequencies (see Section 4.1), in the low frequency (LF) domain below 85 MHz. Of particular interest to understand the origin of FRBs is the emission spectrum, its possible LF turnover or cutoff, its polarisation, possible variations of its dispersion measure (DM) and scattering from event to event (see Section 4.1)...

We propose to unveil these questions with NenuFAR [38]. During the early science phase between July 2019 and December 2021, we will conduct the Pilot-Program ES05, until an observation is confirmed, then this pilot-program will evolve to the Key-Program ES05, allowing for a much larger observation time. After the early science phase, a full P.I. program will be conducted based on the experience gained during the first phase (see Sections 5.2 and 5.2.1).

Since FRBs are produced at cosmological distances (see Section 4.1), their signals are heavily dispersed and scattered during their propagation to Earth. Consequently, intensities towards lower frequencies are diluted. The typical signal intensity of FRBs is from 0.1 up to 420 Jy at frequencies around 1 GHz [272, 273, 274], over emission times lasting up to a few ms. In order to detect such signals at LF, the detector needs to combine a good time and frequency resolution and a good sensitivity. The non-detection of FRBs with the Murchison Widefield Array (MWA) in the frequency range of $30 - 300\,\mathrm{MHz}$, puts soft constraints, limited by the integration time of $0.5\,\mathrm{s}$ [275].

In order to maximise the detection probabilities, the Pilot-Program ES05 focuses on observations of already known and localised FRB repeaters (FRB180814, FRB181030 and FRB121102) (see Section 5.2.2.1) over a time longer than all their previous observations done at higher frequencies (see Section 5.2.2.3). The observation parameters, such as the spectral range limited to the upper half bandwidth of NenuFAR due to large dispersion and temporal broadening at LF, and especially the spectral and temporal resolutions, are optimised through simulations (detailed in Section 5.2.2.2). These simulations tools were developed for LF time-frequency observations, with NenuFAR and GRAND [276].

5.1.1 NenuFAR: low frequency hunter

NenuFAR (New Extension in Nançay Upgrading LOFAR) is a low frequency radio array located at the Nançay Radioastronomy Station, designed as a SKA pathfinder.

NenuFAR will consists[1] in 1938 dual polarisation antennas. Each antenna is designed on the LWA [277] cross-dipole structure with a specific preamplifier designed in France (at the Subatech and Nançay laboratories). The antennas are hierarchically distributed in mini arrays (MA) of 19 antennas in a hexagonal tile pattern, with a step of $5.5\,\mathrm{m}$ between any two antennas inside the MA. 96 of these MA are concentred in a $400\,\mathrm{m}$ core and 6 are located at distances up to $3\,\mathrm{km}$ (see Figure 5.1). This configuration allows for 4560 baselines between $25\,\mathrm{m}$ and $400\,\mathrm{m}$ and 591 baselines from $400\,\mathrm{m}$ to $3\,\mathrm{km}$. All MA are analog phased with delay lines, each delay lines consists of 7 bits systems of switchable cables length, allowing us to point $2^7 = 128$ directions along the two main axis of each MA, resulting for both polarisation in $128 \times 128 = 16384$ possible analog pointing directions between -23° and $+90^\circ$ declination. Digital pointing of the whole array is then performed quasi-continuously with the analog MA beam.

The antennas operate between the Earth ionospheric cut-off at $\sim 10\,\mathrm{MHz}$ and the radio FM band at $\sim 85\,\mathrm{MHz}$. Since the collecting area A is related to the beam width w and the observing wavelength λ via $A \times w = \lambda^2$, the collecting area at zenith varies from $88000\,\mathrm{m}^2$ at $15\,\mathrm{MHz}$ to $8000\,\mathrm{m}^2$ at $85\,\mathrm{MHz}$, the corresponding fields of view range from $\sim 46^\circ$ HPBW to $\sim 8^\circ$ and the angular resolution varies between 2.9° and 0.5° only for the core and up to $23'$ and $4'$ for the whole array in image synthesis mode.

The two linear polarisations (NE-NW) of each antenna are connected in parallel to several receivers, allowing to operate in four distinct modes: a standalone beam-former (with analog phasing and digital summation systems), a waveform capture mode (transient buffer),

---

[1] The array is presently under deployment and 80% should be achieved by the end of 2020.

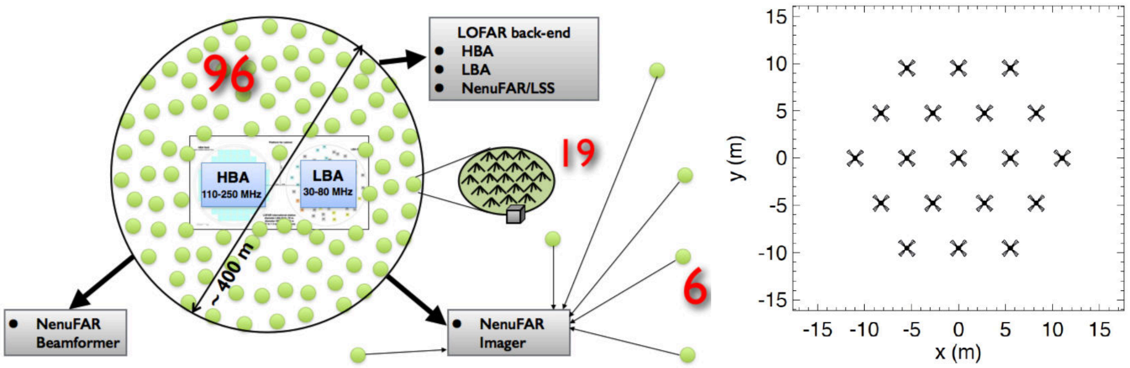

Figure 5.1: *Left:* NenuFAR array configuration. The core gathers 96 mini-arrays (MA) and 6 MA are located up to 3 km away from the core. Each MA contains 19 antennas. *Right:* antennas distribution inside a MA. Taken from [38].

a standalone imager and an upgraded LOFAR station mode called LOFAR Super Station (LSS) combining NenuFAR and the International LOFAR Telescope through the Nançay LOFAR station (FR606). The NenuFAR frequency resolution is $\mathrm{d}f \sim 195\,\mathrm{kHz}$ with a time resolution of $\mathrm{d}t \sim 5\,\mu\mathrm{s}$, which can be numerically channelled down to $\mathrm{d}f \sim 100\,\mathrm{Hz}$ with 2048 channels per sub-band at a cost of a lower time resolution $\mathrm{d}t \sim 10\,\mathrm{ms}$, since $\mathrm{d}t_{\mathrm{num}} = N_{\mathrm{freq}}\,\mathrm{d}t_{\mathrm{init}}$, where $\mathrm{d}t_{\mathrm{num}}$ is the numerical time resolution resulting from channelisation, $\mathrm{d}t_{\mathrm{init}}$ is the initial analogical time resolution and N_{freq} is the number of frequency channel, which increases with the resolution. Finally note that the raw waveform time resolution is 5 ns at 200 MHz, at digitisation ; a polyphase filter bank then splits the waveform in 1024 channels of 195.3125 kHz each (corresponding to 200 MHz/1024) and accordingly changes $\mathrm{d}t$ from 5 ns to $1024 \times 5\,\mathrm{ns} = 5.12\,\mu\mathrm{s}$.

Finally the sensitivity of NenuFAR varies from 130 mJy at 15 MHz to 9 mJy at 85 MHz for one hour integration time with a frequency resolution of $\mathrm{d}f = 10\,\mathrm{MHz}$. This makes NenuFAR one of the most sensitive radio telescopes at LF (below 85 MHz).

5.2 The ES05 Pilot Program

In this section I present the Pilot-Program, which aims at detecting the first FRB in the LF domain.

5.2.1 Expected results and perspectives

At the end of this Pilot-Program we will face two possibilities:

- Either none of the targeted FRBs will have been observed with NenuFAR and strong constraints can be put on the emission of FRBs at LF (at least repeating ones).
- Or at least one FRB will have been observed and characterised in the NenuFAR frequency band, thus allowing us to prove the existence of FRBs at LF and opening the way for a systematic survey of FRBs in the LF band. This survey will then become a NenuFAR Key-Program on its own.

In case a FRB is detected, it will prove the existence of emission at LF and will provide a measurement of its spectrum, polarisation (if any), an accurate estimate of its DM, RM and scattering time, and their variations from one occurrence to another (see Section 4.1). If SNR permits, we may have access to the fine time-frequency structure of the bursts. This characterisation of the emission will provide important new constraints on the FRB models. A detection will also motivate a blind search Key-Program of more LF FRBs, in connexion with the *Pulsars Key-Program* and *Transients Key-Program* currently running in NenuFAR. Additional side results of the blind survey will include other radio transients (e.g. Rotating Radio Transients [278] or Pulsar Giant Pulses [279]).

In the long term perspective, this Pilot-Program and hopefully the subsequent Key-Program on FRB with NenuFAR will lay the ground for an equivalent program to be run with SKA-Low.

5.2.2 Observation strategy

The observation strategy aims at optimising the possibility to detect FRB repeaters. Prior knowledge of the characteristics of these FRBs allows us to run simulations from which the best observing parameters and analysis strategy can be defined. This step was performed while the latest 16 MA of NenuFAR were being installed, totalling 50 operational MA, with which the first observations have been carried on so far (80 MA should be deployed by the end of fall 2020).

5.2.2.1 Targets selection

The Pilot-Program targets repeating sources already observed by CHIME [280], with a known location and accessible with NenuFAR (northern hemisphere). At the beginning of this observation program, CHIME was the radio array with the closest observation frequency range with a detected FRB repeater, it motivated the choice of observing FRBs detected by this experiment[2].

---

[2] The closest radio telescope to NenuFAR in frequency range is Pushchino (111 MHz), however its only potential FRB target was only categorised as candidate repeater. Nevertheless, this Pushchino FRB was recently added to the target list as well as a periodical FRB repeater discovered by CHIME and recently

In order to maximise the detection chances, FRB targets are chosen with relatively low DM (see Section 4.1), high fluence and low scattering time. The targets are therefore close-by and bright, with signals expected not to be too diluted toward the low frequencies. We list below a few selected candidates which are all FRB repeaters (if not mentioned otherwise).

FRB180814 presents exceptionally favourable characteristics for detection at LF by NenuFAR. It has a DM $\sim 190\,\mathrm{pc.cm^{-3}}$. It is relatively intense with a fluence $\sim 10-60$ Jy.ms and duration $10 - 60$ ms, i.e. a flux density of order 1 Jy. It is not excessively scattered, ≤ 3 ms at 400 MHz, corresponding to ≤ 2 s at 8 MHz (with a variation in $\sim f^{-4}$). It is always observable with NenuFAR with R.A = 04 h 22 m 22 s and $\delta = +73°4'$, thus circumpolar as seen from Nançay. It was discovered by CHIME in August 2018 and repeated 6 times in 45 days.

FRB181030 is the closest know FRB with a DM $\sim 100\,\mathrm{pc.cm^{-3}}$, however it is less bright with a fluence ~ 7.3 Jy.ms. No scattering has been measured yet and it is therefore probably very low. Finally the source is also circumpolar, at R.A. = 10 h 54 m, $\delta = +73°44'$.

FRB121102 Is the first discovered repeater and is the most distant source targeted with a high $DM \sim 560\,\mathrm{pc.cm^{-3}}$, and also the lowest fluence ~ 1.2 Jy.ms. The source is not circumpolar, at R.A. = 05 h 31 m 58 s, $\delta = +33°08'$ but it is one the few sources jointly observed with the Nançay Radio Telescope (NRT). Since the NRT has already observed and detected FRB121102, we perform some target opportunity observation (ToO) when this source is in activity and observed with the NRT.

5.2.2.2 Simulation study

As already mentioned, the observation parameters are optimised through simulations. This study consists in simulating FRB-like signals with characteristics matching (or close to) the one of the targeted sources. Then, the simulated signals are used in a detection simulation code to see how we can maximise the SNR, hence the detection capability, by varying the frequency resolution, the time resolution and the number of MA used. These simulation tools have been developed by Philippe Zarka in [276].

Figure 5.2 displays the LF simulated time-frequency signal for parameters close to those of FRB180814. However the fluence at the reference frequency of 400 MHz is chosen much higher for illustration purposes, and the energy spectral index is set to 0 here. However the

---

observed by uGMRT (300 MHz).

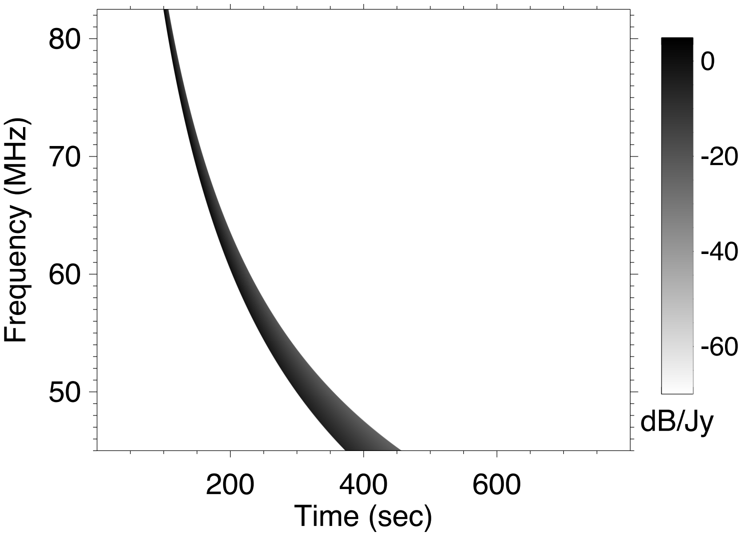

Figure 5.2: FRB simulated signal in the time-frequency plane. The FRB fluence is 600Jy at 400 MHz, with a DM = 190 pc.cm^{-3}, and the fluence spectral index is 0. The dispersion effect can be clearly seen as the delay between the signal arrival at high and low frequencies, and the scattering effect appears in the temporal broadening toward the LF. The signal is introduced at $t_0 = 100$ s.

DM and the scattering time match those of FRB180814. The expected features of LF FRBs can be seen in the time delay of the signal which is intrinsically of few ms at 400 MHz but due to the dispersion, spans over hundreds of seconds at low frequency (f^{-2} dependency, see Section 4.1). In addition, the time broadening of the signal toward the LF domain, appear clearly due to the scattering of the signal. These two effects are mainly responsible for the dilution of the signal. Thus we must choose tuned observational parameters to limit at best the signal losses.

The detection can only be achieved if the source appears brighter than the background sky fluctuations when measured by the array. Figure 5.3 shows the spectral and time characteristics of the sky background, taking into account galactic noise. The left panel displays the intensity of the background noise as a function of frequency, where the increase at low frequency corresponds to the galactic noise component. The right panel displays the time-frequency signal of the background noise, which is stationary at our timescales.

Figure 5.4 presents the resulting FRB signal taking into account the background noise. The difference between the left and right panels is a correction a posteriori on the signal called flattening, and corresponding to an equal re-weighting of the frequencies to diminish the spectral slopes induced by the galactic noise. Note that for NenuFAR the spectral slope is small because $T_{\text{sky}} \propto f^{-2.55}$ and $A_{\text{eff}} \propto f^{-2}$.

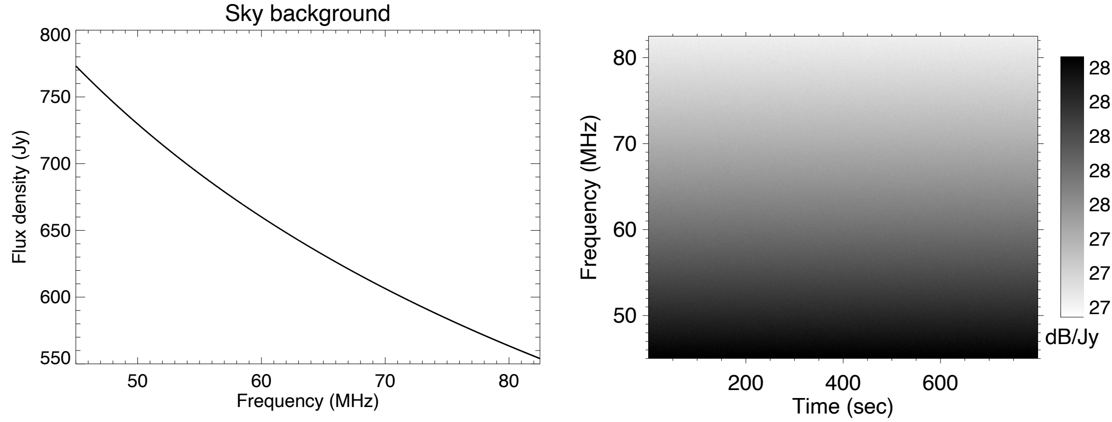

Figure 5.3: Background sky noise as seen by NenuFAR with 96 MA. *Left:* Galactic spectrum for a sky temperature of $T_{\rm sky} \sim 60cf^{-2.55}$ with f the emission frequency and c the vacuum speed of light. *Righ:* Flux density (unpolarised) corresponding to $= 2k_{\rm B}T_{\rm sky}/A$ with $k_{\rm B}$ the Boltzmann constant and $A_{\rm eff}$ the collecting area fo the 96 MA. It can be noticed that for our timescales, the background sky is stationary.

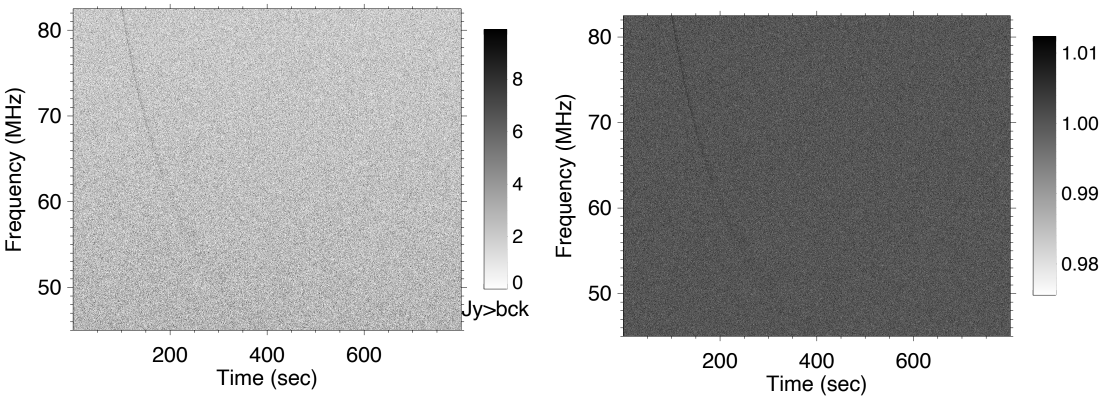

Figure 5.4: FRB simulated signal observed by 96 MA in the time-frequency plane for a frequency and time resolution of $\mathrm{d}f = 3\,\mathrm{kHz}$ and $\mathrm{d}t = 21\,\mathrm{ms}$, taking into account the sky background noise. Left: without any correction. Right: with spectral flattening to correct for the spectral slope induced by the galactic noise (see Section 5.2.3.2).

From the resulting signal obtained on Figure 5.4, the detection procedure consists in testing various DM, and correct for the associated dispersion effect. The correct DM will corresponds to a FRB signal rising from the noise before integrating over all frequencies. Figure 5.5 presents the DM scan: all the time series (of the signal FRB+background at the highest NenuFAR resolution – $\mathrm{d}f = 3\,\mathrm{kHz}$ and $\mathrm{d}t = 1\,\mathrm{ms}$ –) are integrated over all

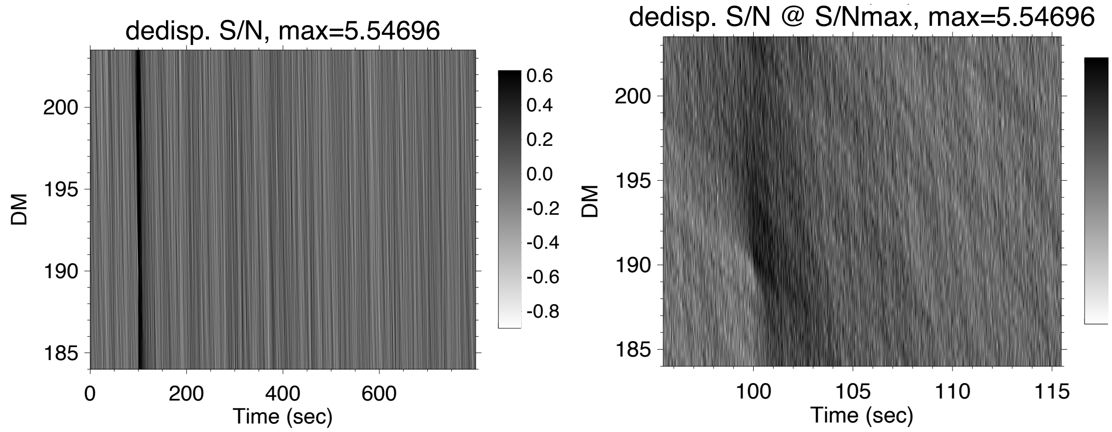

Figure 5.5: Blind DM search for the FRB simulated signal of Figure 5.4. *Left:* full DM and time range. *Right:* zoom on the highest SNR area.

the frequency domain for each DM value. The result is then normalised at each frequency by the standard deviation of the noise, hence a dynamical spectrum of the SNR. On the left panel, we can see that at the time of the signal ($t_0 \sim 100\,\mathrm{s}$) the SNR is larger for any tested DM range but on the right panel, the zoom allows us to clearly see that in fact, the highest SNR is achieved for a DM value of $\sim 193\,\mathrm{cm.pc}^{-3}$ very close to the true DM $\sim 190\,\mathrm{cm.pc}^{-3}$.

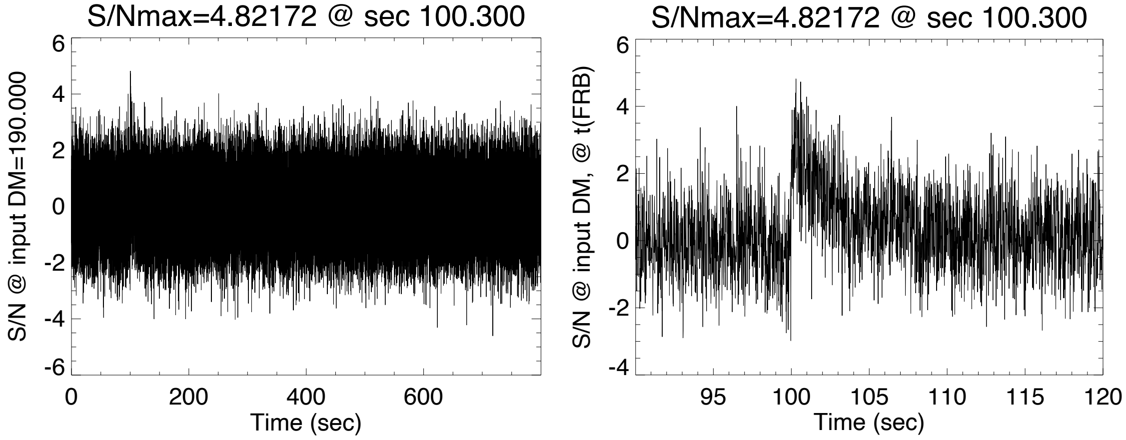

Figure 5.6: Frequency-integrated signal at the true DM of the simulated signal of Figure 5.4. *Left:* full time range. *Righ:* zoom on the highest SNR signal.

Figure 5.6 shows the frequency integrated signal obtained at the true DM ($190\,\mathrm{cm.pc}^{-3}$). The FRB signal can be identified at $t \sim 100\,\mathrm{s}$, with a specific temporal structure very different from the background noise, even though the SNR is only of 4.8.

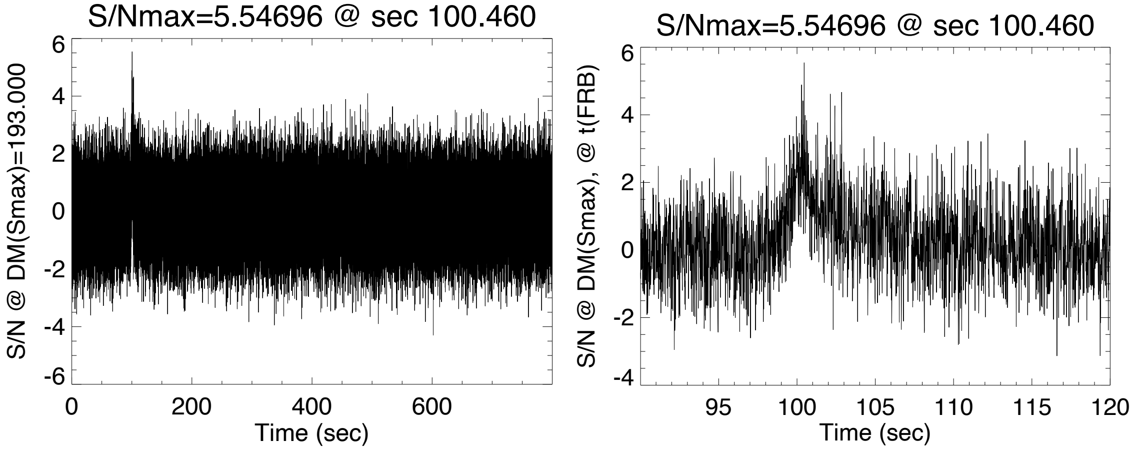

Figure 5.7: Same as Figure 5.6 but for the best DM shown on Figure 5.5.

Figure 5.7 shows the same signal for the best DM $\sim$ 193 found on Figure 5.5. In this case the FRB signal rises at a higher SNR, well above any background signals. The temporal broadening of the signal leads to a slight over-estimation of the DM for a basic SNR search. Indeed, at low frequency the signal is diluted due to the temporal broadening therefore to search the maximum of signal the scan will slightly increase the DM to reach the "middle" of the signal. However this expected result can be corrected a posteriori, to deconvolve the DM and spectral broadening effects on the time delays.

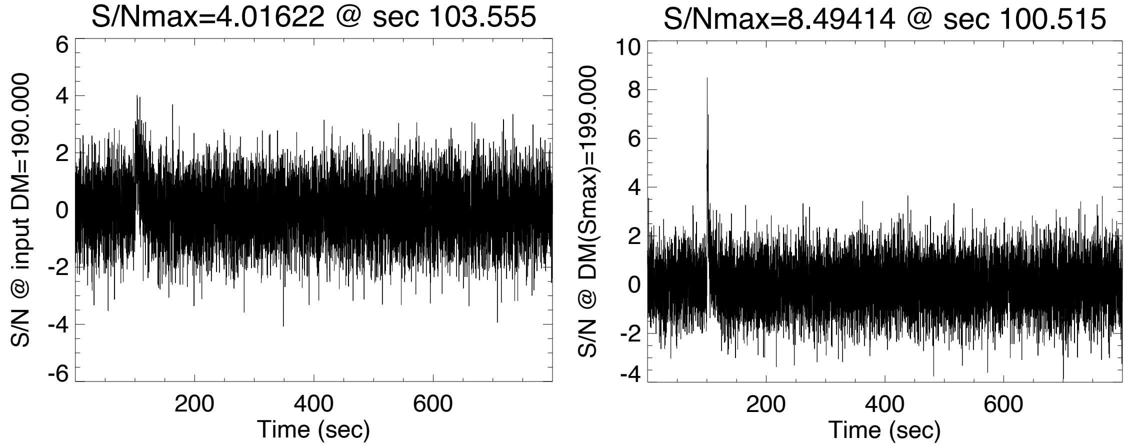

Figure 5.8: Similar to Figures 5.6 and 5.7 for a frequency and time resolution of $\mathrm{d}f = 12\,\mathrm{kHz}$ and $\mathrm{d}t = 84\,\mathrm{ms}$. *Left:* true DM. *Right:* best DM.

Figure 5.8 presents the frequency integrated signals for the true DM (as Figure 5.6) and for the best DM search (as Figure 5.7), for a lower frequency and time resolution $\mathrm{d}f = 12\,\mathrm{kHz}$ and $\mathrm{d}t = 84\,\mathrm{ms}$. In this observation configuration, the signal rises at an SNR above 8 for the best DM found. Again this effect is expected from the temporal broadening of the signal. A lower resolution may indeed attenuates the noise through the averaging but it will also increase the observed temporal broadening and therefore lead to a higher over-estimation of the DM.

Figure 5.9 presents the results of a general study of the effects of the observation parameters on the detection of FRB signals for FRB characteristics close to the FRB180814 target. The left panel presents the effect of the time and frequency resolution on the SNR of a FRB signal similar to FRB180814 and the right panel presents the evolution of the difference between the true DM and the best DM as function of the intrinsic DM and scattering time τ of the FRB signal for the best and second best SNR (corresponding to the set of parameters leading to the second best SNR value). It appears that detection SNR are maximised for two set of time and frequency resolutions $(84\,\mathrm{ms}, 12\,\mathrm{kHz})$ and $(84\,\mathrm{ms}, 6\,\mathrm{kHz})$ but this parameters sets are subject to fluctuations depending on the FRB characteristics.

Therefore, a frequency and time resolution of $(21\,\mathrm{ms}, 3\,\mathrm{kHz})$ are chosen for our observations, in order to account for FRB fluctuations from one target to another and from high frequencies to LF. It is a compromise between space storage optimisation and flexibility for post frequency and time integrations at later stages in the analysis.

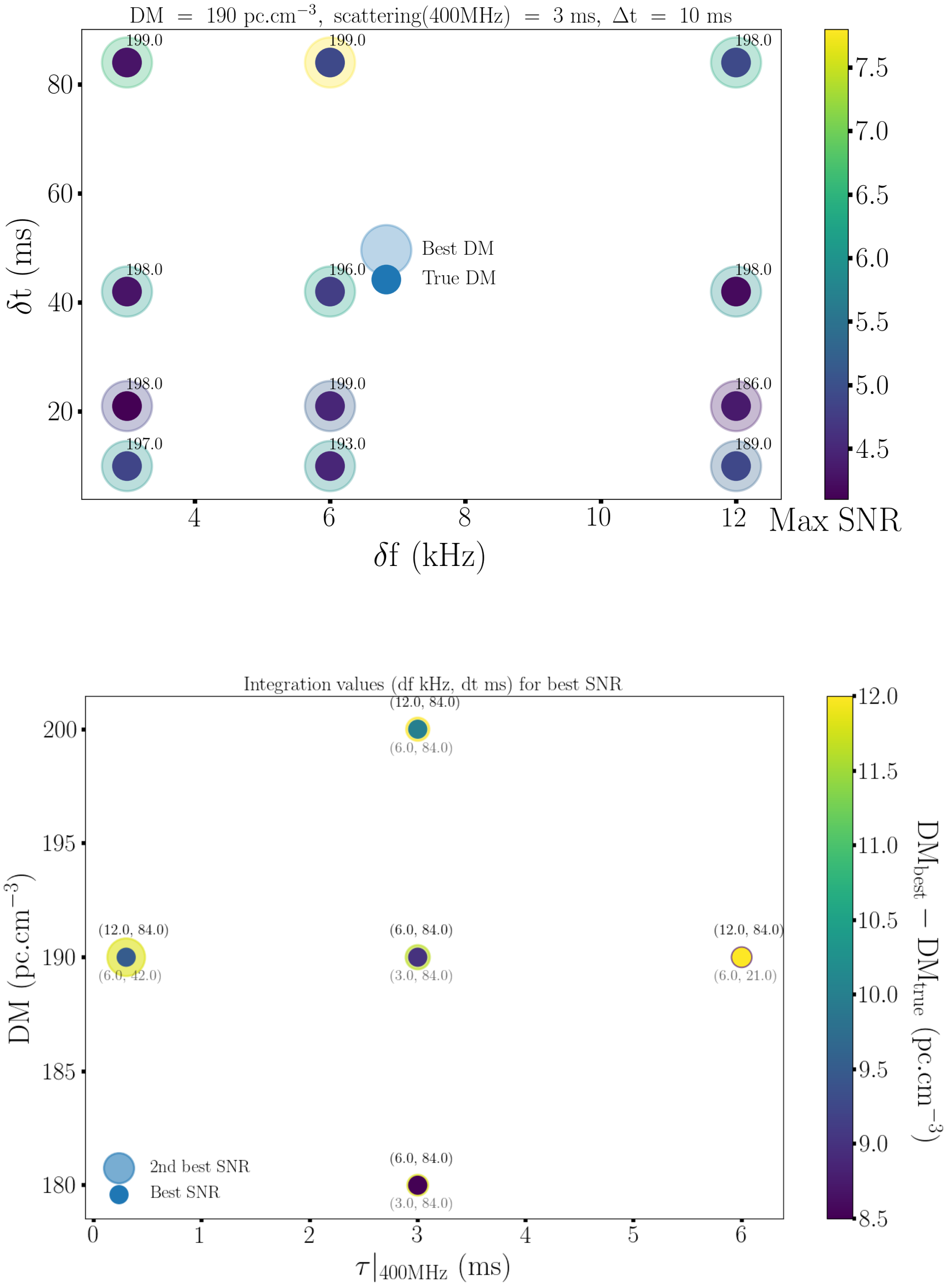

Figure 5.9: Study of the effects of the observation parameters on the detected SNR of FRB signals. *Top:* Evolution of the SNR, for various frequency and time resolution, corresponding to the true DM or the best DM. *Bottom* Evolution of the difference between the true DM and the best DM as a function of the DM and scattering time τ, with the corresponding best SNR and second best SNR for the corresponding observation parameters. High resolutions (in time and frequency) are not required to detect FRB signals with high SNR, therefore a reasonable resolution of $(21\,\mathrm{ms}, 3\,\mathrm{kHz})$ can be chosen as a compromise between space storage convenience and flexibility in the analysis (post integration of signals in order to find the true DM).

5.2.2.3 Technical parameters

In this section, I detail the technical parameters requested for the observation strategy, and for a part based on the simulation study results.

Observation time: a total of 240 h per semester has been requested (and granted), grouped in 10 h observations runs, distributed over the semester. This provides twice the coverage of the initial CHIME observations. There is no constraint in night/day observations nor specific time of the year.

Observing mode: it consists in beam-formed observations, where all MA of the core are used to form one single beam (analog and digital) to ensure maximum sensitivity. The beam continuously tracks the source in the sky (due to Earth rotation). The observation frequency band is chosen between $45 - 82.5$ MHz, resulting in a bandwidth of 37.5 MHz with a 3 kHz frequency resolution thanks to a numerical channelisation. Finally, the time integration is set to 21 ms (see Section 5.2.2.2).

Calibration: the main requirement is a good calibration of all the relative MA phases (done at the beginning of the early science phase) to ensure coherent beam-forming with maximum sensitivity. In case of detection, flux calibration is based on other observations programs or the Galactic background itself, while polarisation calibration in beam-formed mode is based on observation of calibrators such as Jupiter for qualitative measurements or a polarised calibrator as for LOFAR for quantitative measurements.

Possible joint observations: NenuFAR FRB121102 observations are coordinated with observations at higher frequencies from the NRT. It must be noted that the dispersion time delay between high frequencies $\sim$GHz and 80 MHz is ≈ 2 min.

5.2.3 Data analysis strategy

The Stokes parameters [281] of the time-frequency spectrum are derived from the observations outputs. In this data analysis the burst search is solely based on the Stokes parameter I, related to the amplitude of the signal. In a second step, when the burst is detected the circular polarisation parameter V and linear polarisation parameter $L = \sqrt{U^2 + Q^2}$ can be used to study the polarisation characteristics of the signal.

The burst search strategy follows three steps: first the radio frequency interference (RFI) are removed, then the time-frequency spectrum is corrected from instrumental and background features and finally a SNR search is performed following the processing presented in [276, 282].

5.2.3.1 RFI mitigation

RFI are mostly produced by human activity, for instance satellites communications, planes, cars, and so on, but are usually easy to discriminate thanks to their narrow emission frequency or narrow periodic temporal structure. In addition lightnings can also be a source of noise, and corresponds to broadband un-dispersed spikes.

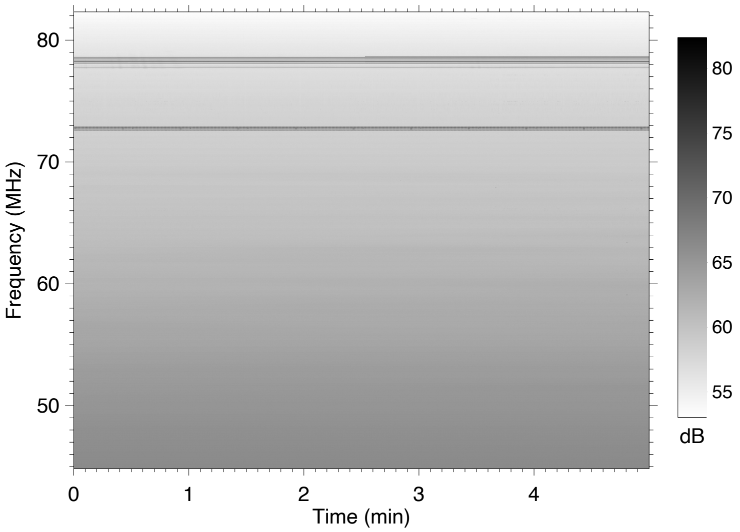

Figure 5.10: Illustration of a dynamical spectrum in the frequency-time plane, corresponding to 5 minutes out of a 10 h observation of the location of FRB181030 in May 2020. In the upper part of the spectrum, intense mono-frequency emissions corresponding to unidentified emitters can be observed.

Figure 5.10 presents an example of dynamical spectrum in the frequency-time plane. In the upper part, corresponding to the highest frequencies of the spectra, several intense horizontal lines can be seen, corresponding to unidentified emitters. Since these frequency bands are polluted at all times, the best procedure is to simply identify and mask these frequency channels

The usual method to remove narrow frequencies consists in integrating the time-frequency spectrum over time, and proceeding iteratively by setting to zero the emission spikes above a given threshold (defined by the desired level of cleaning) around a small number of frequencies (again defined by the desired level of cleaning). For instance if an emission at frequency f_0 is found to be above the SNR threshold, then all emissions contained in a given range $(f_0 - N \times \mathrm{d}f\,, f_0 + N \times \mathrm{d}f)$ are set to zero, where $\mathrm{d}f$ is the frequency resolution and N is the number of frequency pixels selected for cleaning.

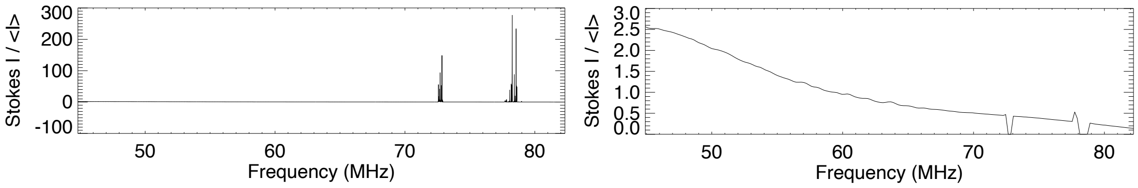

Figure 5.11: Same data as Figure 5.10, projected in the frequency domain. *Left:* without narrow frequency corrections, the large vertical spikes corresponding to the narrow emissions appears clearly around 73 − 78 MHz. *Right:* after narrow frequency correction, all the noise emissions above the correction SNR threshold are set to 0, the spectral slope appears clearly now. Note that the y axis corresponds to the value of the Stokes parameter I normalised to its mean value.

Figure 5.11 displays an example of spectrum in the frequency domain, with narrow frequency emissions (left panel) removed after correction (right panel).

Narrow broadband spikes (e.g. lightnings) can be removed in a similar manner as narrow frequencies. In this case, the time-frequency spectrum is integrated over the frequencies and an iterative cleaning process is applied depending on a SNR threshold value and the desired emission width. For instance if an emission at time t_0 is found to be above the SNR threshold, then all emission contained in a given range $(t_0 - N \times \mathrm{d}t\,, t_0 + N \times \mathrm{d}t)$ are set to zero, where $\mathrm{d}t$ is the time resolution and N is the number of time pixels selected for cleaning.

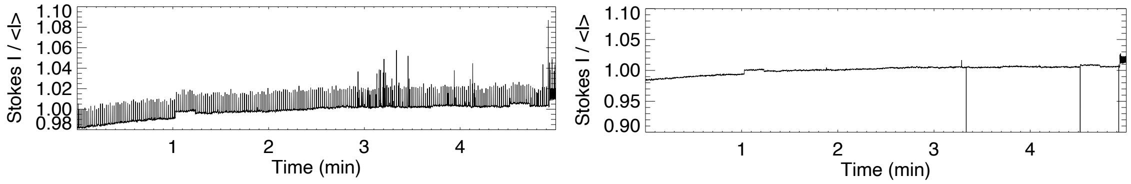

Figure 5.12: Same spectrum as Figure 5.10, corrected from narrow frequencies (see Figure 5.11) and projected in the time domain. *Left:* without narrow temporal corrections, hence the vertical spikes correspond to temporal narrow emissions. *Right:* after narrow temporal correction, all the noise emissions are set to 0, only remain the temporal gain variations. Note that the y axis corresponds to the value of the Stokes parameter I normalised to its mean value.

Figure 5.12 shows an example of spectrum in the time domain, with narrow temporal emissions (left panel) and after correction (right panel).

The RFI mitigations presented here is very basic but relies on the knowledge of the targeted signal and the environment background. More sophisticated methods exist but are of no need in this study due to the very specific shape (strongly dispersed) of the signal and the very clean background in our frequency range.

5.2.3.2 Time-frequency slope corrections

The spectrum resulting from RFI mitigations presents some spectral distortions. Indeed, due to the background frequency dependency (mostly coming from the Galactic noise), the measured spectrum also presents a frequency dependency. In addition, the measured intensity varies in time (beside the intrinsic variations of the source) for several reasons: variations of the signal intensity with the zenith angle, repointing phases leading to intensity jumps, weather conditions, etc. Once again, thanks to the type of signal targeted here, we can easily correct for these distortions by a direct re-weighting of each frequency channel based on the instrument bandpass response, a process called spectral whitening. This brutal process can be applied safely in our case since the bursts identification is achieved via the structure analysis. In addition the spectral content of FRBs is expected to span over a large number of frequency channels, therefore an equal treatment of all the frequency channels will not deteriorate the signal too much.

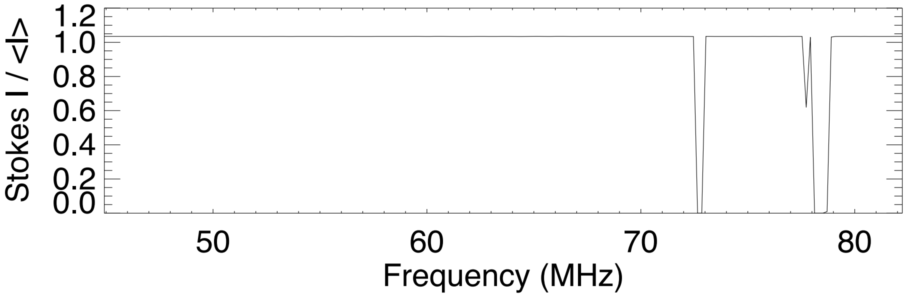

Figure 5.13: Same spectrum as Figure 5.10, corrected from narrow frequencies (see Figure 5.11), narrow temporal emissions (see Figure 5.12) and frequency flattened. The spectral slope observed before is now corrected to 0. Note that the y axis corresponds to the value of the Stokes parameter I normalised to its mean value.

Figure 5.13, provides an illustration of the spectral whitening, the spectrum slope is corrected and now equals to 0 over the whole bandwidth.

The intensity of the signal received in the beam varies with time and with weather conditions. Therefore when the beam is tracking a source in the sky, temporal variations may appear. In addition, due to the analog pointing of NenuFAR, some intensity jumps at tens of second intervals may appear when the telescope is tracking a source. They result from the switching of cable lengths to point the new position, leading to a discrete repointing from one direction to another with a new signal flux from that direction. This correction can be very similar to the spectral whitening.

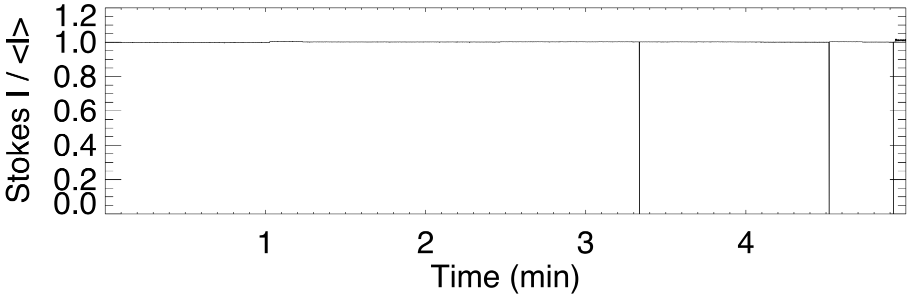

Figure 5.14: Same spectrum as Figure 5.10, corrected from narrow frequencies (see Figure 5.11), corrected from the narrow temporal emissions (see Figure 5.12), frequency flattened and time flattened. Most of the gain variations are suppressed. Note that the y axis corresponds to the value of the Stokes parameter I normalised to its mean value.

Figure 5.14, displays an example of correction applied to the spectra of Figure 5.12 in the time domain.

The spectrum corrections are relatively simple and easy to apply since the targeted signal is very brief in time and large in frequency.

5.2.3.3 Burst search

The burst search relies on an SNR search, after RFI mitigation and spectrum correction. The detection procedure is exactly the same as in the simulations presented in Section 5.2.2.2. A range of DM is explored in order to correct for the dispersion of the signal. Thanks to prior knowledge on the target, the search range can be greatly reduced and therefore explored in greater details. The optimisation of the detection procedure then depends on the choice of time and frequency integration parameters. These parameters can be fine-tuned to reduce the background noise without degrading too much the FRB signal as already explained in Section 5.2.2.2. Finally depending on the SNR, the temporal structure and sub-structures (expected in some FRBs see Section 4.1) could also be detected and would provide a strong criterium for FRB identification.

In practice the order of these three analysis steps is not fully respected. For space storage convenience, the de-dispersion within the bandwidth[3] integrated at the average expected DM (from other radio telescope observations) is first applied (ideally briefly after the observations), and the frequency domain can be reduced by integration to only $2-4$ channels per 194 kHz sub-band, thus allowing almost a factor 100 in space storage reduction. Then, for the burst search, as for simulations, the signal is de-dispersed over all the channels for a refined DM scan, and the frequency or time resolution can be reduced depending on the optimal detection parameters.

5.2.4 Present status of the pilot program

The Pilot-Program ES05 is ongoing, with two semesters of observations completed: July 1st to December 31st of 2019 and January 1st to May 31st of 2020. A third semester is ongoing from June 1st to November 30th of 2020.

Observations status

FRB180814 has been observed for 40 h in 2019 and 80 h in 2020 (so far), corresponding to $\sim$ 2.1TB of data in total.

FRB181030 has been observed for 80 h in 2020 for a total of $\sim$ 1.4 TB of data.

FRB121102 has been observed for 10.5 h in 2019 for a total of $\sim$ 200GB of data.

In support to an observation campaign with INTEGRAL from 2019/08/30 to 2019/09/03, the NRT performed observations of 1 h/day around the transit of the source at Nançay meridian from 2019/08/30 to 2019/09/06. Despite the very large DM of this source, we took this opportunity to perform NenuFAR observations simultaneous to NRT ones, from 2019/08/31 to 2019/09/06, during $\sim$ 1h30 per day (taking into account the delay of several minutes between the NRT observation frequency of 1.5 GHz and the NenuFAR frequency range).

Analysis status is very preliminary. No signal has been detected yet but only a very small fraction of the data have been analysed up to now ($< 1\%$). Analysis tools have been tested and improved during the first semester and beginning of the second. In the next months all the data will be analysed with the stable version of the analysis tools.

---

[3] The idea is to de-dispersed inside each channel at the expected DM, but not over all channels. Doing so a refined search of the optimal DM can be performed over all channels around the expected DM value.

Data reduction status The first step of the analysis will consist in reducing the data volume by a factor 8 to 32 through RFI flagging, de-dispersion and spectral integration at $1-4$ channels per sub-band.

For the third ongoing semester of observations, additional targets will be added to diversify the observed FRB characteristics: FRB151125 observed by the Pushchino observatory (Rodin-2018-Atel-AC), two additional CHIME targets (FRB190303 and FRB180916) and finally a zenith pointing for blind FRB search.

5.3 Toward a GRAND FRB program ?

GRAND will be a giant radio array with thousands of antennas optimised between the frequency domain of NenuFAR and below CHIME. Its primary goal is the study of the UHE neutrino and the astroparticles in general but even un-phased, the array is fully capable of detecting transient radio signals (see Section 2.1.4).

5.3.1 Observation mode

The summing of incoherent Fourier transforms from all the antennas enables the detection of transient radio-signals, with a SNR proportional to $\sqrt{N_{\rm ant}}$ where $N_{\rm ant}$ is the number of antennas. Incoherent summing does not reach the sensitivity of an equivalent phased array, but the large number of antennas in GRAND makes it competitive. For 200 000 units it would corresponds to 775 equivalent phased antenna (summing over all three polarisation leads to the equivalent of $\sqrt{3}$ times more antennas). This method allows to infer the DM of a detected source but not to locate the source, except if the array is subdivided in smaller arrays located at large distances, allowing to triangulate the source (note however it might be difficult due to temporal broadening). This would be at the cost of sensitivity however, since dividing one array in N sub-arrays, leads to a sensitivity divided by $\sqrt{N}$.

The game-changing advantage of the project is that with non phased array the whole sky can be monitored since the field of view of the array is equal to the field of view of one single antenna with a duty cycle of 100%. This full-sky survey would be effective for events with energies above ~ 100 Jy for one hotspot of 10 000 units (see Section 5.3.2), in the best case scenarios, GRAND could detect thousands events per day.

This technique could be already tested on the engineering radio array GP300 with 300 antennas, corresponding to ~ 30 equivalent phased antenna (summing all polarisations).

5.3.2 Typical targets

Following the simulation procedure of Section 5.2.2.2, we can simulate the FRB detection with a GRAND-like spot of 10 000 antennas, through an incoherent summation with a time and frequency resolution $\mathrm{d}f = 25\,\mathrm{kHz}$ and $\mathrm{d}t = 10\,\mathrm{ms}$.

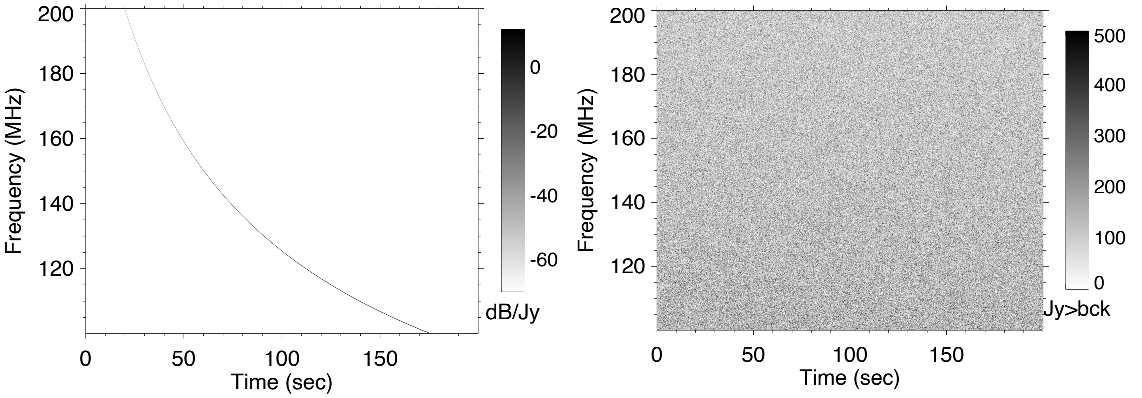

Figure 5.15: FRB simulated signal with DM= $500\,\mathrm{pc.cm}^{-3}$, emission width $\delta w = 10\,\mathrm{ms}$, scattering $\tau = 0.1\,\mathrm{ms}$ at $600\,\mathrm{GHz}$, fluence $F = 20\,\mathrm{Jy.ms}$ at $1\,\mathrm{GHz}$ and spectral index $\alpha = -1.6$.*Left:* signal intensity as function of the frequency.*Right:* signal and background in the time-frequency spectrum.

Figure 5.15 shows a typical FRB target for a GRAND-like array. Since a great diversity of FRBs has been observed, we use this flexibility in the choice of the parameters to build a standard FRB event within the parameters ranges observed: DM $= 500\,\mathrm{pc.cm}^{-3}$, emission width $\delta w = 10\,\mathrm{ms}$, scattering $\tau = 0.1\,\mathrm{ms}$ at $600\,\mathrm{GHz}$, fluence $F = 20\,\mathrm{Jy.ms}$ at $1\,\mathrm{GHz}$ and spectral index $\alpha = -1.6$.

Figure 5.16 displays the blind DM search of the FRB presented on Figure 5.15 and finally Figure 5.17 shows the frequency integrated signal with a clear detection of the FRB at a SNR ~ 8.

The detection of FRB signals even with a non phased array seems feasible with a GRAND-like configuration. Furthermore the wide variety of FRB events and their profusion in the Universe is promising, it seems reasonable that a fraction will be observable with GRAND and even GP300. The question will then be what are the characteristics of these events and which fraction of the total subset do they represent. Additionally we should also expect other radio transient such as the Galactic magnetars, recently observed [31], and maybe even new sources.

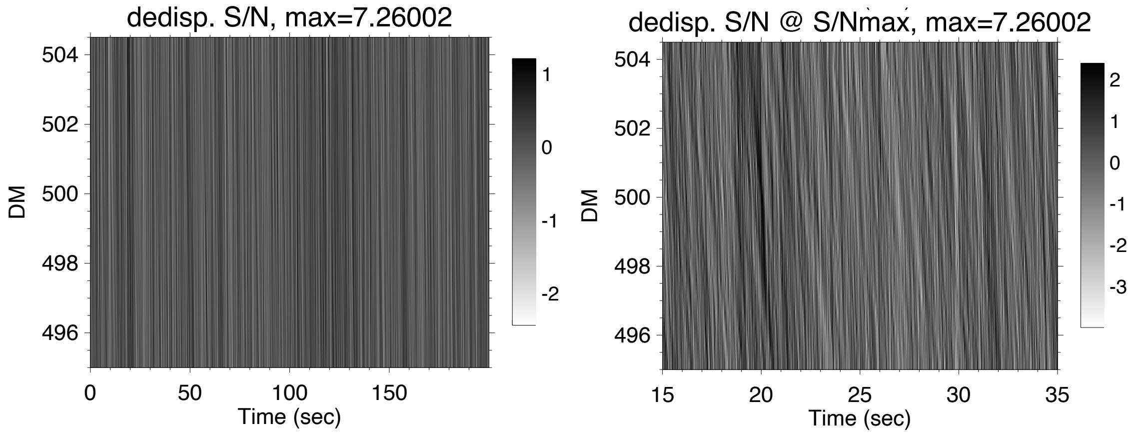

Figure 5.16: Blind SNR search for various DM tests of the FRB signal of Figure 5.15. *Left:* in the full DM range. *Right:* zoomed in the highest SNR range.

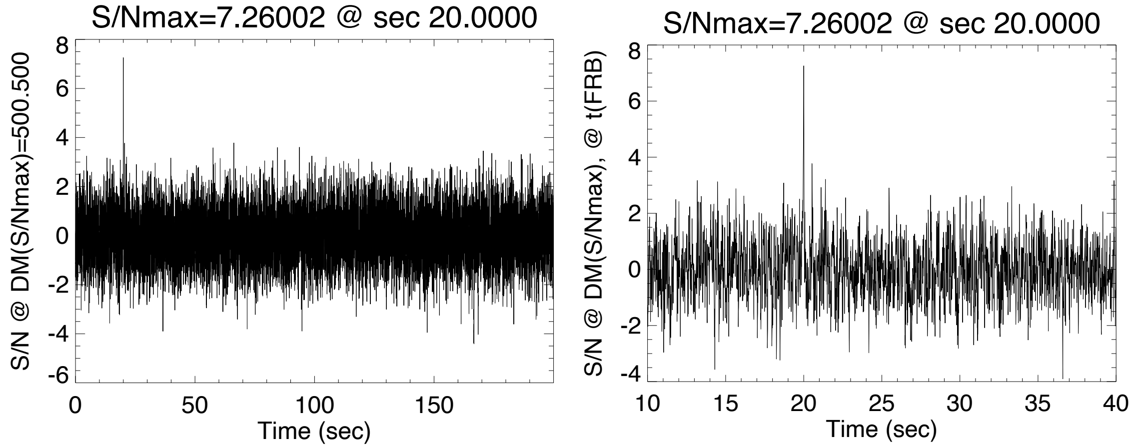

Figure 5.17: Frequency integrated spectra at the best DM found on Figure 5.16. *Left:* over the full simulation time. *Right:* zoomed in the highest SNR range.

Conclusion

My work has been driven by the following perspective: the low-energy end of the electromagnetic spectrum, namely the *radio* band, contains key information on the highest energy Universe. I have worked at the interface between different fields, contributing to radio-detection of astroparticles and to radio-astronomy, and building models of astrophysical sources detected by both techniques.

Since the high-energy neutrinos were detected by IceCube in 2013 [19], two major questions were raised: what are the sources of this diffuse flux, and can we detect neutrinos at higher energies ($> 10^{15}\,\mathrm{eV}$).

Neutrino emissions from neutron star mergers have been extensively studied from the gamma ray burst perspective (see e.g. [44]). Triggered by the first observation of a neutron star merger event in gravitational wave, GW170817 and of its electromagnetic counterpart, GRB170817 [3], I developed in this thesis an *isotropic* neutrino emission model from the kilonova [36]. Following the coalescence of binary neutron stars, debris from the merger which remain marginally bound to the central compact remnant will fall-back at late times, feeding an accretion flow [78]. Under the assumption that such flows can power the acceleration of cosmic rays to ultra-high energies, we calculated their propagation and interactions through the outer dynamical ejecta.

For one of our (optimistic) scenarios, the diffuse flux could contribute to $\sim 10\%$ fraction of the observed IceCube flux. This leaves room for a future experiment with increased effective area such as IceCube-Gen2, to detect an underlying flux, in particular if cross-correlation and stacking searches with gravitational wave signals are conducted [44]. Such searches are favoured in the present model, as the predicted fluxes are isotropic.

The detection of the elusive ultra-high energy neutrinos, guaranteed by the cosmogenic diffuse flux and predicted to be produced by many powerful sources, is tied to the development of new generations of detectors. The current instrumented volumes are indeed not sufficient to reach a sensitivity that would ensure their detection. Today, experimental efforts are directed towards new neutrino observation techniques and large-scale deployment. In this token, the GRAND collaboration endeavours to perform a radio detection of extensive air showers from Earth-skimming neutrinos with a large-scale array [23]. As a member of this collaboration, I have studied the impact of the detector topography on the detection efficiency of the Earth-skimming neutrinos [37]. The trajectories of these neutrino-induced extensive air showers, combined with the strong beaming of the signal lead to significant detection losses for standard flat arrays. However these signal losses can be largely recovered as soon as the detector topography is inclined of a few degrees. Therefore the deployment of arrays in mountainous regions would greatly profit to the technique.

I have also developed new methods for the reconstruction of detected events from the radio signals of extensive air showers, focussing in particular on the arrival direction of the primary neutrino. The method described in this thesis allows us to reach an accuracy better than 0.1°, improving greatly the current performances, and enabling neutrino astronomy with the radio technique. The method offers a new approach to the study of the very inclined and up-going extensive air showers and provides in addition an estimate of the nature of the primary.

The combination of their peculiar radio signatures and of their repeating events makes Fast Radio Burst (FRBs) mysterious and exciting for source modeling [225]. Besides, the lack of observations makes them a fruitful observational target. Any new measured quantities such as polarization or rotation measure is precious to constrain new models. On this topic again, I contributed both on the signal detection and on the source modeling aspects.

In this thesis, I presented a FRB source model based on a population of neutron star-black hole systems. Neutron stars are likely surrounded by winds, gas, debris and asteroid belts. Kozai-Lidov perturbations [233], induced by a distant, but gravitationally bound black hole, can trigger the infall of such orbiting bodies onto the central neutron-star. These effects could lead to the emission of FRBs, e.g., by asteroid-induced wake-fields in the wind of the neutron-star [227]. The infall rate of asteroids in neutron star-black hole binary systems is found to be consistent with the population rates of FRBs and the distribution in widths of the binary system is found to explain the dichotomy between repeating and non-repeating sources. In this model, all FRB progenitors are repeaters, but the activity period of two consecutive bursts spans between day scales to hundreds of years. Therefore, we predict that given our observation window constantly increasing in time, FRBs categorised as non repeater will repeat eventually. One can note finally that FRBs should provide a unique electromagnetic counterpart to the gravitational waves emitted when such systems merge.

The key to the FRB mystery certainly lies in the diversification of the experimental constraints. Although the number of FRB observations did strongly grow over the last years, the radio domain has not been fully explored, and frequencies below 111 MHz remain a dark spot where important clues could lie. In this thesis, I presented an observation program aiming at the detection of FRBs below 85 MHz, initiated by Philippe Zarka and myself. This observation program will provide new constraints on the existence and the characterisation of FRBs at these frequencies. Observations are ongoing and preliminary results will be available soon.

During my Ph.D., I had the opportunity to work on very diverse topics: from astroparticle astronomy to millisecond radio astronomy, through theoretical and experimental approaches. Each of these domains have their own methods and techniques to study the high-energy mysteries of our Universe. It is therefore timely to build bridges between these communities, since the sources of our Universe no longer belong to one particular community with the advent of the multi-messenger era. Now comes the time to use every asset in our astronomy fields, to strengthen the instruments, gather the observation strategies and merge the theoretical models.

Bibliography

[1] B. Abbott, *et al.*, Observation of gravitational waves from a binary black hole merger, *Physical Review Letters* **116** (2016). arXiv:1602.03837.

[2] B. P. Abbott, *et al.*, GW170817: Observation of gravitational waves from a binary neutron star inspiral, *Physical Review Letters* **119** (2017). arXiv:1710.05832.

[3] B. P. Abbott, *et al.*, Gravitational Waves and Gamma-Rays from a Binary Neutron Star Merger: GW170817 and GRB 170817A, *The Astrophysical Journal: Letters* **848** (2017). arXiv:1710.05834.

[4] V. A. Villar, *et al.*, The Combined Ultraviolet, Optical, and Near-Infrared Light Curves of the Kilonova Associated with the Binary Neutron Star Merger GW170817: Unified Data Set, Analytic Models, and Physical Implications, *The Astrophysical Journal* **851** (2017). arXiv:1710.11576.

[5] A. Albert, *et al.*, Search for High-energy Neutrinos from Binary Neutron Star Merger GW170817 with ANTARES, IceCube, and the Pierre Auger Observatory, *The Astrophysical Journal: Letters* **850** (2017). arXiv:1710.05839.

[6] B. P. Abbott, *et al.*, Multi-messenger Observations of a Binary Neutron Star Merger, *The Astrophysical Journal: Letters* **848** (2017). arXiv:1710.05833.

[7] S. Garrappa, *et al.*, Investigation of two Fermi-LAT gamma-ray blazars coincident with high-energy neutrinos detected by IceCube, *The Astrophysical Journal* **880** (2019). arXiv:1901.10806.

[8] IceCube coll., Neutrino emission from the direction of the blazar TXS 0506+056 prior to the IceCube-170922A alert, *Science* **361** (2018). arXiv:1807.08794.

[9] K. Murase, *et al.*, Blazar flares as an origin of high-energy cosmic neutrinos?, *The Astrophysical Journal* **865** (2018). arXiv:1807.04748.

[10] S. Gao, *et al.*, Modelling the coincident observation of a high-energy neutrino and a bright blazar flare, *Nature Astronomy* **3** (2018). arXiv:1807.04275.

[11] M. Cerruti, *et al.*, Leptohadronic single-zone models for the electromagnetic and neutrino emission of TXS 0506+056, *Monthly Notices of the Royal Astronomical Society: Letters* **483** (2018). arXiv:1807.04335.

[12] H. Zhang, *et al.*, Variability and optical polarization can probe the neutrino and electromagnetic emission mechanisms of TXS 0506+056, *pre-print* ~ (2018). arXiv:1807.11069.

[13] A. Gokus, *et al.*, Decomposing blazar spectra into lepto-hadronic emission components, *Astronomische Nachrichten* **339** (2018). arXiv:1808.05540.

[14] N. Sahakyan, Lepto-hadronic γ-ray and neutrino emission from the jet of TXS 0506+056, *The Astrophysical Journal* **866** (2018). arXiv:1808.05651.

[15] R. Stein, *et al.*, A high-energy neutrino coincident with a tidal disruption event, *pre-print* ~ (2020). arXiv:2005.05340.

[16] C. Guépin, *et al.*, Ultra-high-energy cosmic rays and neutrinos from tidal disruptions by massive black holes, *Astronomy & Astrophysics* **616** (2018). arXiv:1711.11274.

[17] W. Winter, C. Lunardini, A concordance scenario for the observation of a neutrino from the Tidal Disruption Event AT2019dsg, *pre-print* ~ (2020). arXiv:2005.06097.

[18] M. Ackermann, *et al.*, Astrophysics uniquely enabled by observations of high-energy cosmic neutrinos, *Bulletin of the American Astronomical Society* **51** (2019). arXiv:1903.04334.

[19] M. G. Aartsen, *et al.*, Observation of High-Energy Astrophysical Neutrinos in Three Years of IceCube Data, *Physical Review Letters* **113** (2014). arXiv:1405.5303.

[20] K. Kotera, *et al.*, Cosmogenic neutrinos: parameter space and detectabilty from pev to zev, *Journal of Cosmology and Astroparticle Physics* **2010** (2010). arXiv:1009.1382.

[21] R. A. Batista, *et al.*, Cosmogenic photon and neutrino fluxes in the auger era, *Journal of Cosmology and Astroparticle Physics* **2019** (2019). arXiv:1806.10879.

[22] D. Ardouin, *et al.*, Geomagnetic origin of the radio emission from cosmic ray induced air showers observed by CODALEMA, *Astroparticle Physics* **31** (2009). arXiv:0901.4502.

[23] J. Alvarez-Muiz, *et al.*, The Giant Radio Array for Neutrino Detection (GRAND): Science and Design, *Science China Physics, Mechanics & Astronomy* **63** (2020). arXiv:1810.09994.

[24] A. Corstanje, *et al.*, The shape of the radio wavefront of extensive air showers as measured with lofar, *Astroparticle Physics* **61** (2015). arXiv:1404.3907.

[25] A. Aab, *et al.*, Energy Estimation of Cosmic Rays with the Engineering Radio Array of the Pierre Auger Observatory, *Physical Review D* **93** (2016). arXiv:1508.04267.

[26] A. Aab, *et al.*, Observation of inclined EeV air showers with the radio detector of the Pierre Auger Observatory, *Journal of Cosmology and Astroparticle Physics* **1810** (2018). arXiv:1806.05386.

[27] M. Gottowik, Measurements of Horizontal Air Showers with the Auger Engineering Radio Array, *EPJ Web Conf.* **216** (2019).

[28] T. Huege, Radio detection of cosmic rays with the auger engineering radio array, *EPJ Web of Conferences* **210** (2019). arXiv:1905.04986.

[29] D. Charrier, *et al.*, Autonomous radio detection of air showers with the TREND50 antenna array, *Astroparticle Physics* **110** (2019). arXiv:1810.03070.

[30] S. Mereghetti, *et al.*, INTEGRAL discovery of a burst with associated radio emission from the magnetar SGR 1935+2154, *pre-print* ∼ (2020). arXiv:2005.06335.

[31] The CHIME/FRB Collaboration, A bright millisecond-duration radio burst from a galactic magnetar, *pre-print* ∼ (2020). arXiv:2005.10324.

[32] K. Murase, *et al.*, Probing the birth of fast rotating magnetars through high-energy neutrinos, *Physical Review D* **79** (2009). arXiv:0904.2509.

[33] K. Kotera, A. V. Olinto, The astrophysics of ultrahigh-energy cosmic rays, *Annual Review of Astronomy and Astrophysics* **49** (2011). arXiv:1101.4256.

[34] K. Fang, *et al.*, Testing the Newborn Pulsar Origin of Ultrahigh Energy Cosmic Rays with EeV Neutrinos, *Physical Review D* **90** (2014). [Erratum: Phys.Rev.D 92, 129901 (2015)], arXiv:1311.2044.

[35] K. Kotera, J. Silk, Ultrahigh-energy Cosmic Rays and Black Hole Mergers, *The Astrophysical Journal: Letter* **823** (2016). arXiv:1602.06961.

[36] V. Decoene, *et al.*, High-energy neutrinos from fallback accretion of binary neutron star merger remnants, *Journal of Cosmology and Astroparticle Physics* **2020** (2020). arXiv:1910.06578.

[37] V. Decoene, *et al.*, Radio-detection of neutrino-induced air showers: influence of topography, *pre-print* ∼ (2019). arXiv:1903.10466.

[38] NenuFAR, `https://nenufar.obs-nancay.fr/en/astronomer/`.

[39] C. Guépin, K. Kotera, Can we observe neutrino flares in coincidence with explosive transients?, *Astronomy & Astrophysics* **603** (2017). arXiv:1701.07038.

[40] T. M. Venters, *et al.*, Poemma's target of opportunity sensitivity to cosmic neutrino transient sources, *pre-print* $\sim$ (2019). arXiv:1906.07209.

[41] S. S. Kimura, *et al.*, High-energy Neutrino Emission from Short Gamma-Ray Bursts: Prospects for Coincident Detection with Gravitational Waves, *The Astrophysical Journal: Letters* **848** (2017). arXiv:1708.07075.

[42] S. S. Kimura, *et al.*, Super-knee Cosmic Rays from Galactic Neutron Star Merger Remnants, *The Astrophysical Journal* **866** (2018). arXiv:1807.03290.

[43] D. Biehl, *et al.*, Expected neutrino fluence from short Gamma-Ray Burst 170817A and off-axis angle constraints, *Monthly Notices of the Royal Astronomical Society* **476** (2018). arXiv:1712.00449.

[44] S. S. Kimura, *et al.*, Transejecta high-energy neutrino emission from binary neutron star mergers, *Physical Review D* **98** (2018). arXiv:1805.11613.

[45] M. Ahlers, L. Halser, Neutrino fluence from gamma-ray bursts: off-axis view of structured jets, *Monthly Notices of the Royal Astronomical Society* **490** (2019). 1908.06953.

[46] B. D. Metzger, *et al.*, Electromagnetic counterparts of compact object mergers powered by the radioactive decay of r-process nuclei, *Monthly Notices of the Royal Astronomical Society* **406** (2010). arXiv:1001.5029.

[47] X. Rodrigues, *et al.*, Leptohadronic Blazar Models Applied to the 2014-2015 Flare of TXS 0506+056, *Astrophysical Journal* **874** (2019). arXiv:1812.05939.

[48] K. Fang, B. D. Metzger, High-energy Neutrinos from Millisecond Magnetars Formed from the Merger of Binary Neutron Stars, *The Astrophysical Journal* **849** (2017). arXiv:1707.04263.

[49] R. Narayan, *et al.*, Gamma-ray bursts as the death throes of massive binary stars, *The Astrophysical Journal: Letters* **395** (1992). arXiv:astro-ph/9204001.

[50] M. A. Aloy, *et al.*, Relativistic outflows from remnants of compact object mergers and their viability for short gamma-ray bursts, *Astronomy & Astrophysics* **436** (2005). arXiv:astro-ph/0408291.

[51] L. Rezzolla, *et al.*, Accurate evolutions of unequal-mass neutron-star binaries: properties of the torus and short GRB engines, *Classical and Quantum Gravity* **27** (2010). arXiv:1001.3074.

[52] M. Ruiz, *et al.*, Binary Neutron Star Mergers: A Jet Engine for Short Gamma-Ray Bursts, *The Astrophysical Journal: Letters* **824** (2016). arXiv:1604.02455.

[53] T. Liu, *et al.*, Neutrino-dominated accretion flows as the central engine of gamma-ray bursts, *New Astronomy Reviews* **79** (2017). arXiv:1705.05516.

[54] J. P. Norris, J. T. Bonnell, Short Gamma-Ray Bursts with Extended Emission, *The Astrophysical Journal* **643** (2006). arXiv:astro-ph/0601190.

[55] H. Gao, *et al.*, Possible High-Energy Neutrino and Photon Signals from Gravitational Wave Bursts due to Double Neutron Star Mergers, *Physical Review* **D88** (2013). arXiv:1306.3006.

[56] T. Di Matteo, *et al.*, Neutrino Trapping and Accretion Models for Gamma-Ray Bursts, *The Astrophysical Journal* **579** (2002). arXiv:astro-ph/0207319.

[57] E. M. Rossi, M. C. Begelman, Delayed X-ray emission from fallback in compact-object mergers, *Monthly Notices of The Royal Astronomical Society* **392** (2009). arXiv:0808.1284.

[58] K. Fang, *et al.*, Newly born pulsars as sources of ultrahigh energy cosmic rays, *The Astrophysical Journal* **750** (2012). arXiv:1201.5197.

[59] C. D. Dermer, G. Menon, *High Energy Radiation from Black Holes: Gamma Rays, Cosmic Rays, and Neutrinos* (Princeton University Press, 2009).

[60] C. Guépin, Chasing the cosmic accelerators with high energy astroparticles, Ph.D. thesis, Sorbonne Université, Université Pierre et Marie Curie, Paris 6 (2019).

[61] M. Lemoine, E. Waxman, Anisotropy vs chemical composition at ultra-high energies, *Journal of Cosmology and Astroparticle Physics* **2009** (2009). arXiv:0907.1354.

[62] S. Mollerach, E. Roulet, Magnetic diffusion effects on the ultra-high energy cosmic ray spectrum and composition, *Journal of Cosmology and Astroparticle Physics* **10** (2013). arXiv:1305.6519.

[63] L. D. Landau, E. M. Lifshitz, *The classical theory of fields* (Butterworth-Heinemann, 1975).

[64] J. D. Jackson, *Classical Electrodynamics, 3rd Edition* (John Wiley & Sons, 1998).

[65] A. Y. Prosekin, *et al.*, Synchrotron-to-curvature transition regime of radiation of charged particles in a dipole magnetic field, *pre-print* $\sim$ (2013). arXiv:1305.0783.

[66] S. Weinberg, *The Quantum Theory of Fields* (Cambridge University Press, 1995).

[67] M. J. Chodorowski, *et al.*, Reaction Rate and Energy-Loss Rate for Photopair Production by Relativistic Nuclei, *The Astrophysical Journal* **400** (1992).

[68] J. P. Rachen, Interaction processes and statistical properties of the propagation of cosmic-rays in photon backgrounds, Phd thesis, Bonn University (1996).

[69] A. M. Atoyan, C. D. Dermer, Neutral beams from blazar jets, *The Astrophysical Journal* **586** (2003). arXiv:astro-ph/0209231.

[70] M. Ruffert, *et al.*, Coalescing neutron stars - a step towards physical models. II. Neutrino emission, neutron tori, and gamma-ray bursts., *Astronomy & Astrophysics* **319** (1997). arXiv:astro-ph/9606181.

[71] M. Shibata, *et al.*, Merger of binary neutron stars of unequal mass in full general relativity, *Physical Review D* **68** (2003). arXiv:gr-qc/0310030.

[72] S. Rosswog, *et al.*, Accretion dynamics in neutron star-black hole binaries, *Monthly Notice of the Royal Astronomical Society* **351** (2004). arXiv:astro-ph/0403500.

[73] R. Popham, *et al.*, Hyperaccreting Black Holes and Gamma-Ray Bursts, *The Astrophysical Journal* **518** (1999). arXiv:astro-ph/9807028.

[74] R. Narayan, *et al.*, Accretion Models of Gamma-Ray Bursts, *The Astrophysical Journal* **557** (2001). arXiv:astro-ph/0103360.

[75] D. M. Siegel, B. D. Metzger, Three-dimensional GRMHD simulations of neutrino-cooled accretion disks from neutron star mergers, *The Astrophysical Journal* **858** (2018). arXiv:1711.00868.

[76] W.-X. Chen, A. M. Beloborodov, Neutrino-cooled accretion disks around spinning black holes, *The Astrophysical Journal* **657** (2007).

[77] B. D. Metzger, *et al.*, Time-dependent models of accretion discs formed from compact object mergers, *Monthly Notice of the Royal Astronomical Society* **390** (2008). arXiv:0805.4415.

[78] S. Rosswog, Fallback accretion in the aftermath of a compact binary merger, *Monthly Notices of the Royal Astronomical Society: Letters* **376** (2007). arXiv:astro-ph/0611440.

[79] B. D. Metzger, Kilonovae, *Living Reviews in Relativity* **20** (2017). arXiv:1610.09381.

[80] R. Fernández, *et al.*, Dynamics, nucleosynthesis, and kilonova signature of black hole-neutron star merger ejecta, *Classical and Quantum Gravity* **34** (2017). arXiv:1612.04829.

[81] R. Margutti, *et al.*, The Binary Neutron Star Event LIGO/Virgo GW170817 160 Days after Merger: Synchrotron Emission across the Electromagnetic Spectrum, *The Astrophysical Journal* **856** (2018). arXiv:1801.03531.

[82] D. M. Siegel, B. D. Metzger, Three-Dimensional General-Relativistic Magnetohydrodynamic Simulations of Remnant Accretion Disks from Neutron Star Merg-

ers: Outflows and r-Process Nucleosynthesis, *Physical Review Letters* **119** (2017). arXiv:1705.05473.

[83] W. E. East, *et al.*, Binary neutron star mergers: Effects of spin and post-merger dynamics, *Physical Review D* **100** (2019). arXiv:1906.05288.

[84] The LIGO Scientific Collaboration, the Virgo Collaboration, GW190425: Observation of a Compact Binary Coalescence with Total Mass $\sim 3.4 M_\odot$, *arXiv e-prints* (2020). arXiv:2001.01761.

[85] R. Narayan, I.-s. Yi, Advection dominated accretion: Selfsimilarity and bipolar outflows, *The Astrophysical Journal* **444** (1995). arXiv:astro-ph/9411058.

[86] J. W. Lynn, *et al.*, Acceleration of Relativistic Electrons by Magnetohydrodynamic Turbulence: Implications for Non-thermal Emission from Black Hole Accretion Disks, *The Astrophysical Journal* **791** (2014). arXiv:1403.3123.

[87] N. I. Shakura, R. A. Sunyaev, Black holes in binary systems. Observational appearance, *Astronomy & Astrophysics* **24** (1973).

[88] M. A. Abramowicz, P. Fragile, Foundations of Black Hole Accretion Disk Theory, *Living Reviews in Relativity* **16** (2013). arXiv:1104.5499.

[89] S. R. Kelner, *et al.*, Energy spectra of gamma rays, electrons, and neutrinos produced at proton-proton interactions in the very high energy regime, *Physical Review D* **74** (2006). arXiv:astro-ph/0606058.

[90] M. A. Riquelme, *et al.*, Local Two-dimensional Particle-in-cell Simulations of the Collisionless Magnetorotational Instability, *The Astrophysical Journal* **755** (2012). arXiv:1201.6407.

[91] M. Hoshino, Particle Acceleration during Magnetorotational Instability in a Collisionless Accretion Disk, *Astrophysical Journal* **773** (2013). arXiv:1306.6720.

[92] M. Hoshino, Angular Momentum Transport and Particle Acceleration during Magnetorotational Instability in a Kinetic Accretion Disk, *Physical Review Letters* **114** (2015). arXiv:1502.02452.

[93] S. S. Kimura, *et al.*, Neutrino and Cosmic-Ray Emission and Cumulative Background from Radiatively Inefficient Accretion Flows in Low-luminosity Active Galactic Nuclei, *The Astrophysical Journal* **806** (2015). arXiv:1411.3588.

[94] J. Dexter, D. Kasen, Supernova Light Curves Powered by Fallback Accretion, *The Astrophysical Journal* **772** (2013). arXiv:1210.7240.

[95] E. V. Derishev, *et al.*, Particle acceleration through multiple conversions from charged into neutral state and back, *Physical Review* **D68** (2003). arXiv:astro-ph/0301263.

[96] K. Kashiyama, *et al.*, Neutron-Proton-Converter Acceleration Mechanism at Subphotospheres of Relativistic Outflows, *Physical Review Letters* **111** (2013). arXiv:1304.1945.

[97] S.-Z. Li, Y.-W. Yu, Shock breakout driven by the remnant of a neutron star binary merger: An X-ray precursor of mergernova emission, *Astrophysical Journal* **819** (2016). arXiv:1511.01229.

[98] D. Xiao, *et al.*, High-energy Neutrino Emission from White Dwarf Mergers, *The Astrophysical Journal* **832** (2016). arXiv:1608.08150.

[99] T. Kawamura, *et al.*, Binary neutron star mergers and short gamma-ray bursts: Effects of magnetic field orientation, equation of state, and mass ratio, *Physical Review D* **94** (2016). arXiv:1607.01791.

[100] R. Ciolfi, *et al.*, General relativistic magnetohydrodynamic simulations of binary neutron star mergers forming a long-lived neutron star, *Physical Review D* **95** (2017). arXiv:1701.08738.

[101] R. Ciolfi, *et al.*, First 100 ms of a long-lived magnetized neutron star formed in a binary neutron star merger, *Physical Review D* **100** (2019). arXiv:1904.10222.

[102] L. Comisso, L. Sironi, The interplay of magnetically-dominated turbulence and magnetic reconnection in producing nonthermal particles, *The Astrophysical Journal* **886** (2019). arXiv:1909.01420.

[103] F. Guo, *et al.*, Particle acceleration and plasma dynamics during magnetic reconnection in the magnetically-dominated regime, *The Astrophysical Journal* **806** (2015). arXiv:1504.02193.

[104] L. Sironi, A. Spitkovsky, Relativistic Reconnection: an efficient source of non-thermal particles, *The Astrophysical Journal* **783** (2014). arXiv:1401.5471.

[105] D. A. Uzdensky, Magnetic reconnection in extreme astrophysical environments, *Space Science Reviews* **160** (2011). arXiv:1101.2472.

[106] D. Giannios, UHECRs from magnetic reconnection in relativistic jets, *Monthly Notices of the Royal Astronomical Society* **408** (2010). arXiv:1007.1522.

[107] E. G. Zweibel, M. Yamada, Magnetic Reconnection in Astrophysical and Laboratory Plasmas, *Annual Review of Astronomy and Astrophysics* **47** (2009).

[108] T. Miwa, *et al.*, Accretion Corona Immersed in Disk Radiation Fields, *Publication of the Astronomical Society of Japan* **50** (1998).

[109] M. R. Drout, *et al.*, Light curves of the neutron star merger GW170817/SSS17a: Implications for r-process nucleosynthesis, *Science* **358** (2017). arXiv:1710.05443.

[110] M. Shibata, K. Hotokezaka, Merger and Mass Ejection of Neutron-Star Binaries, *Annual Review of Nuclear and Particle Science* (2019). arXiv:1908.02350.

[111] J. Barnes, *et al.*, Radioactivity and Thermalization in the Ejecta of Compact Object Mergers and Their Impact on Kilonova Light Curves, *The Astrophysical Journal* **829** (2016). arXiv:1605.07218.

[112] O. Korobkin, *et al.*, On the astrophysical robustness of the neutron star merger r-process, *Monthly Notices of the Royal Astronomical Society* **426** (2012). 1206.2379.

[113] D. Kasen, *et al.*, Origin of the heavy elements in binary neutron-star mergers from a gravitational wave event, *Nature* (2017). [Nature551,80(2017)], arXiv:1710.05463.

[114] R. Chornock, *et al.*, The Electromagnetic Counterpart of the Binary Neutron Star Merger LIGO/VIRGO GW170817. IV. Detection of Near-infrared Signatures of r-process Nucleosynthesis with Gemini-South, *Astrophys. J.* **848** (2017). arXiv:1710.05454.

[115] R. Alves Batista, *et al.*, CRPropa 3 a public astrophysical simulation framework for propagating extraterrestrial ultra-high energy particles, *Journal of Cosmology and Astroparticles Physics* **5** (2016). arXiv:1603.07142.

[116] K. Kotera, *et al.*, Propagation of Ultrahigh Energy Nuclei in Clusters of Galaxies: Resulting Composition and Secondary Emissions, *The Astrophysical Journal* **707** (2009). arXiv:0907.2433.

[117] A. Mücke, *et al.*, Monte Carlo simulations of photohadronic processes in astrophysics, *Computer Physics Communications* **124** (2000). arXiv:astro-ph/9903478.

[118] A. J. Koning, *et al.*, Talys: Comprehensive nuclear reaction modeling, *AIP Conference Proceedings* **769** (2005).

[119] K. Werner, *et al.*, Parton ladder splitting and the rapidity dependence of transverse momentum spectra in deuteron gold collisions at RHIC, *Physical Review* **C74** (2006). arXiv:hep-ph/0506232.

[120] E. Waxman, J. N. Bahcall, High-energy neutrinos from cosmological gamma-ray burst fireballs, *Physical Review Letters* **78** (1997). arXiv:astro-ph/9701231.

[121] N. Kaiser, J. M. Friedrich, Cross-sections for low-energy pi- gamma reactions, *European Physical Journal* **A36** (2008). arXiv:0803.0995.

[122] IceCube-Gen2 Collaboration, Icecube-gen2: A vision for the future of neutrino astronomy in antarctica, *pre-print* ~ (2014). arXiv:1412.5106.

[123] M. Bustamante, M. Ahlers, Inferring the Flavor of High-Energy Astrophysical Neutrinos at Their Sources, *Physical Review Letters* **122** (2019). arXiv:1901.10087.

[124] N. Aghanim, *et al.*, Planck 2018 results. VI. Cosmological parameters, *pre-print* ∼ (2018). arXiv:1807.06209.

[125] M. Chruslinska, *et al.*, Double neutron stars: merger rates revisited, *Monthly Notices of the Royal Astronomical Society* **474** (2018). arXiv:1708.07885.

[126] M. Saleem, *et al.*, Rates of short-GRB afterglows in association with binary neutron star mergers, *Monthly Notices of the Royal Astronomical Society* **475** (2018). arXiv:1710.06111.

[127] K. A. Postnov, L. R. Yungelson, The Evolution of Compact Binary Star Systems, *Living Reviews in Relativity* **17** (2014). arXiv:1403.4754.

[128] M. Dominik, *et al.*, Double Compact Objects. II. Cosmological Merger Rates, *The Astrophysical Journal* **779** (2013). arXiv:1308.1546.

[129] G. Ghirlanda, *et al.*, Short gamma-ray bursts at the dawn of the gravitational wave era, *Astronomy & Astrophysics* **594** (2016). arXiv:1607.07875.

[130] M. Chruslinska, Local merger rates of double neutron stars, *International Astronomical Union Symposium* (2018). arXiv:1811.09296.

[131] A. M. Hopkins, J. F. Beacom, On the normalisation of the cosmic star formation history, *Astrophysical Journal* **651** (2006). arXiv:astro-ph/0601463.

[132] K. Kotera, *et al.*, Cosmogenic neutrinos: parameter space and detectabilty from PeV to ZeV, *Journal of Cosmology and Astroparticle Physics* **2010** (2010). arXiv:1009.1382.

[133] M. G. Aartsen, *et al.*, Observation and characterization of a cosmic muon neutrino flux from the northern hemisphere using six years of icecube data, *The Astrophysical Journal* **833** (2016). arXiv:1607.08006.

[134] K. Fang, *et al.*, A cross-correlation study of high-energy neutrinos and tracers of large-scale structure, *The Astrophysical Journal* **894** (2020). arXiv:2002.06234.

[135] K. Fang, *et al.*, Identifying ultrahigh-energy cosmic-ray accelerators with future ultrahigh-energy neutrino detectors, *Journal of Cosmology and Astroparticle Physics* **12** (2016). arXiv:1609.08027.

[136] M. H. Reno, High energy neutrino cross sections, *Nuclear Physics B Proceedings Supplements* **143** (2005). arXiv:hep-ph/0410109.

[137] D. Fargion, *et al.*, *Proceedings, 26th International Cosmic Ray Conference, August 17-25, 1999, Salt Lake City: Invited, Rapporteur, and Highlight Papers* (1999), p. 396. [2,396(1999)].

[138] T. K. Gaisser, *et al.*, *Cosmic Rays and Particle Physics* (Cambridge University Press, 2016).

[139] S. Jansen, Radio for the masses - Cosmic ray mass composition measurements in the radio frequency domain, Ph.D. thesis, Radboud University (2016).

[140] Huege, T., Falcke, H., Radio emission from cosmic ray air showers - coherent geosynchrotron radiation, *Astronomy & Astrophysics* **412** (2003). arXiv:astro-ph/0309622.

[141] H. A. Bethe, Molière's Theory of Multiple Scattering, *Physical Review* **89** (1953).

[142] R. Engel, *et al.*, Extensive air showers and hadronic interactions at high energy, *Annual Review of Nuclear and Particle Science* **61** (2011).

[143] G. Agnetta, *et al.*, Time structure of the extensive air shower front, *Astroparticle Physics* **6** (1997).

[144] K. Kamata, J. Nishimura, The Lateral and the Angular Structure Functions of Electron Showers, *Progress of Theoretical Physics Supplement* **6** (1958).

[145] K. Greisen, Properties of EAS, *Journal of the Physical Society of Japan Supplement* **17** (1962).

[146] M. Dova, *et al.*, The effect of atmospheric attenuation on inclined cosmic ray air showers, *Astroparticle Physics* **18** (2003). arXiv:astro-ph/0110237.

[147] W. Heitler, *The quantum theory of radiation*, vol. 5 of *International Series of Monographs on Physics* (Oxford University Press, Oxford, 1936).

[148] J. F. Carlson, J. R. Oppenheimer, On multiplicative showers, *Physical Review* **51** (1937).

[149] J. Linsley, *International Cosmic Ray Conference* (1977), vol. 12 of *International Cosmic Ray Conference*, p. 89.

[150] J. Matthews, A Heitler model of extensive air showers, *Astroparticle Physics* **22** (2005).

[151] S. Lafebre, *et al.*, Universality of electron-positron distributions in extensive air showers, *Astroparticle Physics* **31** (2009). arXiv:0902.0548.

[152] A. Aab, *et al.*, Measurement of the radiation energy in the radio signal of extensive air showers as a universal estimator of cosmic-ray energy, *Physical Review Letters* **116** (2016). arXiv:1605.02564.

[153] F. G. Schröder, Radio detection of Cosmic-Ray Air Showers and High-Energy Neutrinos, *Progress in Particle and Nuclear Physics* **93** (2017). arXiv:1607.08781.

[154] J. Alvarez-Muñiz, *et al.*, Search for microwave emission from ultrahigh energy cosmic rays, *Physical Review D* **86** (2012). arXiv:1205.5785.

[155] K. D. de Vries, *et al.*, The air shower maximum probed by Cherenkov effects from radio emission, *Astroparticle Physics* **45** (2013). arXiv:1304.1321.

[156] A. Zilles, *et al.*, Radio Morphing: towards a fast computation of the radio signal from air showers, *Astropart. Phys.* **114** (2020). arXiv:1811.01750.

[157] F. D. Kahn, *et al.*, Radiation from cosmic ray air showers, *Proceedings of the Royal Society A - Maths and Physics* **A-289** (1966).

[158] O. Scholten, *et al.*, What the radio signal tells about the cosmic-ray air shower, *EPJ Web Conf.* **53** (2013). arXiv:1207.1874.

[159] G. A. Askar'yan, Excess negative charge of an electron-photon shower and its coherent radio emission, *Soviet Physical JETP* **14** (1962). [Zh. Eksp. Teor. Fiz.41,616(1961)].

[160] D. Saltzberg, *et al.*, Observation of the askaryan effect: Coherent microwave cherenkov emission from charge asymmetry in high-energy particle cascades, *Physical Review Letters* **86** (2001). arXiv:hep-ex/0011001.

[161] O. Scholten, *et al.*, A macroscopic description of coherent geo-magnetic radiation from cosmic-ray air showers, *Astroparticle Physics* **29** (2008). arXiv:0709.2872.

[162] S. Buitink, *et al.*, Simulation of radio emission from air showers in atmospheric electric fields, *Astroparticle Physics* **33** (2010). arXiv:1002.4849.

[163] K. D. de Vries, S. Prohira, Coherent transition radiation from the geomagnetically induced current in cosmic-ray air showers: Implications for the anomalous events observed by ANITA, *Physical Review Letters* **123** (2019). arXiv:1903.08750.

[164] S. Prohira, *et al.*, Observation of radar echoes from high-energy particle cascades, *Physical Review Letters* **124** (2020). arXiv:1910.12830.

[165] C. W. James, *et al.*, General description of electromagnetic radiation processes based on instantaneous charge acceleration in 'endpoints', *Physical Review E* **84** (2011). arXiv:1007.4146.

[166] J. Alvarez-Muiz, *et al.*, Monte carlo simulations of radio pulses in atmospheric showers using zhaires, *Astroparticle Physics* **35** (2012). arXiv:1107.1189.

[167] T. Huege, *et al.*, Simulating radio emission from air showers with CoREAS, *AIP Conf. Proc.* **1535** (2013). arXiv:1301.2132.

[168] S. J. Sciutto, AIRES: A system for air shower simulations (1999).

[169] D. Heck, *et al.*, CORSIKA: A Monte Carlo code to simulate extensive air showers (1998).

[170] A. Fedynitch, *et al.*, Hadronic interaction model sibyll 2.3c and inclusive lepton fluxes, *Physical Review D* **100** (2019). arXiv:1806.04140.

[171] T. Pierog, K. Werner, EPOS model and ultra high energy cosmic rays, *Nuclear Physics B - Proceedings Supplements* **196** (2009). arXiv:0905.1198.

[172] E. Zas, *et al.*, Electromagnetic pulses from high-energy showers: Implications for neutrino detection, *Physical Review D* **45** (1992).

[173] N. O. National Aerospace Administration (NASA), A. A. (NOAA), U. A. Force, Us standard atmosphere 1976, NASA technical report NASA-TM-X-74335, *NOAA technical report* **NOAA-S/T-76-1562** (1976).

[174] N. C. Gerson, Variations in the index of refraction of the atmosphere, *Geofisica Pura e Applicata* **13** (1948).

[175] C. A. Balanis, *Antenna theory : analysis and design* (John Wiley & Sons, 2012, 2005).

[176] T. Huege, Radio detection of cosmic ray air showers in the digital era, *Physical Reports* **620** (2016). arXiv:1601.07426.

[177] J. V. Jelley, *et al.*, Radio Pulses from Extensive Cosmic-Ray Air Showers, *Nature* **205** (1965).

[178] H. R. Allan, J. K. Jones, Radio Pulses from Extensive Air Showers, *Nature* **212** (1966).

[179] D. Ardouin, *et al.*, Radio-detection signature of high-energy cosmic rays by the codalema experiment, *Nuclear Instruments and Methods in Physics Research Section A* **555** (2005). arXiv:astro-ph/0504297.

[180] H. Falcke, *et al.*, Detection and imaging of atmospheric radio flashes from cosmic ray air showers, *Nature* **435** (2005). arXiv:astro-ph/0505383.

[181] P. Gorham, *et al.*, The antarctic impulsive transient antenna ultra-high energy neutrino detector: Design, performance, and sensitivity for the 2006-2007 balloon flight, *Astroparticle Physics* **32** (2009).

[182] C. Deaconu, Searches for ultra-high energy neutrinos with anita, *Proceedings of Science (ICRC2019)* **867** (2019). arXiv:1908.00923.

[183] P. Allison, *et al.*, Performance of two Askaryan Radio Array stations and first results in the search for ultrahigh energy neutrinos, *Physical Review D* **93** (2016). arXiv:1507.08991.

[184] A. Anker, *et al.*, Targeting ultra-high energy neutrinos with the ARIANNA experiment, *Advances in Space Research* **64** (2019). arXiv:1903.01609.

[185] J. A. Aguilar, *et al.*, The next-generation radio neutrino observatory – multi-messenger neutrino astrophysics at extreme energies, *pre-print* ∼ (2019). arXiv:1907.12526.

[186] P. W. Gorham, *et al.*, Characteristics of four upward-pointing cosmic-ray-like events observed with ANITA, *Physical Review Letters* **117** (2016). arXiv:1603.05218.

[187] P. W. Gorham, *et al.*, Observation of an unusual upward-going cosmic-ray-like event in the third flight of ANITA, *Physical Review Letters* **121** (2018). arXiv:1803.05088.

[188] M. P. van Haarlem, *et al.*, Lofar: The low-frequency array, *Astronomy & Astrophysics* **556** (2013). arXiv:1305.3550.

[189] T. Asch, Self-triggering of radio signals from cosmic ray air showers, Ph.D. thesis, KIT, Karlsruhe (2008).

[190] A. Schmidt, Realization of a self-triggered detector for the radio emission of cosmic rays, Ph.D. thesis, KIT, Karlsruhe (2011).

[191] J. Alvarez-Muñiz, *et al.*, Simulations of reflected radio signals from cosmic ray induced air showers, *Astroparticle Physics* **66** (2015). arXiv:1502.02117.

[192] P. A. Bezyazeekov, *et al.*, Measurement of cosmic-ray air showers with the Tunka Radio Extension (Tunka-Rex), *Nuclear Instrumentation and Methods in Physics Research: A* **802** (2015). arXiv:1509.08624.

[193] S. Buitink, *et al.*, A large light-mass component of cosmic rays at $10^{17} - 10^{17.5}$ eV from radio observations, *Nature* **531** (2016). arXiv:1603.01594.

[194] D. Charrier, *et al.*, Autonomous radio detection of air showers with the TREND50 antenna array, *Astropart. Phys.* **110** (2019). arXiv:1810.03070.

[195] D. Ardouin, *et al.*, First detection of extensive air showers by the TREND self-triggering radio experiment, *Astropart. Phys.* **34** (2011). arXiv:1007.4359.

[196] V. Decoene, Grandproto300: a pathfinder with richastroparticle and radio-astronomy science case, *pre-print* ∼ (2019). arXiv:1909.04893.

[197] V. Niess, O. Martineau-Huynh, Danton: a monte-carlo sampler of τ from ν interacting with the earth, *pre-print* ∼ (2018). arXiv:1810.01978.

[198] V. Niess, Danton: Decaying taus from neutrinos, `https://github.com/niess/danton` (2017–2018). GitHub repository.

[199] G. Burke, *Numerical Electromagnetics Code – NEC-4, Method of Moments, Part I: User's Manual*, Lawrence Livermore National Lab. (1992). Rept. URCL-MA-109338 Pt. I.

[200] K. Fang, *et al.*, The Giant Radio Array for Neutrino Detection (GRAND): Present and Perspectives, *Proceedings of Science* **ICRC2017** (2018). arXiv:1708.05128.

[201] J. Alvarez-Muñiz, *et al.*, Comprehensive approach to tau-lepton production by high-energy tau neutrinos propagating through the Earth, *Physical Review D* **97** (2018). arXiv:1707.00334.

[202] V. Niess, *et al.*, TURTLE: A C library for an optimistic stepping through a topography, *Computer Physics Communications* **247** (2020). arXiv:1904.03435.

[203] A. M. Dziewonski, D. L. Anderson, Preliminary reference earth model, *Physics of the Earth and Planetary Interiors* **25** (1981).

[204] See the following link to the pdg for a discussion about standard rock, `http://pdg.lbl.gov/2015/AtomicNuclearProperties/standardrock.html`.

[205] D. Charrier, *et al.*, Antenna development for astroparticle and radioastronomy experiments, *Nuclear Instrumentation and Methods in Physics Research: A* **662** (2012).

[206] D. García-Fernández, The CODALEMA/EXTASIS experiment: Contributions to the 35th International Cosmic Ray Conference (ICRC 2017), *Proceedings of Science* **ICRC2017** (2018). arXiv:1710.02487.

[207] P. Abreu, *et al.*, Antennas for the detection of radio emission pulses from cosmic-ray, *JINST* **7** (2012). arXiv:1209.3840.

[208] Q. Gou, *et al.*, The GRANDproto35 experiment, *Proceedings of Science* **ICRC2017** (2018).

[209] S. Butterworth, On the Theory of Filter Amplifiers, *Experimental Wireless and the Wireless Engineer* **7** (1930).

[210] F. Führer, *et al.*, Towards online triggering for the radio detection of air showers using deep neural networks, *Proceedings, Acoustic and Radio EeV Neutrino Detection Activities (ARENA 2018)* **216** (2019). arXiv:1809.01934.

[211] M. Erdmann, *et al.*, Classification and Recovery of Radio Signals from Cosmic Ray Induced Air Showers with Deep Learning, *JINST* **14** (2019). arXiv:1901.04079.

[212] H. Zheng, *et al.*, An improved model of diffuse galactic radio emission from 10 MHz to 5 THz, *Monthly Notices of the Royal Astronomical Society* **464** (2017). arXiv:1605.04920.

[213] T. K. Gaisser, *et al.*, Particle astrophysics with high energy neutrinos, *Physics Reports* **258** (1995). arXiv:hep-ph/9410384.

[214] W. Apel, *et al.*, The wavefront of the radio signal emitted by cosmic ray air showers, *Journal of Cosmology and Astroparticle Physics* **2014** (2014). arXiv:1404.3283.

[215] A. Aab, *et al.*, Probing the radio emission from air showers with polarization measurements, *Physical Review D* **89** (2014).

[216] C. Glaser, *et al.*, Simulation of radiation energy release in air showers, *Journal of Cosmology and Astroparticle Physics* **2016** (2016). arXiv:1609.05743.

[217] T. Huege, *et al.*, Symmetrizing the signal distribution of radio emission from inclined air showers, *pre-print* ∼ (2019). arXiv:1908.07840.

[218] F. Schlter, M. Gottowik, T. Huege, J. Rautenberg, Refractive displacement of the radio-emission footprint of inclined air showers simulated with coreas, *The European Physical Journal C* **80** (2020). arXiv:2005.06775.

[219] D. R. Lorimer, *et al.*, A Bright Millisecond Radio Burst of Extragalactic Origin, *Science* **318** (2007). arXiv:0709.4301.

[220] A. Josephy, *et al.*, CHIME/FRB detection of the original repeating fast radio burst source FRB 121102, *The Astrophysical Journal* **882** (2019). arXiv:1906.11305.

[221] D. R. Lorimer, A decade of fast radio bursts, *Nature Astronomy* **2** (2018). arXiv:1811.00195.

[222] C. W. James, Limits on the population of repeating fast radio bursts from the ASKAP/CRAFT lat50 survey, *Monthly Notices of the Royal Astronomical Society* **486** (2019). arXiv:1902.04932.

[223] The CHIME/FRB Collaboration, Periodic activity from a fast radio burst source, *Nature* **582** (2020). arXiv:2001.10275.

[224] C. K. Day, *et al.*, High time resolution and polarisation properties of askap-localised fast radio bursts, *pre-print* ∼ (2020). arXiv:2005.13162.

[225] E. Platts, *et al.*, A Living Theory Catalogue for Fast Radio Bursts, *arXiv e-prints* (2018). arXiv:1810.05836.

[226] FRB Theory Wiki, `https://frbtheorycat.org/index.php/Main_Page`.

[227] F. Mottez, P. Zarka, Radio emissions from pulsar companions: a refutable explanation for galactic transients and fast radio bursts, *Astronomy & Astrophysics* **569** (2014). arXiv:1408.1333.

[228] J. Saur, *et al.*, *Plasma interaction of Io with its plasma torus* (Fran Bagenal, University of Colorado, BoulderTimothy E. Dowling, University of Louisville, Kentucky William B. McKinnon, Washington University, St Louis, 2004).

[229] J. G. Kirk, *et al.*, *The Theory of Pulsar Winds and Nebulae* (Springer Berlin Heidelberg, 2009).

[230] F. Mottez, J. Heyvaerts, The magnetic coupling of planets and small bodies with a pulsar's wind, *Astronomy & Astrophysics* **532** (2011). arXiv:1210.0684.

[231] C. S. Wu, Kinetic cyclotron and synchrotron maser instabilities: Radio emission processes by direct amplification of radiation, *Space Science Reviews* **41** (1985).

[232] P. Zarka, *et al.*, Magnetically-Driven Planetary Radio Emissions and Application to Extrasolar Planets, *Astrophysics and Space Science* **277** (2001).

[233] S. Naoz, The eccentric kozai-lidov effect and its applications, *Annual Review of Astronomy and Astrophysics* **54** (2016). arXiv:1601.07175.

[234] J. J. Delgrande , S. V. Soanes, Kirkwood's Gap in the Asteroid Orbits, *Journal of the Royal Astronomical Society of Canada* **37** (1943).

[235] A. Wolszczan, D. A. Frail, A planetary system around the millisecond pulsar PSR1257 + 12, *Nature* **355** (1992).

[236] J. M. Cordes, R. M. Shannon, Rocking the Lighthouse: Circumpulsar Asteroids and Radio Intermittency, *The Astrophysical Journal* **682** (2008). arXiv:astro-ph/0605145.

[237] R. M. Shannon, *et al.*, An Asteroid Belt Interpretation for the Timing Variations of the Millisecond Pulsar B1937+21, *The Astrophysical Journal* **766** (2013). arXiv:1301.6429.

[238] P. R. Brook, *et al.*, Evidence of an Asteroid Encountering a Pulsar, *The Astrophysical Journal: Letter* **780** (2014). arXiv:1311.3541.

[239] Y.-B. Yu, Y.-F. Huang, Reduced spin-down rate of PSR J0738-4042 explained as due to an asteroid disruption event, *Research in Astronomy and Astrophysics* **16** (2016). arXiv:1503.01571.

[240] F. Mottez, *et al.*, Towards a theory of extremely intermittent pulsars. I. Does something orbit PSR B1931+24?, *Astronomy & Astrophysics* **555** (2013). arXiv:1305.6724.

[241] J. J. Geng, Y. F. Huang, Fast Radio Bursts: Collisions between Neutron Stars and Asteroids/Comets, *The Astrophysical Journal* **809** (2015). arXiv:1502.05171.

[242] Z. G. Dai, *et al.*, Repeating fast radio bursts from highly magnetized pulsars traveling through asteroid belts, *The Astrophysical Journal* **829** (2016). arXiv:1603.08207.

[243] J. L. Smallwood, *et al.*, Investigation of the asteroid–neutron star collision model for the repeating fast radio bursts, *Monthly Notices of the Royal Astronomical Society* **485** (2019).

[244] F. Mottez, *et al.*, Repeating fast radio bursts caused by small bodies orbiting a pulsar or a magnetar, *pre-print* $\sim$ (2020). arXiv:2002.12834.

[245] F. Mottez, *et al.*, Towards a theory of extremely intermittent pulsars. II. Asteroids at a close distance, *Astronomy & Astrophysics* **555** (2013). arXiv:1305.6726.

[246] K. Menou, *et al.*, Stability and Evolution of Supernova Fallback Disks, *The Astrophysical Journal* **559** (2001). arXiv:astro-ph/0102478.

[247] R. Shannon, *et al.*, A Search for Debris Disks around Variable Pulsars, *American Astronomical Society Meeting Abstracts* **213** (2008).

[248] A. Morbidelli, S. N. Raymond, Challenges in planet formation, *Journal of Geophysical Research: Planets* **121** (2016). arXiv:1610.07202.

[249] M. S. Sipior, *et al.*, Recycled pulsars with black hole companions: the high-mass analogues of PSR B2303+46, *Monthly Notices of the Royal Astronomical Society* **354** (2004).

[250] E. Pfahl, *et al.*, Relativistic binary pulsars with black hole companions, *The Astrophysical Journal* **628** (2005). arXiv:astro-ph/0502122.

[251] Y. Shao, X.-D. Li, Black hole/pulsar binaries in the galaxy, *Monthly Notices of the Royal Astronomical Society: Letters* **477** (2018). arXiv:1804.06014.

[252] M. U. Kruckow, *et al.*, Progenitors of gravitational wave mergers: binary evolution with the stellar grid-based code ComBinE, *Monthly Notices of the Royal Astronomical Society* **481** (2018). arXiv:1801.05433.

[253] C.-A. Faucher-Giguère, V. M. Kaspi, Birth and Evolution of Isolated Radio Pulsars, *The Astrophysical Journal* **643** (2006). arXiv:astro-ph/0512585.

[254] S. Johnston, A. Karastergiou, Pulsar braking and the $\mathrm{p}-\dot{P}$ diagram, *Monthly Notices of the Royal Astronomical Society* **467** (2017). arXiv:1702.03616.

[255] M. Gullón, *et al.*, Population synthesis of isolated neutron stars with magneto-rotational evolution, *Monthly Notices of the Royal Astronomical Society* **443** (2014). arXiv:1406.6794.

[256] Minor Planet Center orbit database, `https://minorplanetcenter.net/iau/lists/MPLists.html` (2019).

[257] Y. Ali-Haïmoud, *et al.*, Flaring of tidally compressed dark-matter clumps, *Physical Review D* **93** (2016). arXiv:1511.02232.

[258] K. Kotera, *et al.*, Do asteroids evaporate near pulsars? Induction heating by pulsar waves revisited, *Astronomy & Astrophysics* **592** (2016). arXiv:1605.05746.

[259] M. I. Mishchenko, *et al.*, Light scattering by nonspherical particles' 98: theory, measurements, and applications. Proceedings. Conference, New York, NY (USA), 29 Sep - 1 Oct 1998., *Journal of Quantitative Spectroscopy & Radiative Transfer* **63** (1999).

[260] P. B. Jones, Constraints on fall-back discs in radio pulsars and anomalous X-ray pulsars, *Monthly Notices of the Royal Astronomical Society* **386** (2008). arXiv:0802.0390.

[261] Y. G. Zhang, *et al.*, Fast Radio Burst 121102 Pulse Detection and Periodicity: A Machine Learning Approach, *The Astrophysical Journal* **866** (2018). arXiv:1809.03043.

[262] B. Liu, *et al.*, Suppression of extreme orbital evolution in triple systems with short-range forces, *Monthly Notices of the Royal Astronomical Society* **447** (2015). arXiv:1409.6717.

[263] H. Sana, *et al.*, Binary Interaction Dominates the Evolution of Massive Stars, *Science* **337** (2012). arXiv:1207.6397.

[264] P. Kroupa, *Initial Conditions for Star Clusters* (The Cambridge N-Body Lectures, 2008).

[265] D. Fabrycky, S. Tremaine, Shrinking binary and planetary orbits by kozai cycles with tidal friction, *The Astrophysical Journal* **669** (2007). arXiv:0705.4285.

[266] CHIME/FRB Collaboration, A second source of repeating fast radio bursts, *Nature* **566** (2019). arXiv:1901.04525.

[267] E. Fonseca, *et al.*, Nine new repeating fast radio burst sources from CHIME/FRB, *The Astrophysical Journal* **891** (2020). arXiv:2001.03595.

[268] A. Lamberts, *et al.*, Predicting the binary black hole population of the Milky Way with cosmological simulations, *Monthly Notices of the Royal Astronomical Society* **480** (2018). arXiv:1801.03099.

[269] P. C. Peters, Gravitational radiation and the motion of two point masses, *Physical Review* **136** (1964).

[270] B. Andersen, *et al.*, CHIME/FRB discovery of eight new repeating fast radio burst sources, *The Astrophysical Journal: Letters* **885** (2019). arXiv:1908.03507.

[271] P. Scholz, *et al.*, The repeating fast radio burst FRB121102: multi-wavelength observations and additional bursts, *The Astrophysical Journal* **833** (2016). arXiv:1603.08880.

[272] D. R. Lorimer, *et al.*, A Bright Millisecond Radio Burst of Extragalactic Origin, *Science* **318** (2007). arXiv:0709.4301.

[273] E. Petroff, *et al.*, FRBCAT: The Fast Radio Burst Catalogue, *Publications of the Astronomical Society of Australia* **33** (2016). arXiv:1601.03547.

[274] R. M. Shannon, *et al.*, The dispersion-brightness relation for fast radio bursts from a wide-field survey, *Nature* **562** (2018).

[275] M. Sokolowski, *et al.*, No Low-frequency Emission from Extremely Bright Fast Radio Bursts, *The Astrophysical Journal: Letter* **867** (2018). arXiv:1810.04355.

[276] P. Zarka, F. Mottez, Observations of Fast Radio Bursts and perspectives at low frequencies, *Proceedings of the Annual meeting of the French Society of Astronomy and Astrophysics (SF2A-2016)* (2016).

[277] C. H. Walter, *Traveling Wave Antennas* (Peninsula Publishing, Los Altos, California, 1990).

[278] B. J. Shapiro-Albert, *et al.*, Radio properties of rotating radio transients: Single-pulse spectral and wait-time analyses, *The Astrophysical Journal* **866** (2018). arXiv:1809.06729.

[279] V. Soglasnov, Amazing properties of giant pulses and the nature of pulsar's radio emission, *pre-print* $\sim$ (2007). arXiv:astro-ph/0701190.

[280] CHIME/FRB Collaboration, Observations of fast radio bursts at frequencies down to 400 megahertz, *Nature* **566** (2019). arXiv:1901.04524.

[281] J. J. Condon, S. M. Ransom, *Essential Radio Astronomy* (Princeton University Press, 2016).

[282] J. D. Turner, *et al.*, The search for radio emission from exoplanets using LOFAR low-frequency beam-formed observations: Data pipeline and preliminary results for the 55 Cnc system, *Planetary Radio Emissions VIII* (2017). arXiv:1710.04997.